

Solid-state NMR studies of globular and membrane proteins

Dissertation

Zur Erlangung des Doktorgrades
der Naturwissenschaften

vorgelegt beim Fachbereich chemische und pharmazeutische Wissenschaften (FB14)
der Johann Wolfgang Goethe Universität
in Frankfurt am Main

von

Sorin Luca

aus Bacau

Frankfurt 2003

(DF1)

Vom Fachbereich chemische und pharmazeutische Wissenschaften (FB14) der Johann Wolfgang Goethe Universität als Dissertation angenommen:

Dekan Prof. Dr. W. E. Müller

1. Gutachter Prof. Dr. H. Schwalbe

2. Gutachter Prof. Dr. C. Griesinger

“The spectrometer never lies ...”

*A Korean student visiting
our lab in summer 2001*

When I have finished my undergraduate studies in Physics at the University of Bucharest, Romania, in 1999, I was already very much interested in Biophysics. Actually, I joined the Biophysics department during my last year and worked for another half a year in the similar department at the Leiden University, Netherlands.

After completing my studies, I started my Ph.D. work with Dr. Marc Baldus, at that time also at the Leiden University. As you can expect from the title of this thesis, I was very happy about my future work. I take this opportunity to thank Marc again for accepting me as a Ph.D. student and for taking great care and time to teach me solid-state NMR. For me, working with him was an immense experience, for I have not only understood the technique and applied it to biology. More importantly, I have learnt from him (or at least I hope) to always look for the important questions that you would really like to answer.

During the six months we spent in Leiden, I, overexcited, assisted the installation of the first 750 MHz wide-bore NMR Bruker spectrometer. I want to thank Dr. Huub J. M. de Groot for some interesting scientific conversations we had and Johann Hollander for the nice atmosphere in the lab.

In spring 2000, Marc and I moved to the Max Planck Institute for Biophysical Chemistry in Göttingen, Germany. Initially, we have only been allocated some space and there was no equipment, not even computers. It took half a year until we had the 400 and 600 MHz wide-bore NMR spectrometers installed and fully operational. I thank Gitta Angerstein, the 'spirit' of our group, for her help from the very beginning. I would especially mention the packing of NMR rotors with an ultracentrifuge and all the many administrative problems.

One of the first 'acquisitions' to the group was Adam Lange. I have really enjoyed spending time with him on the spectrometers or answering his many questions. At the time, we started the nice lunch walks to Nordmensa. His initial work on $^{13}\text{C}/^{15}\text{N}$ indirect proton-detection finalized with the establishment of the C/NHHC experiments presented in Section 3.2. Lars Sonnenberg was the second diploma student to join our group and the lunch walks as well. I occasionally helped him on his work on selective ^{13}C - ^{13}C dipolar recoupling and we spent together some interesting time on the spectrometers or getting the simulations running on the NuMeRiCa cluster. Some of the results of this work are described in Section 3.3.

In time, more people joined the group and I would like to acknowledge all of them for the great and nice atmosphere in the lab and for all scientific and other discussions we have had: Karsten Seidel (thanks for the help with TALOS and CNS), Ovidiu Andronesi, Dr. Henrike Heise, Dr. Colan Hughes and Manuel Etzkorn. I also thank Dr. Stefan Becker for his advice and for clarifying my naive questions related to molecular biology.

One of my projects, as described in section 4.2, was concerned with the binding motif of neurotensin, a GPCR-ligand peptide. This work would not have been possible without the expert collaboration with Dr. Reinhard Grisshammer and I want to take this opportunity to thank him. Although the motto of this thesis seemed challenged at times, thanks to the people working at Bruker we were always able to prove it right. I want to thank Walter Knöller and Dr. Hans Förster for their help and advice related to the magnets and spectrometers.

I want to thank our director, Prof. Dr. Christian Griesinger, for the work and effort in setting up the NMR facility for structural biology at the Max Planck Institute. I am happy to have worked in this big NMR centre and 'cathedral' will always have an extra meaning for me!

I would like to thank Prof. Dr. Christian Griesinger and Prof. Dr. Harald Schwalbe for critically reading the manuscript to this thesis. To them and to Prof. Dr. Clemens Glaubitz and Prof. Dr. Ulrich Brandt I am indebted for agreeing to participate in the defense of this thesis.

I am also indebted to Florescu Dragos, the professor who have taught me Physics during the high-school. Several of his former students are scattered around the world and are involved in different areas of research. This is certainly correlated to his passion for teaching this subject and I would like to thank him and express my great respect.

As for my parents, I cannot find proper words to thank for their continuous support during the years I have spent in Romania. I hope that they are happy about what I do and that they can better endure my being so far away from home.

To my dear wife, Oana, special thanks for your support and patience during these three years in Göttingen. I would not have so easily passed the difficult moments and I would not have enjoyed more the moments of success without you.

Sunt de asemenea indatorat profesorului Florescu Dragos, de la care am invatat fizica in timpul liceului. Parte din fostii lui elevi sunt implicati in cercetare in toata lumea si acest lucru nu ar fi posibil fara pasiunea cu care preda acest subiect. Vreau sa ii multumesc si sa imi exprim profundul respect pe aceasta cale.

Nu am cuvinte sa le multumesc parintilor mei pentru tot ajutorul pe care l-am primit in timpul petrecut acasa, in Romania. Sper din toata inima ca sunt bucurosi de ceea ce am facut si ca pot suporta mai usor distanta mare care ne separa.

Dragei mele sotii, Oana, trebuie sa ii multumesc in mod deosebit pentru suportul si rabdarea pe care a avut-o in cei trei ani petrecuti in Göttingen. Momentele grele au trecut mai usor, iar bucuriile le-am trait dublu numai datorita tie.

1. Introduction.....	8
1.1. Nuclear spin interactions.....	10
1.2. Simplifying the Hamiltonian.....	15
1.3. Nuclear spin dynamics.....	20
1.4. Modes of coherence.....	22
1.5. 2D correlation experiments.....	25
1.6. Overview.....	28
2. Spectral editing techniques.....	29
2.1. Multiple quantum spectroscopy.....	35
2.2. The sum and difference experiment.....	50
2.3. Dipolar dephasing of ^{13}C - ^1H couplings.....	61
3. Structure determination with solid-state NMR.....	69
3.1. Peptide secondary structure determination.....	71
3.2. Probing ^1H - ^1H distances in uniformly labeled biomolecules.....	79
3.3. Frequency-selective dipolar recoupling.....	88
4. Applications to proteins and membrane proteins.....	99
4.1. Spectral assignment of microcrystalline Crh.....	101
4.2. Neurotensin bound to its G-protein coupled receptor.....	116
4.3. Confining the two ubiquinones in the Q_o pocket of bc_1	140
5. Conclusions.....	156
6. Abbreviations.....	159
7. Index.....	160
8. Appendices.....	161
8.1. Bruker pulse programs.....	162
8.2. GAMMA-based simulation programs.....	165
9. List of publications.....	169
10. References.....	171

1. Introduction

A number of methods exist to study molecular structure at atomic resolution. When samples that are characterized by long-range order (e.g. 3D or 2D crystals) are available, X-ray crystallography or electron microscopy techniques are most appropriate. Small to medium-size molecules which are rapidly tumbling in solution can be studied with solution-state nuclear magnetic resonance (NMR). Alternatively, NMR techniques have been developed for the study of solid-phase systems (solid-state NMR, SSNMR) which can be suitable to study systems not in the above mentioned categories.

With respect to biological applications, especially in relation to the study of polypeptides and proteins, a number of systems exist for which SSNMR may be the method of choice. For example, fibrous, membrane or aggregated proteins are inherently insoluble, non-crystalline or difficult to crystallize. These systems have been analyzed by SSNMR for several years [1-3]. Improvements in both NMR hardware and methodology could expand the range of future biological applications.

As opposed to solution-state NMR where all anisotropic interactions experienced by the nuclear spins are averaged out by the Brownian motion, these interactions directly influence the solid-state NMR spectrum. Although they all contain valuable structural information, their multiple contributions usually limit a direct spectral analysis. In particular, the size of dipole-dipole interactions can become a major obstacle in studying multiple spin systems in SSNMR.

In the following, the theoretical basis for SSNMR is presented. Further more detailed information can be found in recent books and reviews [4-6]. Here, the various interactions experienced by the nuclear spins are discussed and methods that establish high-resolution

conditions are introduced. The evolution of a system composed of $\frac{1}{2}$ -spins is described in the context of a general two-dimensional experiment. These aspects provide the theoretical foundation for the work described here. Finally, an overview of this work is presented at the end of this section.

1.1. Nuclear spin interactions

NMR probes interactions experienced by nuclear magnetic moments. Usually, the sample is placed in a static magnetic field and exposed to external radio-frequency (r.f.) irradiation. The nuclear magnetic moment is proportional to the nuclear spin angular momentum

$$\boldsymbol{\mu} = \gamma \mathbf{I} \quad (1)$$

where γ is the gyromagnetic ratio of a given nucleus. $\boldsymbol{\mu} = (\mu_x, \mu_y, \mu_z)$ and $\mathbf{I} = (I_x, I_y, I_z)$ represent the magnetic dipole moment and the spin operators, respectively. In the following, we will consider two different $1/2$ -spin species denoted by spin operators \mathbf{I} and \mathbf{S} while the individual spins will be denoted using subscripts j, k for I spins and j', k' for S spins. The following operators will be used:

$$\begin{aligned} F_x^I &= \sum_j I_{xj} \\ F_y^I &= \sum_j I_{yj} \\ F_z^I &= \sum_j I_{zj} \\ F_{\pm}^I &= \sum_j I_{\pm j} = \sum_j I_{xj} \pm i I_{yj} \end{aligned} \quad (2)$$

and similarly for $F_x^S, F_y^S, F_z^S, F_{\pm}^S$.

The interaction with the external static magnetic field $\mathbf{B}_0 = (0, 0, B_0)$ (considered along the z-axis of the laboratory frame), or the Zeeman interaction, differentiates between the isotopes and the corresponding Hamiltonian has the following form:

$$\begin{aligned} H_Z &= -\sum_{jj'} \gamma_I \mathbf{I}_j \cdot \mathbf{B}_0 + \gamma_S \mathbf{S}_{j'} \cdot \mathbf{B}_0 = -\sum_{jj'} \gamma_I I_{zj} B_0 + \gamma_S S_{zj'} B_0 \\ &= \omega_0^I F_z^I + \omega_0^S F_z^S \end{aligned} \quad (3)$$

Here $\omega_0^I = -\gamma_I B_0$ and $\omega_0^S = -\gamma_S B_0$ represent the Larmor frequencies of the two spin species and are proportional to the applied magnetic field.

The interaction with the applied r.f. irradiation is described by a Hamiltonian similar to that for the Zeeman interaction given in Equation (3):

$$H_{rf}(t) = -\sum_{j'} \gamma_j \mathbf{I}_j \mathbf{B}_{rf}^j(t) + \gamma_s \mathbf{S}_j \mathbf{B}_{rf}^s(t) \quad (4)$$

where the r.f. fields are, in general, applied transversal to the static magnetic field \mathbf{B}_0 and are characterized by a frequency ω_{rf} , an amplitude B_1 and a phase φ_{rf} :

$$\begin{aligned} \mathbf{B}_{rf}^I(t) &= 2B_1^I \cos \omega_{rf}^I t (\mathbf{e}_x^{LAB} \cos \varphi_{rf}^I + \mathbf{e}_y^{LAB} \sin \varphi_{rf}^I) \\ \mathbf{B}_{rf}^S(t) &= 2B_1^S \cos \omega_{rf}^S t (\mathbf{e}_x^{LAB} \cos \varphi_{rf}^S + \mathbf{e}_y^{LAB} \sin \varphi_{rf}^S) \end{aligned} \quad (5)$$

The oscillating r.f. field can be decomposed into two counter-rotating fields of amplitude B_1 . Only the component which rotates with a frequency close to the nuclear Larmor frequency, e.g. $\omega_{rf}^{I,S}$; $\omega_0^{I,S}$, has an influence on the spins. This resonance condition is depicted in Figure 1.1.

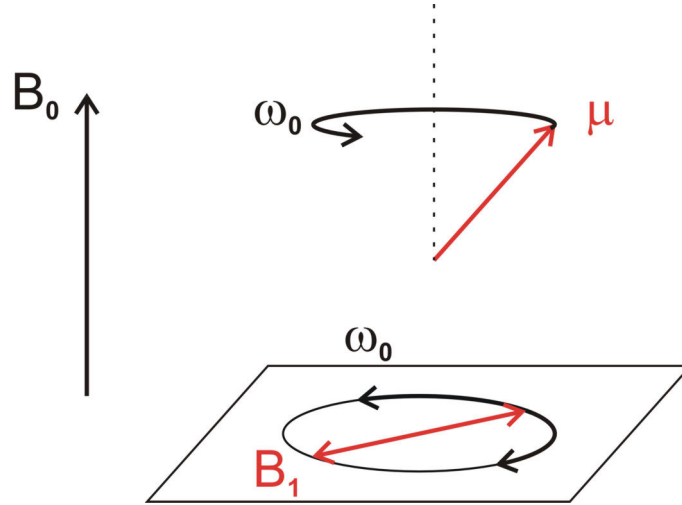


Figure 1.1. Classical description of NMR: the nuclear magnetic moment μ and one component of the applied, rotating r.f. field B_1 precess around the static magnetic field B_0 in the same direction and with the same angular velocity (on-resonance). In a frame rotating with the Larmor frequency around B_0 , they both appear to be static.

Information about local structure and dynamics is encoded in the (usually much weaker) internal interactions: the chemical shielding (CS), the dipolar (D) and the scalar (J) couplings and, only for nuclei with a spin-quantum number larger than $\frac{1}{2}$, the nuclear electric quadrupole interaction (Q). The latter is not relevant in the current context.

$$H_{\text{int}} = H_{\text{CS}} + H_D + H_J \quad (6)$$

All interactions are anisotropic and they manifest in corresponding contributions to the detected resonant frequency. In solution, where molecules are rapidly tumbling, all interactions are dynamically averaged out and only the isotropic interactions determine the spectrum. However, anisotropic interactions contribute to relaxation mechanisms and can be probed indirectly. In the solid-state, the resonant frequency is dependent on both the chemical nature and the orientation of the molecular segment surrounding a given nucleus.

Most easily, these interactions are described in Cartesian tensorial form as $\mathbf{I} \cdot \mathbf{A} \cdot \mathbf{S}$ where the second-rank tensor \mathbf{A} describes both the nuclear spin interaction and its orientation. For each interaction, a special coordinate system (the principal axis system, PAS) can be found where \mathbf{A} is diagonal, with the elements $(a_{xx}^{PAS}, a_{yy}^{PAS}, a_{zz}^{PAS})$. In this case, the trace a , the anisotropy δ and the asymmetry η may be utilized instead of the diagonal elements to describe the tensor \mathbf{A}^{PAS} .

$$\mathbf{A} = \begin{pmatrix} a_{xx} & a_{xy} & a_{xz} \\ a_{yx} & a_{yy} & a_{yz} \\ a_{zx} & a_{zy} & a_{zz} \end{pmatrix} ; \quad \mathbf{A}^{PAS} = \begin{pmatrix} a_{xx}^{PAS} & 0 & 0 \\ 0 & a_{yy}^{PAS} & 0 \\ 0 & 0 & a_{zz}^{PAS} \end{pmatrix} \quad (7)$$

$$\begin{aligned} a &= a_{xx} + a_{yy} + a_{zz} = 3a_{iso} \\ \delta &= a_{zz} - a_{iso} \\ \eta &= (a_{xx} - a_{yy}) / \delta \end{aligned} \quad (8)$$

The Hamiltonians corresponding to the internal interactions are listed below. In the case of two-spin interactions, we differentiate between homonuclear and heteronuclear couplings:

$$\begin{aligned} H_{CS} &= \sum_{jj'} \gamma_I \mathbf{I}_j \cdot \boldsymbol{\sigma}_j \cdot \mathbf{B}_0 + \gamma_S \mathbf{S}_{j'} \cdot \boldsymbol{\sigma}_{j'} \cdot \mathbf{B}_0 \\ H_D^{\text{homo}} &= \sum_{j < k, j' < k'} \mathbf{I}_j \cdot \mathbf{D}_{jk} \cdot \mathbf{I}_k + \mathbf{S}_{j'} \cdot \mathbf{D}_{j'k'} \cdot \mathbf{S}_{k'} \\ H_D^{\text{hetero}} &= \sum_{jj'} \mathbf{I}_j \cdot \mathbf{D}_{jj'} \cdot \mathbf{S}_{j'} \\ H_J^{\text{homo}} &= 2\pi \sum_{j < k, j' < k'} \mathbf{I}_j \cdot \mathbf{J}_{jk} \cdot \mathbf{I}_k + \mathbf{S}_{j'} \cdot \mathbf{J}_{j'k'} \cdot \mathbf{S}_{k'} \\ H_J^{\text{hetero}} &= 2\pi \sum_{jj'} \mathbf{I}_j \cdot \mathbf{J}_{jj'} \cdot \mathbf{S}_{j'} \end{aligned} \quad (9)$$

The electrons surrounding a nucleus shield the applied static magnetic field such that the magnetic field at the spin site is modified. The chemical shielding tensor σ describes the total field experienced by the spin:

$$\mathbf{B} = \mathbf{B}_0 + \sigma\mathbf{B}_0 \quad (10)$$

Only the trace $\sigma_{iso} = \text{Tr}\{\sigma\}/3$ is detected in solution-state NMR and provides the basis for the spectral resolution of chemically distinct spins. In solid-state NMR, both the anisotropy δ and the asymmetry η further influence the resonance position and result in powder patterns [5] in the case of randomly oriented molecules under static conditions.

The magnetic field generated by a nuclear spin is also experienced by neighboring spins and leads to a through-space interaction known as the dipolar coupling. The associated spherical tensor \mathbf{D} is traceless and axially symmetric and the Cartesian diagonal components in its PAS are $(-d, -d, +2d)$. The dipolar coupling constant d (between two spins 1 and 2 separated by the distance r_{12}) is given by

$$d = -\frac{\mu_0 \gamma_1 \gamma_2 \hbar}{4\pi r_{12}^3} \quad (11)$$

Through-bond, or J-couplings or scalar couplings, also exist between nuclei connected by chemical bonds. The associated tensor \mathbf{J} has a non-vanishing trace and can therefore be detected in solution-state NMR. These couplings are usually much weaker than the dipolar ones but, in certain circumstances, they can also be employed in solid-state NMR [7].

The total Hamiltonian for the I and S spin system, in a rigid and static sample, can be written as:

$$H(t) = H_z + H_{\text{int}} + H_{rf}(t) \quad (12)$$

In the following, we treat in Equation (12) H_{int} as a perturbation to the system. In the first order approximation (the secular approximation), we only consider the terms in H_{int} that commute with the much bigger H_z Hamiltonian (the secular terms) and neglect the non-commuting terms (the non-secular terms). This is normally referred to as the high-field approximation and provides the reason for the different forms of the homonuclear and

heteronuclear Hamiltonians in Equation (13). The secular terms can be calculated and expressed in terms of Cartesian spin operators as given below:

$$\begin{aligned}
H_{CS,j} &= \omega_0^I \left[\sigma_{iso,j} + \frac{1}{2} \delta_j (3 \cos^2 \theta_j - 1 + \eta_j \sin^2 \theta_j \cos 2\varphi_j) \right] I_{zj} \\
H_{CS,j'} &= \omega_0^S \left[\sigma_{iso,j'} + \frac{1}{2} \delta_{j'} (3 \cos^2 \theta_{j'} - 1 + \eta_{j'} \sin^2 \theta_{j'} \cos 2\varphi_{j'}) \right] S_{zj'} \\
H_{D,jk}^{\text{homo}} &= d_{jk} \frac{3 \cos^2 \theta_{jk} - 1}{2} (3 I_{zj} I_{zk} - \mathbf{I}_j \mathbf{I}_k) \\
H_{D,j'k'}^{\text{homo}} &= d_{j'k'} \frac{3 \cos^2 \theta_{j'k'} - 1}{2} (3 S_{zj'} S_{zk'} - \mathbf{S}_{j'} \mathbf{S}_{k'}) \\
H_{D,jj'}^{\text{hetero}} &= d_{jj'} \frac{3 \cos^2 \theta_{jj'} - 1}{2} 2 I_{zj} S_{zj'} \\
H_{J,jk}^{\text{homo}} &= 2\pi J_{jk} \mathbf{I}_j \mathbf{I}_k \\
H_{J,j'k'}^{\text{homo}} &= 2\pi J_{j'k'} \mathbf{S}_{j'} \mathbf{S}_{k'} \\
H_{J,jj'}^{\text{hetero}} &= \pi J_{jj'} 2 I_{zj} S_{zj'}
\end{aligned} \tag{13}$$

where for each interaction of interest the PAS is generally different from the laboratory frame and the corresponding polar angles (θ, φ) define the orientation of the static field \mathbf{B}_0 in the PAS of that particular interaction.

It is usually convenient to transform to an interaction frame where the time-dependence due to the r.f. field is removed. This frame is named the rotating frame (Figure 1.1) and the transformation $R_{rf}(t) H R_{rf}^{-1}(t)$ from the laboratory frame to the rotating frame is given by:

$$R_{rf}(t) = \exp \left\{ -i \omega_{rf}^I t F_z^I - i \omega_{rf}^S t F_z^S \right\} \tag{14}$$

In the new frame, both H_Z and $H_{\text{int}}^{\text{secular}}$ do not change (they are invariant under z-rotations), while H_{rf} is rendered time-independent and an extra interaction $-\omega_{rf}^I F_z^I - \omega_{rf}^S F_z^S$ is present:

$$\begin{aligned}
H &= H_{\text{offset}} + H_{\text{int}}^{\text{secular}} + H_{\text{rf}} \\
H_{\text{offset}} &= (\omega_0^I - \omega_{\text{rf}}^I) F_z^I + (\omega_0^S - \omega_{\text{rf}}^S) F_z^S \\
H_{\text{rf}} &= -\gamma_I B_1^I (F_x^I \cos \varphi^I + F_y^I \sin \varphi^I) - \gamma_S B_1^S (F_x^S \cos \varphi^S + F_y^S \sin \varphi^S)
\end{aligned} \tag{15}$$

1.2. Simplifying the Hamiltonian

High-resolution solid-state NMR is intimately related to transformations of the Hamiltonian in both space and spin coordinates. Fast rotations of the Hamiltonian are equivalent to averaging out its anisotropic parts, therefore simplifying the Hamiltonian. For that reason, it is convenient to describe the internal interactions in terms of irreducible spherical tensors [5]. In summary, the isotropic chemical shift (CS), the chemical shift anisotropy (CSA) and the dipolar coupling (D) Hamiltonians (the interactions with which this work is concerned) may be written as (in the secular approximation):

$$\begin{aligned}H_{CS} &= A_{0,0}^{(CS)} \cdot T_{0,0} \\H_{CSA} &= A_{2,0}^{(CS)} \cdot T_{2,0} \\H_D &= A_{2,0}^{(D)} \cdot T_{2,0}\end{aligned}\tag{16}$$

where A and T are used for space and spin parts of the Hamiltonian, respectively. Both of them obey the general transformation rules for rotations. For example, in a new frame, which is related to the old frame by the Euler angles (α, β, γ) , the irreducible spherical tensors of order l can be written as (Figure 1.2):

$$A_{lm}^{(new)} = \sum_{p=-l}^{+l} A_{lp}^{(old)} D_{pm}^l(\alpha, \beta, \gamma)\tag{17}$$

where $D_{pm}^l(\alpha, \beta, \gamma) = \exp(-ip\alpha) d_{pm}^l(\beta) \exp(-im\gamma)$ represent the Wigner rotation matrices and the real numbers $d_{pm}^l(\beta)$ relate to the reduced Wigner elements [6]. Similar relations hold for the transformations of the spin parts T_{lm} .

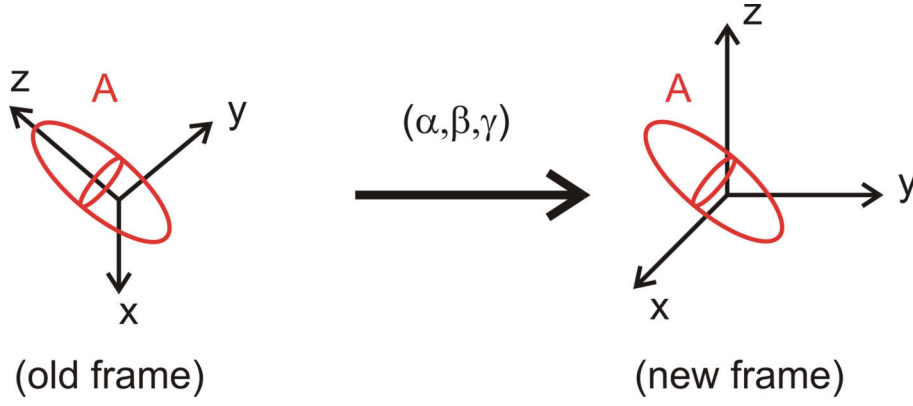


Figure 1.2. A second-rank tensor A can be expressed in different frames. Here, the new frame is related to the old frame by a rotation specified by the Euler angles (α, β, γ) .

In the PAS of a given interaction, the non-zero components of A_{lm} are:

$$\begin{aligned}
 A_{0,0}^{PAS} &= -\sqrt{\frac{1}{3}}a = -\sqrt{3}a_{iso} \\
 A_{2,0}^{PAS} &= \sqrt{\frac{3}{2}}\delta \\
 A_{2,\pm 2}^{PAS} &= \frac{1}{2}\delta\eta
 \end{aligned} \tag{18}$$

For example, $A_{2,0}^{D,PAS} = \sqrt{6}d$ is the only non-zero component for the dipolar coupling tensor. Such transformations may be used to calculate the Hamiltonians given in Equation (13) where a rotation described by the Euler angles $(\varphi, \theta, 0)$ is employed to transform from the PAS (where the tensors are diagonal) to the laboratory frame.

Spin tensors can be calculated and are shown below:

$$\begin{aligned}
 T_{0,0} &= -\sqrt{\frac{1}{3}}I \cdot S & T_{2,0} &= \sqrt{\frac{1}{6}}(3I_z S_z - I \cdot S) \\
 T_{1,0} &= \frac{1}{2\sqrt{2}}(-I_+ S_- + I_- S_+) & T_{2,\pm 1} &= m \frac{1}{2}(I_z S_{\pm} + I_{\pm} S_z) \\
 T_{1,\pm 1} &= \frac{1}{2}(I_z S_{\pm} - I_{\pm} S_z) & T_{2,\pm 2} &= \frac{1}{2}I_{\pm} S_{\pm}
 \end{aligned} \tag{19}$$

In the case of the chemical shielding, the \mathbf{S} operator is replaced by \mathbf{B}_0 such that, for example,

$$T_{0,0} = -\sqrt{\frac{1}{3}}I_z B_0 \quad ; \quad T_{2,0} = \frac{2}{\sqrt{6}}I_z B_0. \tag{20}$$

Both transform as rank-one tensors under rotations in spin space.

The space part of the Hamiltonian may be simplified by macroscopic sample alignment (in the context of polypeptides interacting with oriented lipid bilayers) or it can be rendered time-dependent through mechanical rotations of the sample (around an axis tilted with respect to the static magnetic field \mathbf{B}_0 by an angle θ_R and with an angular velocity ω_R). In the latter case, the space tensors in the laboratory (LAB) frame may be derived from the PAS frame by two subsequent rotations. A first rotation of arbitrary (in the context of randomly oriented molecules) Euler angles (α, β, γ) changes the PAS to a rotor fixed (ROT) frame. A second rotation of Euler angles $(\omega_R t, \theta_R, 0)$ finally transforms from the ROT frame to the LAB frame (Figure 1.3). In the case of the chemical shift anisotropy (if ρ is the CSA tensor in its PAS) we find that:

$$\begin{aligned} A_{2,0}^{CSA}(t) &= \sum_{m,n=-2}^{+2} \rho_{2,m} D_{m,n}^2(\alpha, \beta, \gamma) D_{n,0}^2(\omega_R t, \theta_R, 0) \\ &= \sum_{m,n=-2}^{+2} \rho_{2,m} D_{m,n}^2(\alpha, \beta, \gamma) d_{n,0}^2(\theta_R) \exp(-in\omega_R t) \end{aligned} \quad (21)$$

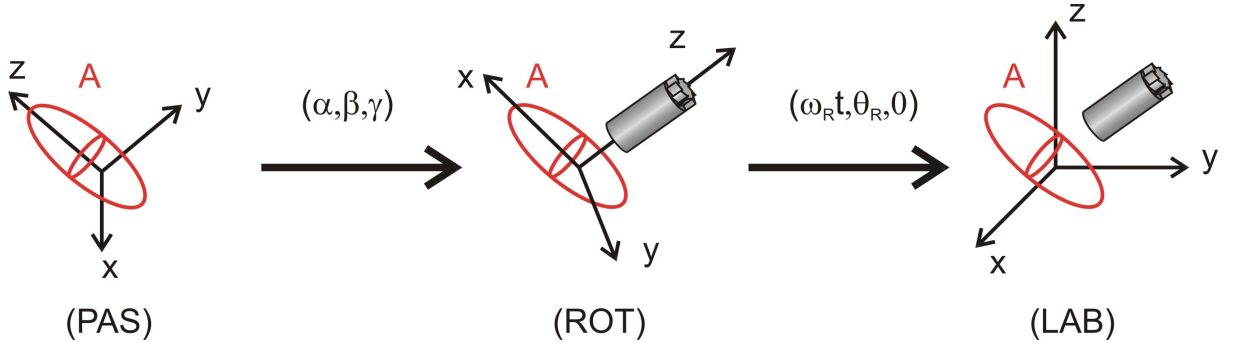


Figure 1.3. Transformation of a spherical tensor A from the PAS frame to the LAB frame is done through the intermediate ROT frame.

In the case of $\theta_R = \theta_{MA} = 54.74^\circ$ (the magic angle) $d_{0,0}^2(\theta_R)$ vanishes and only the terms $d_{n,0}^2(\theta_R)$ with $n \neq 0$ given above are non-zero but are modulated by the spinning speed. In the fast spinning regime (e.g. the anisotropy δ is smaller than the spinning frequency) they are averaged out over one rotor period. Thus, *magic angle spinning* (MAS, Figure 1.4, [8]) averages out all second-rank, weak interactions and provides high-resolution conditions. If the interactions are strong or if low spinning speeds are used (compared to the chemical shift

anisotropy δ) the anisotropic interactions will manifest themselves through the appearance of spinning sidebands [5, 9].

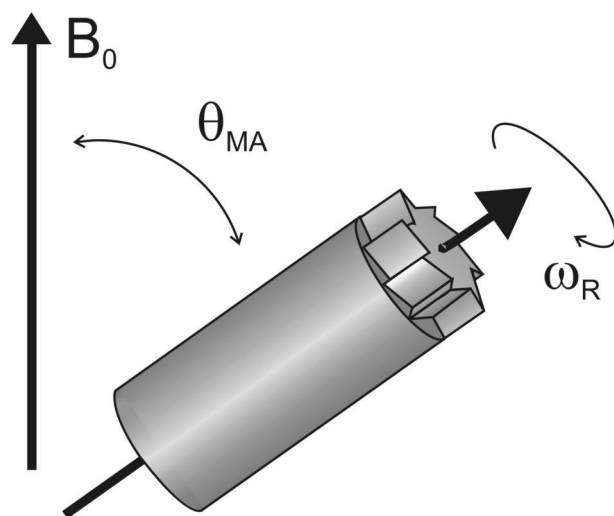


Figure 1.4. High-resolution in solid-state NMR is achieved by the magic angle spinning (MAS, [8]) technique. The NMR rotor is tilted around the magic angle $\theta_{MA} = 54.74^\circ$ with respect to the static magnetic field and rotated around this axis with the angular velocity ω_r (up to 30 kHz for small rotors, e.g. 2.5 mm in diameter).

^{13}C - ^1H or ^1H - ^1H dipolar couplings are, on the other hand, too large to be averaged out by MAS alone. Averaging in the spin space by appropriate r.f. pulse schemes may assist, for example, proton decoupling during ^{13}C direct detection ([10, 11]) or homonuclear dipolar decoupling ([12, 13]). MAS successfully suppresses smaller dipolar couplings, such as between ^{13}C - ^{13}C , which contain important information about the spin topology. To observe these dipolar interactions under MAS conditions, a variety of (usually rotor-synchronized) r.f. sequences have been introduced ([14, 15], Figure 1.5).

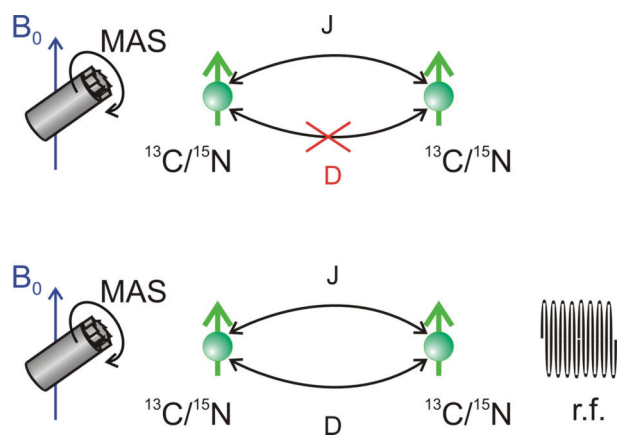


Figure 1.5. Under MAS, anisotropic interactions such as the dipolar coupling (D) are averaged out. On the other hand, scalar through-bond couplings (J) are not affected by the macroscopic sample orientation. Both mechanisms can be probed in high-resolution with the help of appropriate r.f. pulse sequences.

1.3. Nuclear spin dynamics

The density operator characterizes the nuclear spin system at any given instance in time. Under a Hamiltonian $H(t)$ its time evolution is described by the Liouville-von Neumann equation [4]:

$$\frac{d}{dt}\rho(t) = -i[H(t), \rho(t)] \quad (22)$$

If the Hamiltonian is time-independent, Equation (22) can be solved analytically:

$$\rho(t) = U(t)\rho(0)U^{-1}(t) \quad ; \quad U(t) = e^{-iHt} \quad (23)$$

Any time-dependent Hamiltonian may be approximated by a series of Hamiltonians H_n which are time-independent for subsequent short periods of time τ_n ($n = 1, 2, \dots, N$). The density operator may be then calculated from Equation (23) as:

$$\rho(t = \tau_1 + \dots + \tau_N) = e^{-iH_N\tau_N} \dots e^{-iH_2\tau_2} e^{-iH_1\tau_1} \rho(0) e^{+iH_1\tau_1} e^{+iH_2\tau_2} \dots e^{+iH_N\tau_N} \quad (24)$$

This approach is utilized in the context of performing numerical calculations of the spin system dynamics with the aid of computers, for example, in the C++ based GAMMA environment [16].

Given that the density operator is known as a function of time, the expectation value of any observable operator A can be calculated to be:

$$\langle A(t) \rangle = \text{Tr}\{A\rho(t)\} \quad (25)$$

For example, transversal magnetization is monitored at the end of an NMR experiment, such that the detected signal may be written as:

$$signal_x(t) = \langle F_x^I \rho(t) \rangle = \text{Tr}\{F_x^I \rho(t)\} \quad (26)$$

Under a time-dependent Hamiltonian, the following formal solution can be given for Equation (22):

$$\rho(t) = U(t)\rho(0)U(t)^{-1}, \quad (27)$$

where the propagator $U(t)$ reads as:

$$U(t) = T \exp \left\{ -i \int_0^t H(t') dt' \right\} = \exp \{ -i\bar{H}t \} \quad (28)$$

and T represents the Dyson time-ordering operator. According to Equations (27) and (28), the spin system dynamics may be described by the effect of an average Hamiltonian \bar{H} . Expanding the exponent and collecting terms of equal orders we can find the various orders of the average Hamiltonian \bar{H} :

$$\begin{aligned} \bar{H}_0 &= \frac{1}{t} \int_0^t dt_1 H(t_1) \\ \bar{H}_1 &= \frac{-i}{2t} \int_0^t dt_2 \int_0^{t_1} dt_1 [H(t_2), H(t_1)] \\ \bar{H}_2 &= \frac{1}{6t} \int_0^t dt_3 \int_0^{t_3} dt_2 \int_0^{t_2} dt_1 [H(t_3), [H(t_2), H(t_1)]] \\ &\quad + [[H(t_3), H(t_2)], H(t_1)] \end{aligned} \quad (29)$$

which is known as the Magnus expansion and permits one to calculate the average Hamiltonian up to the relevant orders.

1.4. Modes of coherence

For each spin system, the density operator, which can be derived from Equation (22), can be expressed in terms of the Cartesian spin operators, as defined in Equation (1), and products thereof. Together they form a normalized basis of the Liouville space for the spin system in question. For a two $\frac{1}{2}$ -spin system, for example, such a set is formed by $I_x, I_y, I_z, S_x, S_y, S_z, 2I_xS_x, 2I_xS_y, 2I_xS_z, 2I_yS_x, 2I_yS_y, 2I_yS_z, 2I_zS_x, 2I_zS_y, 2I_zS_z$ and the unity operator $E/2$. Alternatively, I_x, I_y, S_x and S_y operators may be expressed in terms of the raising and lowering operators I_{\pm}, S_{\pm} , respectively, as shown in Equation (2). For example, single-spin modes such as I_{\pm} and S_{\pm} focus on one spin only and represent transverse magnetization derived from single-quantum coherence. Operators such as $2I_+S_+$ and $2I_+S_-$ refer to two-spin modes and are related to double- and zero-quantum coherences (see Section 2.1).

The angular spin operators obey the well-known commutation rules:

$$\begin{aligned} [I_z, I_x] &= iI_y \\ [S_z, S_x] &= iS_y \end{aligned} \quad (30)$$

and similar relations for any cyclic permutation of the indices. Other rules may be found for the rest of the terms of the basis set such as, for example,

$$\begin{aligned} [2I_zS_z, I_x] &= iI_y \\ [2I_zS_z, S_x] &= iS_y \end{aligned} \quad (31)$$

In general, fictitious $\frac{1}{2}$ -spin operators (denoted by I_x^{rs}, I_y^{rs} and I_z^{rs}) can be defined to describe any two-level subsystem formed by the states $|r\rangle$ and $|s\rangle$ of a multilevel spin system [4]. Similar to the commutation rules above, the following relations are also true in this case:

$$[I_z^{rs}, I_x^{rs}] = iI_y^{rs} \quad (32)$$

Additionally, commutation rules such as

$$\begin{aligned} [I_x^{rs}, I_x^{st}] &= \frac{i}{2} I_y^{rt} \\ [I_x^{rs}, I_y^{st}] &= -\frac{i}{2} I_x^{rt} \end{aligned} \quad (33)$$

which relate to different three-dimensional subspaces (given by pairs of the states $|r\rangle$, $|s\rangle$ and $|t\rangle$) can be established.

A straightforward interpretation of the above equations is visualized graphically as rotations in the corresponding subspace of the entire Liouville space characterizing the spin system. For example, in the subspace (I_x, I_y, I_z) , the commutation relation

$$[I_z, I_x] = iI_y \quad (34)$$

expresses a rotation of the operator I_x (which represents transverse magnetization) around I_z (which may represent a chemical shift Hamiltonian), as shown in Figure 1.6. This is the analogy to the classical description of NMR given in Figure 1.1. Mathematically, this can be expressed, see Equation (23), as:

$$e^{-i\omega t I_z} I_x e^{+i\omega t I_z} = I_x \cos \omega t + I_y \sin \omega t \quad (35)$$

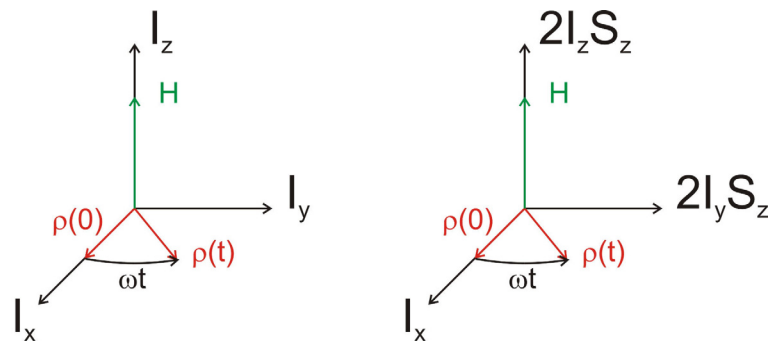


Figure 1.6. (Left) In the Liouville subspace (I_x, I_y, I_z) the evolution of the transverse magnetization $\rho(0) = I_x$ under the chemical shift Hamiltonian $H = \omega I_z$ can be described as a rotation of the density operator ρ around the Hamiltonian H . (Right) The same applies to the density operator $\rho(0) = I_x$ under a heteronuclear dipolar Hamiltonian $H = \omega 2I_z S_z$ in the Liouville subspace $(I_x, 2I_y S_z, 2I_z S_z)$.

Other rules such as:

$$[2I_z S_z, I_x] = iI_y \quad (36)$$

describe the effect of a heteronuclear dipolar coupling (Hamiltonian proportional to $2I_zS_z$) on the transverse magnetization I_x as a rotation in the subspace $(I_x, 2I_yS_z, 2I_zS_z)$ also depicted in Figure 1.6. Mathematically this can be expressed in analogy to Equation (35) as:

$$e^{-i\omega t 2I_zS_z} I_x e^{+i\omega t 2I_zS_z} = I_x \cos \omega t + 2I_yS_z \sin \omega t \quad (37)$$

In this case, in-phase I_x and antiphase $2I_yS_z$ magnetization exchange in an oscillatory manner under the weak bilinear coupling $\omega \cdot 2I_zS_z$.

Similarly, the Equation (53) in Section 2.1.1 relate to the double- and zero-quantum subspace of a two $\frac{1}{2}$ -spin system and describe the excitation of double- and zero-quantum coherences under suitable Hamiltonians, as shown in Section 2.1.2. Or, commutation rules such as given in Equation (33) link different three-dimensional subspaces and allow for generic transfer of coherences.

In general, the commutation rules allow for a simple description of coherence transfer using the product operator formalism. This can be denoted by the equivalence of the next relations:

$$\begin{aligned} [C, A] &= i\lambda B \\ e^{-i\alpha C} A e^{+i\alpha C} &= A \cos \alpha\lambda + B \sin \alpha\lambda \end{aligned} \quad (38)$$

An extensive analysis of coherence transfer under various Hamiltonians, as well as numerical calculations that relate to the dipolar truncation phenomenon can be found in a recent review [6].

1.5. 2D correlation experiments

Biological applications of solid-state NMR are normally related to ^1H , ^{13}C and ^{15}N nuclei while occasionally use of ^2H , ^{19}F , ^{23}Na and ^{31}P nuclei may be employed. Due to the size of the various nuclear anisotropic interactions in the solid-phase, investigations of multiply ^{13}C and/or ^{15}N peptides and proteins mostly rely on the high-resolution provided by these isotopes under MAS [8]. Extensions to two-dimensional experiments [4] represent a powerful means to increase the spectral dispersion and to correlate the resonances of interacting spins.

The general two-dimensional double-channel (^1H and ^{13}C , for example) experiment is depicted in Figure 1.7. As already mentioned, high-resolution is achieved during t_1 and t_2 (where only ^{13}C isotropic chemical shifts are present) due to coherent averaging by MAS [8] and proton decoupling sequences such as TPPM [10]. A preparation block is used to generate the ^{13}C magnetization before evolution in t_1 . In most cases, this unit involves cross-polarization [17, 18] from abundant ^1H spins (the pulse sequence used is denoted by its propagator U_p). Before the t_2 acquisition, a mixing sequence is used, for example, to transfer magnetization from one spin to another. In this case, the two-dimensional spectrum will then reveal connectivities between coupled spins in a multi-spin system. The mixing block is denoted by U_M in Figure 1.7.

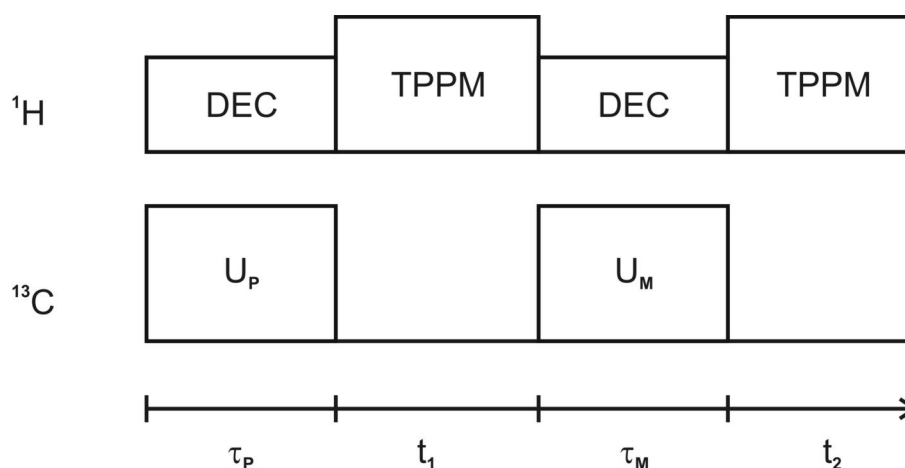


Figure 1.7. General two-dimensional high-resolution experiment involving ^1H and ^{13}C nuclei. The timing of the sequence is shown at the bottom: preparation (τ_p), t_1 evolution, mixing (τ_M) and t_2 acquisition. The TPPI [19] method ensures quadrature detection in the indirect dimension t_1 .

We now calculate the signal detected at the end of the experiment shown in Figure 1.7. We assume the same time-independent high-resolution Hamiltonian H , during both t_1 and t_2 , which consists only of the isotropic chemical shifts of the ^{13}C spins (i.e. I spins):

$$H = \sum_j \Omega_j I_{zj} \quad (39)$$

where Ω_j represents the isotropic chemical shift of spin j . This is achieved during high-power decoupling under MAS and is referred to as high-resolution solid-state NMR (HR-SSNMR) in the following. If τ_p and τ_m are the employed times for the preparation and mixing blocks, respectively, the density operator at an arbitrary time t_2 during acquisition is, according to Equation (24), given by:

$$\begin{aligned} \rho(\tau_p + t_1 + \tau_m + t_2) &= e^{-iHt_2} U_M^-(\tau_m) e^{-iHt_1} U_P^-(\tau_p) \\ &\times \rho(0) U_P(\tau_p) e^{+iHt_1} U_M(\tau_m) e^{+iHt_2} \end{aligned} \quad (40)$$

In general we assume an initial density operator F_z^I . During t_2 we detect transversal magnetization given by the operator $F_+^I = F_x^I + iF_y^I$ (see Equation (2) for a definition of F_+^I , F_x^I , and F_y^I). Thus, we can calculate the signal that we detect from Equation (25):

$$\begin{aligned} \text{signal}(\tau_p + t_1 + \tau_m + t_2) &= \text{Tr} \left\{ F_+^I \rho(\tau_p + t_1 + \tau_m + t_2) \right\} \\ &= \text{Tr} \left\{ U_M e^{+iHt_2} F_+^I e^{-iHt_2} U_M^- e^{-iHt_1} U_P^- F_z^I U_P e^{+iHt_1} \right\} \end{aligned} \quad (41)$$

Due to the commutation rules, we find:

$$\begin{aligned} e^{+iHt_2} F_+^I e^{-iHt_2} &= e^{+it_2 \sum_j \Omega_j I_{zj}} \sum_k (I_{xk} + iI_{yk}) e^{-it_2 \sum_j \Omega_j I_{zj}} \\ &= \sum_j e^{+i\Omega_j t_2 I_{zj}} (I_{xj} + iI_{yj}) e^{-i\Omega_j t_2 I_{zj}} \\ &= \sum_j I_{+j} e^{-i\Omega_j t_2} \end{aligned} \quad (42)$$

Furthermore, we define the mixing operator for the spin j

$$M_j(\tau_m) = U_M I_{j+} U_M^- \quad (43)$$

and the preparation operator

$$P(\tau_p) = U_p^- F_z U_p \quad (44)$$

Substitution of Equations (42), (43) and (44) into Equation (41) results in:

$$\begin{aligned} signal(\tau_p + t_1 + \tau_M + t_2) &= \text{Tr} \left\{ \sum_j e^{-i\Omega_j t_2} M_j(\tau_M) e^{-iH t_1} P(\tau_p) e^{iH t_1} \right\} \\ &= \sum_j e^{-i\Omega_j t_2} \text{Tr} \left\{ M_j(\tau_M) e^{-iH t_1} P(\tau_p) e^{iH t_1} \right\} \end{aligned} \quad (45)$$

If we express the operators in terms of the eigenstates $|r\rangle$ and $|s\rangle$ of the Hamiltonian H (with corresponding energies ω_r and ω_s), then we obtain

$$\begin{aligned} signal(\tau_p + t_1 + \tau_M + t_2) &= \sum_j e^{-i\Omega_j t_2} \text{Tr} \left\{ M_j(\tau_M) e^{-iH t_1} P(\tau_p) e^{iH t_1} \right\} \\ &= \sum_j \sum_{r,s} M_{j,rs}(\tau_M) P_{sr}(\tau_p) e^{-i(\omega_r - \omega_s)t_1} e^{-i\Omega_j t_2} \end{aligned} \quad (46)$$

Recovery of the dipolar coupling under MAS or the effect of scalar interactions during mixing (the $M_j(\tau_M)$ mixing operator in Equation (43)) ensures transfer of magnetization between spin j and its coupled partners. In the resulting 2D spectrum, this coupling results in cross-peaks characterized by frequencies $(\omega_1 = \omega_r - \omega_s, \omega_2 = \omega_j)$. Cross-peaks amplitudes and/or signs reveal the spin-spin correlations [6]. Phase cycling and appropriate co-addition of experiments ensures selection of the desired coherence during t_1 and single-quantum (1Q) coherence during t_2 [4]. For example, selection of double-quantum (2Q) terms in the preparation operator $P(\tau_p)$ results in 2Q correlation experiments [20-22].

1.6. Overview

The main goal of the work to be presented in the following sections was concerned with the application of solid-state NMR to biological problems. Out of the big diversity of systems which may be addressed with SSNMR, we concentrate only on peptides and proteins (with membrane proteins in mind) and mostly on uniformly [^{13}C , ^{15}N]-labeled versions of them.

One of the first questions that arise relates to enhancing the resolution of the spectra obtained on multiple-labeled polypeptides. In the solid-state, even under high-resolution conditions, great overlap among the resonances exhibited by the spins constitutes a limit to the amount of information that may be obtained in a particular case or to the size of the molecules that can be studied. This issue is dealt with in Section 2 where several efficient spectral editing techniques are being examined or proposed.

To date, there is no established protocol for structure determination of uniformly labeled proteins under MAS, although methods that provide structural insight are beginning to emerge. In this respect, in Section 3, experiments that determine the protein fold are established. These experiments analyze the secondary structure (through the determination of the ψ and ϕ torsion angles) as well as the tertiary structure (confined by proton-proton or selected carbon-carbon distance restraints). The set of structural constraints thus obtained helps to determine the 3D structure of a protein (or, in the general case, of a biomolecule) through the study of a single, uniformly labeled protein sample.

Applications to biologically relevant systems are shown in the last part, in Section 4. The complete spectral assignment of a protein in microcrystalline phase is shown in Section 4.1 from which elements of secondary structure can be readily analyzed. The structure of a high-affinity GPCR-peptide ligand is investigated, for the first time, with solid-state NMR. The experimental data predicts an extended conformation for the bound neurotensin peptide and is presented in Section 4.2. There are many applications of SSNMR to macromolecules of known, but incomplete, structure. In Section 4.3, distance constraints determined in the big enzymatic complex bc₁ are described.

2. Spectral editing techniques

Similar to other spectroscopic methods, spectral resolution and sensitivity often determine whether solid-state NMR is the appropriate tool to address a given biophysical problem. In the solution-state, both aspects can be dramatically improved by increasing the static magnetic field strength B_0 . In the solid-state, not only the size of local electronic and spin-spin interactions but also the macroscopic sample orientation determine the resonant frequency and correspondingly influence both sensitivity and spectral resolution. For a long time, biophysical studies using solid-state NMR were hence restricted to selectively isotope-labeled proteins. Recent experimental results have shown that the combination of ultra-high magnetic fields (i.e. magnetic fields above 14 Tesla) and state-of-the-art NMR instrumentation can lead to high sensitivity and adequate spectral resolution in multiply-labeled polypeptides. Recently, solid-state r.f. pulse schemes that make use of these high-resolution conditions and permit the detection of multiple structural parameters from a single protein sample or NMR data set have been proposed [3].

Before a structural characterization in a multiply-labeled sample can proceed, the signals must be identified and attributed to the NMR-detectable nuclei [6]. As a spectroscopic quantity that measures local electronic environments, the isotropic chemical shift is exquisitely sensitive to the amino acid type and hence primary sequence of the polypeptide of interest. As a result, intra-residue resonance assignment in polypeptides usually begins with homonuclear (^{13}C , ^{13}C) correlation experiments (the CC experiment, Figure 2.1.a) that permit identification of different amino acid types based on their characteristic chemical shift correlation patterns. Carbon-carbon correlations can also be related to nearest neighbor ^{15}N spins (Figure 2.1.b). For example, selective polarization transfer from NH to C_α carbon atoms, can, in conjunction

with subsequent (^{13}C , ^{13}C) transfer steps, be used to complete heteronuclear $^{15}\text{N}/^{13}\text{C}$ intra-residue spectral assignments (the NCACB experiment, [23, 24]). The connectivity between adjacent polypeptide residues (inter-residue assignment) can be established by directing the $^{15}\text{N}/^{13}\text{C}$ transfer from the NH resonance to the nearest neighbor carbonyl group. This transfer scheme correlates the ^{15}N resonance of residue i with ^{13}CO resonance of residue $i - 1$ (Figure 2.1.b). Due to the small chemical shift dispersion of carbonyl NMR signals, further homonuclear broadband mixing to transfer magnetization to C_α carbon atoms is usually necessary (the NCOACB experiment, [6, 23, 24]).

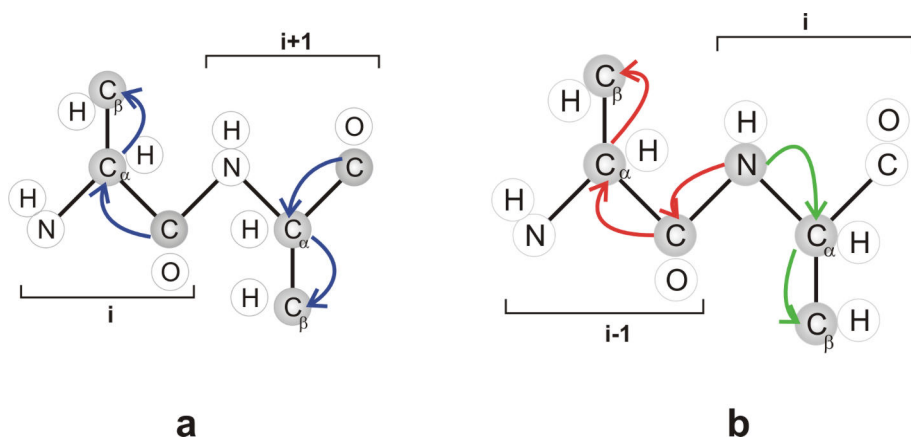


Figure 2.1. Various pathways for magnetization transfer in (a) homonuclear (^{13}C , ^{13}C) and (b) heteronuclear (^{15}N , ^{13}C) correlation experiments that can be performed in polypeptides. The combination of experiments may provide, under favorable circumstances, the complete assignment of a uniformly [^{13}C , ^{15}N]-labeled polypeptide.

Examples of both homonuclear and heteronuclear types of experiments are shown in Figure 2.2 (a, b) and (c, d), respectively, on the uniformly [^{13}C , ^{15}N]-labeled tripeptide Ala-Gly-Gly. In this case, all resonances (of 7 ^{13}C spins and 3 ^{15}N spins) are well separated and can be assigned easily using the combination of experiments shown in Figure 2.1. As already mentioned, CC (Figure 2.2.a, b) and NCACB (Figure 2.2.c) experiments allow for amino acid type identification of both ^{13}C and ^{15}N resonances. Subsequently, a NCOACB (Figure 2.2.d) experiment permits the detection of correlations between ^{15}N and ^{13}C spins in adjacent residues and results in the complete assignment of the tripeptide.

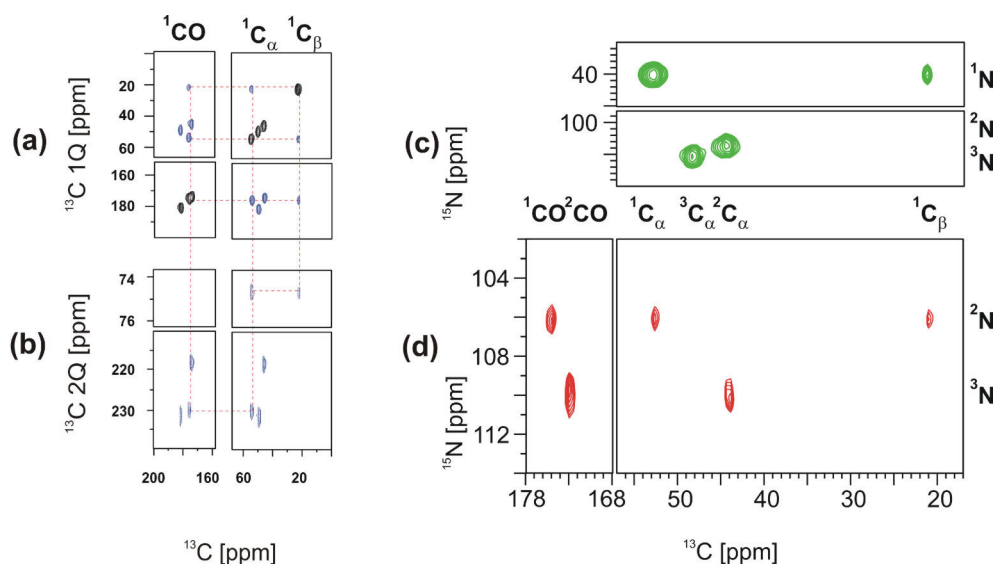


Figure 2.2. Examples of (a, b) homonuclear (^{13}C , ^{13}C) and (c, d) heteronuclear (^{15}N , ^{13}C) correlation experiments. In (a) a proton-driven spin diffusion [25] and in (b) a double quantum [22] correlation experiments are shown. In (c) NCACB and in (d) NCOACB type of experiments [24] are presented. All experiments were applied to a microcrystalline sample of uniformly [^{13}C , ^{15}N]-labeled tripeptide Ala-Gly-Gly. Connecting (red) lines (in a and b) relate to the Ala residue.

Extensive solution-state NMR studies of polypeptides and proteins have shown that all 20 amino acids naturally occurring in proteins have characteristic ^1H , ^{13}C and ^{15}N chemical shifts (see the database of chemical shifts BioMagResBank). The resonances of, for instance, $^{13}\text{C}_\alpha$, backbone ^{15}N and amide ^1H have characteristic but similar frequencies among the different amino acids. In addition to the resonance frequency, the experimentally observed linewidth also influences the resolution of the spectrum. For example, ^{13}C line widths between 0.5 and 1 or 2 ppm (75 to 300 Hz on a 600 MHz spectrometer) are detected under MAS conditions. For comparison, the overall dispersion of the backbone carbonyl resonances is less than 10 ppm (1500 Hz on the same magnet). Furthermore, scalar couplings, sample conformational heterogeneity and other line-broadening mechanisms contribute to the overall spectral resolution in the solid-state. Apart from the dipolar truncation effects (which limit the amount of structural parameters that can be obtained, see Sections 3.2 and 3.3), spectral resolution can hence be the major determinant in studying multiply [^{13}C , ^{15}N]-labeled molecules with HR-SSNMR.

Next, we exemplify the spectral overlap associated with ^{13}C and ^{15}N detection in one-dimensional CPMAS [17, 18] experiments. Two uniformly [^{13}C , ^{15}N]-labeled samples are considered here: the 76-residue protein ubiquitin and the 85-residue protein Crh. Both

proteins were slightly hydrated in the NMR rotor (about 0.5 μ l of deionized water per 1 mg of sample) to improve the overall resolution. Carbon and nitrogen spectra are shown in Figure 2.3 and Figure 2.4, respectively. In both cases, the acquisition time was set to 15 ms and the spectra were processed with an exponential multiplication windowing function of 10 Hz. Individual resonances can be observed and they indicate well-ordered proteins. A further spectral analysis is, however, difficult.

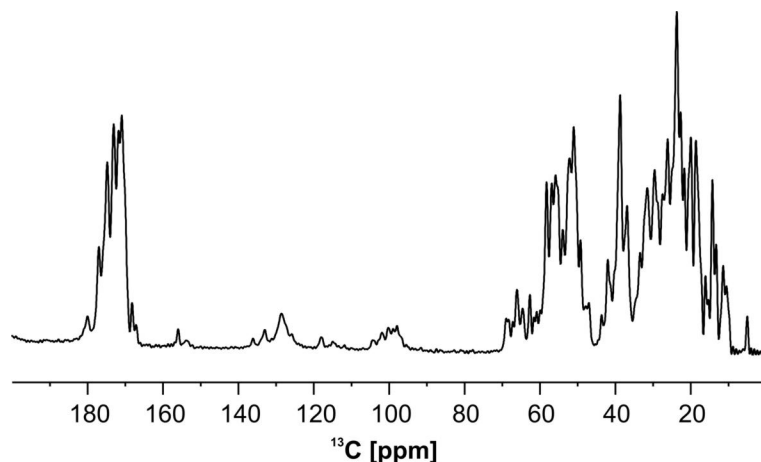


Figure 2.3. CP [17, 18] ^{13}C spectrum of uniformly [^{13}C , ^{15}N]-labeled ubiquitin at 600 MHz and 11 kHz MAS. TPPM [10] proton decoupling of 85 kHz was employed during acquisition.

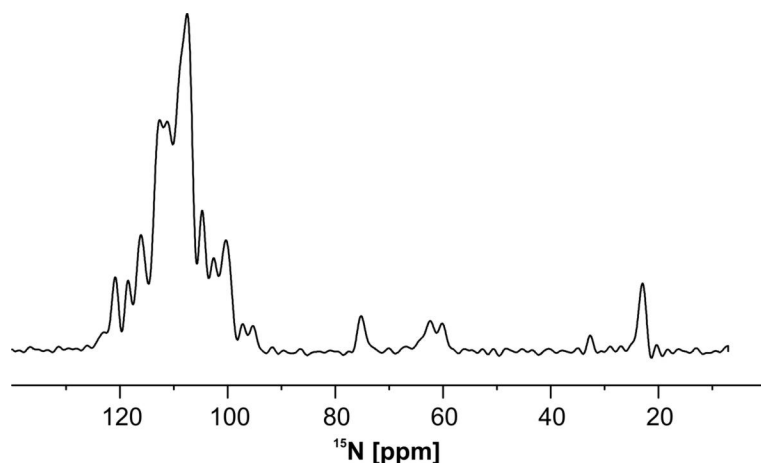


Figure 2.4. CP [17, 18] ^{15}N spectrum of uniformly [^{13}C , ^{15}N]-labeled Crh. Experimental details are as in Figure 2.3.

Multi-dimensional experiments dramatically increase the spectral resolution by correlating resonances in different spectral dimensions [4]. For example, homonuclear ^{13}C - ^{13}C and heteronuclear ^{15}N - ^{13}C experiments can lead to the complete assignment of a protein under MAS, as shown recently in [24, 26].

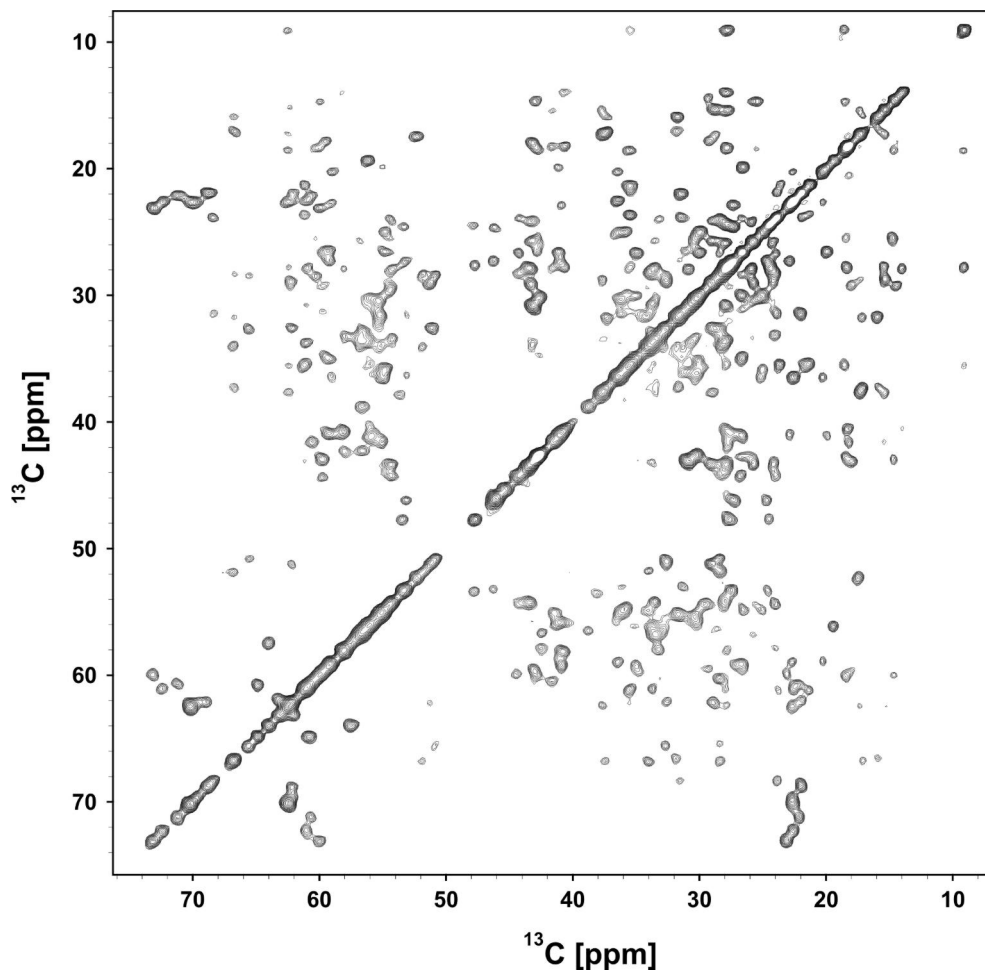


Figure 2.5. Homonuclear CC experiment on ubiquitin using a proton driven spin diffusion block [25] of 40 ms. Experiment recorded on a 600 MHz magnet under 11 kHz MAS and at -5°C .

In Figure 2.5.a ^{13}C - ^{13}C homonuclear experiment on ubiquitin and in Figure 2.6.a ^{15}N - ^{13}C heteronuclear experiment on Crh are presented. The first experiment utilizes a proton-driven spin diffusion block [25] as mixing. The second experiment first uses SPECIFIC-CP [23] to transfer magnetization from backbone ^{15}N to $^{13}\text{C}_{\alpha}$ and a subsequent HORROR [27] mixing block to further transfer magnetization into the sidechain (to $^{13}\text{C}_{\beta}$ and to $^{13}\text{C}_{\gamma}$).

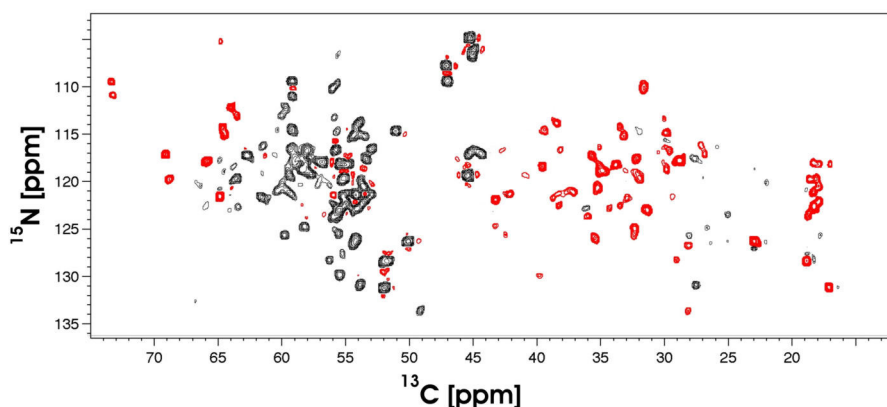


Figure 2.6. Heteronuclear NCACB experiment using SPECIFIC-CP [23] on a 600 MHz magnet under 11 kHz MAS and at -5°C . A HORROR block [27] was used to transfer magnetization to neighboring C_{β} which results in negative (red) peaks.

These experiments (in a series) performed in our laboratory have resulted in partial [28] to complete assignments [26] of the ^{13}C and ^{15}N resonances. In many cases, techniques which further simplify two-dimensional spectra may be of interest in the context of multiply ^{13}C and ^{15}N labeled proteins. Importantly, the efficiency of such methods should not compromise the sensitivity of solid-state NMR biomolecular applications.

The experiments shown in Figure 2.5 and in Figure 2.6 correspond to NMR studies of well-ordered proteins with very sharp ^{13}C and ^{15}N resonances. In other applications this may not be the case due to the physical and chemical properties of the sample (e.g. non-homogeneous samples or studies of unfolded proteins) or due to the primary sequence of the polypeptide (some amino acids occurring frequently in the sequence).

In the following sections we will present several spectral editing techniques that simplify multi-dimensional spectra under MAS. They involve multiple-quantum techniques, the manipulation of the secondary chemical shifts of $^{13}\text{C}_{\alpha}$ and $^{13}\text{C}_{\beta}$ nuclei and the signal dephasing due to the size of the (effective) ^{13}C - ^1H dipolar couplings. All experiments proposed are shown to be readily applicable to samples of biological interest.

2.1. Multiple quantum spectroscopy

Multiple-quantum transitions have been introduced to NMR for more than half a century [29, 30] in conventional slow-passage techniques. In Fourier NMR, only single-quantum coherences can be detected directly. Nevertheless, multiple-quantum coherences may be detected indirectly in two-dimensional experiments [31]. Multiple-quantum spectroscopy was then used for various purposes like spin-counting [32, 33] and the detection of natural abundance ^{13}C - ^{13}C scalar couplings [34]. The MQ frequencies thus detected depend not only on the chemical shifts of the involved spins, but also on the local molecular topology. INADEQUATE-like experiments have also been demonstrated in solid-state NMR [21, 22, 35-39]. In the following we describe multiple quantum coherences and their indirect detection in Fourier NMR, under HR-SSNMR conditions. The spectral simplification provided by MQ correlation experiments will then be discussed using a statistical analysis of the ^{13}C chemical shifts of polypeptides and demonstrated experimentally on uniformly [^{13}C , ^{15}N]-labeled proteins.

2.1.1. Description of multiple quantum coherences

We introduce the concept of multiple-quantum coherences in a system of N $\frac{1}{2}$ -spins of type I. We will make the assumption that all internal interactions in this system are small compared to the Zeeman interaction. Hence, the basic energy levels of our spin system are dictated by the Zeeman Hamiltonian (Equation (3)), while the internal Hamiltonian in the secular approximation (Equation (13)) has only small contributions to these levels (e.g. shifts and/or splittings). Correspondingly, each eigenstate $|r\rangle$ of the Zeeman Hamiltonian may be characterized by its eigenvalue M_r :

$$F_z^I |r\rangle = M_r |r\rangle \quad (47)$$

Here, M_r denotes the component of the total spin angular momentum in the direction of the applied magnetic field (z-axis of the laboratory frame). The general scenario is exemplified in Figure 2.7 for a three $\frac{1}{2}$ -spin system, where M_r may take the values $+3/2$, $+1/2$, $-1/2$, $-3/2$. As shown in Figure 2.7, there is only one state for the extreme $M_r = \pm 3/2$ cases, but there are

three different possible states for each $M_r = \pm 1/2$. In general, for N $1/2$ -spins, there will be $N+1$ Zeeman manifolds, each manifold M_r containing [20]

$$\binom{N}{N/2 + M_r} = \frac{N!}{(N/2 + M_r)!(N/2 - M_r)!}$$

different states. We further assume that the smaller internal interactions (like dipolar couplings) may further split the energy levels as shown in Figure 2.7.

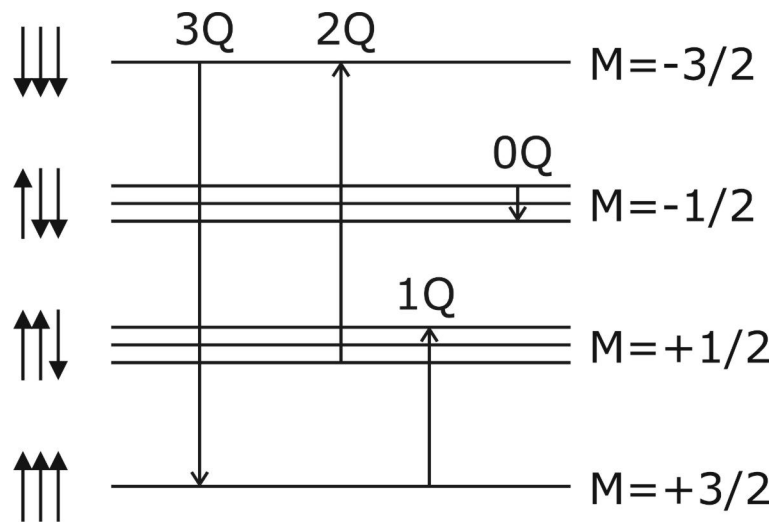


Figure 2.7. The energy levels of a three $1/2$ -spin system in a magnetic field consist of Zeeman levels which are further degenerated by small internal interactions. The total magnetic quantum number M for each state is shown on the right and a “spin-up spin-down” representation on the left. A transition between two states is characterized by the corresponding change in M ; some representative transitions are depicted.

The various transitions between any two of these states may be classified by the change in M_r induced: a transition between the states $|r\rangle$ and $|s\rangle$ is associated with a number $\Delta M_{rs} = M_r - M_s$ which is referred to as the transition or coherence order. For example, zero-quantum (0Q) transitions, single-quantum (1Q) transitions and double-quantum (2Q) transitions correspond to absolute values of ΔM_{rs} equal to 0, 1 and 2, respectively. The number of possible transitions depends on their order: in Figure 2.7 there are six 0Q transitions, but only one triple-quantum (3Q) transition between the two states $M_r = \pm 3/2$.

The density operator at any given instance in time contains information about the population of states and the probability for transitions. We can express the density operator in terms of the eigenstates of the Zeeman Hamiltonian:

$$\rho(t) = \sum_{rs} \rho_{rs}(t) |r\rangle\langle s| \quad (48)$$

Then, the diagonal elements $\rho_{rr}(t)$ represent the probability for the spin system to be in the eigenstate $|r\rangle$. Off diagonal elements $\rho_{rs}(t)$ indicate the complex amplitudes of a coherence (transition) represented by the operator $|r\rangle\langle s|$. The order of a coherence $|r\rangle\langle s|$ is again $\Delta M_{rs} = M_r - M_s$ and the various terms of the density operator may be classified by their coherence order $p = \Delta M_{rs} = M_r - M_s$:

$$\rho^p(t) = \sum_{rs}^{\Delta M_{rs}=p} \rho_{rs}(t) |r\rangle\langle s| \quad (49)$$

Coherences of a given order p transform under z-rotations according to:

$$\begin{aligned} e^{-i\phi F_z^I} \rho^p e^{+i\phi F_z^I} &= \sum_{rs}^{\Delta M_{rs}=p} \rho_{rs} e^{-i\phi F_z^I} |r\rangle\langle s| e^{+i\phi F_z^I} \\ &= \sum_{rs}^{\Delta M_{rs}=p} \rho_{rs} e^{-i\phi M_r} |r\rangle\langle s| e^{+i\phi M_s} \\ &= e^{-i\phi p} \rho^p \end{aligned} \quad (50)$$

Here we have made use of the relation $\exp\{-i\phi F_z^I\} |r\rangle = \exp\{-i\phi M_r\} |r\rangle$ which can be easily deduced from Equation (47). Hence, coherences of different orders p have different symmetry properties under z-rotations which allow one to individually manipulate them.

Coherences may be conveniently expressed using Cartesian spin operators $I_{\pm j}$ or I_{xj}, I_{yj} . For example, the 2Q and 0Q in-phase components (involving two spins j and k) can be described by:

$$\begin{aligned} \{2Q\}_{jk}^x &= \frac{1}{2} [I_j^+ I_k^+ + I_j^- I_k^-] = I_j^x I_k^x - I_j^y I_k^y \\ \{2Q\}_{jk}^y &= \frac{1}{2i} [I_j^+ I_k^+ - I_j^- I_k^-] = I_j^x I_k^y + I_j^y I_k^x \end{aligned} \quad (51)$$

$$\begin{aligned} \{0Q\}_{jk}^x &= \frac{1}{2} [I_j^+ I_k^- + I_j^- I_k^+] = I_j^x I_k^x + I_j^y I_k^y \\ \{0Q\}_{jk}^y &= \frac{1}{2i} [I_j^+ I_k^- - I_j^- I_k^+] = I_j^y I_k^x - I_j^x I_k^y \end{aligned} \quad (52)$$

The following commutation rules can be deduced:

$$\begin{aligned} \left[\{2Q\}_{jk}^x, \{2Q\}_{jk}^y \right] &= i(I_{zj} + I_{zk})/2 \\ \left[\{0Q\}_{jk}^x, \{0Q\}_{jk}^y \right] &= i(I_{zj} - I_{zk})/2 \end{aligned} \quad (53)$$

Similar relations are obtained from cyclic permutations of the terms and will be used in the next section.

2.1.2. Indirect detection of multiple-quantum transitions

The only degrees of freedom directly observable by an NMR receiver are the transverse components of the macroscopic magnetization [4]:

$$\langle \mu_{x,y} \rangle = \langle \gamma_I \hbar F_{x,y}^I \rangle \quad (54)$$

Hence, only single-quantum coherences can be detected. Multiple-quantum coherences may be nevertheless probed indirectly, for example during the t_1 dimension of a two-dimensional experiment (Figure 2.8).

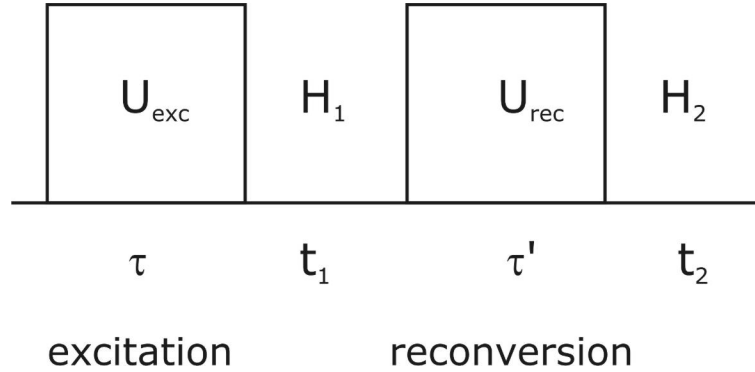


Figure 2.8. Generic two-dimensional multiple-quantum experiment. MQ coherences are excited with a pulse sequence in the preparation period (excitation) and subsequently evolve under the H_1 Hamiltonian in the t_1 dimension. The mixing period converts MQ into 1Q coherences (reconversion) to allow signal detection in t_2 . Phase cycling [4] ensures the selection of the desired MQ coherences in t_1 .

The generic multiple-quantum correlation experiment is depicted in Figure 2.8 [20-22]. We will consider the double-quantum case here and analyze first the excitation of 2Q coherences. Suppose that a two (j and k) $1/2$ -spin system initially at thermal equilibrium

$$\rho(0) = I_{zj} + I_{zk} \quad (55)$$

first evolves under the influence of a 2Q Hamiltonian like:

$$H_{exc} = d_{jk} \{2Q\}_{jk}^x = d_{jk} (I_{xj}I_{xk} - I_{yj}I_{yk}) \quad (56)$$

Such conditions are provided by various recoupling sequences under MAS [6, 14, 15]. Here d_{jk} relates to the (possibly scaled) dipolar coupling between the two spins which is recovered under MAS during excitation. In this case, the propagator for the excitation period τ reads as

$$U_{exc}(\tau) = \exp(-id_{jk}\tau \{2Q\}_{jk}^x) \quad (57)$$

and 2Q coherences will be excited, according to Equation (53) as

$$\begin{aligned} \rho(\tau) &= U_{exc}(\tau) \rho(0) U_{exc}^{-1}(\tau) \\ &= \exp(-id_{jk}\tau \{2Q\}_{jk}^x) (I_{zj} + I_{zk}) \exp(+id_{jk}\tau \{2Q\}_{jk}^x) \\ &= (I_{zj} + I_{zk}) \cos(d_{jk}\tau) - \{2Q\}_{jk}^y \sin(d_{jk}\tau) \end{aligned} \quad (58)$$

The individual 2Q coherences build up in an oscillatory manner as a function of the excitation time τ and the coupling d_{jk} .

Once created, 2Q coherences will evolve only under the isotropic chemical shifts under HR-SSNMR conditions (where CSA and dipolar couplings can be ignored). The relevant Hamiltonian is given by:

$$\begin{aligned} H_1 &= \Omega_j I_{zj} + \Omega_k I_{zk} \\ &= (\Omega_j + \Omega_k) \frac{I_{zj} + I_{zk}}{2} + (\Omega_j - \Omega_k) \frac{I_{zj} - I_{zk}}{2} \end{aligned} \quad (59)$$

and the 2Q term from $\rho(\tau)$ (which is selected experimentally via phase cycling [4]) will evolve only under the influence of the first term of this Hamiltonian (53) as:

$$\begin{aligned} \rho(\tau + t_1) &= \exp\left\{-i(\Omega_j + \Omega_k)t_1 \frac{I_{zj} + I_{zk}}{2}\right\} \{2Q\}_{jk}^y \exp\left\{+i(\Omega_j + \Omega_k)t_1 \frac{I_{zj} + I_{zk}}{2}\right\} \\ &= \{2Q\}_{jk}^y \cos(\Omega_j + \Omega_k)t_1 - \{2Q\}_{jk}^x \sin(\Omega_j + \Omega_k)t_1 \end{aligned} \quad (60)$$

In Equation (60) we have omitted the factor $-\sin(d_{12}\tau)$ for simplicity (we will reintroduce it later). We observe the time-dependent modulation of the density operator at the frequency $(\Omega_j + \Omega_k)$ - the sum of the chemical shifts of the two nuclei. This frequency will be detected in the indirect dimension ω_1 of the experiment.

After the t_1 evolution period, a reconversion block is employed to convert 2Q coherences into 1Q coherences which are subsequently detected. We chose here a pulse sequence that delivers a reconversion Hamiltonian of the type

$$H_{rec} = -d_{jk} \{2Q\}_{jk}^x = d_{jk} (I_{yj}I_{yk} - I_{xj}I_{xk}) \quad (61)$$

and will explain its significance later. Usually such a reconversion unit can be generated by r.f. phase shifts of the excitation r.f. pulse sequence. The reconversion propagator is now (compare with Equation (56)), if τ' is the timing of the reconversion block, given by:

$$U_{rec}(\tau') = \exp(-id_{jk}\tau' \{2Q\}_{jk}^x) = U_{exc}^*(\tau') \quad (62)$$

Only the $\{2Q\}_{jk}^y$ term in Equation (59) will be affected by this propagator and will be converted into longitudinal magnetization as shown below:

$$\begin{aligned} \rho(\tau + t_1 + \tau') &= U_{rec}(\tau') \{2Q\}_{12}^y U_{rec}^*(\tau') \\ &= \exp(+id_{jk}\tau' \{2Q\}_{jk}^x) \{2Q\}_{jk}^y \exp(-id_{jk}\tau' \{2Q\}_{jk}^x) \\ &= \{2Q\}_{jk}^y \cos(d_{jk}\tau') + (I_{zj} + I_{zk}) \sin(d_{jk}\tau') \end{aligned} \quad (63)$$

In Equation (63) we have again neglected the modulation $\cos(\Omega_j + \Omega_k)t_1$ found in Equation (60). Considering all the factors we obtain the final signal:

$$\rho(\tau + t_1 + \tau' + t_2) = (I_{zj} + I_{zk}) \sin(d_{jk}\tau) \sin(d_{jk}\tau') \cos(\Omega_j + \Omega_k)t_1 \quad (64)$$

If $\tau = \tau'$ then the signal is

$$\rho(\tau + t_1 + \tau' + t_2) = (I_{zj} + I_{zk}) \sin^2(d_{jk}\tau) \cos(\Omega_j + \Omega_k)t_1 \quad (65)$$

In a powder-like sample d_{jk} is dependent on the orientation of the internuclear vector \mathbf{r}_{jk} with respect to the static magnetic field. Hence, only under the condition provided by Equation (65) all individual contributions will add up in a constructive manner independent of excitation time. The condition $U_{rec}(\tau') = U_{exc}^*(\tau)$ is known as time reversal [22]. Under this condition, the dipolar dephasing which takes place during excitation is refocused during the reconversion sequence. If this is not accomplished, individual 2Q contributions of different crystallites in a powder-like sample to the overall signal will cancel each other and reduce the sensitivity of the experiment (compare Equation (64) with Equation (65)). It should be mentioned that the negative sign in Equation (61) is not necessary here: a reconversion Hamiltonian equal to the excitation one would result in the same efficiency for the 2Q filtering.

In Equation (65), the term $\sin^2(d_{jk}\tau)$ defines the amplitude of the signal for a pair of spins j and k through both d_{jk} and τ . The amplitude may be negligible for two reasons: the coupling between the two spins is too small or the duration of the excitation/reconversion sequence was not long enough. One immediate consequence is that isolated ^{13}C spins (found in natural abundance, for example) will not contribute signal to the experiment (the method is known as double-quantum filtering, 2QF [34]) because of the large distances between these spins. Nevertheless, there is a $1\% \times 1\% = 10^{-4}$ probability to find pairs of ^{13}C spins in natural abundance which will contribute signal in the 2QF experiment.

2.1.3. MQ spectral editing in polypeptides: A statistical analysis

We now describe the general benefits of a multiple-quantum correlation experiment in the context of uniformly ^{13}C labeled polypeptides. We start by analyzing the resonance pattern expected in a ^{13}C homonuclear 1Q-1Q experiment (Figure 2.9) which shows only the aliphatic region (from 10 to 80 ppm) of the spectrum. Average chemical shifts calculated from the empirical database BMRB [40] were used and only the C_α , C_β and C_γ nuclei were considered in this prediction. Note that all 20 amino acids are present in this prediction and that standard deviations of the chemical shifts (due to differences in conformation) are not explicitly indicated.

We first analyze the cross-peaks in the spectrum. While extensive spectral overlap is found in some regions, one can identify distinct regions with well separated resonances. For example, C_α - C_β correlations like Ser (Ω_{C_α} =58.6 ppm, Ω_{C_β} =63.8 ppm), Thr (Ω_{C_α} =62.2 ppm, Ω_{C_β} =69.6 ppm) and Ala (Ω_{C_α} = 53.2 ppm, Ω_{C_α} =18.9 ppm) and C_β - C_γ correlations like Thr (Ω_{C_β} =69.6 ppm, Ω_{C_γ} =21.4 ppm), Ile (Ω_{C_β} =38.6 ppm, $\Omega_{C_{\gamma 2}}$ =17.4 ppm) and Leu (Ω_{C_β} =42.4 ppm, Ω_{C_γ} =26.8 ppm) appear at distinct, specific positions in the spectrum.

Next we investigate the presence of the diagonal resonances: they are due to magnetization which is not transferred between spins during the mixing sequence of the experiment. Signal from natural abundance ^{13}C thus also appears along the diagonal. In biological applications this signal contribution can become quite large, especially in relation to membrane proteins which have to be solubilized in detergent or reconstituted in lipids. Correspondingly, this may thus seriously obscure cross-peaks close to the diagonal in homonuclear (^{13}C , ^{13}C) correlation experiments.

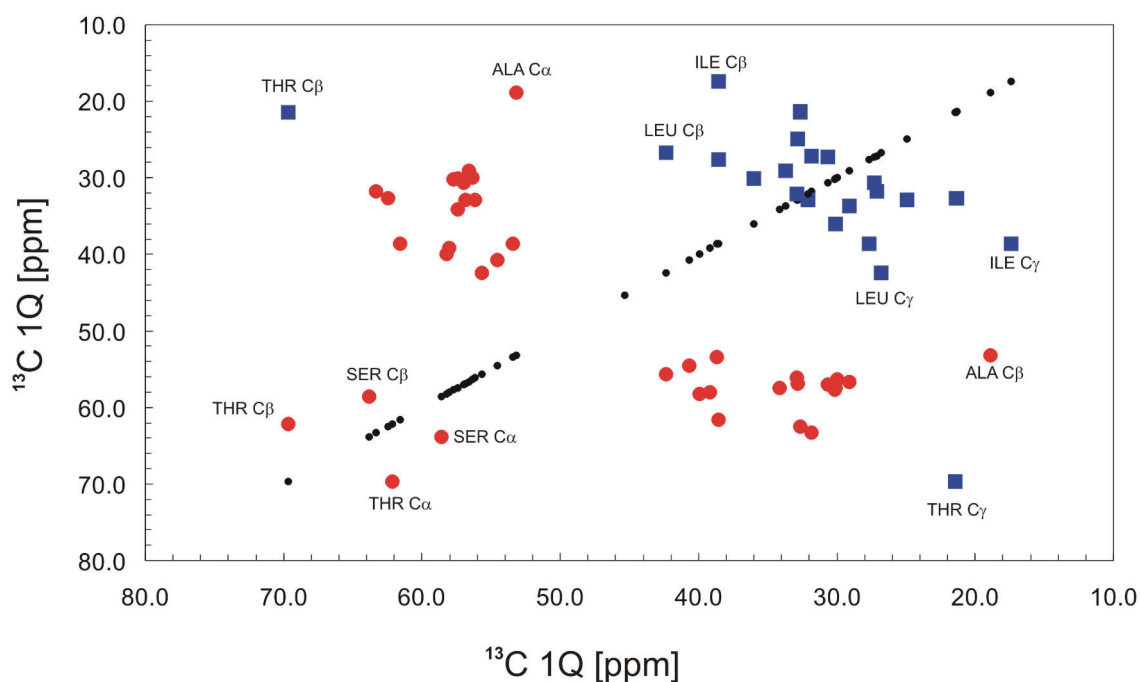


Figure 2.9. Expected ^{13}C homonuclear 1Q-1Q correlations in the sidechain of all 20 amino acids. Only the C_α - C_β (red circles) and C_β - C_γ (blue squares) correlations are depicted. Diagonal resonances are indicated by small black circles.

This issue may be addressed by employing double-quantum correlation experiments (2Q-1Q). A prediction similar to that for a 1Q-1Q experiment (Figure 2.9) is shown in Figure 2.10.

Here, autocorrelation resonances are removed and all C_{β} - C_{γ} connectivities are better resolved (in the absence of the diagonal resonances). We note that correlations involving glycine do not appear in this spectrum (because it has no sidechain) unless broadband dipolar recoupling is employed and C' - C_{α} 2Q coherences are excited.

Since the sum of the chemical shifts of the coupled spins is observed in the indirect dimension, the overall dispersion appears to be larger: 80 ppm as compared to 60 ppm in the 1Q-1Q experiment. Nevertheless typical resonances appear in areas spanning similar frequency domains in both cases. For example, C_{β} - C_{γ} correlations are spread over about 20 ppm in both cases. In the lower part of the spectrum a Trp C_{β} resonance (from the C_{β} - C_{γ} correlation) is observed.

Analysis of the most dispersed resonances leads to similar results when compared to 1Q-1Q case. Additionally, the two resonances exhibited by the coupled spins validate the assignment: the frequency in the indirect dimension is determined by the sum of the individual frequencies in the direct dimension. In conclusion, the most important feature of a double-quantum correlation experiment in terms of resolution improvement is the double-quantum filtering. This results in a simplified spectrum, free of diagonal signal (possibly containing natural abundance signal). On the other hand, the overall spectral dispersion in ω_1 is comparable to the one obtained in a 1Q-1Q experiment.

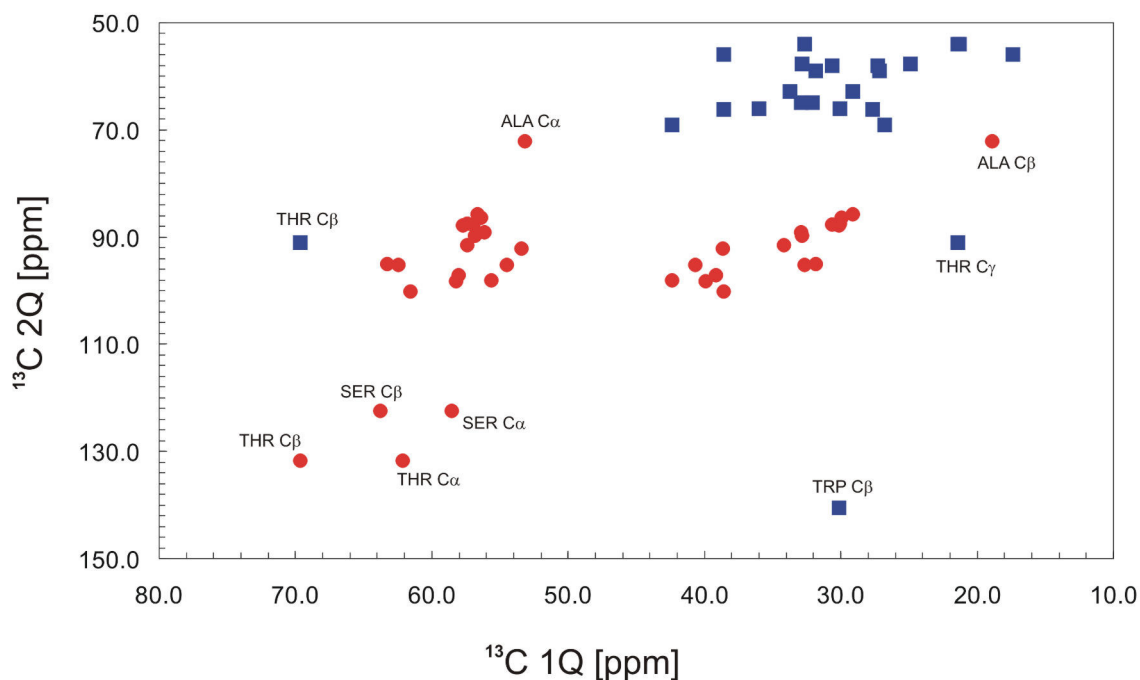


Figure 2.10. Expected ^{13}C homonuclear 2Q-1Q correlations in the sidechain of all 20 amino acids. Only the C_α - C_β (red circles) and C_β - C_γ (blue squares) correlations are depicted.

Furthermore, the prediction of the resonances in a 3Q-1Q experiment is shown in Figure 2.11. This spectrum exhibits a much simpler pattern as many residues do not have a C_γ or the corresponding frequency is found downfield and does not appear in this spectral region. For example, at the bottom of the spectrum a Trp correlation involving C_α , C_β , and C_γ is present although the C_γ resonance is outside the displayed region ($\Omega_{\text{C}_\gamma}=110.4$ ppm). As a result, only three-spin correlations from Arg, Gln, Glu, Ile, Leu, Lys, Met, Pro, Thr and Val are observed in the spectral region shown in Figure 2.11 and this accounts for half the total number of amino acids. Additionally, C_α - C_β - C_γ connectivities from five more amino acids Asn, Asp, Phe, Trp and Tyr will be detected but downfield in the indirect dimension (more than 200 ppm, not shown in Figure 2.11). As a general result, the spectrum associated with multiple-quantum correlation experiments simplifies as the order of the detected coherence increases. Unfortunately, the reduced sensitivity associated with excitation and reconversion of 3Q (and higher) coherences [41, 42] prevents the application of these experiments to biological systems.

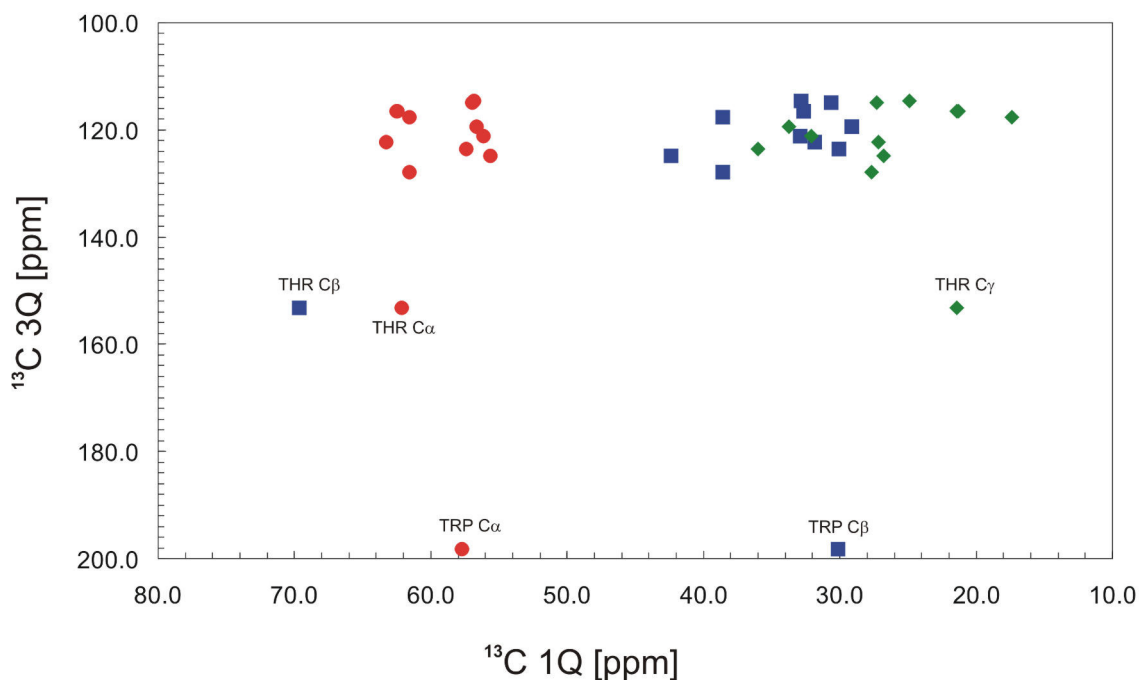


Figure 2.11. Expected ^{13}C homonuclear 3Q-1Q correlations in the sidechain of all 20 amino acids. C_α , C_β and C_γ spins are depicted by red circles, blue squares and green diamonds, respectively.

2.1.4. Applications of 2Q and 3Q correlation experiments

We first present 2Q correlation spectra on uniformly [^{13}C , ^{15}N]-labeled proteins recorded on a 600 MHz spectrometer at 7 kHz MAS and at a temperature of -5°C . Various pulse sequences exist for the recoupling of the homonuclear dipolar interaction under MAS. Here we made use of POST-C7 [43] and SPC5 [44].

Placing the carrier frequency in the aliphatic spectral region allows for the excitation of 2Q coherences involving aliphatic carbons only (even with broadband recoupling sequences), as shown in Figure 2.12 for the Crh protein [26]. The favorable linewidth of this sample (that exists in a microcrystalline form) results in high-resolution 2Q correlation spectra. Many resonances are resolved and assist the classification of resonances according to the residue type [26].

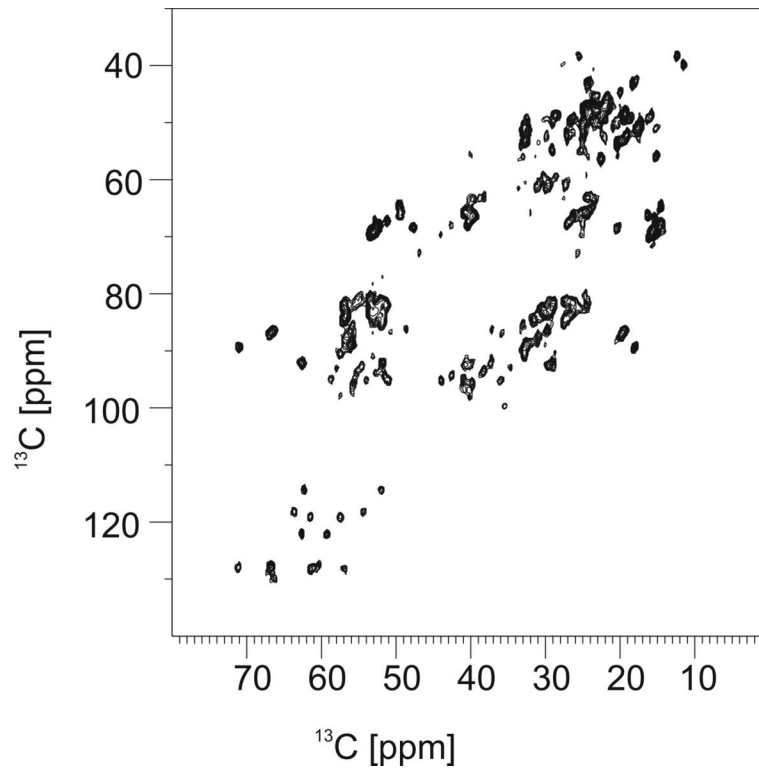


Figure 2.12. 2Q correlation experiment in the sidechain region of the uniformly [^{13}C , ^{15}N]-labeled protein Crh. The SPC5 [44] sequence was used to excite 2Q coherences for 4 rotor periods. High CW [11] proton decoupling of 85 kHz was employed during the excitation and reconversion blocks.

Alternatively, broadband recoupling may be achieved by placing the carrier frequency in the middle of the ^{13}C spectrum. Apart for the correlations shown above, 2Q involving carbonyl ^{13}C may be excited. In Figure 2.13 the aliphatic region of the spectrum where these ^{13}CO - $^{13}\text{C}_\alpha$ correlations are found is shown.

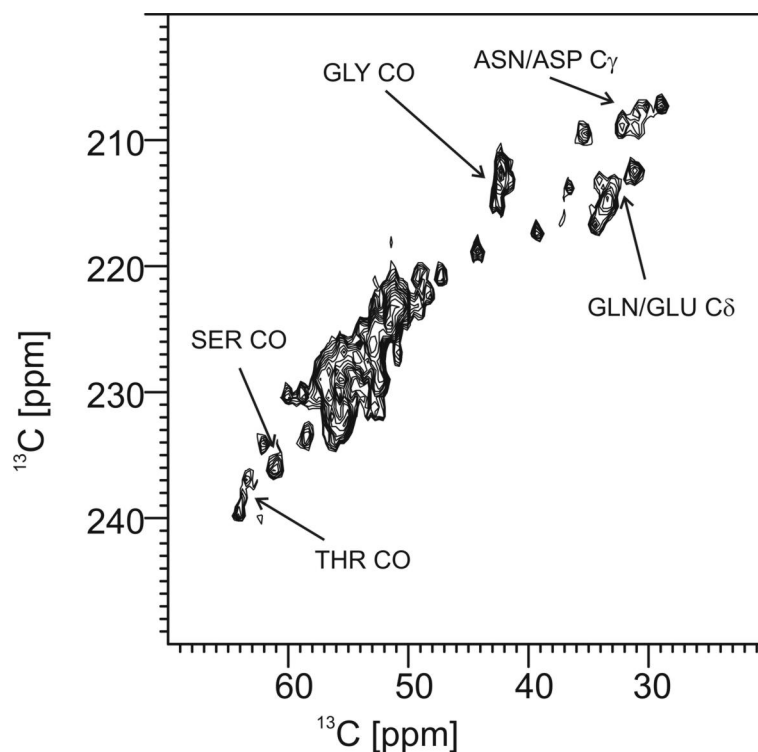


Figure 2.13. Broadband 2Q correlation experiment on the uniformly [^{13}C , ^{15}N]-labeled protein Crh. Only the aliphatic spectral region exhibiting 2Q correlations ^{13}CO - $^{13}\text{C}_\alpha$ is presented. The POST-C7 [43] sequence was used to excite 2Q coherences for 4 rotor periods. High CW [11] proton decoupling (100 kHz) was employed during excitation and reconversion blocks.

Here, in the direct dimension between 30 and 40 ppm, resonances of the type C_β - C_γ for Asn and Asp and of the type C_γ - C_δ for Gln and Glu are found (C_γ and respectively C_δ are carbonyls in these cases). In this case, all resonances are resolved and can be assigned. Additionally, correlations of the type $^{13}\text{C}_\text{O}$ - $^{13}\text{C}_\alpha$ for Gly (at around 45 ppm in ω_2) are the only resonances involving Gly. Downfield in ω_2 , Ser (at 59 ppm) and Thr (at 62 ppm) C_O - C_α correlations are observed. Except the already mentioned groups of correlations, the majority of the resonances are overlapping in the spectral region ω_1 =(220 ppm, 230 ppm) and ω_2 =(50 ppm, 60 ppm) where any further investigations are difficult at such protein size and resolution and additional experiments are required [26].

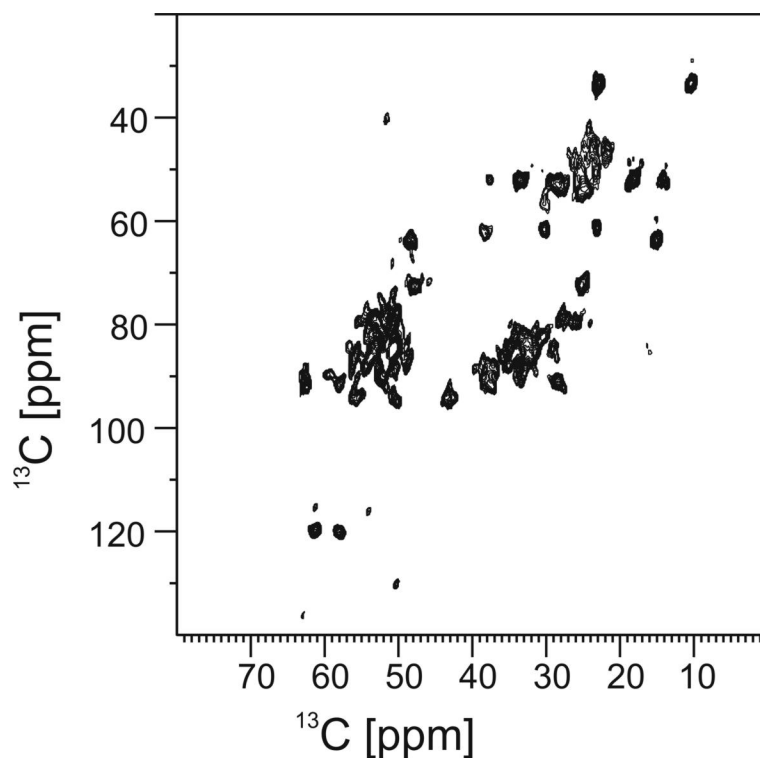


Figure 2.14. 2Q correlation experiment in the sidechain of the uniformly [^{13}C , ^{15}N]-labeled toxin KTX. The SPC5 [44] sequence was used to excite 2Q coherences for 4 rotor periods. High CW [11] proton decoupling of 85 kHz was employed during excitation and reconversion blocks.

Furthermore, we investigate KTX, a 38-residue polypeptide scorpion toxin ([45, 46]) that blocks a variety of K^+ channels ([47-49]) with high affinity (i.e. sub-nanomolar). At an initial stage of solid-state NMR studies of this system, we compare the secondary structure of the solid-phase KTX with the structure determined using solution-state NMR. The 2Q correlation spectrum shown in Figure 2.14 can be directly compared with the corresponding solution-state NMR spectrum. ^{13}C chemical shifts from solution-state NMR are not available, but they can be predicted from the known structure ([50]) by the SHIFTS program ([51]). Although SSNMR resonance assignment was not performed for this sample yet, tentative comparison with the solution-state ^{13}C 2Q pattern favors a similar backbone conformation. Further experiments that study the toxin free and when bound to a K^+ channel ([47]) are ongoing.

In Figure 2.15 we present a 3Q correlation experiment on the uniformly [^{13}C , ^{15}N]-labeled valine amino acid on a 400 MHz magnet. The very low efficiency associated with the detection of 3Q coherences is manifested in the large amount of material and/or long experimental times needed to acquire a spectrum. Here, a 4 mm NMR rotor was filled with 60 mg of microcrystalline sample. The experiment, comprising 64 points in t_1 , was run for 2

days. The efficiency of the 3Q filtering ([41, 42]) was estimated to about 3% of the direct CP [17, 18] signal in this case. 3Q coherences between the strongest dipolar coupled three-spin systems (i.e. CO-C α -C β , C α -C β -C $\gamma_{1,2}$ and C β -C γ_1 -C γ_2 where two pairs of carbons are directly bonded) are excited with greatest efficiency. They are all found in the spectrum presented in Figure 2.15 along with sidebands in ω_1 . For the sake of simplicity, the sidebands were removed from the spectrum.

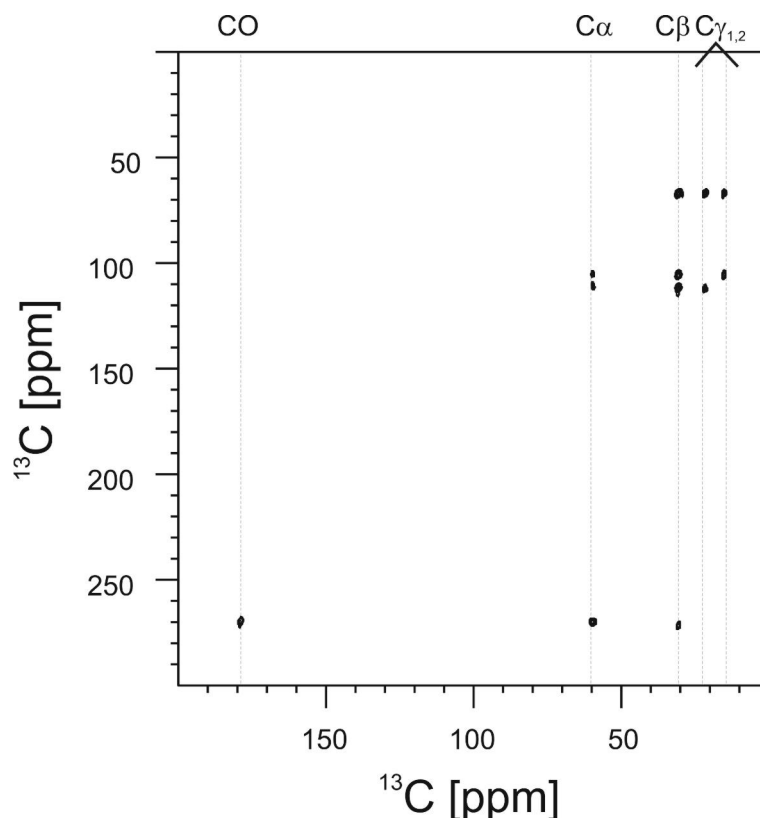


Figure 2.15. 3Q correlation experiment on uniformly [^{13}C , ^{15}N]-labeled valine. The MELODRAMA [52] sequence was used to excite 3Q coherences for 8 rotor periods. High CW [11] proton decoupling of 80 kHz was employed during excitation and reconversion blocks.

2.2. The sum and difference experiment

The isotropic chemical shifts of the various ^1H , ^{13}C and/or ^{15}N spins in polypeptides can be significantly influenced by conformation-dependent contributions under both solution-state ([53-56]) or solid-phase ([57-59]) conditions. The relationship between the protein secondary structure and the observed isotropic chemical shift has been investigated experimentally ([53-56, 60]) and theoretically ([60, 61]). For example, empirical solution state studies have found a remarkable correlation between C_α and C_β isotropic chemical shift values and protein secondary structure [56]. Correspondingly, the calculated difference between the experimentally observed C_α and C_β isotropic chemical shift values has been correlated with protein backbone structure in solution and solid-phase applications ([59, 62]). The sum of the two chemical shift values can be readily obtained from the evolution dimension of a double-quantum correlation experiment ([20, 34]). In the following we examine whether the sum chemical shift may serve as a qualitative indicator of protein backbone conformation.

2.2.1. Statistics of C_A and C_B chemical shifts

A database of chemical shifts as determined in solution-state NMR experiments [63] was used to perform the statistical analysis presented below. The database contains chemical shifts assignments of 40 globular proteins in solution-state. A PERL script was used to select all C_α and C_β chemical shifts and separate them based on residue type and secondary structure. For simplicity, only the residues found in α -helix (abbreviated as H here) or in β -sheet (E) were considered. Because Gly has no side chain, it is omitted in our discussion.

For each residue type, average chemical shifts were calculated for C_α and C_β chemical shifts in the α -helix ($\overline{\Omega}_{CA,H}$ and $\overline{\Omega}_{CB,H}$, respectively) and β -sheet ($\overline{\Omega}_{CA,E}$ and $\overline{\Omega}_{CB,E}$, respectively) conformations as follows:

$$\begin{aligned}\overline{\Omega}_{CA,X} &= \frac{1}{N_X} \sum_{i=1}^N \Omega_{CA,X} \\ \overline{\Omega}_{CB,X} &= \frac{1}{N_X} \sum_{i=1}^N \Omega_{CB,X}\end{aligned}\tag{66}$$

where X may be H or E and N_X is the number of corresponding database entries found in each case. More precisely, these numbers are, for each conformation and residue type: Ala ($N_H=100$, $N_E=42$), Arg ($N_H=52$, $N_E=28$), Asn ($N_H=32$, $N_E=16$), Asp ($N_H=35$, $N_E=23$), Cys ($N_H=11$, $N_E=16$), Gln ($N_H=41$, $N_E=21$), Glu ($N_H=100$, $N_E=54$), Gly ($N_H=0$, $N_E=0$), His ($N_H=15$, $N_E=8$), Ile ($N_H=48$, $N_E=78$), Leu ($N_H=93$, $N_E=74$), Lys ($N_H=77$, $N_E=55$), Met ($N_H=27$, $N_E=18$), Phe ($N_H=48$, $N_E=45$), Pro ($N_H=13$, $N_E=12$), Ser ($N_H=30$, $N_E=42$), Thr ($N_H=39$, $N_E=77$), Trp ($N_H=12$, $N_E=13$), Tyr ($N_H=266$, $N_E=36$), Val ($N_H=56$, $N_E=96$). It is worth mentioning that standard deviations are found in the range of 1 to 2 ppm for all cases.

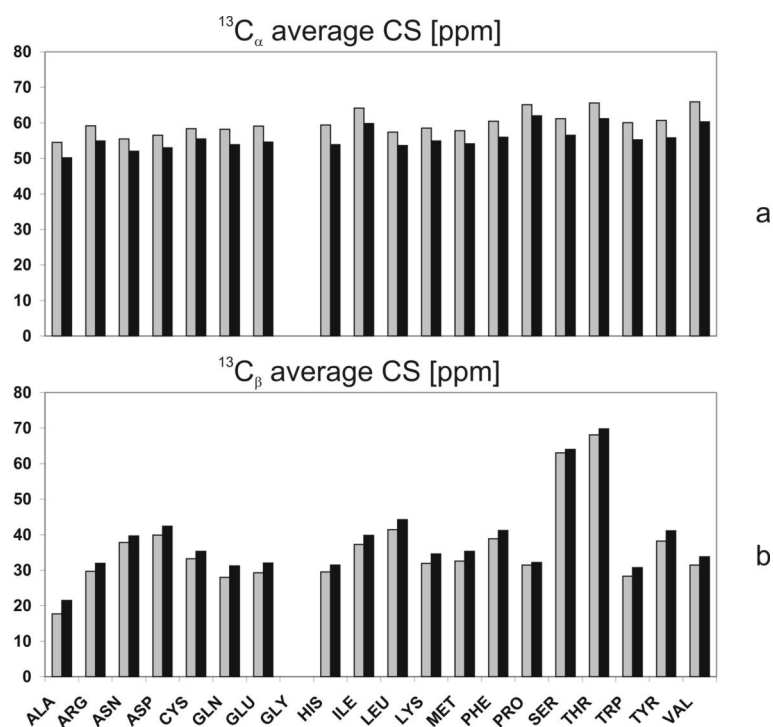


Figure 2.16. Average chemical shifts for (a) C_α and (b) C_β calculated as according to Equation (66) for α -helix (gray) and β -sheet (black) conformations. Both graphs (a and b) exhibit the same scale and can be readily compared.

The resulting average chemical shifts are plotted in Figure 2.16. Unlike the C_α , the C_β chemical shifts exhibit a significant dependence on residue type: the former span about 15 ppm and the latter cover almost 50 ppm. On the other hand, there is systematic dependence on secondary structure: one finds a difference of a few ppm in the chemical shifts between α -helix and β -sheet for both C_α and C_β but in opposite directions [56, 59]. Subsequently, this dependence on the secondary structure is expected to be diminished when the sum frequency is detected and to be amplified when the difference in the chemical shifts is monitored.

To exemplify this, we have calculated the average sum and difference of the C_α and C_β chemical shifts. For each amino acid type, these parameters are:

$$\begin{aligned}\overline{\Sigma\Omega}_X &= \overline{\Omega}_{CA,X} + \overline{\Omega}_{CB,X} \\ \overline{\Delta\Omega}_X &= \overline{\Omega}_{CA,X} - \overline{\Omega}_{CB,X}\end{aligned}\quad (67)$$

where again X may be H or E corresponding to the helix or sheet conformation, respectively. The results shown in Figure 2.17 demonstrate that the parameter $\overline{\Sigma\Omega}_{H,E}$ does not considerably depend on the secondary structure: differences amount to as much as 2 to 3 ppm between the two conformations. On the other hand the parameter $\overline{\Delta\Omega}_{H,E}$ displays increased sensitivity to secondary structure for all residues (differences as large as 10 ppm may be observed between the two conformations). It is also observed that both parameters are sensitive probes for residue type.

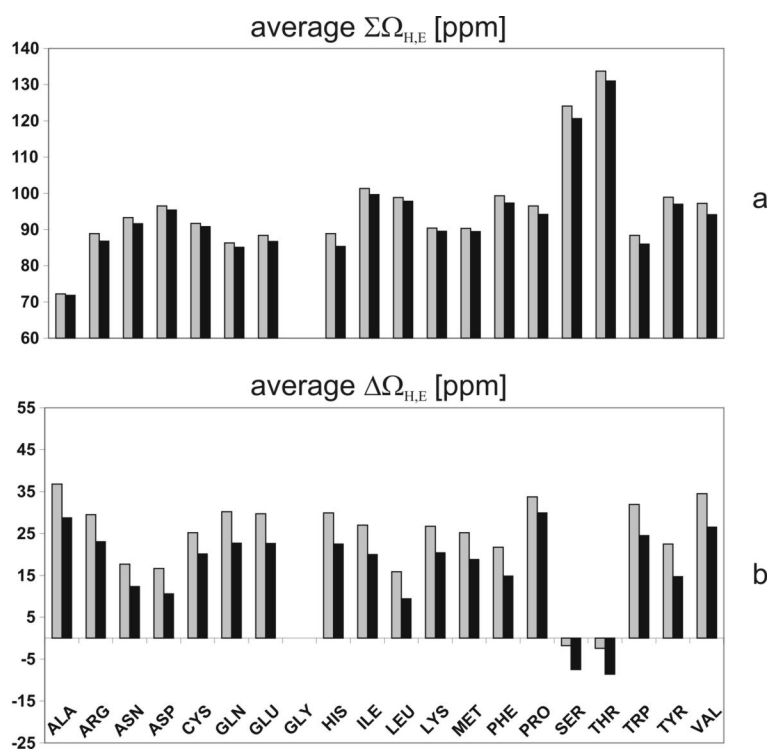


Figure 2.17. Dependence on residue type and secondary conformation (α -helix in gray and β -sheet in black) for the (a) sum and (b) difference of the C_α and C_β chemical shifts as calculated from Equation (67). Both scales span 80 ppm such as bars may be compared directly (also with bars in Figure 2.16).

Finally, to further demonstrate the concept introduced we define for each amino acid type the parameters:

$$\begin{aligned}\Sigma_{H,E} &= \Sigma\bar{\Omega}_H - \Sigma\bar{\Omega}_E \\ \Delta_{H,E} &= \Delta\bar{\Omega}_H - \Delta\bar{\Omega}_E\end{aligned}\tag{68}$$

to quantify the difference in the parameters $\Sigma\bar{\Omega}_H$ and $\Sigma\bar{\Omega}_E$ on one side and between $\Delta\bar{\Omega}_H$ and $\Delta\bar{\Omega}_E$ on the other side. The interpretation of these parameters is as follows: for example, $\Delta_{H,E}$ represents the average separation of the 0Q frequencies (involving C_α and C_β spins) exhibited by some amino acid between α -helix and β -sheet conformations. The larger this parameter is, the bigger the separation of the resonances, e.g. the better the sensitivity to secondary structure. Direct comparison of the two parameters relating to 2Q and 0Q frequencies is done in Figure 2.18.

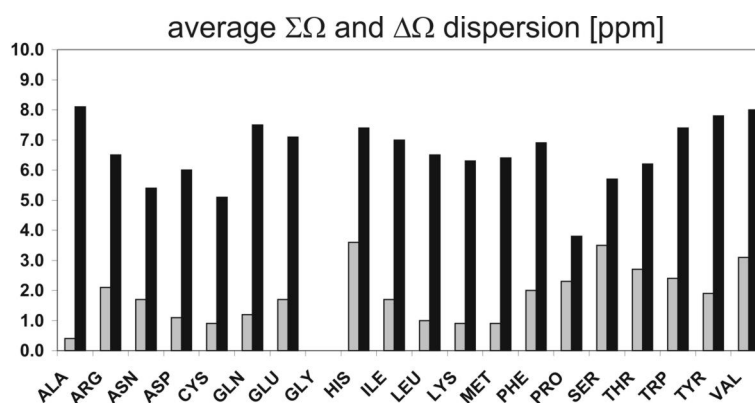


Figure 2.18. Summary of average contributions from residue type and defined secondary conformation to the dispersion in 2Q ($\Sigma\bar{\Omega}$, gray) and 0Q ($\Delta\bar{\Omega}$, black) frequencies, as calculated in Equation (68) for all amino acids.

In Figure 2.18, one can easily observe that the dispersion in the difference is considerably larger than the dispersion in the sum of the chemical shifts for the considered backbone conformations.

2.2.2. The S/D correlation experiment

In the previous section we have proposed that detecting the sum and the difference of the chemical shifts of C_α and C_β spins might improve the spectral resolution. This could be achieved by 2Q and 0Q correlation experiments, respectively. These methods have been demonstrated in both solution-state ([34, 64]) and solid-state ([35, 65, 66]) NMR. Alternatively, we propose here a novel experiment which encodes both the sum and the

difference in chemical shifts of two coupled nuclei in the indirect dimension. Accordingly, we name this the S/D (sum and difference) correlation experiment.

In Figure 2.19.a the generic pulse scheme of the S/D experiment is depicted. It comprises two synchronously incremented evolution periods t_{1a} and t_{1b} connected by a mixing block. Depending on the exact mixing sequence used, dipolar or scalar spins might be correlated in t_{1a} and t_{1b} . For example, a proton-driven spin diffusion (SD, [25]) mixing block may be employed (Figure 2.19.b).

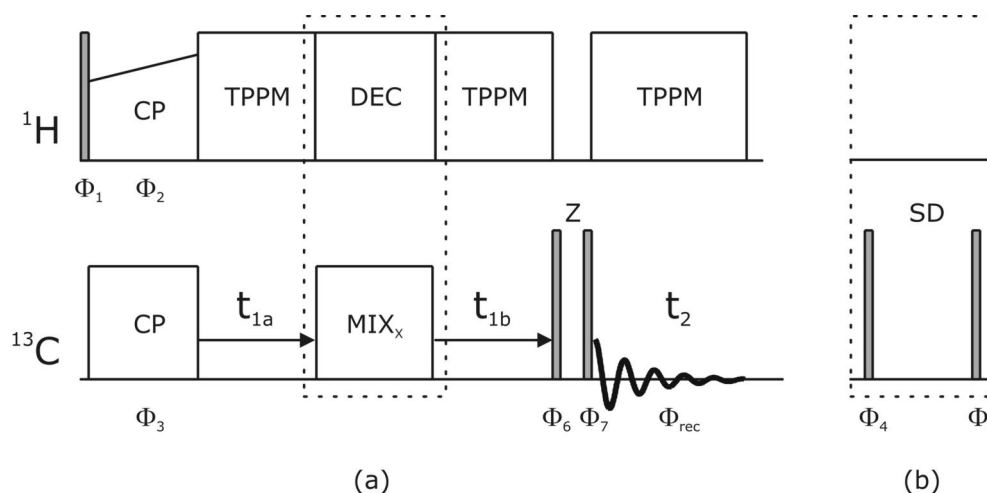


Figure 2.19. (a) The generic pulse sequence for the proposed S/D (sum and difference) experiment. Here, a proton-driven spin diffusion block was used for mixing (b).

Conventional amplitude modulated [67, 68] cross polarization [17, 18] from ^1H to ^{13}C nuclei creates initial ^{13}C polarization along the x-axis in the rotating frame:

$$\rho(t_{1a} = 0) = \sum_j I_{xj} \quad (69)$$

During evolution times we neglect dipolar and CSA interactions under HR-SSNMR conditions, such that evolution takes only place under the influence of isotropic chemical shifts Ω_j :

$$\rho(t_{1a}) = \sum_j I_{xj} \cos(\Omega_j t_{1a}) + I_{yj} \sin(\Omega_j t_{1a}) \quad (70)$$

The subsequent mixing block transfers selectively the x component of the magnetization to coupled partners:

$$\begin{aligned}\rho(t_{1b} = 0) = & \sum_j I_{xj} d_{jx,jx}(\tau) \cos(\Omega_j t_{1a}) \\ & + \sum_{j,k} I_{xk} d_{jx,kx}(\tau) \cos(\Omega_j t_{1a})\end{aligned}\quad (71)$$

Generally, we have allowed for partial transfer of magnetization from spin j to spin k encoded in the coefficients $d_{jx,jx}(\tau)$ and $d_{jx,kx}(\tau)$ which explicitly depend on the choice of the mixing block and its timing τ . Subsequent evolution renders the density operator in the rotating frame:

$$\begin{aligned}\rho(t_{1b}) = & \sum_j I_{xj} d_{jx,jx}(\tau) \cos(\Omega_j t_{1a}) \cos(\Omega_j t_{1b}) \\ & + \sum_{j,k} I_{xk} d_{jx,kx}(\tau) \cos(\Omega_j t_{1a}) \cos(\Omega_k t_{1b})\end{aligned}\quad (72)$$

Only the x-components of the magnetization, to be selected by the subsequent z-filter [4], have been considered.

The exact phase cycling in the case of the spin diffusion mixing block Figure 2.19.b is presented here (see the figure for phase notations): $\phi_1 = \{+y\}_4, \{-y\}_4$; $\phi_2 = +x$; $\phi_3 = +x$; $\phi_4 = +y$; $\phi_5 = -y$; $\phi_6 = +y$; $\phi_7 = \{-y, +x, +y, -x\}$; $\phi_{rec} = \{+x, +y, -x, -y, -x, -y, +x, +y\}$. Incrementing the phase ϕ_3 by 90° in successive experiments in t_1 allows implementation of TPPI [19] to construct a complex signal amplitude along t_1 .

In the density operator above the first term will give rise to auto-peaks (magnetization not transferred), while the second term will give rise to cross-peaks (magnetization transferred between spins j and k). If $t_{1a} = t_{1b} = t_1$ at any time during the experiment, the following coefficients in Equation (72) may be rewritten as:

$$\begin{aligned}2 \cos(\Omega_j t_{1a}) \cos(\Omega_k t_{1b}) & \xrightarrow{t_{1a}=t_{1b}=t_1} \cos(\Omega_j + \Omega_k) t_1 + \cos(\Omega_j - \Omega_k) t_1 \\ 2 \cos(\Omega_j t_{1a}) \cos(\Omega_j t_{1b}) & \xrightarrow{t_{1a}=t_{1b}=t_1} \cos(\Omega_j + \Omega_j) t_1 + \cos(\Omega_j - \Omega_j) t_1\end{aligned}\quad (73)$$

Equation (73) shows two sets of cross-peaks will be observed that in the indirect dimension: one at the sum ($\omega_1 = \Omega_j + \Omega_k, \omega_2 = \Omega_{j,k}$) and the other at the difference ($\omega_1 = \Omega_j - \Omega_k, \omega_2 = \Omega_{j,k}$) of the chemical shifts of the coupled spins j and k . There will also be two sets of auto-peaks present in the spectrum: one along the diagonal

$(\omega_1 = \Omega_j - \Omega_j = 0, \omega_2 = \Omega_j)$ and one along the diagonal $(\omega_1 = \Omega_j + \Omega_j = 2\Omega_j, \omega_2 = \Omega_j)$. These last correlations only increase the spectral overlap and can be minimized by utilizing scalar through-bond transfer schemes [7] or adiabatic through-space transfer mechanisms [69, 70], which minimize $d_{jx,jx}(\tau)$ and maximize $d_{jx,kx}(\tau)$ in Equation (72).

The concept of concerted evolution periods has been previously used, both in solution-state ([71, 72]) and solid-state NMR ([73]), to reduce the dimensionality of triple-resonance experiments. This has been done with the purpose of combining both ^{13}C and ^{15}N evolutions into a single dimension (the heteronuclear version of the experiment). It is also important to note that only single-quantum coherences are involved and the linewidth in both dimensions of the experiment is given by the normal transverse 1Q relaxation rate.

We now demonstrate the principle of the experiment on a mixture of the uniformly [^{13}C , ^{15}N]-labeled amino acid valine and tripeptide Ala-Gly-Gly. The aliphatic region of the spectrum is shown in Figure 2.20. Only the Val and Ala residues have sidechains and lead to cross-peaks in the spectrum (resonances involving C_γ of Val are not visible in the chosen spectral region). Along the two diagonals, resonances from the two Gly are visible.

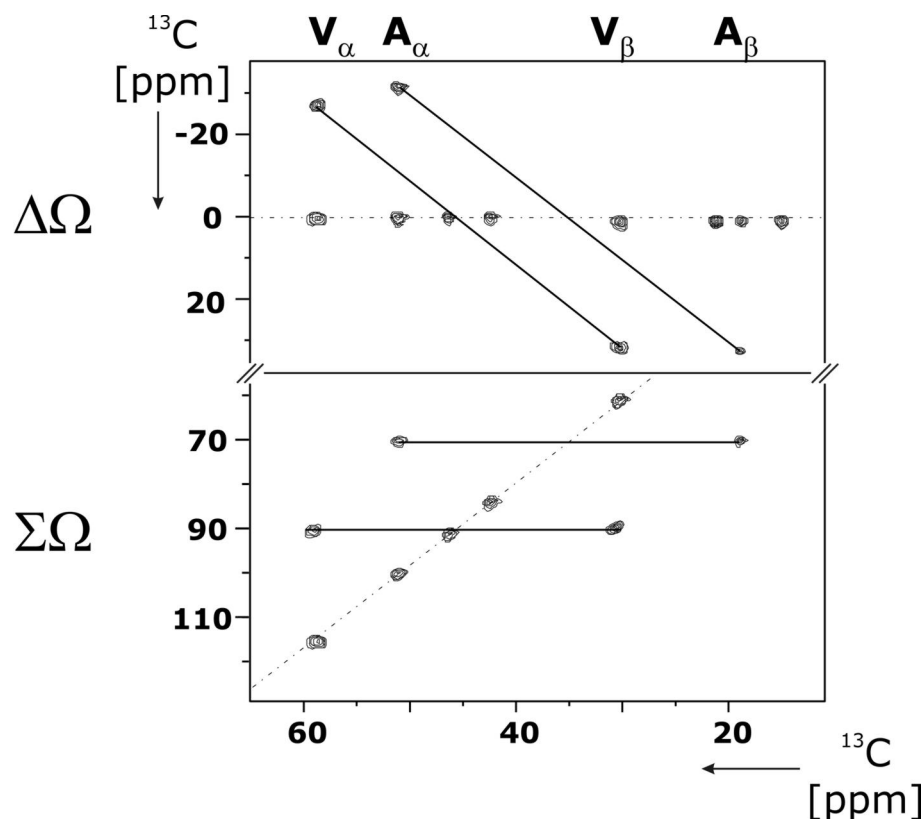


Figure 2.20. The S/D experiment applied to a mixture of the amino acid Val and the tripeptide Ala-Gly-Gly, both uniformly labeled. The experiment was conducted on a Bruker 400 MHz spectrometer at 11 kHz MAS.

In this sample, secondary structure contributions cannot be observed, but only residue type differences. As expected from a close inspection of Figure 2.17.a, there is a larger separation of the 2Q frequencies for Ala and Val. This amounts to about 20 ppm independently of the backbone conformation. The corresponding dispersion of the 0Q frequencies is significantly smaller, less than about 5 ppm (Figure 2.17.b). Both cases are experimentally verified in Figure 2.20.

2.2.3. Experimental results on ubiquitin

To demonstrate the sensitivity of the S/D correlation experiment to peptide secondary structure, a 5 mg hydrated sample of uniformly [^{13}C , ^{15}N]-labeled ubiquitin was studied. Selected parts of the spectra are shown in Figure 2.21. The sum and the difference chemical shift spectra are identical to a 2Q respectively 0Q correlation pattern except the diagonals (2Ω , Ω) and (0 , Ω). Tentative assignments were done based on chemical shifts from solution-state NMR. This should be possible given that the X-ray crystal structure [74] and the solution-state NMR structure [75] are very similar.

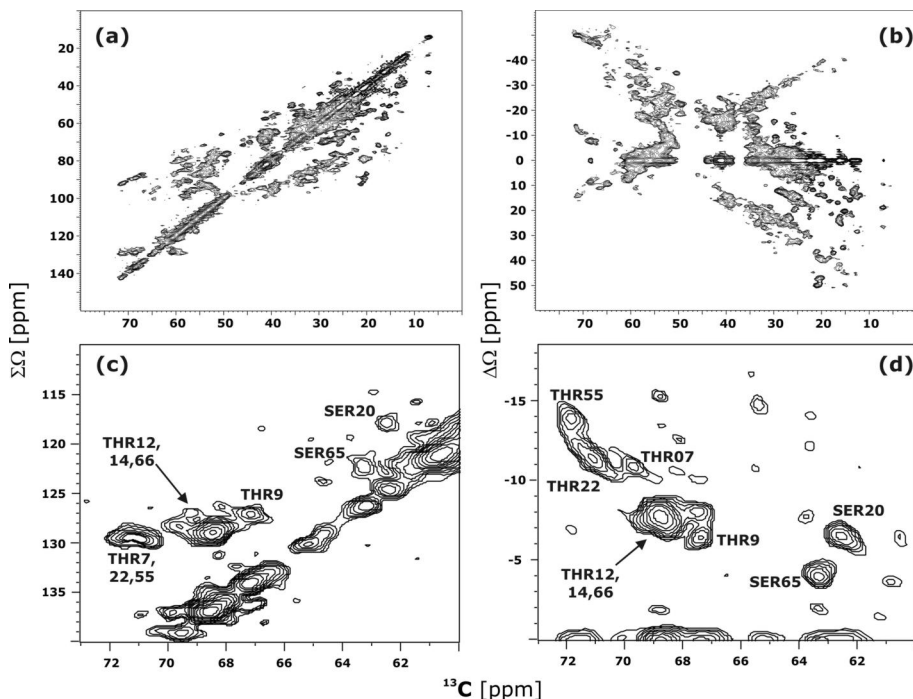


Figure 2.21. S/D experiment performed on U- ^{13}C , ^{15}N -labeled ubiquitin. Displayed are spectral regions involving $\Sigma\Omega$ (a, c) and $\Delta\Omega$ (b, d). Calibration of the ω_1 axis was done independently in the two cases to match conventional 2Q and 0Q referencing. The lower spectra are expanded regions containing Thr and Ser resonances. The experiment was performed on a 400 MHz magnet, at 11 kHz MAS and -5°C .

First we concentrate on the isolated regions in Figure 2.21 (c, d) displaying the C_α - C_β correlations of Thr and Ser. In the sum case, good separation is found for the two amino acids in ω_1 : about 3 to 4 ppm. In the difference case, there is overlap between these resonances in ω_1 . If we concentrate on the seven Thr residues found in ubiquitin, we can observe that they span about 3 ppm and almost 9 ppm in ω_1 in the sum and difference cases, respectively. This result demonstrates that the difference $\Omega_{CA} - \Omega_{CB}$ encodes the secondary structure and can separate resonances accordingly.

Other resonances summarized in Table 2.1 with assigned sum and difference chemical shifts and torsion angles from the known 3D structure support the following conclusions: (1) the sum chemical shift enhances spectral dispersion for different amino acids or amino acids in similar (secondary structure) conformations and (2) the difference chemical shift enhances spectral dispersion for different amino acids or amino acids found in different (secondary structure) conformations.

Residue		¹³ C chemical shift [ppm]		Torsion angles		
Type	Number	$\Sigma\Omega$	$\Delta\Omega$	ψ	ϕ	conf.
ALA	28	72	37	-38.1	-66.1	H
	46	66	35	46.0	48.2	T
ASN	25	92	18	-44.4	-65.5	H
	60	91	16	45.4	57.9	T
GLU	24	85	33	-40.5	-57.6	H
	64	82.5	33	19.1	66.9	T
ILE	3	99	16	163.0	-131.1	E
	13	99	18.5	142.0	-109.5	E
	23	97	28.5	-37.2	-61.3	H
	30	100	29	-39.6	-70.0	H
LEU	15	97	6	154.0	-126.4	E
	43	95.5	7	130.2	-103.6	E
PRO	19	94.5	33	-24.5	-54.9	T
	37	91	30	137.0	-57.0	L
	38	97	32.5	-32.2	-57.2	G
SER	20	118	-6.5	-8.1	-79.8	T
	65	122	-4	159.5	-71.1	L
THR	7	129.5	-11	170.8	-99.6	E
	9	127	-6	14.9	-101.4	T
	12	129	-7.5	131.8	-119.9	E
	14	129	-7.5	139.7	-101.4	E
	22	129.5	-11.5	160.4	-83.7	B
	55	129.5	-14	164.6	-104.5	B
	66	129	-7.5	126.7	-119.2	E
VAL	5	93.5	27	114.2	-118.0	E
	17	91	22	170.7	-139.0	L
	26	97	37	-46.4	-58.4	H
	70	93.5	27	139.9	-108.1	E

Table 2.1. Tentative solid-state NMR assignments of ubiquitin from the S/D spectrum shown in Figure 2.21. Indicated are the sum and difference chemical shifts $\Sigma\Omega=\Omega_{CA}+\Omega_{CB}$ and $\Delta\Omega=\Omega_{CA}-\Omega_{CB}$ (recorded in the S/D experiment) that can be utilized to calculate the chemical shifts of C_{α} and C_{β} nuclei, individually. In addition, dihedral angles as obtained from solution-state NMR (PDB entry 1D3Z) along with a one letter notation for the actual secondary structure conformation (H = α -helix, B = isolated beta-bridge, E = β -sheet, T = hydrogen bonded turn, G = 3/10 helix, L = loop) are given.

For example in Table 2.1, the two Ala residues found in α -helix and hydrogen bonded turn conformations are dispersed by 6 ppm and 2 ppm in the sum and difference chemical shifts,

respectively. On the other hand, the two groups of Ile residues found in α -helix and β -sheet conformations are separated by 2 ppm and 10 ppm in the sum and difference chemical shifts, respectively.

The experimental results obtained on ubiquitin indicate that even small variations in backbone conformation may suffice to disperse protein signals in an S/D 2D (^{13}C , ^{13}C) correlation experiment. In our applications, signal losses during the longer evolution time and the z-filter are not considerable and the sensitivity of the S/D experiment is comparable to a conventional 1Q-1Q correlation experiment assuming the same mixing scheme. In cases where amino acid type and backbone conformation are both similar, additional resolution might be obtained from an investigation of the side chain correlations, possibly by extending the method to three spectral dimensions or from further inter-residue correlation experiments [76].

We expect the current method to be of particular interest in cases where spectral overlap e.g. due to protein size, primary sequence or sample heterogeneity limits the applicability of other correlation experiments. Biophysical applications could include membrane protein ligands, protein aggregates or partially folded proteins in the solid-phase or in the solution-state. Our results obtained on a 400 MHz NMR instrument suggest that the resulting 2D correlation spectra might be sensitive to even small variations in backbone structure, in particular when studied under ultra-high magnetic field conditions. For applications in helical membrane proteins, extensions to three spectral dimensions that include additional side chain correlations, the incorporation of heteronuclear (^{15}N , ^{13}C) correlation methods or the study of macroscopically oriented samples could further enhance the spectral resolution. A preliminary analysis of other protein resonances e.g. including ^1H and ^{15}N nuclei indicates that the proposed experimental scheme might also be helpful for the characterization of other peptide and protein segments when studied under MAS conditions.

2.3. Dipolar dephasing of ^{13}C - ^1H couplings

Another NMR parameter that might be useful for spectral editing is the strength of the ^{13}C - ^1H dipolar coupling in solids. On one hand, there are carbons weakly coupled to protons. These are of two types: methyl carbons (due to the intrinsic fast proton rotation [77-81]) and non-protonated carbons (e.g. carbonyl carbons which have no directly bonded proton). Methyl carbons play a particular role in determining protein folding by NMR as they usually represent the end of the sidechain and are therefore close to other (remote) parts of the molecule. Many ^1H - ^1H medium and long-range distance constraints involve hydrogens of methyl groups and are of great importance for structure determination under NMR. On the other hand, carbons that are strongly dipolar coupled to protons have one or two directly bonded hydrogen atoms (methine and methylene groups). With regard to spectral resolution, it is reasonable to separate the two groups of carbons as there is spectral overlap between the methyl carbons and some of the methylene carbons that resonate in the upfield region of the ^{13}C spectrum (Figure 2.22).

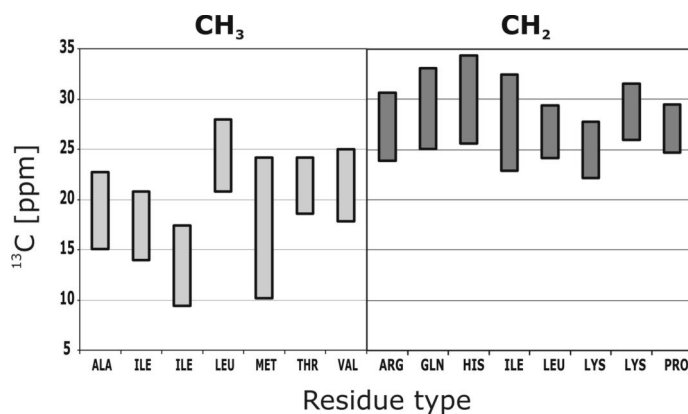


Figure 2.22. Spectral overlap expected for ^{13}C resonances in the upfield region of the spectrum: (left) methyl carbons and (right) selected methylene carbons. Statistical data from BMRB [40] (the restricted set of amino acid chemical shifts) was used as follows: bars centered at the average chemical shift and wide four times the standard deviation were drawn for each resonance. The exact nuclei are, from left to right: Ala C_β , Ile C_{γ_2} and C_{δ_1} , Leu $\text{C}_{\delta_{1,2}}$, Met C_ϵ , Thr C_{γ_2} , Val $\text{C}_{\gamma_{1,2}}$, Arg C_γ , Gln C_β , His C_β , Ile C_{γ_1} , Leu C_γ (a CH group), Lys C_γ and C_δ and Pro C_γ .

¹³ C spin	¹³ C- ¹ H dipolar coupling [kHz]	¹³ C- ¹ H distance [Å]
C	3.81	2.00
CH	22.92	1.09
CH ₃	7.33	1.11

Table 2.2. ¹³C-¹H dipolar couplings for different carbon spins (quaternary, methine, methylene and methyl).

Since the dipolar coupling scales inversely with the 3rd power of the internuclear distance, a large difference in the CH dipolar coupling is expected for carbons with and without directly attached protons (Table 2.2). Only the strongest coupling (e.g. the shortest internuclear distance) is shown for each case. For methyl carbons, the fast internal rotation about its C_{3v} axis reduces the effective dipolar coupling by a factor of $(3\cos^2\zeta - 1)/2$. Here, ζ is the angle between a C-H bond and the rotation axis, usually about 70°. The axially symmetric dipolar tensor is also redirected along the rotation axis, the effective dipolar interaction being identical to that of a simple spin pair ([82], Table 2.2).

This difference in ¹H-¹³C (effective) dipolar couplings can be used to efficiently separate the two classes of carbons with, for example, the experiments depicted in Figure 2.23. Both of the chosen experiments are simple and efficient as it has been demonstrated before [83]. The first experiment Figure 2.23.a implements a dipolar dephasing period [83]: during a short delay ¹³C spins are allowed to process in the local ¹H dipolar fields (proton decoupling is not employed). A π pulse is used to refocus the chemical shift evolution during the dipolar dephasing block (τ_d is set to an even multiple of the rotor periods). Destructive interference among the dipolar splittings and ¹H spin diffusion causes a rapid loss of the magnetization of ¹³C strongly coupled to ¹H (which is accomplished for sufficiently long τ_d periods). Thus, only non-protonated and methyl carbons are observed in the following acquisition period. Alternatively, in Figure 2.23.b a simple one-dimensional cross-polarization ¹³C [17, 18] experiment is presented. Here the τ_{CP} contact time is very short such that proton magnetization will be transferred efficiently only to the strongly coupled carbons which are subsequently detected.

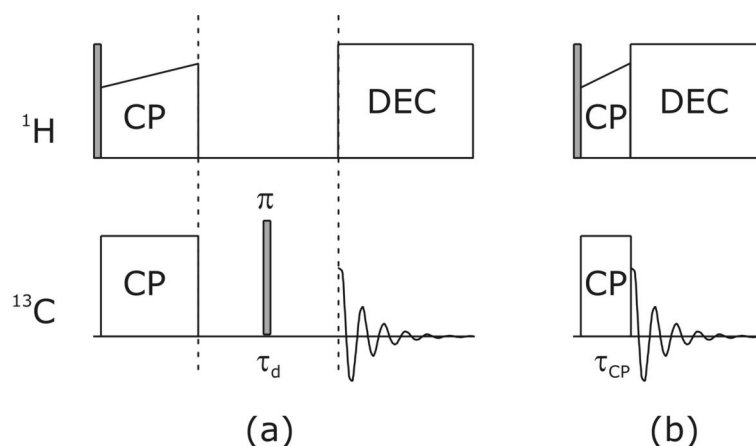


Figure 2.23. Simple experiments to recover signals of ^{13}C (a) weakly and (b) strongly dipolar coupled to ^1H with high efficiency. In the first case the dipolar dephasing time τ_d is long enough to achieve destructive interference among magnetization of ^{13}C strongly interacting with ^1H . In the second case the CP contact time τ_{CP} is very short such that ^{13}C weakly interacting with ^1H will not be transferred magnetization.

In Figure 2.24 the dephasing of various resonances of uniformly [^{13}C , ^{15}N]-labeled Val is monitored as a function of the dephasing time τ_d . It can be observed that after 4 to 6 rotor periods of dipolar dephasing, the signal intensity of the C_α and C_β resonances (both CH groups) decays almost completely, while the intensity of the CO (carbonyl) and $\text{C}_{\gamma,1,2}$ (CH_3 groups) is about 40% of the direct CP intensity (with respect to which the curves are normalized). This demonstrates that the presented spectral isolation of non-protonated and methyl ^{13}C resonances is efficient.

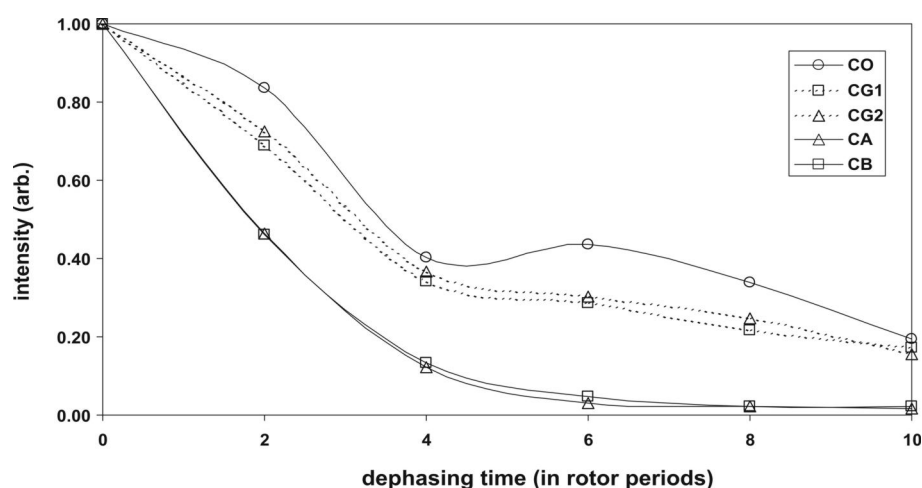


Figure 2.24. Experimental dipolar dephasing curves of the resonances of uniformly ^{13}C , ^{15}N labeled amino acid valine. Experiments as described in Figure 2.23.a were performed for each indicated dipolar dephasing time τ_d and signal intensities were monitored. Spectra were recorded on a 600 MHz spectrometer at 11 kHz MAS and 5°C .

Cross-polarization build-up curves monitored on a sample of uniformly [^{13}C , ^{15}N]-labeled ubiquitin are shown in Figure 2.25 for some selected resonances. One-dimensional experiments with increasing CP contact times were performed and resonance intensity monitored. Typically, after 100-200 μs the ^{13}CH and $^{13}\text{CH}_2$ carbons achieve almost full magnetization transfer while ^{13}CO and $^{13}\text{CH}_3$ carbons require up to 700-1000 μs of transfer to achieve full magnetization transfer. With CP contact times of about 100 μs magnetization transferred to ^{13}CO and $^{13}\text{CH}_3$ is significantly smaller when compared to other ^{13}CH and $^{13}\text{CH}_2$ spins.

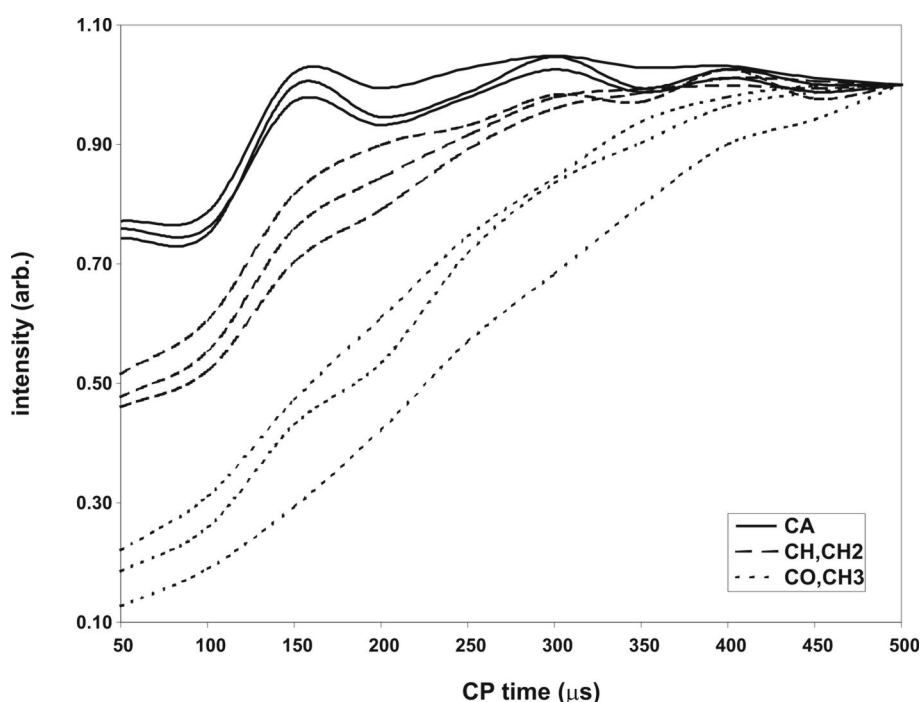


Figure 2.25. CP build up for various resonances in uniformly [^{13}C , ^{15}N]-labeled ubiquitin. Resonances in the $^{13}\text{C}_\alpha$ (CA, 50-60 ppm), $^{13}\text{C}_\beta$ and $^{13}\text{C}_\gamma$ (CH,CH₂, 30-40 ppm) and ^{13}CO and $^{13}\text{C}_{\gamma/\delta}$ (170-180 ppm and 10-20 ppm, respectively) were monitored. For the last class of spins, the signal builds up for CP times longer than shown here. Spectra were recorded on a 600 MHz spectrometer at 11 kHz MAS and -5°C . Curves were normalized to unity for 500 μs CP time.

Next we will demonstrate how these simple r.f. pulse schemes may be used in 2D experiments for the purpose of spectral simplification. We start with the 2Q correlation experiment in Figure 2.26 where a dipolar dephasing block is added to the experiment. As a result, ^{13}CO and $^{13}\text{CH}_3$ magnetization is selected as either (a) initial magnetization for the 2Q excitation block or (b) final magnetization to be detected. Consequently, only correlations involving at least one ^{13}CO or $^{13}\text{CH}_3$ will be observed in the 2D pattern in the first case. It should be noted that it is not required that both spins have initial magnetization for a 2Q coherence to be excited,

but the amplitude of the resulting 2Q coherence is correspondingly smaller (by a factor of two). In the second case, the resulting 2Q pattern is affected just before acquisition, all ^{13}CH and $^{13}\text{CH}_2$ resonances being effectively suppressed.

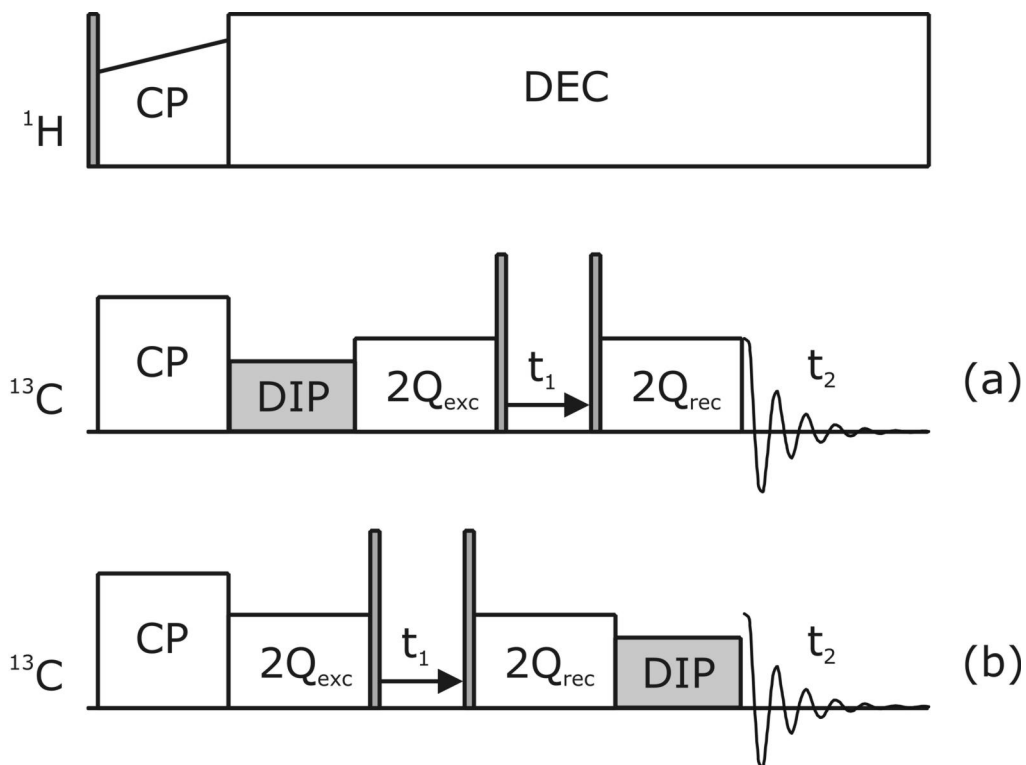


Figure 2.26. Various ways to incorporate the dipolar dephasing filter in a double-quantum correlation experiment: (a) before or (b) after the 2Q excitation and reconversion sequence.

The proposed experiment is demonstrated on uniformly ^{13}C , ^{15}N labeled Val in Figure 2.27. Here the usual 2Q correlation experiment is shown in Figure 2.27.a. For the experiment in Figure 2.26.a, the corresponding spectrum in Figure 2.27.b shows, as expected, only the correlations involving $^{13}\text{C}_{\gamma 1}$ or $^{13}\text{C}_{\gamma 2}$ (both CH_3 groups for Val) while the correlation $^{13}\text{C}_{\alpha}$ - $^{13}\text{C}_{\beta}$ (CH-CH) is absent. The experiment depicted in Figure 2.26.b results in the spectrum shown in Figure 2.27.c. As explained above, when compared to Figure 2.27.a, all correlations that do not involve $^{13}\text{CH}_3$ in both dimensions are suppressed. This results in the simplest spectrum and, importantly, the pattern found in Figure 2.27.b can be reconstructed if needed.

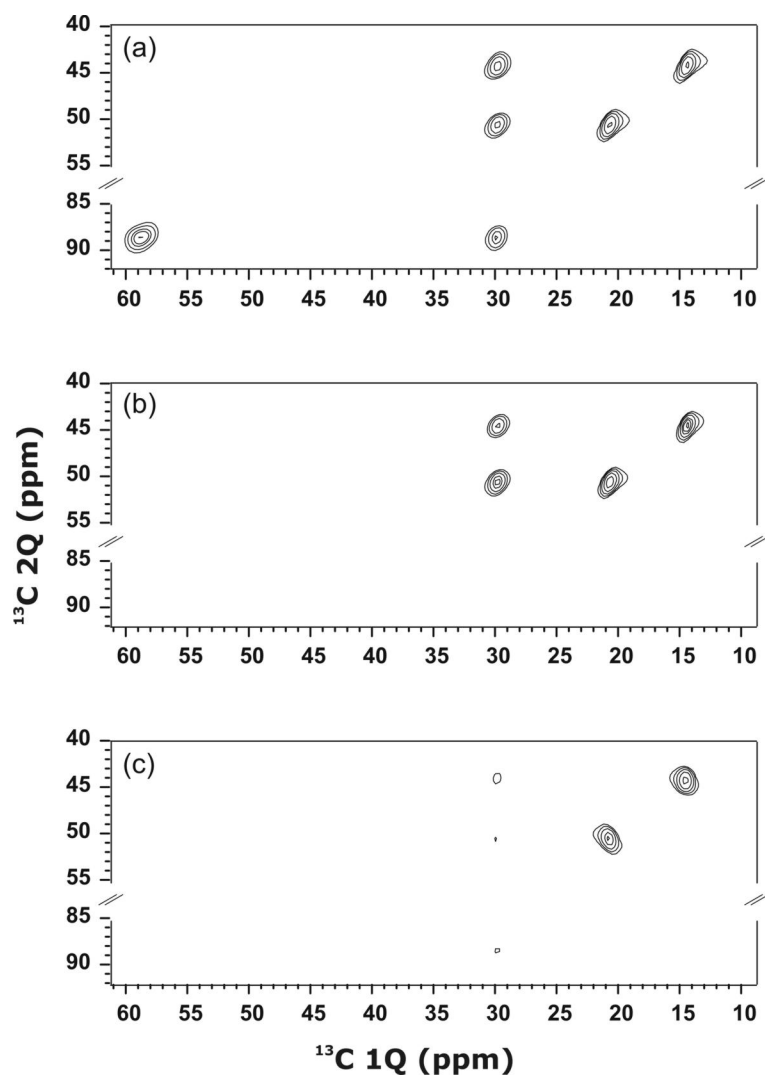


Figure 2.27. (a) Double-quantum correlation spectrum of uniformly [^{13}C , ^{15}N]-labeled valine. Filtered versions with a dipolar dephasing (b) before and (c) after the 2Q block as shown in Figure 2.26. For 2Q excitation and reconversion the SPC5 [44] sequence was used selectively in the aliphatic spectral region. In (b, c) a dephasing time of 6 rotor periods was employed. Spectra were recorded on a 600 MHz spectrometer at 11 kHz MAS and 5°C .

Results on uniformly [^{13}C , ^{15}N]-labeled ubiquitin are shown in Figure 2.28. The spectrum compares well with the prediction made using solution-state chemical shifts [75]. The filtering should be especially helpful for the resonances around 20-25 ppm in the direct dimension (shown in black in the prediction). In these cases, the pairing resonance is found in the same spectral range and causes serious overlap even in 2Q correlation experiments (where the diagonal resonances are not present). Because there are no $^{13}\text{CH}_3$ - $^{13}\text{CH}_3$ correlations (due to dipolar truncation), the spectrum is largely simplified here, the number of overlapping resonances being effectively halved. Additional resonances are observed in the spectrum (around 70 ppm in the indirect dimension) probably due to the mobility caused in the sample

by the hydration. Thus, the dipolar dephasing block probes not only the intrinsic fast rotation within the methyl groups, but also the dynamics of flexible segments of the protein.

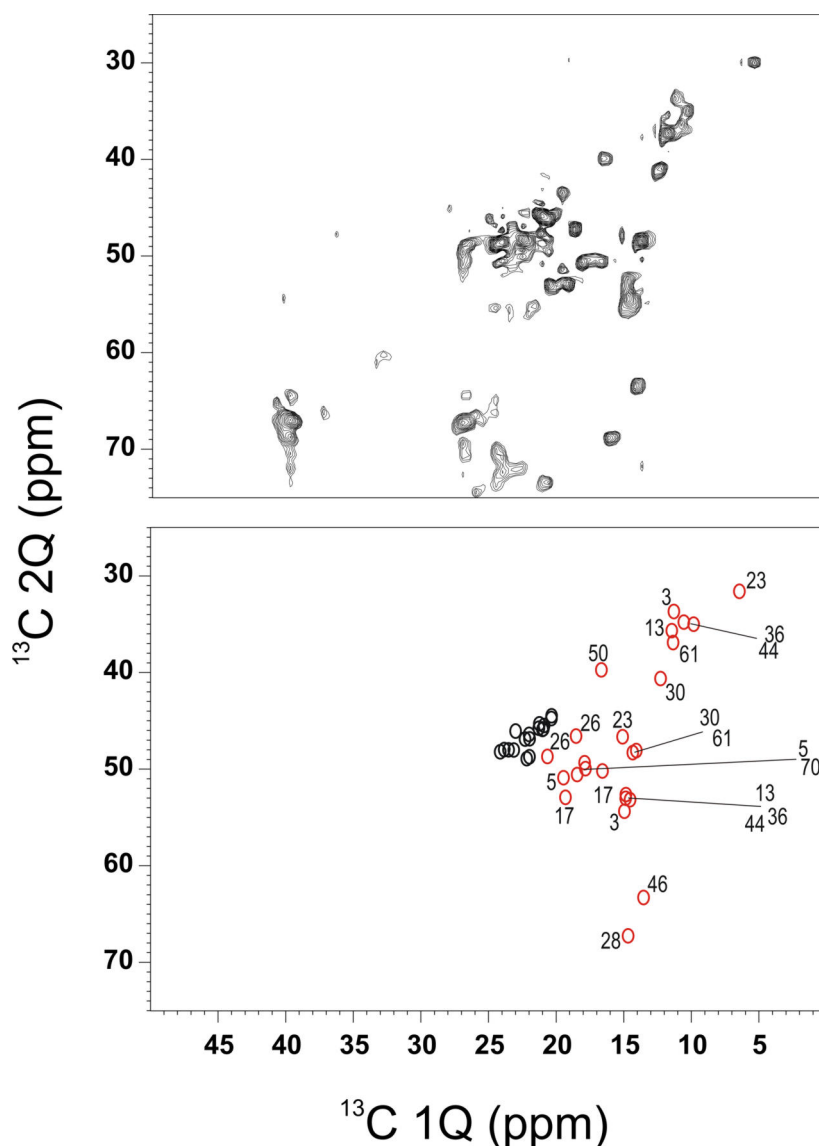


Figure 2.28. (Top) 2Q correlation spectrum of uniformly [^{13}C , ^{15}N]-labeled ubiquitin with an additional dipolar dephasing block (as in Figure 2.26.b). For 2Q excitation and reconversion the SPC5 sequence [44] was used selectively in the aliphatic spectral region. A dephasing time of 6 rotor periods was employed. Spectra were recorded on a 600 MHz spectrometer at 11 kHz MAS and -5°C . (Bottom) Prediction of the expected pattern using solution-state chemical shifts [75]. For the resolved (red) resonances the number of the residue in the primary sequence is indicated.

A similar experiment is demonstrated on the uniformly ^{13}C , ^{15}N labeled Crh sample in Figure 2.29. Additional resonances due to solvent are also observed here around 66 ppm in the indirect dimension. The spectral region shown here contains correlations from threonine C_α - C_β (C_β being a methyl group) visible at about 90 ppm in the indirect dimension.

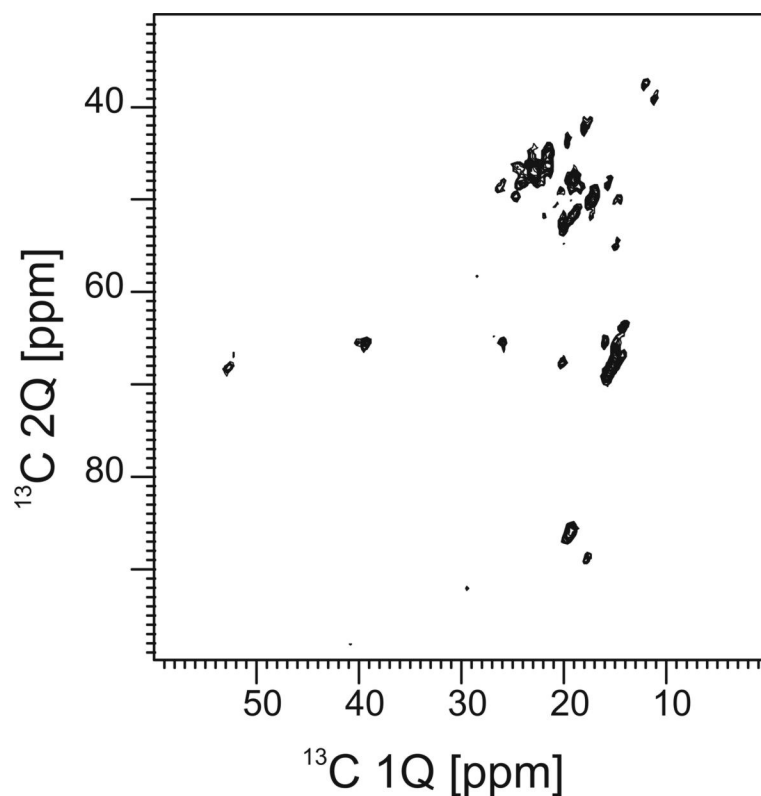


Figure 2.29. The same experiment as in Figure 2.28 performed on a sample of uniformly ^{13}C , ^{15}N labeled Crh.

These experiments have been shown to simplify the spectral regions involving methyl carbons in ^{13}C - ^{13}C two-dimensional experiments, especially in relation to 2Q correlation experiments. Nevertheless, the dipolar dephasing block can be incorporated in other experiments where similar spectral simplification is required. Alternatively, the selection of protonated carbons is possible by employing short cross-polarization times. The importance of this will be exemplified in Section 3.1 in relation to CHHC type of experiments [84].

3. Structure determination with solid-state NMR

A recent goal of solid-state NMR is to establish a methodology to investigate the 3D structure of solid-phase peptides and proteins under MAS. Within this frame, the best approach is to study uniformly [^{13}C , ^{15}N]-labeled proteins under HR-SSNMR conditions [3]. A first step towards this goal is to assign all ^{13}C and ^{15}N resonances of the protein. In the case of highly ordered samples (e.g. microcrystalline), it was already demonstrated that complete assignments are feasible [24, 26]. In other cases, the ^{13}C and ^{15}N lines are usually inhomogeneously broadened by the structural molecular disorder and only partial assignments may be possible [85-87]. Here, additional spectral editing methods (such as those discussed in Section 2) may increase the spectral resolution and the number of assigned resonances.

The second step towards structure determination involves the collection of a sufficient number of structural constraints which can be used to calculate molecular conformations consistent with these restraints. In this context, isotropic chemical shifts and internuclear distances are the parameters of interest. For example, the chemical shifts are available once the assignment has been performed. Similar to solution-state, the chemical shifts of particular spins relate directly to the local conformation of the protein in the solid-phase. Internuclear distances are encoded as dipolar couplings (see Equation (11)) which can be measured by a variety of methods in the solid-state.

(^{13}C , ^{13}C) or (^{15}N , ^{13}C) distances of interest for structure determination purposes exceed 2.5\AA such that the magnitude of the recoupled interaction is usually smaller than 500 Hz. In selectively labeled samples, where only one pair of isotopes (e.g. ^{13}C and/or ^{15}N) is present, dipolar evolution or build-up curves are usually detected experimentally [1, 14, 15]. These

curves reflect not only on the strength of the dipolar coupling of interest, but also other factors like r.f. pulse imperfections, residual couplings to protons and various relaxation mechanisms. In multiply labeled samples, additional stronger dipolar couplings (to directly bonded nuclei, for example) are experienced by the spins. These couplings generally determine the spin dynamics and obscure the effects of the small couplings of interest [6]. To detect small couplings, advanced isotope labeling schemes [88, 89] which remove the strong dipolar couplings have been demonstrated [90, 91]. Alternatively, frequency selective recoupling methods [92-97] result in structural constraints in uniformly [^{13}C , ^{15}N]-labeled biomolecules. In contrast to contacts between rare spins the strongest ^1H - ^1H distances encode information about the three-dimensional fold of a protein and are important for structure determination in solution-state NMR. Proton-proton contacts may also be determined in solid-state NMR in high resolution [84, 98].

In this Section, methods which provide structural constraints in uniformly [^{13}C , ^{15}N]-labeled proteins are presented. As already mentioned, they are generally applicable to proteins where (nearly) complete ^{13}C and ^{15}N assignments are available.

3.1. Peptide secondary structure determination

Due to the simplified isotropic Hamiltonian, a large repository of NMR chemical shifts has been created for soluble biomolecules (BioMagResBank, [40]). The ultimate goal was to determine the structure of globular proteins [99], comparable to X-ray in precision and resolution. This was largely accelerated by the following advents: (1) the introduction of 2D experiments [4, 100], (2) the introduction of sequence-specific assignments [101], (3) the use of heteronuclei (^{13}C and ^{15}N) in combination with isotope enrichment and (4) the availability of higher magnetic fields and the improvement of NMR probe-head design.

Some NMR parameters, such as dipolar and scalar couplings, result from well-defined pairwise interactions and can be readily interpreted. Chemical shifts, on the other hand, reflect the cumulated effect of various contributions for which adequate theoretical treatment is not readily available. Chemical shifts are extremely sensitive to steric and electronic effects in general and to 3D structure in particular. As shown in Figure 3.1, this translates into structural parameters like bond lengths and angles, torsion angles.

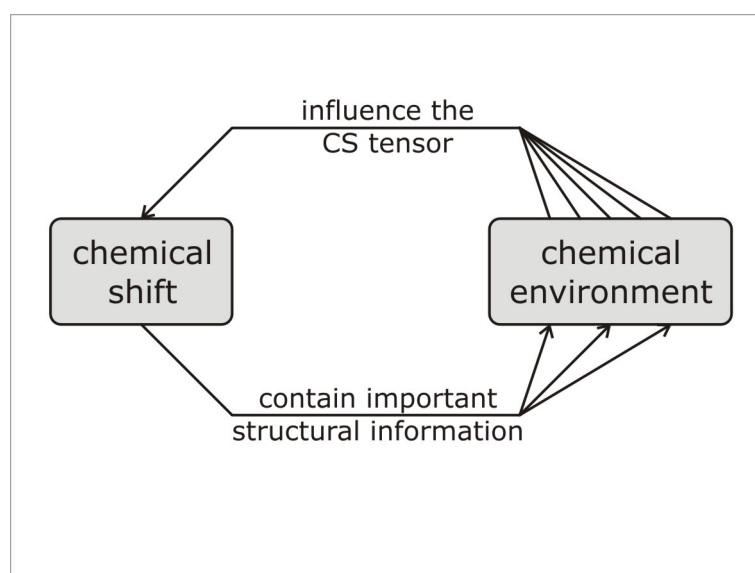


Figure 3.1. The chemical shift comprises many contributions, which may be difficult to differentiate.

The empirical relationship between the chemical shift detected in NMR and local structural motifs in peptides and proteins has been utilized in solution [53, 54] and solid-phase systems [57, 102] for a long time. In the absence of other spectroscopic methods, early studies on the

backbone conformation of immobilized polypeptides required the accumulation of chemical shift data in systems with known secondary structures [57]. The observed chemical shifts were classified for various structural motifs [57, 58] providing an analytical basis for studies in fibrous proteins [103-105] and membrane proteins [106, 107]. Similar to many applications that measure distances and dihedral angles in high precision [14, 108-111], the studies involved site or residue specific labeling schemes.

In solution-state NMR, the corresponding secondary chemical shifts, i.e. the difference between the experimentally observed isotropic chemical shift and the random coil value [56, 60] were combined with multiple-spin labeling and a suite of multi-dimensional correlation techniques [4, 101, 112]. As a result, these statistics have become of great value at an early stage of the structure determination process [113] or they provide important information for the study of folding mechanisms [114] in globular proteins.

Recent advancements in solid-state NMR methodology and hardware instrumentation have permitted to fully [115] or at least partially assign resonances in multiple-labeled peptides [116-118], proteins [85, 86, 119] and membrane proteins [120] under MAS [8] conditions. In principle, these results can be utilized to characterize the protein backbone conformation in the solid-state. For several reasons however, care must be exercised in directly comparing MAS-based correlation spectra of multi-labeled peptides and proteins to results obtained in isotropic solutions. Anisotropic chemical shielding and dipolar interactions may be comparable in size or even exceed MAS or radio frequency (r.f.) modulation rates. As a result, coherent recoupling effects (see e.g. [121, 122]; [123] that may affect peak position and line width need to be minimized. Moreover, even if MAS frequencies can be employed that exceed all anisotropic interactions, conformational heterogeneity, bond-distortions by sample packing and variations in local susceptibility or motion may influence solid-state NMR spectra [58, 124].

With these aspects in mind it seems appropriate to investigate the concept of secondary chemical shifts in multiple-labeled peptides and proteins under MAS conditions in more detail. Obviously, such a study can currently only include a very limited number of systems. A selection of three polypeptides of variable length and chemical environment used here gives a general indication on whether MAS-based structural studies may profit from correlations

regularly observed in solution-state NMR. For this purpose, we considered in the present analysis the tri-peptide AlaGlyGly, a 62 residue SH3 domain from α -spectrin [125, 126] and the LH2 light-harvesting complex from the photosynthetic bacterium *Rhodospseudomonas acidophila* [127]. In each case, fully labeled variants were studied which allows for an analysis of a significant number of peptide residues and dihedral angles. For all three systems, we compare our experimental findings to structural data from X-ray crystallography. Unlike the liquid-state, we relied solely on secondary chemical shifts obtained on ^{13}C signals since carbon spectroscopy is in general more sensitive than direct ^{15}N detection and it can usually be obtained at higher resolution than proton chemical shift information.

3.1.1. Chemical shift analysis of C_A and C_B spins

In the following analysis, we compare the experimentally observed (obs) carbon chemical shifts under MAS to standard, isotropic random coil (rc) values. For this purpose, we define:

$$\Delta\delta = \delta_{C_\alpha} - \delta_{C_\beta} = \{\delta_{C_\alpha}(\text{obs}) - \delta_{C_\alpha}(\text{rc})\} - \{\delta_{C_\beta}(\text{obs}) - \delta_{C_\beta}(\text{rc})\} \quad (74)$$

With the exception of Gly residues (for which we assume $\delta_{C_\beta}(\text{obs}, \text{rc}) = 0$), $\Delta\delta$ represents the difference between C_α and C_β secondary shifts usually employed in solution-state NMR. Here, a (dimensionless) chemical shift index (CSI) that is closely related to $\Delta\delta$ given in Equation (74) was suggested [60]. In the solid-state, the experimental line width of ^{13}C resonances under MAS is usually significantly larger than in liquids and we prefer the definition in Equation (74) that allows for a direct comparison of $\Delta\delta$ (given in ppm) to the experimentally detected line width.

In solution, experimentally observed random coil values are in very close agreement to the statistical averages of α -helical and β -strand chemical shifts [60]. Hence we utilized for all amino acid residues under study statistical average chemical shift values as random coil references. Previous solution studies have revealed that C_α and C_β secondary shifts are affected by conformation dependent chemical shift changes in opposite ways [56]. Any correlation between carbon chemical shifts and protein secondary structure should therefore be strongly reflected by the parameter $\Delta\delta$ that measures the difference between both quantities. Since the number of solid-phase systems that can be studied by Equation (74) is

currently small we do not attempt to compare other statistical approaches e.g. containing an analysis of C_α and C_β resonances individually, the inclusion of additional ^{15}N or ^1H chemical shifts or any other spectroscopic parameters. A future analysis of a larger number of peptides and proteins might result in other statistical approaches that describe the empirical relation between chemical shift and protein structure more effectively in the solid-state.

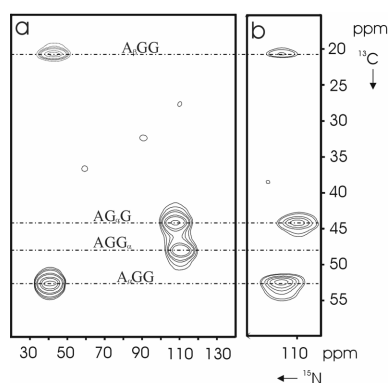


Figure 3.2. Heteronuclear ^{15}N - ^{13}C correlation experiments on a uniformly [^{13}C , ^{15}N]-labeled variant of the tripeptide AlaGlyGly. In a) results of a NCACB-type experiment are shown in which a band-selective cross polarization step [23, 115] is used to transfer polarization from amide nitrogens to C_α carbons. Subsequently, a band-selective double-quantum transfer [69, 115] is used to excite C_β (Ala) resonances in negative intensity (dotted contour levels in Fig.1a). Results of an NCOCACB -type of experiment are shown in b). Inter-residue NH-CO transfer was established by readjusting the band-selective ^{15}N to ^{13}C transfer [23, 115]. Subsequently, proton driven spin diffusion [25, 115] was employed for a mixing time of 15 ms giving rise to positive (NH,CO), (NH, C_α) and (NH, C_β) correlations. Only the side chain regions of the resulting 2D spectra are shown. Horizontal lines identify the carbon backbone and side chain resonances (indicated by the subscript) of all NH- $C_{\alpha,\beta}$ sets in AGG. Both experiments were conducted at 400 MHz using a triple resonance 4 mm MAS probe at 277 K and a MAS frequency of 11 kHz.

We begin with the tri-peptide Ala-Gly-Gly that has previously been studied by X-ray crystallography [128] and solid-state NMR [129]. For our purposes, we prepared a uniformly labeled variant of AGG and we employed heteronuclear NCACB and NCOCACB - type of experiments leading to the results of Figure 3.2. The spectra were obtained using band-selective (^{15}N , ^{13}C) transfers [23] followed by homonuclear (^{13}C , ^{13}C) transfer units. In the NCACB case (Figure 3.2.a), band-selective double-quantum transfer was employed [115] that is characterized by ‘up-down’ single quantum intensities [130]. In Figure 3.2.b, proton driven spin diffusion was used to observe inter-residue NHCO, NHC_α and NHC_β correlations. Following Equation (74) the resulting resonance assignments are calculated in Figure 3.3 with respect to random coil predictions (upper row). For reference, Figure 3.3 (lower row) contains the backbone dihedral angle ψ as obtained from X-ray crystallography [128] and indicates a

qualitative agreement for the AG segment for which a backbone dihedral angle ψ can be defined. Similar to the liquid-state, we observe negative values of $\Delta\delta$ for large positive values of ψ . These independent measurements are in close agreement to the values obtained in X-ray crystallography and to the qualitative observation in Figure 3.3.

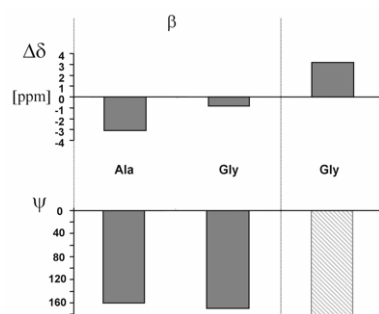


Figure 3.3. Upper row: Experimentally observed secondary chemical shift parameter $\Delta\delta$ compared to (lower row) the backbone dihedral angle ψ as obtained from X-ray crystallography in AlaGlyGly [128]. Random coil values were obtained from statistical averages obtained in solution-state NMR ([131]). The N-terminal Ala and the subsequent Gly residue are characterized by dihedral angles typically observed in β -strands. For the C-terminal Gly residue (where a backbone angle ψ can not be defined), the angle given in the original X-ray study is shaded.

Figure 3.4 contains experimental results for a 62-residue protein (SH3 domain from α spectrin, 7.2kD) of which spectral assignments were recently published [115]. Again, the carbon secondary chemical shift parameters $\Delta\delta$ are plotted against the backbone angle ψ derived from the X-ray structure (PDB entry 1SHG, [125]). To facilitate the analysis, we have drawn vertical lines that indicate beta sheet or alpha helical regions of the protein. A remarkable correlation between both parameters is observed throughout the polypeptide chain, in particular for the beta strands $\beta_1, \beta_3, \beta_4, \beta_5$ and the helical region α_1 (A55-Y57). Qualitative agreement is also detected for many of the connecting loop regions, such as L12-D29. Larger deviations are observed for the residues (I30-N35) that encompass the second beta strand of the molecule. Here, most residues exhibit negative $\Delta\delta$ parameters in qualitative agreement with the crystallographic data but their absolute values are significantly smaller than those of other beta strands in the protein. In the case of SH3, the ^{13}C chemical shifts obtained in the solid-state agree well with data obtained in solution. It is thus unlikely that these differences are caused by macroscopic sample conditions. On the other hand, mobility effects or conformational heterogeneity could lead to a reduction of the observed $\Delta\delta$ values [114].

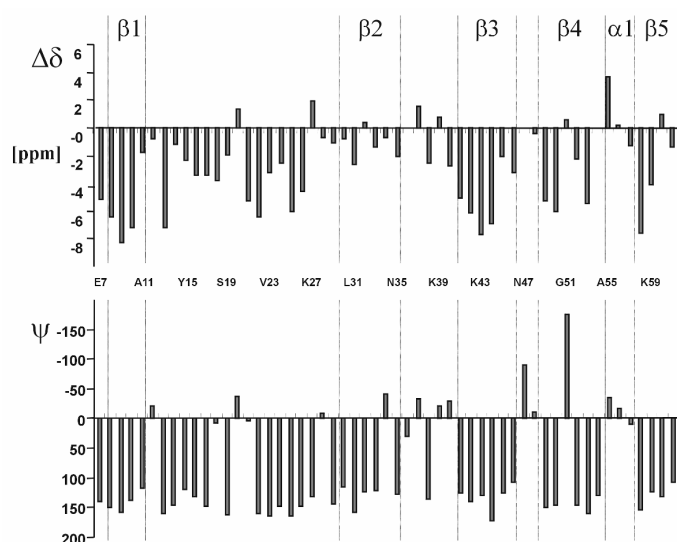


Figure 3.4. Upper row: Chemical shift parameter (74) calculated from the SSNMR assignments obtained for the SH3 domain from α -spectrin [115] and random coil standards in solution-state NMR. Lower row: Backbone angles as obtained from X-ray crystallography (PDB entry 1SHG). To facilitate the analysis, we have drawn vertical lines that indicate beta sheet or alpha helical regions of the protein. Residues of the peptide sequence are given in single letter notation.

Finally, we plot in Figure 3.5 an analogous comparison using experimental results recently obtained on a uniformly [^{13}C , ^{15}N]-labeled version of the LH2 light-harvesting complex from the photosynthetic bacterium *Rhodospseudomonas acidophila*. The crystal structure (PDB entry 1KZU) contains three asymmetric units each including three protomer complexes. These complexes consist of α (53 amino acid residues) and β (41 amino acid residues) apo-proteins that are arranged in high symmetry in the 150 kD membrane protein complex [127]. For LH2, a complete spectral assignment using MAS-based Solid-state NMR methods is not yet available and we concentrate on the residues assigned in [120]. In contrast to the polypeptides discussed so far, the X-ray structure of LH2 shows a mostly alpha helical arrangement that is well reproduced in the chemical shift statistics (i.e. $\Delta\delta > 0$) for protein subunit α (containing helix α in Figure 3.5). For the assigned Gly residues we find deviations for δ_{c_α} indicating that only the parameter defined in Equation (74) gives a qualitative measure for the secondary structure in the solid-state. In apo-protein β only a small number of residues have so far been identified in the helical segment. Except for G18 (apo-protein β) the observed values of $\Delta\delta$ are in qualitative agreement with the X-ray results. Moreover, the helix-turn interface S35-T37 shows a significant change from positive to negative $\Delta\delta$ values in line with the crystallographic data and general observations in liquid-state NMR experiments on globular proteins.

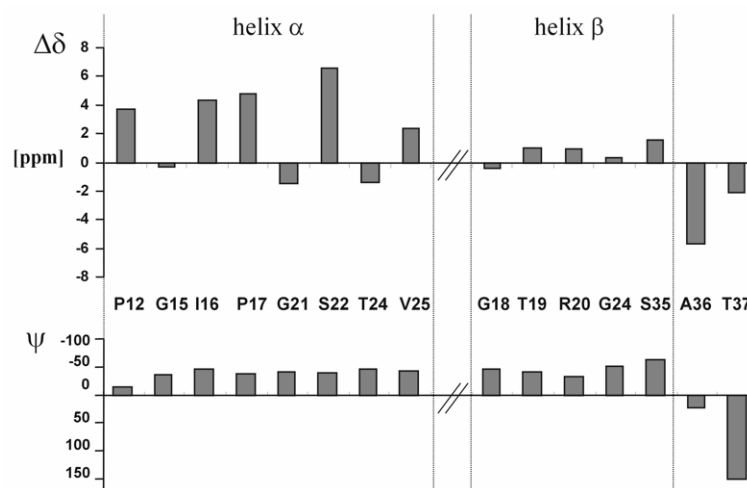


Figure 3.5. Comparison of experimentally observed secondary chemical shift parameter (upper row) [120] to backbone dihedral angles as obtained from [127]. The crystal structure (PDB entry 1KZU) contains three asymmetric units each including three protomer complexes. These complexes consist of α (53 amino acid residues) and β (41 amino acid residues) apo-proteins that are arranged in high symmetry. Here, helix α relates to residues found in subunit α whereas helix β contains residues found in the helical region of apo-protein β .

In all cases, we find a remarkable correlation between the parameter $\Delta\delta$ that reflects the difference in C_α and C_β secondary chemical shifts under MAS and the backbone dihedral angle ψ obtained using X-ray crystallography. In close analogy to liquid-state NMR, we observe negative values of $\Delta\delta$ in β -strand conformations and positive values for α -helical segments of an immobilized polypeptide. In the case of the SH3 domain from α spectrin, qualitative agreement is also found for many of the connecting loop regions of the protein. Deviations are predominantly observed for Glycine residues for which ab initio quantum mechanical studies predict a reduced sensitivity of (isotropic and anisotropic) chemical shift values to secondary structure [132]. A more detailed investigation could be attempted when additional NMR data in immobilized polypeptides under MAS are available.

Our analysis confirms that low-resolution structural models of immobilized polypeptides might be obtained from a simple analysis of a small number of characteristic chemical shift values that identify elements of secondary structure and a subsequent measurement of selected through-space interactions. Unlike to previous approaches that relied on the study of selectively labeled peptides and proteins, our results indicate that fully labeled compounds can be utilized enhancing the general applicability and reliability of the method. Results in the tripeptide AlaGlyGly suggest that this concept can also be helpful in the study of small peptide fragments bound to larger (possibly membrane-spanning) complexes. In the current context,

we have only relied on isotropic chemical shift information that can in principle be obtained from standard two- or higher dimensional correlation spectroscopy. Moreover, coherent methods that e.g. monitor the evolution of multiple-quantum coherence in the backbone or side chain sections of the protein can be employed. As shown by several research groups in doubly labeled compounds [133, 134] the accuracy of these methods can be very high.

Today, secondary chemical shifts are of great value in the structure determination process and for the rapid calculation of global protein folds [135-137] in liquid-state NMR. Our results suggest that a similar analysis can provide a qualitative basis for the complete and rapid (low-resolution) structural characterization of multiple-labeled membrane proteins or protein aggregates under MAS conditions. Since chemical shift assignments are sufficient, this method could be of particular interest for cases in which signal to noise considerations limit the application of more sophisticated NMR methods at present.

3.2. Probing ^1H - ^1H distances in uniformly labeled biomolecules

Structure determination of biomolecules in solution-state NMR heavily relies on the detection of the many short proton-proton distances that characterize the three-dimensional fold of the molecule. In contrast, the shortest carbon-carbon or carbon-nitrogen distances are of limited use in protein structure determination as these atoms are directly bonded and the distances represent one-bond lengths (Figure 3.6). In solid-state NMR, ^{13}C and ^{15}N are usually detected due to the increased resolution. ^1H spectroscopy, which would result in structure determination of solid-phase polypeptides using methods well established in solution-state NMR, is not possible due to the size of the dipolar ^1H - ^1H couplings and the reduced spectral dispersion among ^1H resonances.

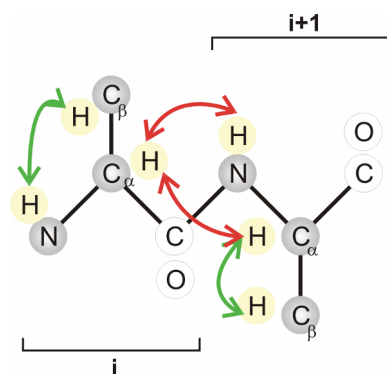


Figure 3.6. The shortest carbon-carbon or carbon-nitrogen distances in a polypeptide relate only to one-bond contacts. On the other hand, the shortest proton-proton contacts in polypeptides contain structural information about the three-dimensional fold of the protein. They constrain both the side-chain of a residue (intra-residue contacts, green lines) and the backbone or the relative positioning of different sidechains (inter-residue contacts, red lines).

An alternative approach to detect ^1H - ^1H contacts is to encode in high-resolution the proton magnetization on rare spins like ^{13}C and ^{15}N . The proposed experiment that achieves this is shown in Figure 3.7. It has been previously demonstrated in the context of ^1H spin counting [138, 139], two-dimensional rare-spin correlation spectroscopy [84, 98, 140, 141] and rare-spin signal enhancement [142]. A CP [17, 18] step followed by a z-filter is used to prepare ^{13}C transversal magnetization and to dephase ^1H transversal magnetization. Subsequent to the t_1 indirect detection period, a short CP ensures that magnetization is transferred from ^{13}C spins to the nearest ^1H spins (usually the proton nuclei directly bonded). A homonuclear block (H

mix) allows for ^1H - ^1H contacts to be established while a final short CP transfers magnetization back to ^{13}C for detection in t_2 . A variant of this CHHC experiment can be obtained by performing the first two CP steps and the t_1 evolution on ^{15}N channel (the NHHC experiment).

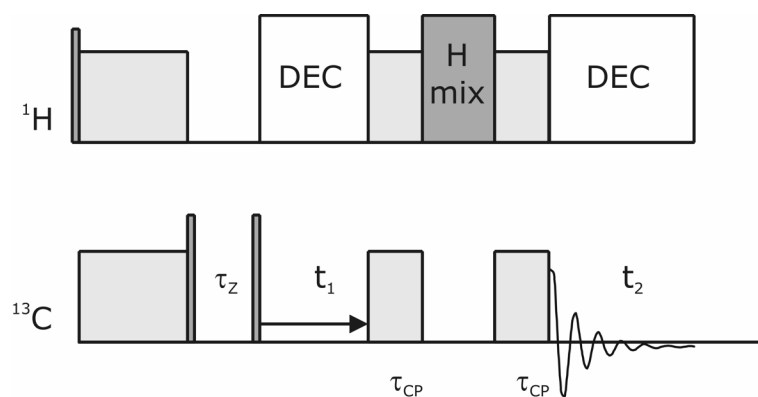


Figure 3.7. The pulse sequence for the CHHC experiment. After the first CP step (gray rectangles), a z-filter is applied on the ^{13}C during which the ^1H magnetization dephases. The indirect dimension t_1 encodes the ^{13}C resonances. A short CP transfers magnetization to and then to neighboring protons during a homonuclear mixing block (H mix). Magnetization is transferred back to carbons by a last short CP and is detected in t_2 .

The (^1H , ^1H) mixing sequences have to be selected based on optimal relaxation behavior under r.f. irradiation. For this purpose, ^1H signals on unlabeled Ala-Gly-Gly were recorded under the conditions of r.f. pulse spin-locking and nutation with phase inversion as a function of the ratio of r.f. field and MAS rate $\kappa = \omega_1 / \omega_R$. In Figure 3.8 signal intensities are plotted after an evolution time (r.f. spin-lock or nutation) of 200 μs . For both experimental cases, we observe distinct resonance minima at the higher MAS rate (25 kHz) if $\kappa \in [0.5, 1, 2]$, in line with results obtained in rare-spin applications [23, 69, 121, 143, 144]. For the lower spinning speed (11 kHz) the overall signal pattern is further complicated. For both MAS rates, spin locking is most efficient for the strongest applied r.f. fields (Figure 3.8.a). Signal loss under r.f. nutation (Figure 3.8.c) is minimal for very small or large r.f. fields, and one finds broadened resonance minima around the $\kappa = 0.5, 1, 2$ conditions that narrow with increasing MAS rates. So as to insure that the experimentally observed signal loss is indeed induced by strong dipolar (^1H , ^1H) couplings, full quantum mechanical simulations within the numerical simulation routine GAMMA [16, 145] were carried out. Since dipolar (^1H , ^1H) interactions can be of comparable size to the applied MAS rate, a step-wise integration procedure [6] of the relevant two-spin Hamiltonian was performed. In Figure 3.8, the spin-lock (b) and nutation (d)

behavior predicted for the two MAS rates considered experimentally is shown. Again, the signal intensity was determined after 200 μs of spin system evolution as a function of $\kappa = \omega_1 / \omega_R$. In full agreement with our experimental results, favorable spin-lock and nutation behavior is detected for large ratios $\kappa = \omega_1 / \omega_R$. Small values of κ are also possible for nutation experiments. Hence, the theoretical treatment of a homonuclear dipolar coupled two-spin system agrees qualitatively with the empirical findings. A further improvement between simulation and experiment may be obtained by taking into account r.f. inhomogeneity and offset effects or by including additional spins in the quantum mechanical calculations. R.f. schemes compatible with the theoretical and experimental results are longitudinal mixing, RFDR [146] and POST-C7 [43]. Longitudinal mixing and polarization transfer schemes characterized by relatively high values of κ fulfill the experimental restrictions obtained. The RFDR scheme involves strong rotor-synchronized π -pulses and can be used to promote ($^1\text{H}, ^1\text{H}$) dipolar transfer. Both longitudinal mixing and RFDR mixing are characterized by zero-quantum polarization transfer. Rotating frame double-quantum schemes that are characterized by large values of κ , like POST-C7, can also be utilized.

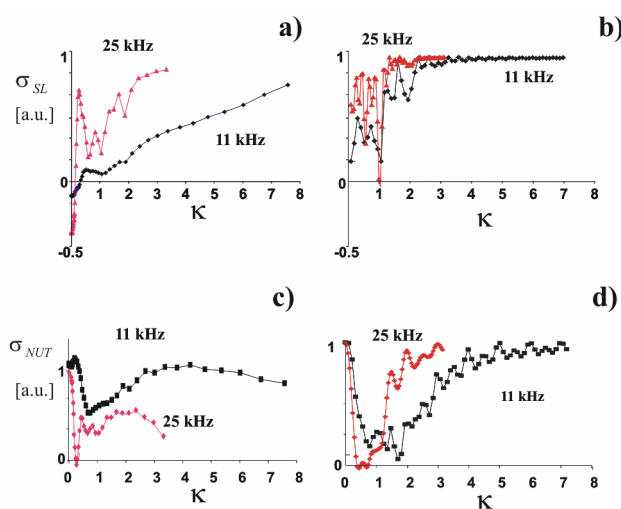


Figure 3.8. Spin-lock (a, b) and nutation (c, d) behavior of ^1H resonances in the tri-peptide AGG for the two indicated MAS rates. Experimental results (a, c) were obtained on a 600 MHz wide-bore (Bruker/Germany) NMR instrument. Numerical simulations of the spin-lock (b) and nutation (d) behavior result from considering a dipolar coupled two-spin system for the two indicated MAS rates. All simulations were obtained using the C++ based NMR simulation environment GAMMA. The total signal intensity after an evolution of 200 μs is shown as a function of $\kappa = \omega_1 / \omega_R$.

Buildup rates obtained for the two zero-quantum mixing sequences can be analyzed within the concept of spectral spin diffusion [147-149]. Here, the (ω_k, ω_j) cross peak signal intensity is described by an exponential buildup:

$$I_{z,k \rightarrow j}(t) = 1 - \exp(-t / T_{SD}^{jk}) \quad (75)$$

In the static case, the spin-diffusion time constant T_{SD}^{jk} is given by the ^1H internuclear distance r_{jk} of interest and the zero-quantum (0Q) line-shape function evaluated at the isotropic chemical difference Δ_{jk} between spin j and k:

$$\frac{1}{T_{SD}^{jk}} = (\mu_0 / 4\pi)^2 \frac{\hbar^2 \gamma^4}{r_{jk}^6} J^{0Q}(\Delta_{jk}) \quad (76)$$

To lowest approximation, Equation (76) remains valid under MAS and/or the presence of a r.f. scheme assuming a modified 0Q-line-shape function $J^{0Q.RF}(\Delta_{jk}, \omega_R)$ [149]. For a further analysis, cross-peak intensities were monitored during a CHHC experiment utilizing the longitudinal mixing scheme on uniformly [^{13}C , ^{15}N]-labeled His-HCl at 11 kHz on a 400 MHz instrument. CP times before and after proton mixing were optimized for polarization transfer within CH_x ($x=1$ to 3) groups only.

Experimental data points are shown (Figure 3.9) for the pairs $\text{C}_\alpha\text{-C}_\beta$ (filled squares) and $\text{C}_\beta\text{-C}_\delta$ (filled diamonds). From neutron diffraction data [150] (1H, 1H) distances in His-HCl are predicted to be 2.22 Å for the ($\text{C}_\alpha\text{-C}_\beta$) pair and 3.08 Å for the nearest neighbor ($\text{C}_\beta\text{-C}_\delta$) pair. A simple inspection of Figure 3.9 reveals that the shorter (^1H , ^1H) distance is characterized by a significantly faster buildup and, correspondingly, a stronger transfer efficiency in the initial rate regime (τ_{HH} between 0 and 200 μs). For the ($\text{C}_\alpha\text{-C}_\beta$) pair, the maximum transfer efficiency is reached after about 200 μs . Cross peak intensities relating to the $\text{C}_\beta\text{-C}_\delta$ spin pair increase for mixing times up to 600 μs . Theoretical results shown in Figure 3.9 were obtained using Equation (75). Since the (^1H , ^1H) distances are known, we can determine the value of the zero-quantum (0Q) line-shape function and find $J^{0Q.LM}(\Delta) = 208 \mu\text{s}$. In agreement with the theoretical model, the signal buildup is exponential and the zero-quantum spin diffusion rate under LM mixing scales inversely with the 6th power of the internuclear (^1H , ^1H) distance.

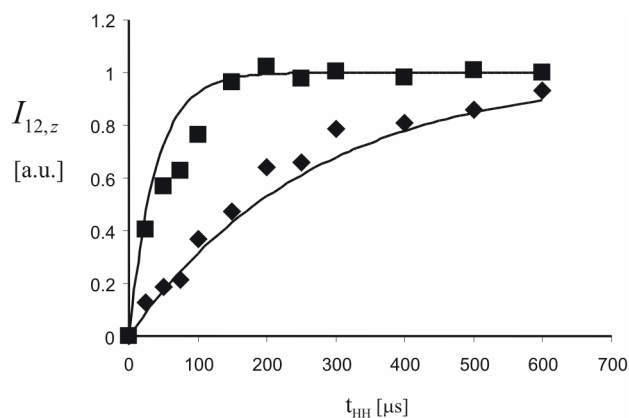


Figure 3.9. Experimentally observed polarization transfer rates under longitudinal mixing on uniformly [^{13}C , ^{15}N]-labeled His-HCl. The observed cross peak intensities for the C_{α} - C_{β} (filled squares) and C_{β} - C_{δ} (filled diamonds) are normalized against the total intensity of the 2D spectrum. Indicated lines correspond to numerical simulations using the 0Q line-shape function given in the text and the following simulation parameters: $r_{12} = 2.22 \text{ \AA}$ (C_{α} - C_{β} spin pair) and $r_{12} = 3.06 \text{ \AA}$ (C_{β} - C_{δ} spin pair).

Experimental results on the uniformly [^{13}C , ^{15}N]-labeled tripeptide AlaGlyGly are shown for a CHHC experiment (Figure 3.10.a) and for a NHHC experiment (Figure 3.10.b). Only the protonated rare-spins are considered and spectra can be restricted to the ^{13}C aliphatic region. Inter-residue contacts are observed in contrast to conventional rare-spin correlation spectra. From the analysis of the buildup CHHC and NHHC curves (not shown here), it can be inferred that one two-dimensional experiment is sufficient to identify nearest neighbor correlation. For example, two $\text{NH}(i+1)\text{-C}_{\alpha}(i)$ ($i=1$ and 2) contacts are observed in Figure 3.10.b and are in strong agreement of the AlaGlyGly β -strand arrangement found in the crystal structure.

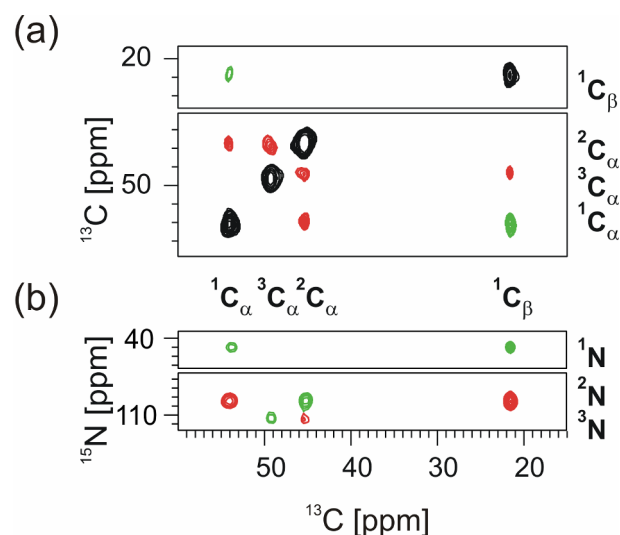


Figure 3.10. The CHHC (a) and NHHC (b) experiments performed on uniformly [^{13}C , ^{15}N]-labeled Ala-Gly-Gly sample. The assignment of the resonances is shown on the sides of the spectra and digits corresponding to residue number. Intra-residue correlations are shown in green and inter-residue correlations in red. Longitudinal mixing was used in both cases for ^1H - ^1H transfer and τ_{HH} was set to (a) 150 μs and (b) 208 μs . Experiments were performed on a 400 MHz magnet at 11 kHz MAS.

CHHC type of experiments using longitudinal mixing were also performed on a uniformly ^{13}C , ^{15}N labeled ubiquitin and are shown in Figure 3.11 and Figure 3.12. Different ^1H mixing times were employed (150 μs and 300 μs) and for the longer times, an increase in the intensity of cross peaks or more cross peaks is observed in the spectrum.

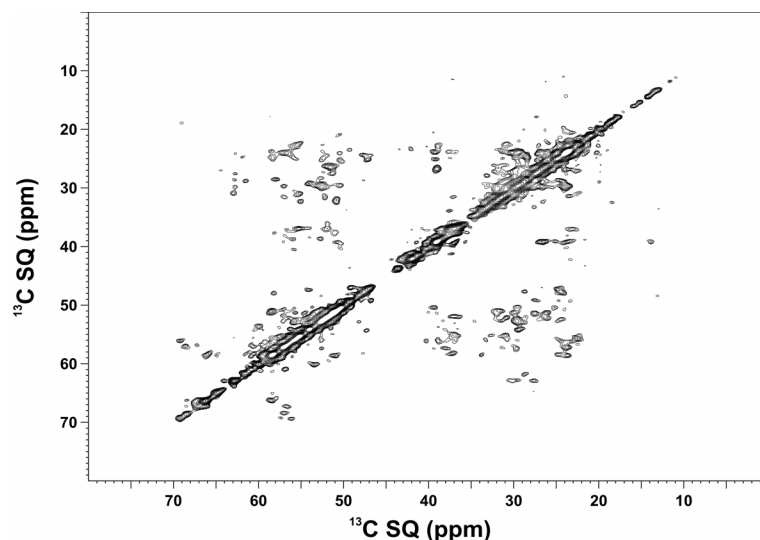


Figure 3.11. A CHHC experiment on uniformly [^{13}C , ^{15}N]-labeled ubiquitin using 150 μs ^1H longitudinal mixing (τ_{HH}) and 75 μs CP times (τ_{CP}) for encoding ^1H - ^1H contacts. Spectra were recorded on a 600 MHz spectrometer at 11 kHz MAS and -5°C .

The two CP pulses encoding the ^1H magnetization on the ^{13}C spins (τ_{CP}) were optimized to achieve maximum polarization transfer within CH and CH_2 groups. Interestingly, the polarization transfer within CH_3 groups is drastically reduced and correlations involving methyl ^{13}C are not present in the spectra.

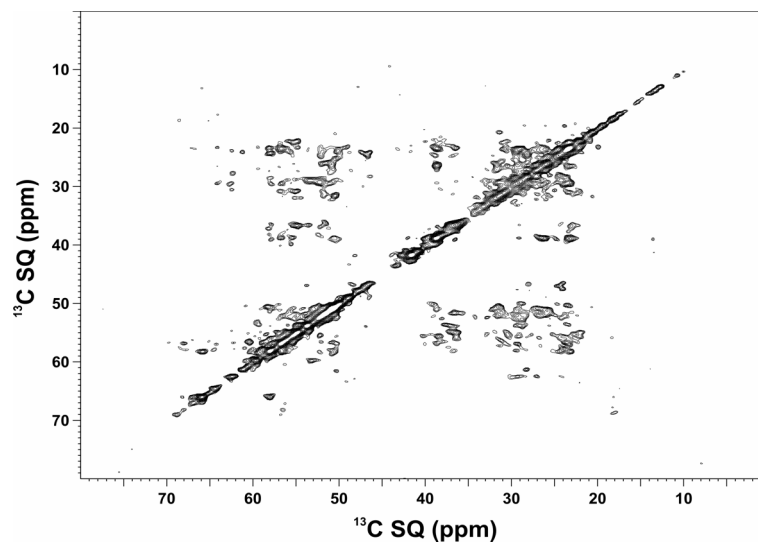


Figure 3.12. Same as in Figure 3.11 except for a $300\ \mu\text{s}$ ^1H longitudinal mixing time being used.

The correlations involving methyl ^{13}C provide important constraints for the structure determination algorithms. In order to observe these correlations increased τ_{CP} times (from 100 to $500\ \mu\text{s}$) were probed. In Figure 3.13 the CHHC correlation corresponding to $\tau_{\text{CP}} = 350\ \mu\text{s}$ is shown and cross-peaks in the spectral region from 5 to 25 ppm are clearly visible in both dimensions. Optionally, a dipolar dephasing block may be utilized just before acquisition to select only the $^{13}\text{CH}_3$ resonances in the direct dimension t_2 and the corresponding simplified spectrum is shown in Figure 3.14.

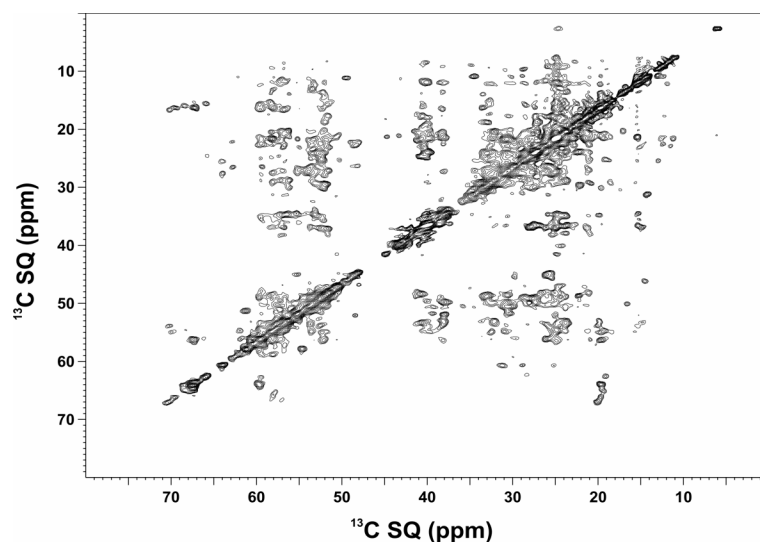


Figure 3.13. Same as in Figure 3.11 except for a $\tau_{CP} = 350 \mu s$ CP time being used to encode 1H - 1H contacts also on $^{13}CH_3$ groups.

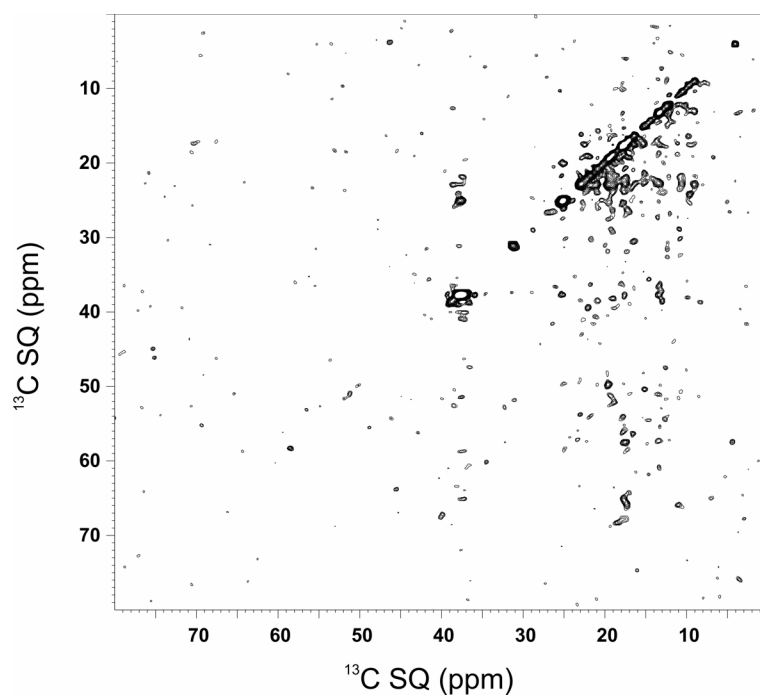


Figure 3.14. Same as in Figure 3.13 except for a dipolar dephasing block (6 rotor periods long) is used before acquisition to select $^{13}CH_3$ only resonances in ω_2 .

A prediction of the expected contacts involving methyl ^{13}C based on solution-state [75] isotropic chemical shifts and proton-proton distances (shorter than 3 \AA) is shown in Figure 3.15. Both spectra in Figure 3.13 and Figure 3.14 compare favorably with the prediction made in Figure 3.15.

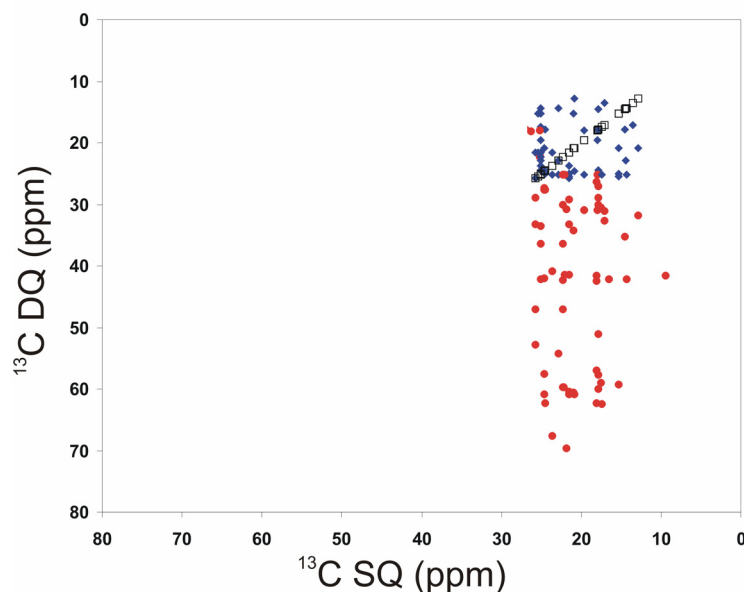


Figure 3.15 ^1H - ^1H contacts up to 3 Å, encoded on $^{13}\text{CH}_3$ in ω_2 are predicted using solution-state isotropic chemical shifts and structure of ubiquitin [75]. Contacts in blue involve two methyls, those in red only one. Diagonal resonances are shown in black symbols.

Similar to the NOESY [151] type of experiments that are used in solution-state NMR, we have introduced the C/NHHC experiment which allows for detection of ^1H - ^1H distances in HR-SSNMR. In contrast to rare spins correlations (e.g. ^{13}C - ^{13}C or ^{13}C - ^{15}N) which relate to trivial one-bond distances in uniformly [^{13}C , ^{15}N]-labeled molecules, the shortest ^1H - ^1H distances reflect backbone or side chain conformation in polypeptides. For proton zero-quantum polarization transfer under longitudinal mixing, the spin dynamics may be well described within a semi classical relaxation theory and lead to an exponential transfer. In the case of 0Q-CHHC, transfer rates depend on the inverse 6th power of the ^1H - ^1H distance and the initial cross peak buildup regime is thus sensitive to the internuclear distance.

3.3. Frequency-selective dipolar recoupling

Many of the biological applications of HR-SSNMR reported previously have been concerned with the determination of dipolar couplings between pairs of dilute isotopes (like ^{13}C , ^{15}N or ^{19}F) selectively incorporated into the molecule of interest [2, 152]. Dipolar couplings translate directly into distances or torsion angles of interest. Multiple structural parameters are thus obtained by performing the same experiment on several samples, each with different isotope labeling patterns. Under MAS [8], rotor-driven (e.g. rotational resonance, RR [92, 153, 154]) or r.f.-driven (e.g. RFDR [155], REDOR [156]) techniques that reintroduce homonuclear or heteronuclear dipolar couplings have been used [14, 15]. Biologically relevant carbon-carbon or carbon-nitrogen distances exceed 2.5\AA and the (recovered) dipolar couplings are thus less than 500 Hz. Consequently, recoupling r.f. pulse sequences have to be applied for long periods (e.g. several milliseconds) in order to observe the effects of these weak interactions on the spin dynamics. In this case, effects due to r.f. inhomogeneity and heating, residual couplings to protons, chemical shift anisotropies and various relaxation mechanisms become important. Constant-time versions of these techniques [129, 157] have been proposed to address some of these problems.

Probing selected dipolar couplings in multiply isotope labeled biomolecules represents an interesting alternative approach [3]. In this case, several experiments performed on the same sample may result in multiple structural constraints. The effects of the weak dipolar couplings of interest cannot be observed directly in the presence of strong couplings [6]. As a consequence, selective techniques that reintroduce only particular dipolar couplings must be employed. Experimentally, selection of pairs of spins (and hence of their dipolar couplings) can be made on the basis of the dispersion in the isotropic chemical shifts.

Dipolar recoupling can be achieved independently of the isotropic chemical shift range (broadband recoupling), for a defined spectral range (band-selective recoupling) or for the precise chemical shifts of a spin pair (chemical shift selective, CSS recoupling). Chemical shift selective pulse sequences can be obtained, for example, by employing weak r.f. fields such that offset effects become significant. Couplings of interest can be actively reintroduced based on the chemical shift separation of the spins and may be monitored in the presence of

other couplings (which are not completely suppressed by MAS, for example). In favorable circumstances, distances can be measured quantitatively.

Both homonuclear (^{13}C , ^{13}C) and heteronuclear (^{13}C , ^{15}N) CSS recoupling sequences have been proposed. A variety of recoupling conditions may be achieved by fulfilling particular selection rules regarding the MAS rate, the chemical shift separation and the applied r.f. field amplitudes. For example, the RR experiment [92, 153, 154] reintroduces the dipolar coupling between pairs of spins for which the difference in the chemical shifts matches a small integer of the MAS rate. The experiment and variations thereof [93, 94, 158, 159] have been mostly applied to doubly ^{13}C -labeled samples and only recently it has been used to study a uniformly [^{13}C , ^{15}N]-labeled amino acid [96] and different multiply ^{13}C -labeled compounds [160]. SPECIFIC-CP [23] is an example of a selective heteronuclear recoupling experiment which has been used to design NCACB and NCOCA like experiments in solid-state NMR for spectral assignment of uniformly labeled proteins [24]. Here the selectivity is obtained by rendering the conventional Hartmann-Hahn cross-polarization technique [17, 18] frequency dependent in the tilted frame. Alternatively, broadband recoupling techniques become frequency selective by employing selective pulses. This has been recently demonstrated with frequency selective REDOR [95] and applied to uniformly [^{13}C , ^{15}N]-labeled amino acids and di- and tripeptides to probe nitrogen-carbon distances.

In the following, we address the influence of various interactions on the probing of selectively recoupled weak ^{13}C - ^{13}C dipolar couplings in uniformly [^{13}C , ^{15}N]-labeled polypeptides and proteins. Among these perturbing interactions, most important are strong homonuclear and residual dipolar couplings to protons. For this purpose, we apply the constant-time variant [157] of the rotational-resonance [92, 153, 154] experiment to uniformly [^{13}C , ^{15}N]-labeled polycrystalline histidine-HCl. Experimental results are compared with extensive quantum mechanical simulations (performed in the GAMMA environment [16]) to verify which contributions are relevant for the spin dynamics. In order to extend the range of applications to larger biomolecules, we propose a novel two-dimensional experiment termed 2DCT-RRTR. It combines both the rotational resonance in the tilted frame (RRTR, [93, 94, 159]) and the constant-time rotational resonance (CT-RR, [157]) in a 2D experiment. The use of

this experiment to probe long carbon-carbon contacts (i.e. up to 5 Å) is demonstrated on a uniformly [^{13}C , ^{15}N]-labeled, well-ordered sample of ubiquitin.

3.3.1. Constant-time rotational resonance

The constant-time rotational resonance experiment (CT-RR, [157]) is presented in Figure 3.16. The MAS frequency and the difference in the chemical shifts for a pair of I spins j and k must fulfill the rotational resonance condition:

$$|\Omega_j - \Omega_k| = n\omega_R \quad ; \quad n = 1, 2 \quad (77)$$

After an amplitude-modulated [161] CP [17, 18] step, ^{13}C longitudinal polarization is created by a $\pi/2$ pulse. After a period of time τ , a selective π pulse (about 300 μs long) is applied on resonance to one of the spins j or k . Here, a (weak) selective π pulse is used instead of an inversion delay to invert one of these two spins. The polarization transfer is then monitored in the signal intensities as a function of t_{mix} . From this point, the density operator $I_{zj} - I_{zk}$ evolves under the zero-quantum Hamiltonian provided by the RR condition for the time t_{mix} . A final $\pi/2$ converts longitudinal polarization into transversal magnetization which is detected under proton TPPM [10] decoupling (r.f. field of 83 kHz). The total time $\tau + t_{\text{mix}}$ is kept constant such that probe heating due to r.f. irradiation is identical in all experiments. CW [11] or TPPM [10] proton decoupling (r.f. field of 83 kHz) is applied during mixing. The evolution of the $I_{zj} - I_{zk}$ density operator is monitored as a function of t_{mix} in a series of experiments.

We make use of a sample of polycrystalline histidine-HCl of which 10% is uniformly [^{13}C , ^{15}N]-labeled. A one-dimensional ^{13}C CP/MAS experiment is shown in Figure 3.17 to exemplify the range of isotropic chemical shift differences between spin pairs. All CT-RR experiments presented here were recorded at the $n = 1$ rotational resonance condition (see Equation (77)).

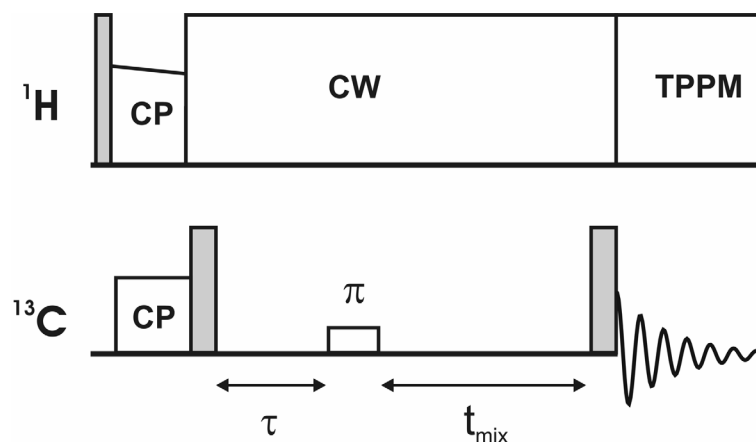


Figure 3.16. The constant-time version of the rotational resonance experiment as described in [157].

The polarization transfer between two weakly dipolar coupled ^{13}C spins which are selectively recoupled in a multi-spin system is influenced by various factors such as additional homonuclear couplings and residual couplings to protons. These are dependent on the local molecular topology and, as a result, a simple analysis is usually not possible. Quantification of the distance results only from comparison of the empirically detected spin dynamics with quantum mechanical simulations. In the past, the various effects on the magnetization transfer have been included in the form of zero-quantum relaxation phenomena [162-165]. Hence, empirical parameters are needed to describe the spin dynamics such that applications to other molecules are difficult.

Alternatively, we conduct a full quantum-mechanical Hilbert space analysis that only relies on chemical shift assignments and knowledge about the spin system of interest. All simulations were performed in the GAMMA environment [16] on a Linux cluster of 2*3 Pentium III processors (760 MHz). In this case, distances as determined from a neutron diffraction structure [150] were used. CSA tensors as described in [166] (neglecting their relative orientation) and scalar couplings (both ^{13}C - ^1H of 140 Hz and ^{13}C - ^{13}C of 35 Hz) were assumed. If protons were included in the spin system, CW [11] or TPPM [10] proton decoupling using a 83 kHz r.f. field was also incorporated into the simulation.

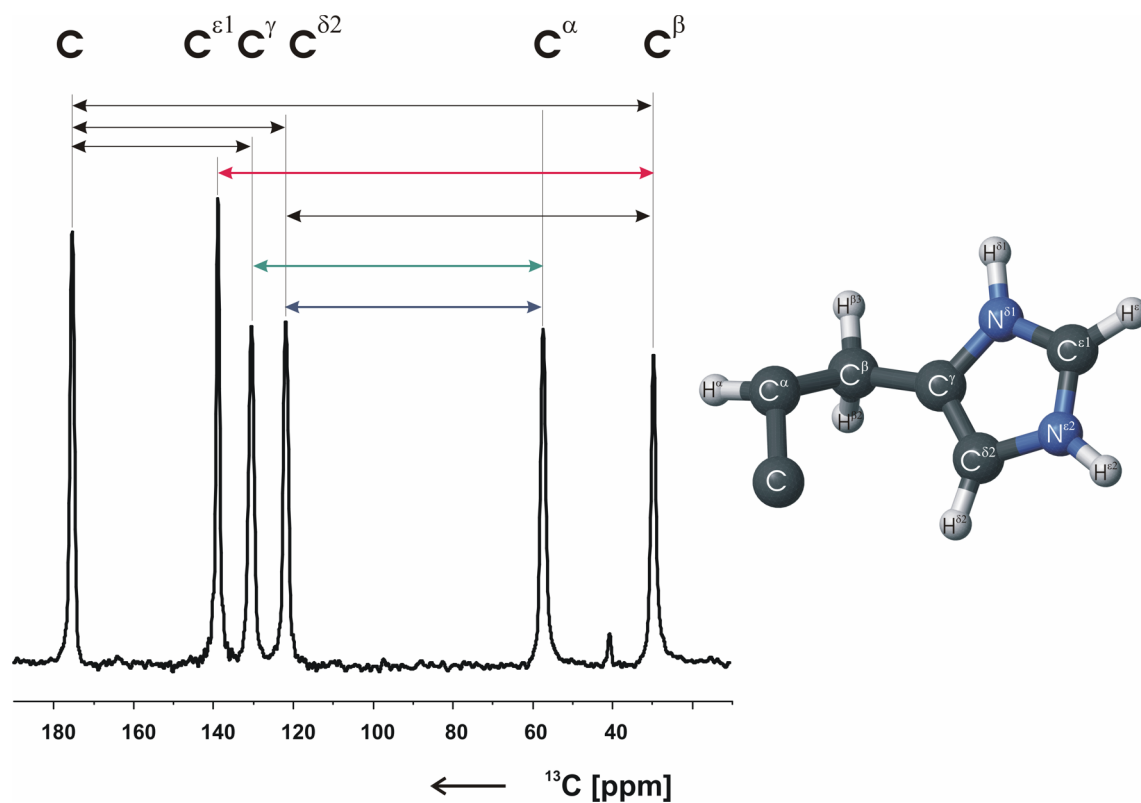


Figure 3.17. The CP/MAS [17, 18] spectrum of a polycrystalline sample of histidine-HCl (of which 10% is uniformly ^{13}C , ^{15}N -labeled). The experiment was performed on a 400 MHz spectrometer at MAS rate of 11 kHz and 5°C. The structure as obtained from neutron diffraction [150] is shown on the right.

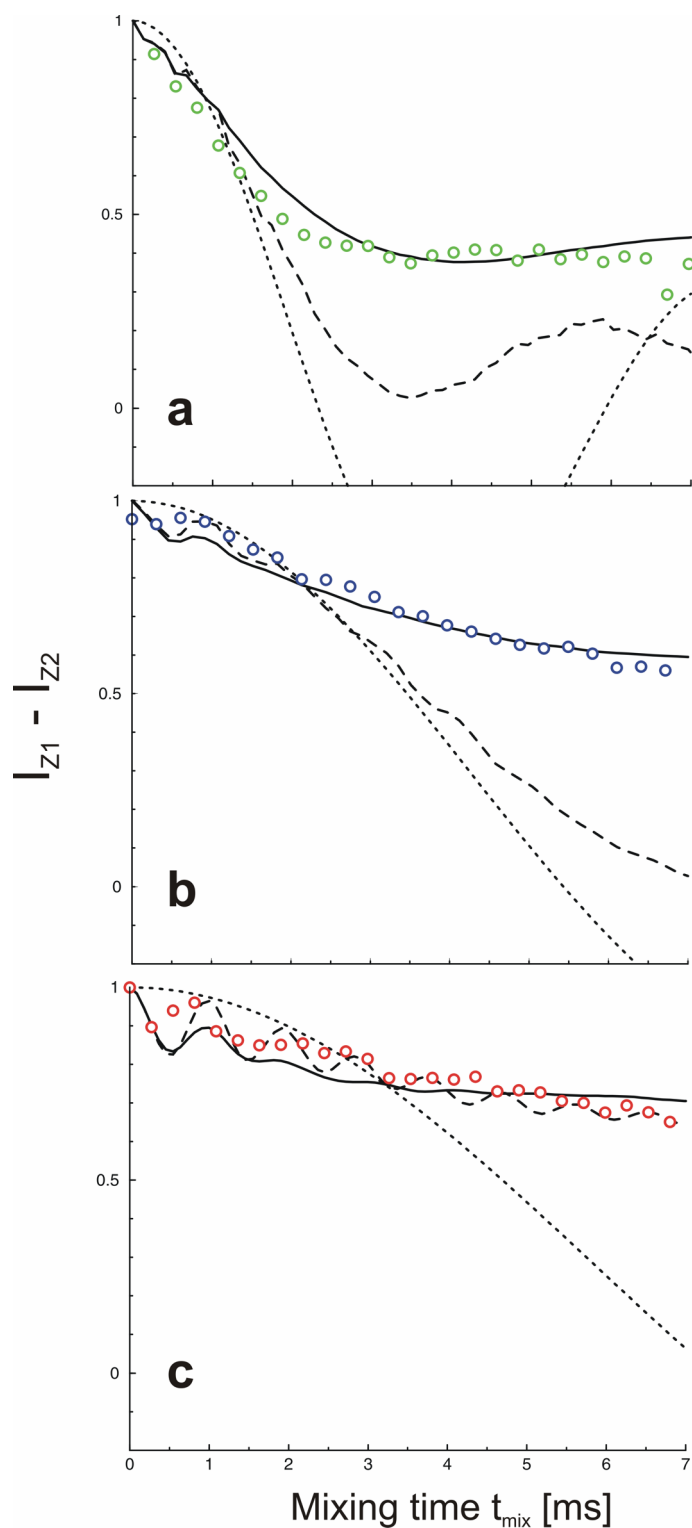


Figure 3.18. Polarization transfer curves measured experimentally for the selectively dipolar recoupled pairs of spins (a) C_α - C_γ , (b) C_α - $C_{\delta 2}$ and (c) C_β - $C_{\epsilon 1}$ as shown with circles. Spectra were recorded on a 400 MHz spectrometer using CT-RR at MAS rates of (a) 7459, (b) 6553 and (c) 11025 Hz and a temperature of 5°C. Superimposed are simulations including all the dipolar couplings among (dotted lines) the active spins, (interrupted lines) the passive spins and (continuous lines) the reduced spin system.

We have measured the polarization transfer curves for the selective recoupling of the dipolar couplings between the following pairs of spins: C_{α} - C_{γ} (2.5 Å), C_{α} - $C_{\delta 2}$ (3.3 Å) and C_{β} - $C_{\epsilon 1}$ (3.6 Å) which are shown in Figure 3.18.a, b, and c, respectively. For each case, simulations including the selectively recoupled dipolar coupling as well as a number of other ^{13}C - ^{13}C , ^{13}C - ^1H and ^1H - ^1H dipolar couplings have been performed. Some of the relevant simulations are shown in Figure 3.18. The great discrepancy between the experimental data and the simulated transfer curves considering the selectively recoupled dipolar coupling only (dotted lines in Figure 3.18) demonstrates that additional interactions are important in all considered cases. A simple two-spin approximation (where the two spins are denoted as *active spins*) is not appropriate in the case of a multi-spin system. We investigate if the reduced dampening in the transfer curves can be explained by considering other dipolar couplings to neighboring spins.

Inclusion of additional ^{13}C - ^{13}C dipolar couplings reveals that only the spins directly bonded to either j or k spins (e.g. the largest homonuclear couplings) influence the simulated transfer curves. These carbon spins are denoted as *passive spins*. These couplings are strongly suppressed by MAS and maybe partially reintroduced by the RR condition (for these pairs of spins the resonance condition is not fulfilled). Nevertheless, they are shown to influence the magnetization transfer (interrupted line in Figure 3.18). Their influence on the polarization transfer does not always suffice to match the experimental data, as in the C_{β} - $C_{\epsilon 1}$ (Figure 3.18.c) case where the simulation agrees well with the measured curves.

Next, additional ^1H spins are considered. Series of simulations, performed for each case in Figure 3.18, revealed that only the couplings between the active and passive ^{13}C spins and all directly attached ^1H spins influence the spin dynamics. Actually, only the ^{13}C - ^1H couplings between spins separated by as many as two bonds are relevant. As shown in Figure 3.18 (continuous lines), the simulations match the experimental polarization transfer curves in all three cases. The simplest spin system that suffices to describe the spin dynamics during CSS recoupling sequences is denoted here as the *reduced spin system*. In Figure 3.19, an example for a reduced spin system is given. In conclusion, it consists of the selectively recoupled spins (active spins), their directly bounded ^{13}C spins (the passive spins) and all ^1H spins bonded to active or passive spins. Only homonuclear and heteronuclear couplings between spin separated by one and maximum two bonds, respectively, have to be considered. This is an

important result, because *a priori* information about the local spin topology is not needed, except for trivial distances (bond lengths and bond angles).

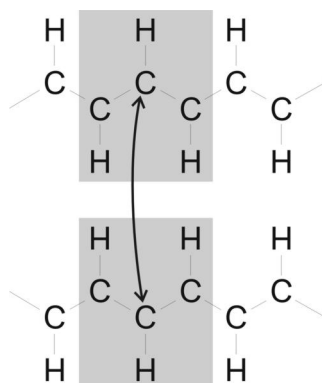


Figure 3.19. Example of a reduced spin system relevant (highlighted in gray) for describing the spin dynamics during CSS recoupling sequences. The selectively recoupled spins are connected by a thick line.

The magnitude of the residual ^{13}C - ^1H is dependent on the decoupling efficiency and we investigate the effect of the CW decoupling field on the polarization transfer in Figure 3.20. As expected, increased decoupling results in better polarization transfer due to the reduced influence of the neighboring protons, in line with results obtained from corresponding simulations Figure 3.20.

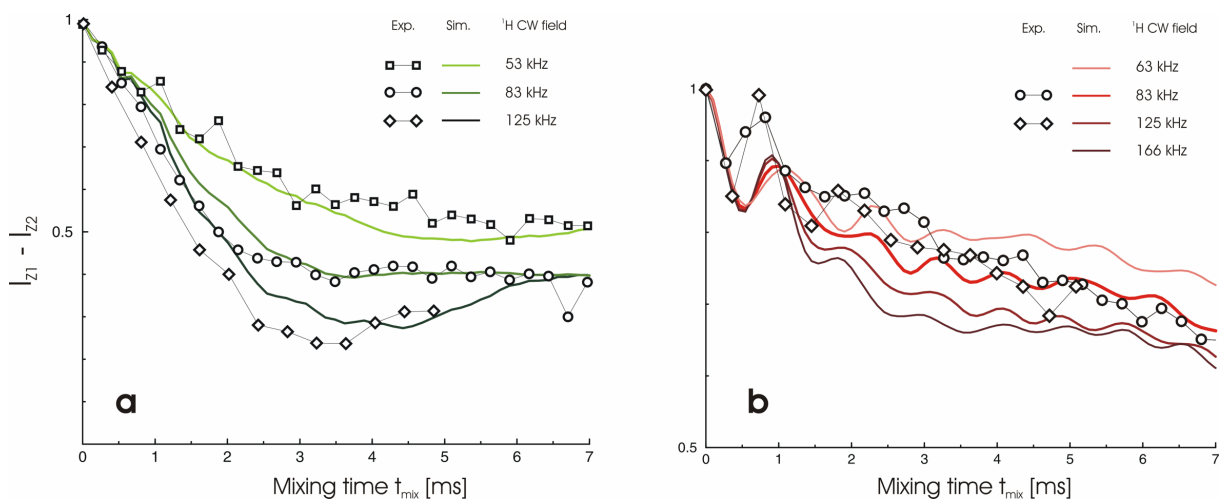


Figure 3.20. Polarization transfer curves (lines with symbols) for (a) $\text{C}_\alpha\text{-C}_{\delta 2}$ and (b) $\text{C}_\beta\text{-C}_{\epsilon 1}$, measured as in Figure 3.18 but with CW decoupling fields as shown in the insets. Corresponding simulations (continuous lines) using the reduced spin systems are also shown.

3.3.2. Two-dimensional constant-time RRTR experiment

A modified version of the two-dimensional RRTR experiment first proposed in [93] is shown in Figure 3.21 and referred to as 2DCT-RRTR. Similar to the pulse sequence in Figure 3.16, the experiment is rendered constant-time by including a longitudinal mixing τ period before the indirect dimension t_1 . During the mixing period, polarization transfer is achieved by the RRTR method [94] modified as in [159] to a ramped version to allow for adiabatic manipulation of the polarization in the rotating frame. The ramp-in and ramp-out pulses are typically set to about 30 μ s. Under the RRTR dipolar recoupling resonance condition, double-quantum or zero-quantum transfer can be achieved by manipulating both the applied r.f. field and the MAS frequency for a given pair of spins j and k . As a result, the recoupling condition can be established with greater flexibility. The intensity of the (Ω_j, Ω_k) cross-peak in the 2D correlation pattern reports on the magnetization transfer from spin j to spin k . In a multi-spin system the 2D extension of the experiment allows for resonances to be resolved while the polarization transfer curves are influenced by the dipolar couplings within the corresponding reduced spin system. A series of 2D experiments are recorded with increasing mixing times t_{mix} to obtain the magnetization transfer curve for a given pair of selectively dipolar recoupled spins. At any time during the 2D experiments or among 2D experiments in a series, the total time $\tau + t_1 + t_{mix}$ is kept constant.

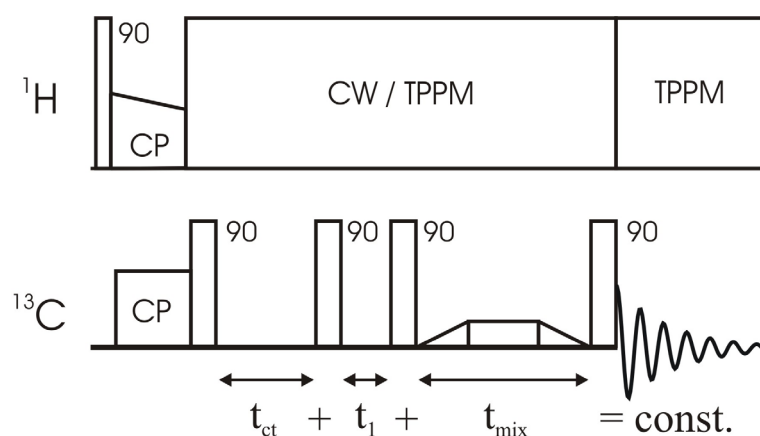


Figure 3.21. The proposed 2D constant-time RRTR experiment (2DCT-RRTR).

We have applied this experiment to a sample of uniformly [^{13}C , ^{15}N]-labeled ubiquitin on 400 and 600 MHz magnets. The structures from x-ray (PDB code 1UBQ, [74]) and solution-state NMR (PDB code 1D3Z, [75]) were used, as well as isotropic chemical shifts from solution-

state NMR [75] and SSNMR [28, 167]. Several quasi-isolated pairs of ^{13}C spins can then be found in ubiquitin. Two of them, $^{22\text{THR}}\text{CO}-^{22\text{THR}}\text{C}_\beta$ and $^{55\text{THR}}\text{CO}-^{55\text{THR}}\text{C}_\beta$ are isolated but overlap and cannot be differentiated. Nevertheless the same internuclear distance of 2.47 Å respectively 2.45 Å is found in the structure and identical reduced spin systems are expected in both cases.

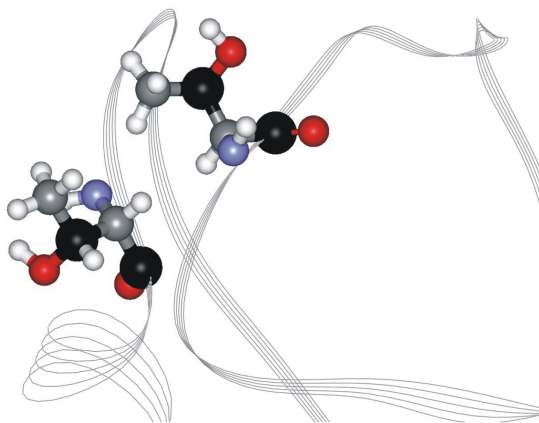


Figure 3.22. A segment of the ubiquitin backbone is shown with gray lines. Residues 22THR and 55THR are highlighted with stick and ball representation. The black balls are the CO and C_α atoms for which the internuclear distance is probed with the 2DCT-RRTR experiment.

Results of the experiment shown in Figure 3.21 on uniformly [^{13}C , ^{15}N] labeled ubiquitin are presented in Figure 3.23. Measurements were done on a 400 MHz magnet at a MAS rate of 11044 Hz. A double-quantum RRTR resonance condition was established using a $\omega_1=1500$ Hz r.f. field. The indicated cross-peak corresponds to the CO- C_β transfer in the two Threonine residues. The experimentally measured polarization transfer curve is also shown in Figure 3.21 together with the simulation for an internuclear distance of 2.45 Å including the dipolar couplings within the reduced spin system. Very good correlation is found between the experimental and the simulated data.

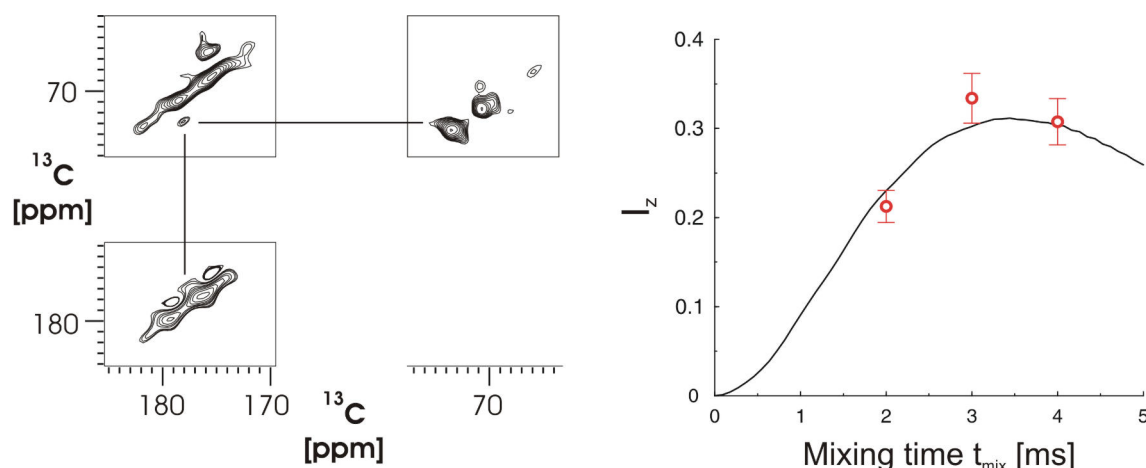


Figure 3.23. The 2DCT-RRTR experiment performed on uniformly [^{13}C , ^{15}N]-labeled ubiquitin results in the spectrum (partially) shown on the left. The highlighted cross peak corresponds to ^{13}CO - $^{13}\text{C}_\beta$ in both 22THR and 55THR. The polarization transfer curve obtained for three RRTR mixing times is shown on the right together with the simulation (the 2D spectrum was obtained for 3ms mixing).

Additional constraints were probed in ubiquitin. These included two more intra-residue distances $^{30\text{ILE}}\text{C}_\alpha$ - $^{30\text{ILE}}\text{C}_{\gamma 2}$ (2.52 Å in X-ray structure), $^{23\text{ILE}}\text{C}_\alpha$ - $^{23\text{ILE}}\text{C}_{\delta 1}$ (2.98 Å in X-ray structure). Inter-residue contacts such as $^{61\text{ILE}}\text{C}_{\gamma 2}$ - $^{65\text{SER}}\text{C}_\beta$ (3.4 Å in X-ray structure), $^{44\text{ILE}}\text{C}_{\delta 1}$ - $^{49\text{GLU}}\text{C}_\alpha$ (3.6 Å in X-ray structure), $^{23\text{ILE}}\text{C}_{\delta 1}$ - $^{50\text{LEU}}\text{C}_\beta$ (3.94 Å in X-ray structure) and $^{19\text{PRO}}\text{C}_\beta$ - $^{57\text{SER}}\text{C}_\beta$ (4.0 Å in X-ray structure) were also tested. A polarization transfer curve could be measured only for the first of these spin pairs due to the large internuclear distances. In the other cases only cross-peaks at long (e.g. 7 or 8 ms) RRTR mixing times could be observed, indicative that a contact (especially between different residues) exists.

In summary, we have shown here that inter-residue, non-trivial ^{13}C - ^{13}C contacts, up to 5 Å, can be probed in relatively large, uniformly [^{13}C , ^{15}N]-labeled proteins. Although the corresponding distances can not be determined quantitatively with great accuracy, they may be important in the process of structure determination. Constraints such as torsion angles (see Section 0) and proton-proton distances (see Section 3.1) obtained in uniformly [^{13}C , ^{15}N]-labeled biomolecule may result in a structure which is less defined in specific regions. Distance restraints targeting these protein areas can be obtained by chemical shift selective methods and may help to refine the structure. Although ambiguous, the importance of such structural parameters in the context of 3D structure calculation has been demonstrated before [168].

4. Applications to proteins and membrane proteins

This chapter is concerned with biological applications of HR-SSNMR techniques. Other well-established methods for structural characterization of (bio-) molecules are X-ray crystallography and solution-state NMR. Both methods have been applied to study the Crh molecule and resulted in two different conformations. In solution, it is found as a monomer, while in the single crystal it adopts a dimeric structure. In addition to these studies, HR-SSNMR may be used to investigate the transition from the monomeric to the dimeric form. As a prerequisite for such studies, the nearly complete ^{13}C and ^{15}N chemical shift assignment was performed for a microcrystalline, well-ordered version of the uniformly [^{13}C , ^{15}N]-labeled Crh. This study, which also resulted in the determination of the secondary structure elements, is presented in Section 0.

Furthermore, HR-SSNMR can be used to study the conformation of peptides and polypeptides that bind in high-affinity (e.g. nano and subnanomolar) to membrane proteins [109]. If these complexes are difficult to crystallize or solubilize, solid-state NMR can probe the structure of the bound, uniformly [^{13}C , ^{15}N]-labeled ligand or its interaction with the receptor. Such an approach is exemplified in Section 4.1, where the structure of neurotensin bound to a G-protein coupled receptor is investigated.

The complete understanding of the function of biomolecules usually relies on results obtained from a variety of biophysical techniques. SSNMR can solve open questions regarding the function of a membrane receptor, given that isotopes can be biochemically incorporated at the sites of interest. In the case of the mitochondrial *bc₁* complex, several X-ray structures have been obtained. Nevertheless, the process in which the ubiquinol molecules are oxidized in the

oxidation reaction centre Q_o is still not fully understood. This part of the Q cycle (in which electrons and protons are transferred) was investigated by SSNMR and is presented in Section 4.2.

4.1. Spectral assignment of microcrystalline Crh

Bacteria are able to utilize for energy purposes different carbon sources from the environment. For this reason, they have developed a complex enzyme system known as the sugar-transporting phosphotransferase system (PTS). PTS is functionally complex as it transports sugars across the cell membrane, phosphorylates these sugars and serves as a chemoreception system (allowing bacteria to orient towards sugar sources). It consists of two phosphotransfer proteins, enzyme I (EI) and HPr, as well as a multitude of sugar-specific enzyme II complexes (EII), each with at least one transport system or permease. If bacteria are provided with a mixture of nutrients, they preferably utilize the one that allows the fastest growth. This selection is achieved through the repression of genes whose products are concerned with consumption of the alternative, less efficient carbon sources. The mechanism is generally known as carbon catabolite repression (CCR) [169] and proceeds, for example, if bacteria are supplied with glucose, through the activation of global control proteins such as the catabolite gene activator protein (CAP) in Gram-negative bacteria or the catabolite control protein (CcpA) in Gram-positive bacteria (Figure 4.1).

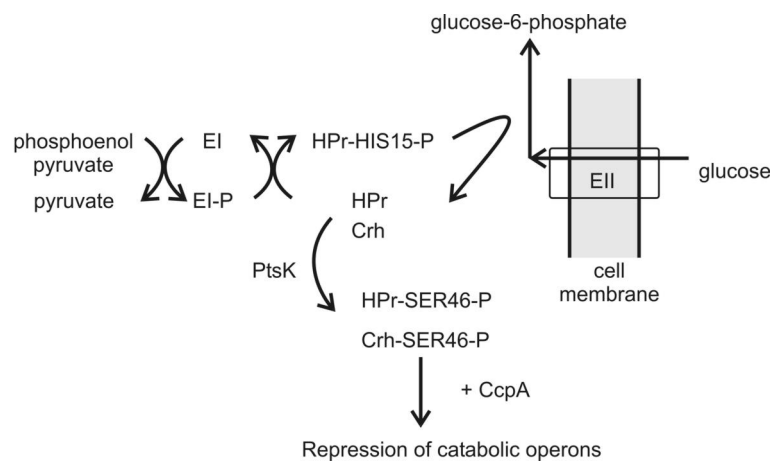


Figure 4.1. Carbon catabolite repression in Gram-positive bacteria by activation of global control proteins (CcpA). Glucose enters the cell via its corresponding enzyme II (EII) and it is phosphorylated. The phosphate is transferred from phosphoenolpyruvate via enzyme I (EI) and HPr to the glucose. HPr and Crh kinases (PtsK) phosphorylate them at SER46 and, in combination with CcpA control the expression of catabolic operons.

The catabolite repression histidine-containing phosphocarrier protein (Crh) has been found to date only in Gram-positive, spore-forming bacteria, such as *Bacillus subtilis* [170, 171]. The specific function of Crh remains unknown [172] and, in contrast to its homologue HPr, it is

not involved in sugar transport, since a GLN occupies position 15 instead of a HIS (Figure 4.2). Similar to HPr, Crh is phosphorylated by Ptsk on Ser 46, and was shown to interact with CcpA [170, 171, 173, 174]. The resulting protein complexes, CcpA/HPr-SER46-P or CcpA/Crh-SER46-P, specifically interact with the catabolite response elements and regulate the expression of numerous genes [175] (Figure 4.1).

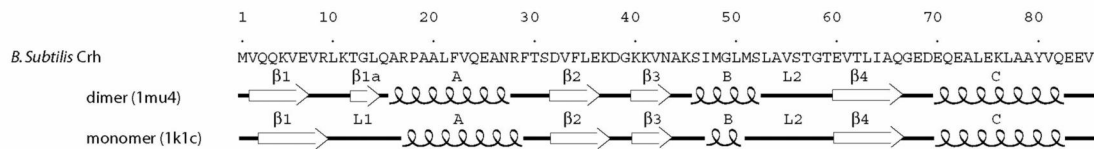


Figure 4.2. Amino acid sequence and secondary structure of the Bacillus Subtilis Crh dimer and monomer. PDB entries 1mu4 [176] and respectively 1k1c [177] were used.

Besides its biological relevance, Crh has been shown to exist in remarkably different conformations. In solution, Crh forms a mixture of monomers and dimers in a slowly (i.e. time scale of hours) exchanging equilibrium [178]. NMR spectroscopy on Crh solutions containing monomers and dimers led to the 3D structure determination of the monomer and enabled to partially identify the dimer interface [177]. Sequential assignments of the residues located in the dimer region were not possible using liquid state NMR methods due to the low intensity of the corresponding resonances and the tendency of the dimer to precipitate under all tested liquid state NMR conditions. Solid state NMR investigations on these precipitates indicated a partially unfolded protein state and were of limited use to gain insight into the Crh dimer structure. Crh single crystals could be obtained and subsequent X-ray diffraction studied (at 1.8Å resolution) revealed a domain-swapped Crh dimer structure formed by β 1-strand swapping of two monomers [176].

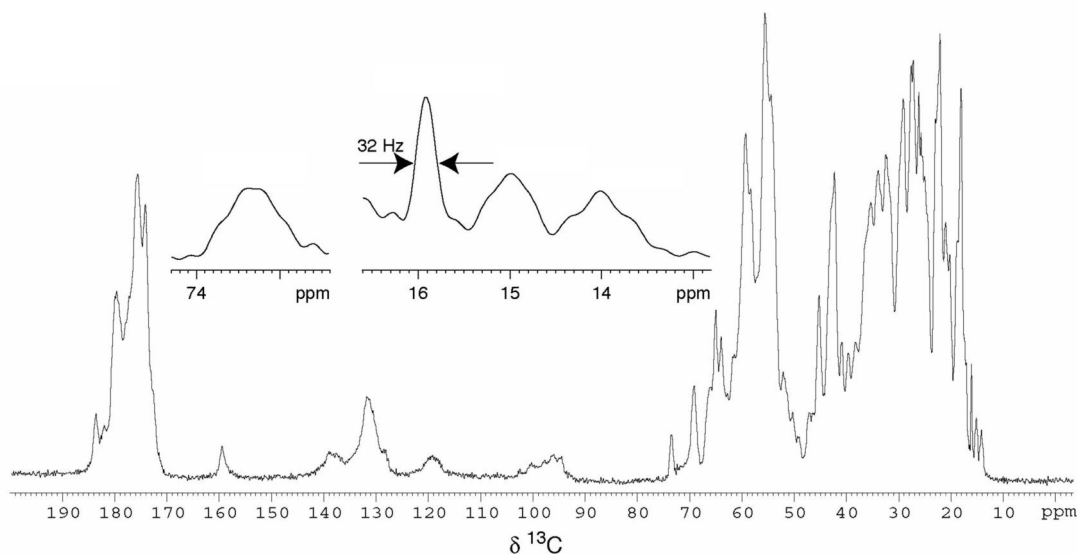


Figure 4.3. 1D ^{13}C CP-MAS [17, 18] spectrum of PEG precipitated Crh recorded at 500 MHz, 10 kHz spinning speed and 75 kHz proton decoupling using the TPPM [10] decoupling scheme. The extracts show selected isolated resonances.

A microcrystalline form of Crh was prepared by precipitation in the presence of PEG [26] which is suitable for HR-SSNMR studies. Figure 4.3 shows the 1D ^{13}C CP-MAS [17, 18] spectrum of microcrystalline Crh taken at about 5°C sample temperature. The spectrum is characterized by the spectral dispersion and line widths of a well-folded and well-ordered protein. For example, the line width of, probably a methyl ^{13}C (at about 16 ppm, see inset in Figure 4.3), amounts to 32 Hz. The remaining lines show some fine structure which is likely to result in highly resolved 2D spectra. In order to investigate the solid-phase Crh protein with HR-SSNMR, we are first interested in a complete assignment of ^{13}C and ^{15}N resonances. This preliminary study is presented in the following.

4.1.1. Solid-state NMR spectroscopy

A series of solid-state NMR experiments were performed with the goal to assign ^{13}C and ^{15}N resonances of the microcrystalline form of Crh. Measurements were performed on Bruker AVANCE DSX 500 and 600 MHz wide bore spectrometers, both equipped with double (^1H , ^{13}C) and triple (^1H , ^{13}C , ^{15}N) resonance Bruker MAS probes, at spinning speeds of 10 and 11 kHz. All experiments were carried out between -10 and -5°C probe temperature (sample temperature about 5 - 10°C). A ramped cross-polarization [161, 179] was used in all experiments to transfer proton magnetization to the ^{13}C or ^{15}N spins. High power proton

decoupling using the TPPM decoupling scheme [10] was applied during evolution and detection periods.

Homonuclear ^{13}C 2D correlation spectra (Figure 4.4) were recorded using transfer via dipolar interactions. In particular, proton driven spin diffusion (PDS, [25]), RFDR [146], and double-quantum SPC-5 [44] were employed. A 2D ^{13}C PDS spectrum was recorded at 500 MHz, using a 800 μs cross polarization (CP) period, and 10 ms mixing time. Acquisition times were 30 ms in t_2 , and 9.5 ms in t_1 . The total acquisition time was 67 hours. R.f. fields during proton TPPM decoupling and 90° nutation pulses on the observe channel were set to 76 kHz and 63 kHz, respectively. An additional PDS spectrum was recorded at 600 MHz, using a 1 ms CP period, and 100 ms mixing time. Acquisition times were set to 10 ms and 5 ms in t_2 and t_1 , using r.f. ^1H decoupling of 94 kHz and ^{13}C fields of 50 kHz, respectively. The total acquisition time was 36 hours. The RFDR spectrum was recorded at 500 MHz, using a 1 ms CP and a 1.8 ms mixing time.

Acquisition times were 25ms in t_2 , and 9ms in t_1 . The total acquisition time was 41h. The proton decoupling power was set to 75 kHz using TPPM. The carbon power used was 63 kHz for CP and $\pi/2$ pulses, and 25 kHz for the π pulses during the mixing period. Several 2Q spectra were recorded at 600 MHz using the SPC-5 sequence [44] for excitation and reconversion (time: 550 μs). In the 2Q spectrum shown in Figure 4.4, the carrier frequency was centered in the aliphatic region of the carbon spectrum. Evolution and t_2 detection times were set to 5ms and 15ms, respectively, using TPPM decoupling at 80 kHz. The total acquisition time was 15h. The ^{13}C r.f. field strength during CP was set to 63 kHz and 45 kHz for the $\pi/2$ pulses during mixing. J-decoupled PDS spectra [180] were taken at 500 MHz, using mixing times of 30 and 100 ms. The carbonyl selective pulse was a snob pulse, centered at the carbonyl region, of 500 μs length and applied with 5 kHz carbon field strength. Acquisition times were 20 ms in t_2 , and 18 s in t_1 . The total acquisition time was 88h. The proton decoupling power was set to 75 kHz using TPPM. The carbon power used for the CP and hard pulses was 69 kHz.

An NCACB ^{13}C 2Q spectrum (Figure 4.5.a) was taken using a N-C α selective SPECIFIC-CP [23] transfer sequence with a mixing time of 2 ms centered at 50 ppm ^{13}C and 105 ppm ^{15}N , employing r.f. field strengths of 15 kHz and 5 kHz for ^{13}C and ^{15}N , respectively. 2Q mixing

was achieved using the band-selective HORROR sequence [69, 181] for a mixing time of 455 μ s. Acquisition times were 15 ms in t_2 and 12 ms in t_1 using TPPM ^1H decoupling at 87 kHz in both dimensions. The total acquisition time was 21 hours. Two NCOCACB 2D correlation spectra (Figure 4.5.b) were recorded using different samples and spectral widths. In both cases, selective N-CO SPECIFIC-CP transfer sequence with a mixing time of 3 ms was centered within the CO region as a first transfer step. Subsequently, RFDR [146] mixing (mixing time 1.6 ms) was employed to transfer polarization from CO to $\text{C}\alpha$ resonances. Transfer to side-chain resonances was achieved using PDSB for a mixing time of 10 ms. Acquisition times were 10ms in the indirect dimension and 8 or 5ms in the direct dimension. The spectral widths in the indirect dimension were 40 and 110 ppm respectively. The total acquisition times were 71 hours for the less concentrated sample, and 25 hours for the 20 mg sample. For the ^1H - ^{15}N CP, transfer times of 1 and 2 ms, respectively, were used.

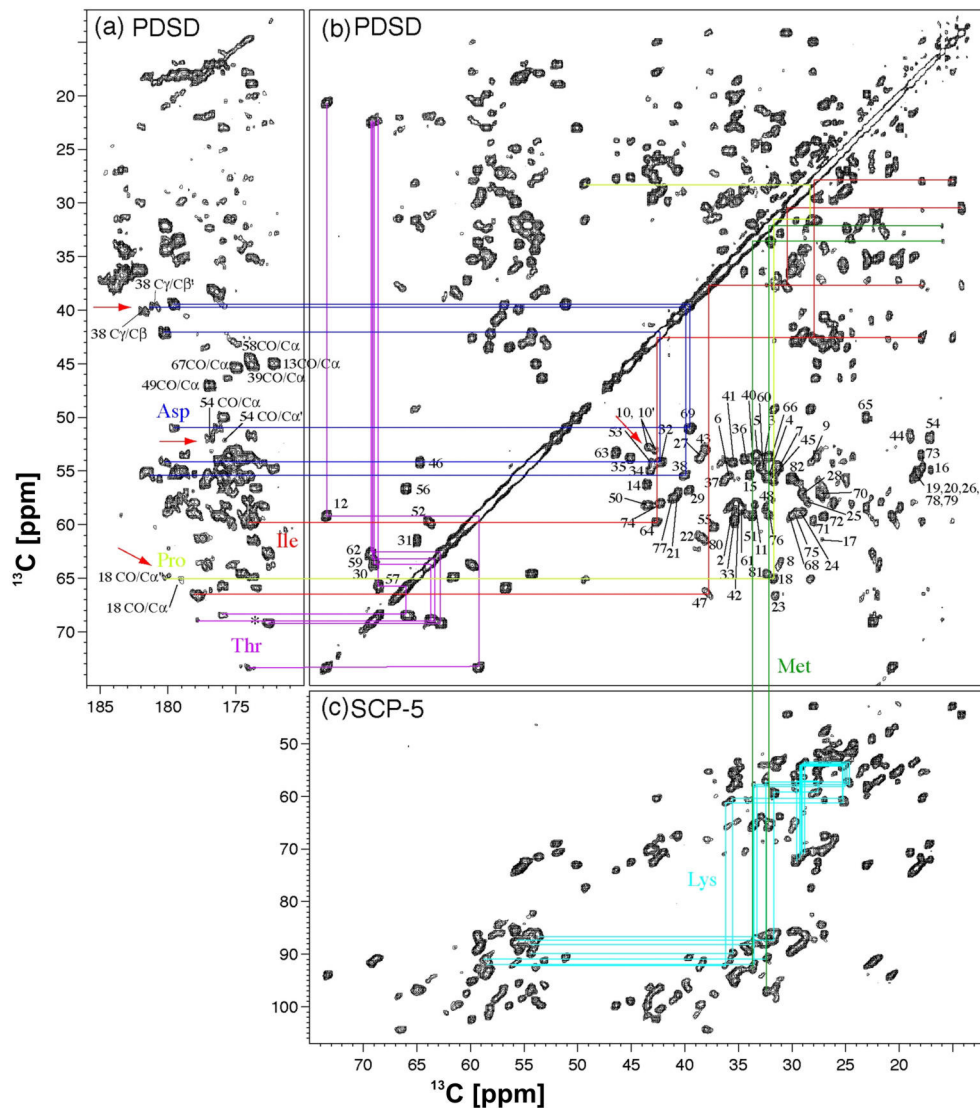


Figure 4.4. 2D ^{13}C homonuclear correlation spectra of Crh. Spin systems of selected amino acid types are color coded: Asp, violet; Ile, red; Lys, cyan; Met, green; Pro, black; Thr, purple. (a) Carbonyl region of the 2D ^{13}C PDS correlation spectrum recorded at 500 MHz. The data were processed using linear prediction in the indirect dimension (f1), zero-filling up to 4096 points, a cosine filter and automatic baseline correction in both dimensions. The asterisk indicates the Thr 59 CO/C α cross peak observed near the noise level. Gly CO/C α resonance are assigned, and the doubled resonances of Pro 18 CO/C α , Asp 38 C δ /C γ and Ala 54 CO/C α are indicated by red arrows. (b) Aliphatic region of the 2D ^{13}C PDS correlation spectrum recorded at 500 MHz. Numbers indicate the C α /C β cross signals of the corresponding amino acid. The pair of Leu 10 C α /C β resonances is highlighted by a red arrow. (c) ^{13}C SPC-5 aliphatic 2Q correlation spectrum (recorded at 600 MHz). The data were processed using linear prediction in f1, zero-filling up to 4096 points, a cosine filter and automatic baseline correction in both dimensions.

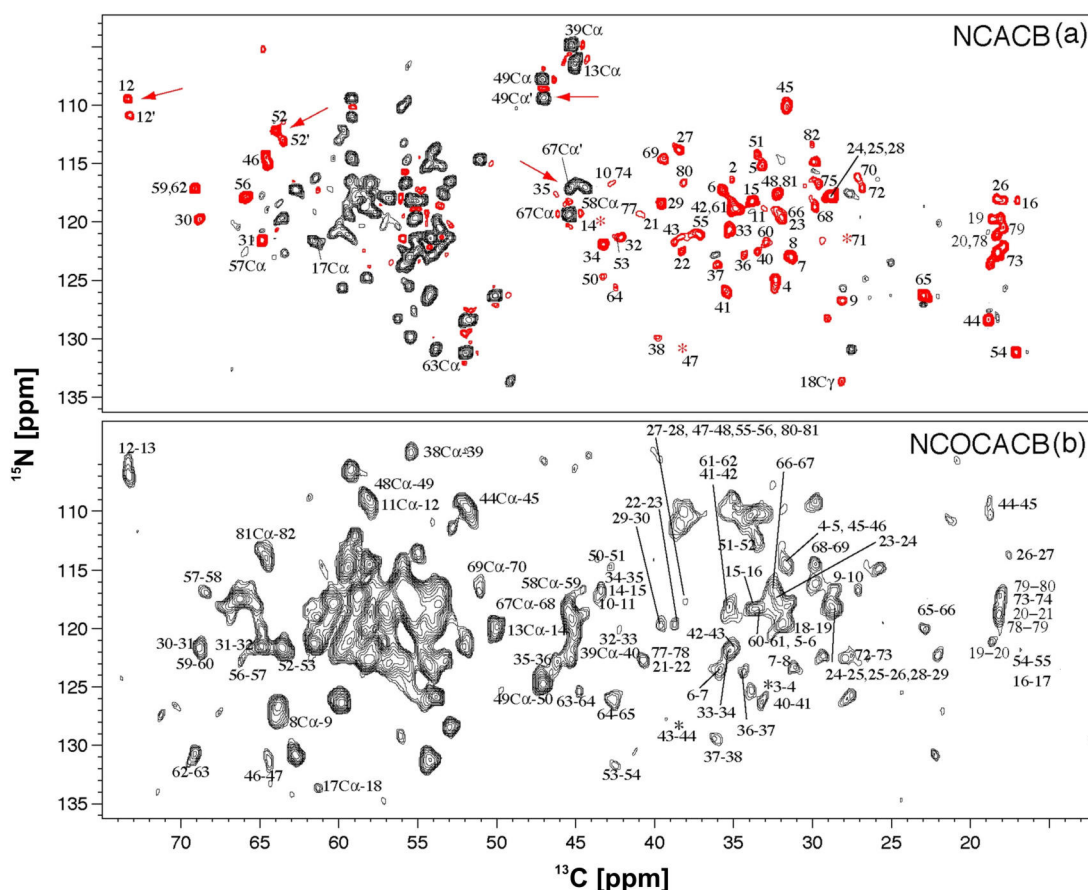


Figure 4.5. (a) NCACB 2Q correlation spectrum recorded at 600 MHz. The data were processed with linear prediction up to 240 points in f_1 , zero filling to 4096 points, cosine filters and automatic baseline correction in both dimensions. Positive peaks (black) correspond to ^{15}N - ^{13}C one- and three-bond correlations, and negative (red) to two-bond correlations. Amino acid assignments are shown for the N-C β cross signals. When this was not possible, N-C α or C γ correlations are indicated instead. Red arrows point to doubled resonance signals. (b) NCOACB correlation spectrum recorded at 600 MHz. The data is processed with linear prediction up to 160 points in f_1 , zero filling to 4096 points, cosine filters and automatic baseline correction in both dimensions. Sequential assignments for N(i)-C β (i-1) correlations are indicated on the spectrum. For some amino acids, only the Ni-C α (i-1) could be observed. Positions marked with an asterisk indicate either signals close to the noise or signals only observed in another NCOACB correlation spectrum (data not shown).

4.1.2. Spectral assignment

As in liquid state NMR, solid state NMR assignments were firstly done by using homo- and heteronuclear spectra correlating spins in the same residue to identify different amino acids and spin systems. For sequential assignments, heteronuclear inter-residue correlations were subsequently established using heteronuclear (^{15}N , ^{13}C) polarization transfer experiments.

Similarly to previous studies involving uniformly [^{13}C , ^{15}N]-labeled proteins under MAS conditions [85, 86, 126], intra-residue studies involved, in the first stage, homonuclear (^{13}C ,

^{13}C) correlation experiments. 2D (1Q, 1Q) correlation experiments employing PDS as a mixing scheme were selected to observe two and three-bond correlations that greatly simplify the identification of amino acid chemical shift systems in the spectrum. In addition, (2Q, 1Q) correlation spectra with short 2Q excitation and reconversion times helped to discriminate between one- and multiple-bond correlations. 2Q filtered spectra were also indispensable for the identification of spin systems close to the diagonal of the (1Q, 1Q) spectrum. Combination of both types of NMR pulse schemes enabled residue type identification. J-decoupled CO-C(aliphatic) correlation spectra [180] were recorded to identify CO resonances and for the spectral resolution of the highly abundant Glu and Gln C δ resonances.

Combination of homonuclear (^{13}C , ^{13}C) correlation experiments with heteronuclear N(i)-C α (i)-C β (i) (NCACB) and N(i)-CO(i-1)-C α (i-1)-C β (i-1) (NCOACB) experiments allows for sequential assignments by rare-spin correlation spectroscopy [115, 116, 118, 119, 182-184]. Similar to previous studies [115, 183, 184], frequency selective N-C polarization transfer was established using SPECIFIC-CP conditions [23]. Likewise, CA-CB polarization transfer involved zero-quantum (0Q) PDS or double-quantum (2Q) transfer. For polarization transfer originating from non-protonated CO to aliphatic carbons within NCOCA-type experiments, we implemented the RFDR [146] mixing scheme. As previously demonstrated [23, 146], RFDR mixing is particularly well suited for band-selective polarization transfer around $\Delta\Omega \sim n\omega_R$ where $\Delta\Omega$ represents the isotopic chemical shift difference in the spin pair of interest and ω_R the MAS rate. RFDR-based CO-CA polarization transfer is hence most effective for typical CO-CA chemical differences at magnetic fields at or above 500 MHz for medium to high MAS rates. Additional attempts to replace the subsequent ^{13}C - ^{13}C spin diffusion step by double-quantum (r.f. driven) polarization transfer failed as it resulted in sample heating and signal loss by excess of r.f. irradiation.

In general, peak intensities and transfer efficiencies vary for different protein segments. For some residues, a straightforward relationship between NMR intensities and structural properties can be found. Typically, residues found in the central part of the fourth strand β -sheet show intense cross signals and good transfers. Amino acids located in the hydrophobic core of the protein are in general characterized by larger transfer efficiencies to side chain carbons than charged ones, probably due to their rigid position in the hydrophobic protein

core. However, additional factors can influence the experimentally observed peak intensities, and no simple general correlation could be established. It should be noted that for a restricted set of residues, two chemical shifts were observed for the same spin (red arrows in Figure 4.4). Overall assignments were successful for 99% for N, C α , and C β atoms, 67% for CO, and 87% of the side chain carbons, resulting in a total of 88%.

4.1.3. Structural analysis

We present in Figure 4.6. a comparison between the N, C α and C β monomer liquid state NMR resonance assignments and the solid state chemical shifts. Note that no liquid state chemical shifts were reported for residues 1-3 [177]. ^{15}N chemical shifts show in general larger deviations with a mean value of 2 ppm (Figure 4.6.a) compared to an average of 1 ppm for ^{13}C chemical shifts (Figure 4.6.b and Figure 4.6.c), which might be partly due to the difference of the pH between the liquid state and solid state samples.

The largest chemical shift differences between liquid state and solid state NMR resonance assignments are observed in three regions of the protein. This is illustrated in Figure 4.6.d and Figure 4.6.e, where the sum of the absolute values of the chemical shift differences from N, C α and C β are color coded on the Crh dimer (Figure 4.6.d, PDB code 1mu4 [176]) and on the monomer (Figure 4.6.e, PDB code 1k1c [177]) structures. Deep blue corresponds to the smallest differences, red to the largest differences, as indicated on the scale.

The large chemical shift differences between solution and solid state NMR can be attributed to the dimerization state of Crh, as illustrated in Figure 4.6.d,e. Indeed, in a single crystalline state, Crh undergoes conformational changes upon dimerization in several regions of the monomer structure [176]. The most drastic conformational differences are observed in the hinge region and comprise residues Lys 11- Gln 15, which cross the dimer interface and connect the core of each chain to its corresponding swapped β 1-strand. In the NMR-derived structure of the monomer, this segment forms loop 1, which is folded onto the hydrophobic core of the protein to create a flat surface. Domain swapping also induces β -strand 1 to shift by two residues on Crh dimerization, to complete the 4 strand β -sheet with β -strands 2-4 from the other monomer, but with different hydrogen bonding partners [176]. Furthermore, conformational rearrangements upon dimerization are observed for helix B where several

residues undergo significant displacements. Helix B is extended in the dimeric form and comprises residues Ser 46 –Ser 52, as opposed to Ile 47 - Leu 50 in the monomer. Residues Met 51-Thr 59 in the monomer form loop 2 (Leu 53 - Thr 59 in the dimer). This loop stabilizes loop 1 in the monomer, while it is located at the dimer interface in the crystal structure [176].

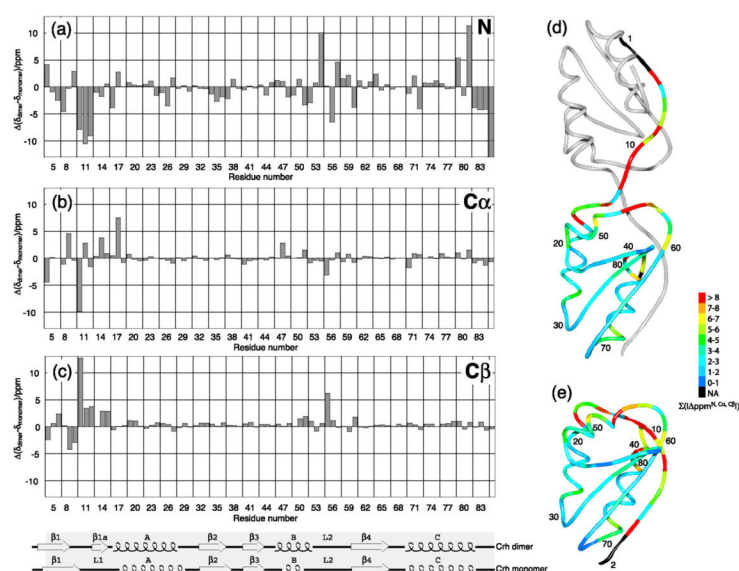


Figure 4.6. Chemical shift differences between the liquid state NMR Crh monomer and solid state NMR Crh dimer. Secondary structures of the monomeric and dimeric form are shown below the graphs. (a) ¹⁵N backbone, (b) ¹³Cα, (c) ¹³Cβ chemical shift differences for Crh residues 3-84 (no liquid state assignments are available for residues 1-3 [177]). (d) Sum of the absolute values of ¹⁵N backbone, ¹³Cα, and ¹³Cβ chemical shift differences color coded on the Crh dimer crystal structure (PDB code 1mu4 [176]) and (e) on the Crh monomer structure (PDB code 1k1c [177]). Colors vary from blue for smallest chemical shift differences, to red for largest deviations, corresponding chemical shift differences are indicated. Black stands for not applicable. All structures were drawn using Swiss-PDBViewer [185] and rendered with POV-Ray™.

With these conformational changes in mind, the observed chemical shift differences become clear. The first group of residues with very different chemical shifts is located at the N-terminus around residues Gln 4 - Arg 17, corresponding to β1-strand and loop 1 in the Crh monomer (illustrated in Figure 4.6.d, e). As a result of the conformational changes detailed above, β-strand 1 hydrogen bonding partners are different for residues Val 2-Arg 9 in the dimer, and Val 8 and Arg 9 form no longer part of the β1-strand. Hydrogen bonding patterns and torsion angles of residues Leu 10 – Leu 14 forming the β1a-sheet in the hinge region of the dimer are altogether different in the monomer.

The second region with large chemical shift differences concerns residues Ile 47- Glu 60. Residues Ile 47 - Leu 50 form helix B in the monomer, experiencing important conformational changes upon dimerization as described above. Loop 2 forms hydrogen bonds with loop 1 in the monomer, while it is located at the dimer interface in the crystal structure. For example, Thr 57 forms an intermolecular hydrogen bond with Thr 12 in the dimer, whereas Thr 12 is hydrogen bonded to Ala 54 in the monomer. The third region is located near the C-terminal, and its conformation strongly differs between the monomer and dimer. Probably, crystal contacts determine the conformation of the C-terminus including the six-residues His extension, whereas this part of the protein is flexible in solution.

The chemical shift assignments obtained on microcrystalline Crh can be used to define conformation dependent chemical shifts. Employing the TALOS program [113] these parameters have been exploited to predict dihedral angles from the assigned N, CO, C α and C β solid state NMR chemical shifts. Figure 4.7.a shows the differences between the predicted ψ angles and those of the Crh monomer structure. Most angles differ by less than 40 degrees, with a mean value of 34 degrees. Notably, three regions can be identified where significantly larger deviations are observed. These include residues Arg 9-Gln 15, Leu 53 – Val 55, and Gly 67-Glu 70. The corresponding residues are indicated in red on the monomer structure in Figure 4.7.c. Two of these regions (Arg 9-Gln 15, Leu 53-Val 55) overlap with those already identified by the variations in chemical shifts between liquid state and solid state NMR data. As described in the preceding paragraph, these regions experience the most pronounced conformational changes during the monomer to dimer transition. Thr 30 and Gly 67-Glu 70 are located in loops pointing to the outside of the protein, and could possibly show different conformations induced by crystal contacts in the dimer.

In Figure 4.7.b, we present a comparison between the dihedral angles calculated from the solid state NMR chemical shifts with the ones observed for the domain swapped dimeric structure determined by X-ray crystallography (Figure 4.7.d). Only Thr 30 and Gln 83,84 show large differences and are highlighted in red on the dimer structure in Figure 4.7.d. Conformational differences within these residues could be explained by variations in crystal contacts between the microcrystalline and single-crystal form of Crh prepared under different

experimental conditions. Taken together, these data strongly suggest that Crh almost certainly exists as a dimer in the microcrystals.

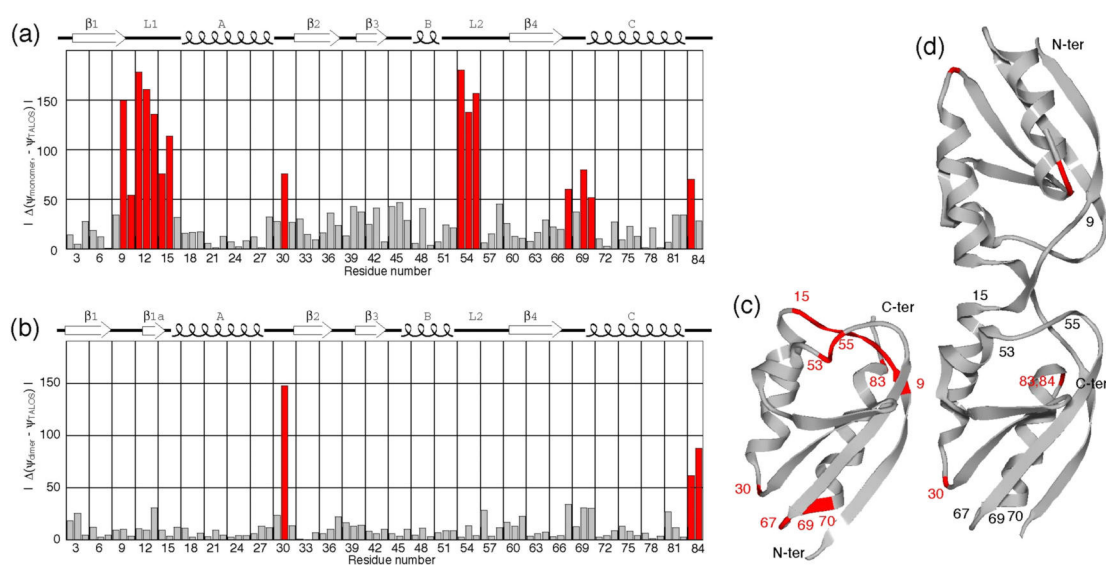


Figure 4.7. Comparison between the dihedral ψ angles predicted from the solid state NMR chemical shifts using the TALOS [113] software and those of the monomer and dimer Crh structure. (a) Absolute values $|\Delta(\psi_{\text{monomer}} - \psi_{\text{TALOS}})|$ plotted as a function of residue number. Residues showing large deviations are highlighted in red. The secondary structure of the Crh monomer is shown above the graph. (b) Absolute values $|\Delta(\psi_{\text{dimer}} - \psi_{\text{TALOS}})|$ plotted as a function of residue number. Residues with large deviations are highlighted in red. The secondary structure of the Crh dimer is shown above the graph. (c) Location of highlighted amino acids on the monomer structure (PDB code 1k1c [177]) and (d) on the dimer structure (PDB code 1mu4 [176]).

Remarkably, several residues are characterized by doubled NMR resonance signals (indicated by arrows in Figure 4.4.a,b and Figure 4.5.a). Two sets of nitrogen chemical shifts were detected for Thr 12, Gly 49, Ser 52 and Gly 67 (Figure 4.5.a). In addition, ^{13}C signal pairs were identified for the $\text{C}\alpha$, $\text{C}\beta$ shifts of Leu 10, the CO of Pro 18 and Ala 54 and the $\text{C}\delta$, $\text{C}\gamma$ of Asp 38 (Figure 4.4.a,b, indicated by red arrows). It is striking that all but two of the residues showing NMR signal pairs are located at the dimer interface or near helix B (residues Leu 10, Thr 12, Pro 18, Gly 49, Ser 52 and Ala 54, color coded in red in Figure 4.8, referred to as group one). Asp 38 and Gly 67 form the second group and are found in loops exposed on the surface of the protein (labeled in green in Figure 4.8).

There are at least three different possible rationales for these spectroscopic observations. First, the two signals could reflect conformational differences between the two monomers in the dimer. This is however not very likely, since in the dimer structure determined by X-ray crystallography [176], only minor differences exist between the conformations of the two

monomers, with average differences between ϕ and ψ dihedral angles smaller than 5° , and an overall rmsd of 0.7 Å for backbone atoms. A second possibility is that the two signals have their origin in different conformations of the Crh dimers in the crystallographic unit cell caused by different crystal contacts. A third explanation could involve dynamic behavior, for instance slow exchange between two conformational states.

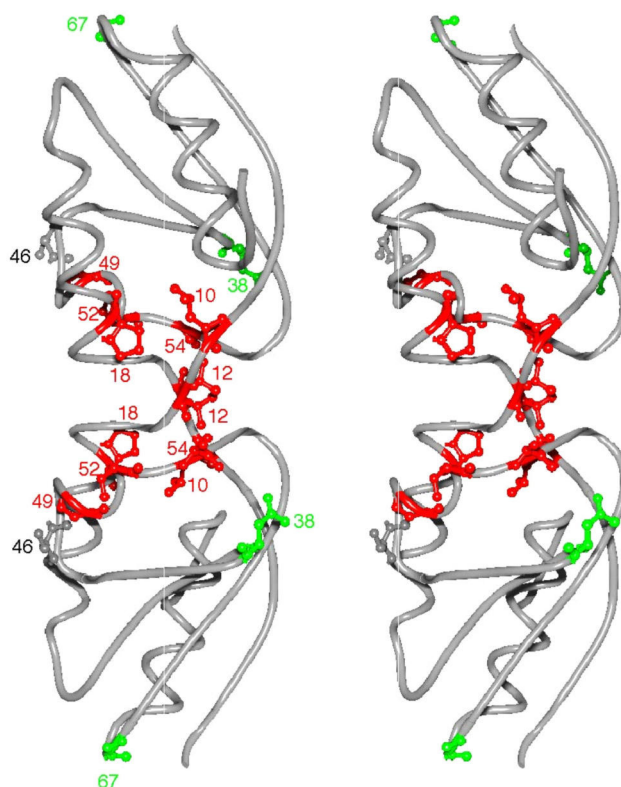


Figure 4.8. Stereo view of the 3D Crh dimer crystal structure (PDB code 1mu4 [176]). The residues characterized by doubled resonance signals are highlighted. Color coded in green are residues located in the loop regions; in red residues located in helix B, loop 2 and the dimer interface. The active site Ser 46 is shown in gray.

In the first group of residues located at the dimer interface and the nearby helix B, all concerned atoms belong to the backbone or to buried side chains. For these residues, different crystal contacts seem to be a less convincing explanation. In contrast, an increased flexibility of the Crh polypeptide chain in this region might be important for binding of Crh to its biological partners, as Helix B and loop 2 should be key positions as to the interaction between Crh with CcpA [174] or HprK/P [186]. Furthermore, flexibility might even play a major role in the domain swapping mechanism, which particularly affects this region [176].

For the second group of doubled resonances including Asp 38 and Gly 67, both different crystal contacts, as well as increased loop dynamics, could be plausible explanations.

Notably, increased flexibility has been identified in the Crh monomer liquid state NMR study for the turn connecting the β -strands 2 and 3 (including Asp 38), as well as for helix B (residues Met 48 - Ala 54) [177]. The time scale of these dynamic processes was shown to include contributions on the nanosecond timescale, as well as on the millisecond timescale. The authors concluded that the increased flexibility of the Crh polypeptide chain observed near the regulatory site may be important for binding in the active site of HprK/P and/or the interaction with CcpA. However, further experimental investigations are needed in order to confirm the static or dynamic nature of the observed peak doubling in the dimeric form of Crh.

Nearly complete ^{13}C and ^{15}N sequential assignments of the 85 residues was performed using 500 and 600 MHz NMR 2D spectroscopy at moderate magic angle spinning [76] rates. This study allows for a structural comparison to Crh structures in the solution state [177] and as a single crystal form [176]. Resonance assignments obtained in the solid state differ from NMR data obtained in the solution state for several protein segments. A subsequent prediction using TALOS [113] led to backbone dihedral angles that are consistent with a microcrystalline dimeric form of Crh that closely resembles the single crystal structure. Chemical shift assignments are hence consistent with the investigation of a 85x2 residue dimer in the solid state. Finally, dynamic and/or static disorder has been detected for a restricted number of residues located mainly at the dimer interface. These observations could potentially be important for explaining the mechanism of domain swapping and for the interaction of Crh with other molecules.

Here we demonstrate that optimized sample preparation and a selected set of homo- and heteronuclear correlation experiments can lead to nearly complete spectral assignments of a uniformly [^{13}C , ^{15}N]-labeled, 10kDa, solid-phase protein at medium-size magnetic fields. Our study confirms that solid-state NMR studies using uniformly labeled protein variants permit a detailed analysis of the backbone conformation of the protein. In the current context, backbone dihedral predictions can be derived from chemical shifts that allow for a direct structural comparison of the solid-phase sample to isoforms of the protein in other chemical

environments. Our data strongly indicate that the microcrystalline Crh sample adopts a conformation that is highly similar to the 3D domain swapped dimeric Crh structure observed in a single crystal study. Chemical shift changes discriminating the monomeric from the dimeric structure of Crh are easily identified. Doubled resonance signals of several residues might indicate dynamics present in the protein potentially important for interactions between Crh and its partners, and/or the domain swapping mechanism.

The presented data provide a solid basis for further structural investigations of Crh and its interaction partners. For instance, solid state NMR chemical shift mapping should already supply an answer as to the multimerization state of P-Ser-Crh on interaction with CcpA. In addition, our data, together with NMR data obtained in the solution state, may serve as a valuable reference to investigate disordered states, as observed in the spontaneously formed precipitate mentioned above. Investigation of other disordered states might help to elucidate the conformational transition of the solution state monomer to a crystalline domain swapped dimer. Moreover, Crh may serve as a valuable model system for additional solid state NMR technique developments, for example in the context of studying protein structure, dynamics or protein-protein interactions. Solid state NMR studies as outlined here may hence provide a complementary means to investigate multimerization processes and other protein-protein interactions at atomic resolution. In particular, they may form the basis for structural investigations of large protein-protein complexes that are difficult to study by solution state methods.

4.2. Neurotensin bound to its G-protein coupled receptor

Neurotensin (NT, Figure 4.9) is a 13-residue peptide [187] that is involved in a variety of neuromodulatory functions in the central nervous system and endocrine/paracrine actions in the periphery [188]. Three receptors (NTS1, NTS2 and NTS3, named in the order in which they were discovered) have been identified so far. The first two of them are G-protein-coupled receptors belonging to the A family (rhodopsin-like family) and share 60% homology. Cloning and expression of neurotensin receptors from mouse, rat and human brain have been described. For example, in Figure 4.10, the aligned amino acid sequences for NTS1 and NTS2 are shown. Neurotensin binds with high-affinity (dissociation constant $K_D=0.2$ nM) to the levocabastine-insensitive receptor NTS1 [189-191] and with lower-affinity ($K_D=2-3$ nM) to the levocabastine-sensitive receptor NTS2 [192, 193]. The non-peptide antagonist SR 48692 (Figure 4.9, [194]) binds preferentially to NTS1 and blocks many of the central and peripheral effects of neurotensin (which are consequently attributed to NTS1).

NT	pELYENKPRRPYIL-OH
NT(8-13)	Ac-RRPYIL-OH
NT(9-13)	Ac-RPYIL-OH

SR 48692

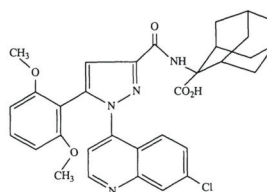


Figure 4.9. The sequence of neurotensin (NT) and its pharmacophore NT(8-13). Only the residues marked in red are important for binding to the levocabastine-insensitive neurotensin receptor NTS1. NT(9-13), which binds NTS1 with very low affinity, is also depicted (it was obtained as a by-product during peptide synthesis of NT(8-13)). The structure of the antagonist SR 48692 is also shown.

The N-terminal truncated NT(8-13) (Figure 4.9) exhibits even higher affinity for NTS1, while NT(1-8) totally lacks the ability to bind to NTS1 [190]. Any other shorter variant of NT(8-13), for example NT(9-13) is less effective (by orders of magnitude in dissociation constants) than NT(8-13) in binding NTS1. Thus, it can be concluded that the hexapeptide formed by the last residues of neurotensin, NT(8-13), is entirely involved in the interaction with NTS1.

Subsequently, biophysical and biochemical studies of the binding of NT to NTS1 can be performed using the shorter version NT(8-13).

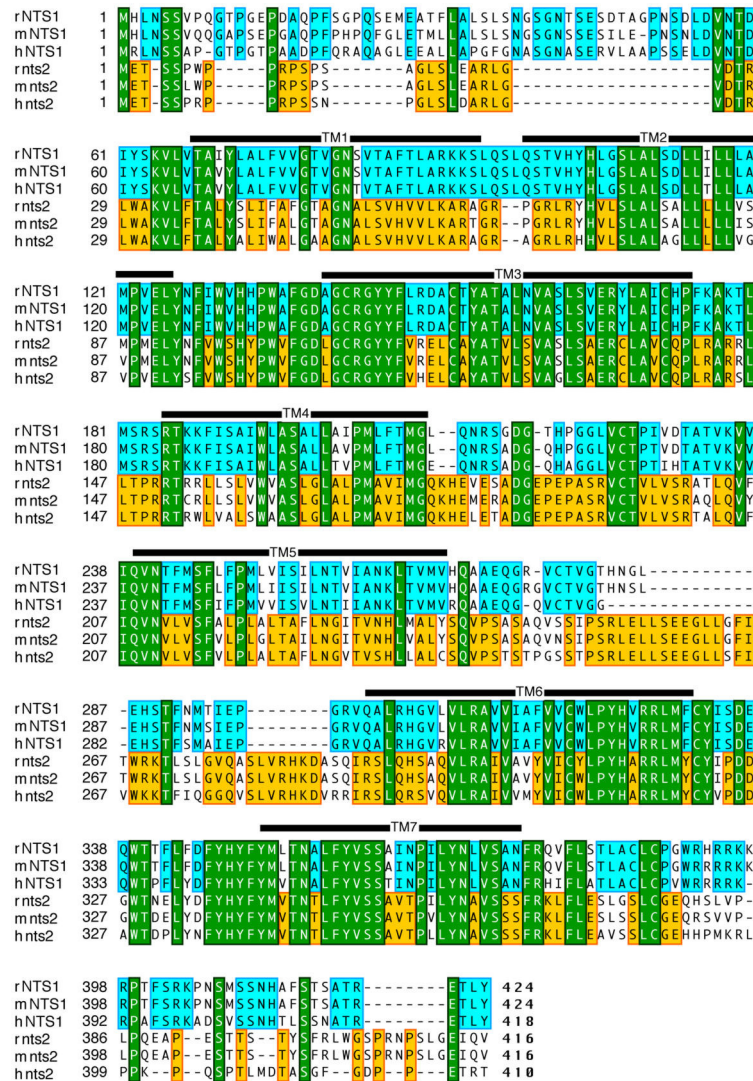


Figure 4.10. Aligned amino acid sequences of the (r) rat, (m) mouse and (h) human NTS1 and NTS2. Highlighted are conserved residues in all NTS1 and NTS2 sequences (green), in NTS1 only (blue) and in NTS2 only (yellow). The position of the transmembrane segments is indicated (TM1 to TM7). Reproduced from [195].

4.2.1. G-protein-coupled receptors

G-protein-coupled receptors (GPCRs) form one of the largest families of plasma membrane receptors and mediate cellular responses upon interaction with a great diversity of signals such as photons, odorants, sugars, hormones and neurotransmitters. All GPCRs are characterized by a signature of seven transmembrane (TM) helices and are therefore also known as seven trans-membrane (7TM) receptors. Their name derives from the fact that the

receptor signals by activating heterotrimeric G-proteins Figure 4.11, although some 7TM receptors have alternative signaling mechanisms [196]. The family of GPCRs is a very large one. More than 800 genes encoding various receptors exist and more than 3000 sequences from different organisms are known. In humans, the GPCR genes correspond to 3% of the entire genome.

Because GPCRs are heavily involved in the communication of the cell with the environment (including other cells in multi cellular organisms), they are associated with many pathological processes. Consequently, they constitute an important target for medical agents and about 50% of all recent drugs act (directly or indirectly) on GPCRs [197]. In Figure 4.12, a list of the top 20 (by sales profit) drugs targeted at GPCRs is given. In this respect, rational drug design techniques which may provide alternative agonists or antagonists for GPCRs are of great pharmacological interest. Such studies critically depend upon the availability of structural information for a given receptor interacting with its natural ligand. Up to date, only the structure of rhodopsin has been determined by X-ray crystallography [198]. In the absence of the high-resolution structure of a GPCR, ligand-based drug design may be employed [199]. In this context, determining the structure of the bound ligand is, therefore, an important biochemical task.

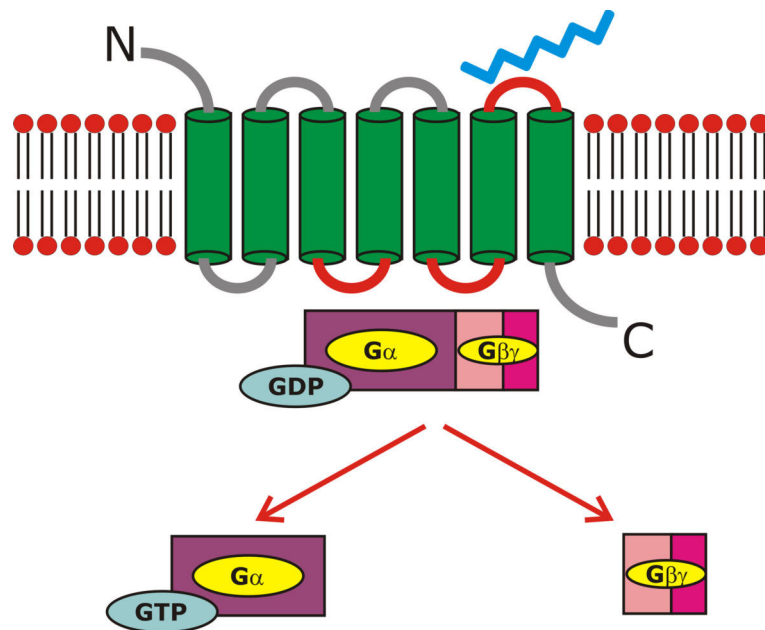


Figure 4.11. Example of GPCR signaling: the highly selective binding of the agonist activates the receptor. The conformational changes induced in the receptor (shown in red) in turn activate the bound G-protein. This will replace bound-GDP by GTP and subsequently dissociate into the G_{α} and $G_{\beta\gamma}$ subunits and from the receptor. Both G_{α} and $G_{\beta\gamma}$ will inhibit or stimulate the production of intracellular secondary messengers (like cAMP or Ca^{2+}).

In the next section we will discuss various biochemical and biophysical methods that allow studying the interaction of a ligand (with emphasis on polypeptide or protein ligands) with a membrane protein (membrane receptor or ion channel). In particular we are interested in obtaining high-resolution structural information of the bound conformation of the ligand. The biophysical methods discussed make use of differences in the physical and chemical properties of the samples. For example, crystalline variants of the complexes ligand/receptor may be available. Differences in the affinity of the ligand (e.g. high or low), in the solubility of the either the complex ligand-receptor or of the ligand and in the size of the ligand-receptor complex may be employed. In this context, the role of solid-state NMR in structural characterization of peptide ligands binding with high-affinity to membrane proteins of unrestricted molecular weight and solubility is shown.

Table 1. Annual worldwide sales of drugs acting at GPCRs in the top 100 best selling prescription drugs in 2000.

Trademark	Generic name	Company	Disease	Target receptor	million \$
Claritin	loratadine	Schering-Plough	allergies	H ₁ antagonist	3011
Zyprexa	olanzapine	Eli Lilly	schizophrenia	mixed D ₂ /D ₁ /5-HT ₂	2350
Cozaar	losartan	Merck & Co	hypertension	AT ₁ antagonist	1715
Risperdal	risperidone	Johnson & Johnson	psychosis	mixed D ₂ /5-HT _{2A}	1603
Leuplin/Lupron	leuprolide	Takeda	cancer	LH-RH agonist	1394
Neurontin	gabapentin	Pfizer	neurogenic pain	GABA B agonist	1334
Allegra/Telfast	feofenadine	Aventis	allergies	H ₁ antagonist	1070
Imigran/Imitex	sumatriptan	GlaxoSmithKline	migrane	5-HT ₁ agonist	1068
Serevent	salmeterol	GlaxoSmithKline	asthma	β ₂ agonist	942
Plavix	clapidoogrel	Bristol-Myers Squibb	stroke	P2Y ₁₂ antagonist	903
Zantac	ranitidine	GlaxoSmithKline	ulcers	H ₂ antagonist	871
Singulair	montelukast	Merck & Co	asthma	LTD4 antagonist	860
Pepcidine	famotidine	Merck & Co	ulcers	H ₂ antagonist	850
Cardura	doxazosin	Pfizer	hypertension	α ₁ antagonist	795
Gaster	famotidine	Vamanouchi	ulcers	H ₂ antagonist	763
Zofran	ondansetron	GlaxoSmithKline	antiemetic	5-HT ₃ antagonist	744
Zoladex	goserelin	AstraZeneca	cancer	LH-RH agonist	734
Diovan	valsartan	Novartis	hypertension	AT ₁ antagonist	727
BuSpar	buspirone	Bristol-Myers	depression	5-HT ₁ agonist	709
Zyrtec/Reactine	cetirizine	Pfizer	allergies	H ₁ antagonist	699
Duragesic	fentanyl	Johnson & Johnson	pain	opioid agonist	656
Atrovent	ipratropium	Boehringer Ingelheim	asthma	anticholinergic	598
Seloken	metoprolol	AstraZeneca	hypertension	β ₁ antagonist	577

Figure 4.12. Listing of the drugs acting on GPCRs according to the profit made by the corresponding companies in 2000. Data reproduced from [199].

4.2.2. Studies of receptor-ligand interaction

Numerous biological processes involve interactions of proteins with other molecules termed ligands, such as peptides, nucleic acids, carbohydrates, steroids, vitamins, or even proteins. Specific interactions between pairs of molecules are the basis for molecular recognition, which is crucial in signal transduction, gene transcription, immune response, enzymatic regulation and drug design. Structural data on the bound complex are required to fully explore the conformation-activity relationship. Here we focus on the range of possible structural studies of a, usually much smaller, peptide ligand molecule bound to a membrane protein.

In a simple but general approach, the binding site of the ligand can be investigated by *mutagenesis studies*. Mutations in the membrane protein of the residues that are interacting with the ligand result in lower affinity for the ligand which can be observed experimentally (e.g. binding constants can be measured in vitro or receptor activity monitored in vivo). For example, in the case of the rat neurotensin receptor rNTS1, the following residues have been found to interact with the non-peptide antagonist SR 48692 [200]: Met208 (in TM4), TYR324, ARG327 and PHE331 (in TM6) and TYR351, THR354, PHE358 and TYR359 (in TM7). Similarly, the residues involved in the binding of neurotensin were determined [201]: MET208 (in TM4), ARG327 and PHE331 (in TM4), TRP339, PHE 344 and TYR347 (in E3). Additionally, simultaneous mutations on the peptide ligand and structure-activity studies

using these ligand analogs reveal the pairs of interacting amino acids. In this way it was found that TYR11 in the neurotensin molecule interacts strongly with TYR347 in the extracellular loop 3 (E3) of rNTS1. The results of these studies [200-202] are summarized in Figure 4.13. Combined with molecular modeling techniques they were used to predict a possible conformation of the bound neurotensin [201].

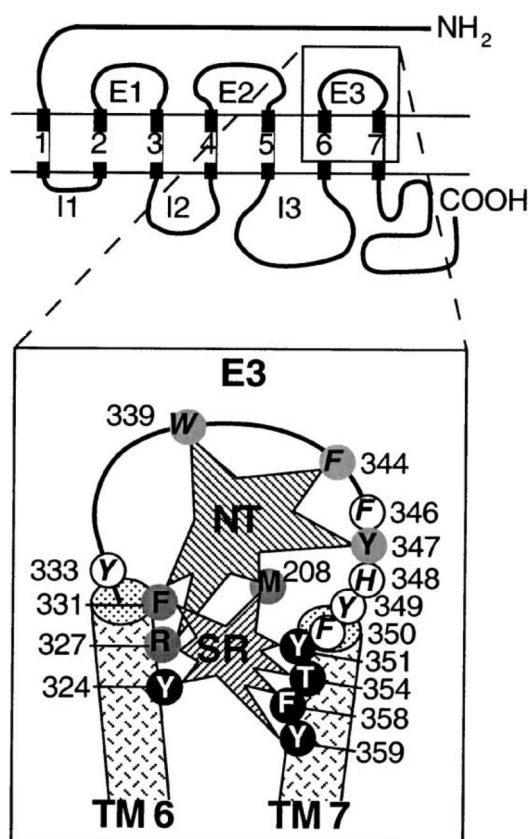


Figure 4.13. (top) Schematic representation of the rNTS1 binding site (shown as a rectangle) for both neurotensin (NT) and SR 48692 (SR). (bottom) The enlarged binding site depicting the actual residues involved in binding of NT only (light gray), SR only (black) and both NT and SR (gray). Reproduced from [202].

In *weakly bound complexes* of large receptors and small ligands, the ligand is in rapid exchange between the free and bound state. Standard high-resolution *solution-state NMR* spectroscopy of the free ligand allows then to study the structure of the bound ligand. If the bound and free form of the ligand are in fast exchange on the NMR time scale, average cross-relaxation rates are detected. Due to the much larger relaxation of the bound form (in the slowly tumbling complex), its contribution dominates the average cross-relaxation even in excess of the free ligand. The traditional transferred NOE (TrNOE) thus provides proton-proton restraints for the bound ligand [203, 204]. Similarly, cross-correlated relaxation rates

(which also depend linearly on the correlation time) can be used in transfer-type experiments. In this context, the transferred cross-correlated relaxation (TrCCR) experiment has been recently introduced [205, 206].

For example, the pituitary adenylate cyclase activating polypeptide (PACAP) hormone has a high-affinity ($K_d=3.1$ nM at pH 6.3) towards its GPCR receptor (the PACAP receptor) belonging to the type B family (glucagon/secretin receptor family). The interaction of this 27-residue peptide with the receptor hence cannot be studied by solution-state NMR. Alternatively, the C-terminal truncated form PACAP(1-21)NH₂, which binds with moderate affinity ($K_d=18$ μ M at pH 6.3) was recently studied [207], despite of the C-terminal region being important for binding to the receptor. In this case, the truncated ligand still acts as a full agonist, although with a much weaker binding.

A two-step process for peptide ligand binding to receptor has been proposed [208]. In this model, the ligand first binds nonspecifically to the membrane [209] and adopts a specific conformation which energetically favors receptor binding. Subsequent two-dimensional diffusion at the membrane surface leads to specific binding to the targeted membrane receptor upon a second conformational change. Peptide ligand conformations in micelles are generally regarded as appropriate models for their membrane bound form and the structure of the PACAP hormone was also determined in dodecylphosphocholine micelles [207]. Here the C-terminal residues of both receptor-bound PACAP(1-21) and micelle-bound PACAP are found in a α -helix conformation, while the N-terminal in the former case adopts a β -coil structure and is unstructured in the later. If the two-step model is correct, receptor binding induces conformational changes only at the N-terminus as shown in Figure 4.14. Similar studies on other GPCR-binding peptides (the bovine pancreatic polypeptide (bPP) [210] and the neuropeptide Y (NPY) [211]) interacting with micelles have been performed. In these cases, the interaction of the ligand with the receptor is not known, such that the two-step model cannot be confirmed.

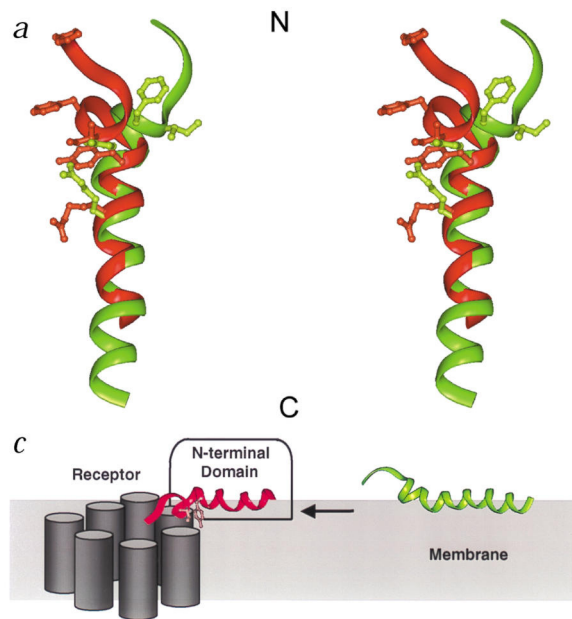


Figure 4.14. (top) Receptor bound (red) structure of PACAP(1-21) and micelle bound (green) conformation of PACAP as determined by solution-state NMR. (bottom) Two-step model of PACAP binding to its GPCR receptor. Reproduced with modification from [207].

Alternatively, *tightly bound complexes* can be studied with *diffraction techniques*, provided that high quality crystals are available. To date, only the structure of rhodopsin was obtained [198, 212], possibly due to the large amounts of protein that can be found naturally and purified from cellular membranes. In this case, the interaction with the ligand is very special as the chromophore retinal is covalently bound deeply in the hydrophobic core of the receptor.

In the absence of 2D or 3D crystals, multi-dimensional *solution-state NMR* spectroscopy may be employed to study ligand binding in high-affinity. In this case one is restricted to complexes that show sufficient fast rotational diffusion. The current size limit for studies of such tightly bound complexes is in the order of 40-50kDa, although recent developments in methods may push this limit further [213-219]. In addition to the much larger size of GPCRs, the need to suitably solubilize the protein increases the effective molecular weight substantially. Consequently, such systems represent a significant challenge to solution-state NMR.

Weight, molecular long-range order and sample homogeneity or solubility are of reduced concern to *solid-state NMR* spectroscopy.

4.2.3. Solid-state NMR methodology

Already available solid-state techniques can be successfully used to address focused questions on membrane proteins [2, 109, 220]. In the following we will describe the methodology we have developed to study high-affinity peptide binding to membrane proteins. Binding of ligands to membrane proteins is likely to induce structural changes in the membrane protein and/or the ligand, at least locally. In particular, small and flexible peptides usually lack a preferred conformation in solution, but adopt a distinct structure upon binding to receptor (or to the membrane). Our objective is to provide a HR-SSNMR approach that results in precise structural information on the bound structure of high-affinity peptide ligands.

Study of the bound ligand with solid-state NMR requires selective or multiply [^{13}C , ^{15}N] labeling of the ligand only. Given the generally extensive and expensive efforts to express and purify membrane proteins for biophysical studies, the uniform isotope labeling is preferred. Thus, experiments that result in complete resonance assignments and provide structural restraints using a single sample have to be employed. Uniform isotope labeling also enhances the selection of the ligand signal among the ^{13}C natural abundance signal, as shown below.

Maintaining membrane protein functionality usually requires detergent solubilization or reconstitution into phospholipid vesicles which may also limit protein concentration. Typically, low to very low amounts of functional membrane protein may be loaded in NMR rotors (with a total volume up to 80 μl , for example). Correspondingly, even if the protein/ligand ratio in the NMR sample is close to unity, small amounts of ligand (i.e. micromolar) have to be studied. ^{13}C spectroscopy, which is more sensitive and exhibits higher resolution, is usually preferred. However, a large signal background from natural abundance (NAB) 1% ^{13}C present in the sample (e.g. protein, detergents and/or lipids) is expected. Separating the ligand signal from the background signal has to be performed in order to unambiguously assign and analyze the resonances of interest.

In the case of neurotensin, a previous NMR study of uniformly [^{13}C , ^{15}N]-labeled NT has been performed [221]. Here, most of the ^{13}C resonances of the bound ligand were obscured by the background signal. For example, most backbone carbonyl and all $^{13}\text{C}_\alpha$ and $^{13}\text{C}_\beta$ resonances which relate to the peptide backbone conformation could not be observed. 1D

experiments were employed on both detergent solubilized and NTS1 bound neurotensin. Similarities in resonances were used to attribute several resonances to the NTS1 bound neurotensin. This approach does not, in a general way, allow complete and unambiguous assignment of the bound ligand. Moreover, there is no straightforward interpretation of the experimental data in terms of the 3D conformation of the bound ligand.

In general, only the relative size of ligand (L) and natural abundance background (NAB, including receptor, lipids, etc.) determine whether the signal of the bound ligand can be detected unequivocally. For example, simple ^{13}C isotope labeling has been sufficient for structural investigations of membrane proteins [152, 222, 223] or peptide/protein complexes [224] where $L/NAB > 10^{-2}$ M/M using single-quantum experiments.

To separate ^{13}C signal of the labeled ligand, two-spin correlation methods may be employed. For example, effective ^{13}C double-quantum filtering [225, 226] results in suppression of NAB signal up to 4 orders of magnitude, and allows for studies of systems where $L/NAB > 10^{-4}$ (M/M). This is due to the fact that the probability to find NAB neighboring ^{13}C - ^{13}C pairs is 0.01% (e.g. 1% times 1%). During the SSNMR experiment, extensive phase cycling that ensures suppression of direct ^{13}C signal must be employed. Experimental results on the [^{13}C , ^{15}N] natural abundance tripeptide Ala-Gly-Gly are shown in Figure 4.15. Here, 2Q excitation in the aliphatic spectral region results in the excitation of the (NAB) $^{13}\text{C}_{\alpha}$ - $^{13}\text{C}_{\beta}$ 2Q coherences of the alanine residue only. On the other hand, the much bigger signal (by two orders of magnitude) of the (NAB) $^{13}\text{C}_{\alpha}$ from the glycine residues (which lack a sidechain and therefore cannot contribute to 2Q signal) is suppressed beyond detection.

Thus, experiments employing 2Q techniques allow for studying the NT(8-13) (1kDa) and NTS1 (101kDa) complex in a detergent or lipid environment. As shown previously by SSNMR experiments and ab initio calculations [227], the resulting resonance frequencies are not only diagnostic for each individual peptide residue [112, 228] but they are also very sensitive to polypeptide backbone conformation [59, 105, 183, 228-231]. As we will show below, extending the 2Q filtering to two spectral dimensions and the study of a uniformly labeled version of NT(8-13) enables the derivation of the backbone structure from a single 2D NMR experiment.

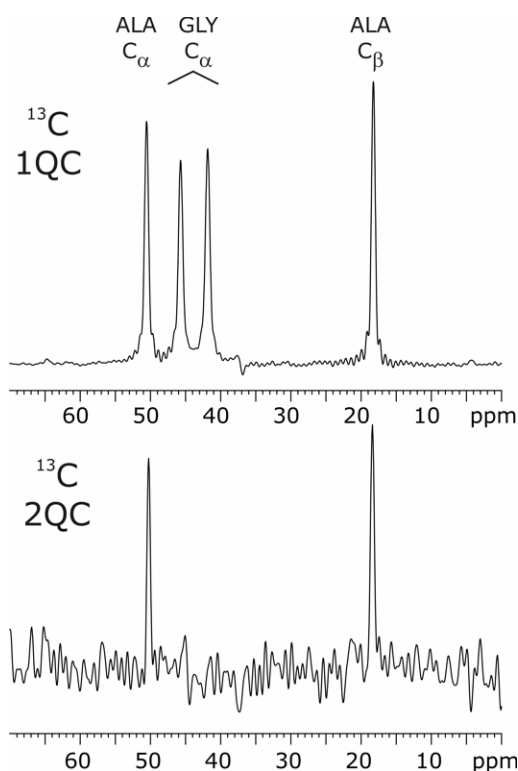


Figure 4.15. (top) A CP/MAS [17, 232] and (bottom) a 2Q filtered spectrum recorded on the natural abundance tripeptide Ala-Gly-Gly. Experiments were performed on a 600 MHz magnet at 7 kHz MAS and 5°C. The POST-C7 [43] dipolar recoupling scheme was employed for 2Q excitation and reconversion blocks.

Alternatively, ^{15}N - ^{13}C transfer steps may be employed within the solid-state NMR experiment. Nitrogen is not found in detergent and lipids. In polypeptides, it is found in NAB in even smaller proportions (0.3%) than ^{13}C . Thus, such (^{15}N , ^{13}C) experiments are equivalent to ^{13}C 2Q methods in terms of spectrally selecting the signal from the uniformly [^{13}C , ^{15}N]-labeled ligand.

Once the resonances of the labeled ligand are isolated, spectral assignment results from homonuclear ^{13}C - ^{13}C double-quantum and heteronuclear ^{15}N - ^{13}C 2D correlation experiments [6]. As already mentioned (see Section 0), $^{13}\text{C}_\alpha$ and $^{13}\text{C}_\beta$ chemical shifts may be readily interpreted in terms of the backbone conformation of the peptide ligand [59]. Thus the secondary structure of the bound ligand may be determined. Additional newly introduced experiments ([3], see also Sections 3.1 and 3.2) may further constrain the backbone and the sidechains of the bound ligand and result in its complete structure.

Sample preparation is a key point because the sensitivity of the experiment is not only dictated by the amount of labeled ligand (and correspondingly of NAB membrane protein).

For example, sample mobility diminishes the effective dipolar couplings and results in overall decreased sensitivity and/or additional requirements on the employed r.f. power. Temperature, especially in combination with the use of cryoprotectants (such as glycerol), therefore affects the sample mobility and may be a critical experimental parameter.

4.2.4. Sample preparation and experimental methods

Uniformly [^{13}C , ^{15}N]-labeled NT(8-13) (Figure 4.9) was prepared via solid-phase Fmoc-chemistry on a Wang resin (74 μmol scale) with BOP/HOBt activation using an ABI 433A (Applied Biosystems/Perkin-Elmer) peptide synthesizer (for a review on Fmoc chemistry, see e.g. ref. [233]). All isotope-labeled amino acid Fmoc derivatives were purchased from Cambridge Isotope Laboratories, Inc. (USA). The lyophilized isotope labeled hexapeptide was obtained in 40% yield. In addition, the uniformly [^{13}C , ^{15}N]-labeled pentamer NT(9-13) (Figure 4.9), which resulted from incomplete coupling of the last amino acid, could be readily isolated in 14% yield. For NMR experiments with solid-phase NT(9-13), 2 mg of the lyophilized peptide were loaded into a 4mm MAS rotor. To reduce sample heterogeneity, 1 μl of distilled water was added. For NMR experiments with NT(8-13), 0.1 mg of the peptide was dissolved in detergent-containing buffer (25mM TrisHCl pH 7.4, 5% glycerol, 1mM EDTA, 50 mM NaCl, 0.1% n-dodecyl- β -D-maltoside (LM), 0.2% 3-[(3-cholamidopropyl)dimethylammonio]-1-propanesulfonate (CHAPS), 0.04% cholesteryl hemisuccinate (CHS)) and placed into the MAS rotor.

Firstly, a sample containing purified, detergent-solubilized NTS1 in complex with uniformly [^{13}C , ^{15}N]-labeled NT(8-13) was prepared: *sample NT/NTS-1A*. The NTS-1A fusion protein MBP-rT43NTS1-TrxA-H10 (Figure 4.16) consisted of the E. coli maltose-binding protein (MBP), followed by the N-terminally truncated rat NTS1 (rT43NTS1), the E. coli thioredoxin (TrxA) and a decahistidine tail (H10) [234]. The receptor fusion protein was expressed in functional form in E. coli [234] (50 liters) and purified at large scale (2 purifications) in the presence of the detergents LM and CHAPS, and CHS, by immobilized metal affinity chromatography (60-ml Ni-NTA column), followed by a 10 ml NT column and anion exchange chromatography (5 ml HiTrap Q-Sepharose column), as described for the human NTS1 fusion protein MBP-huNTR-TrxA-H10 [235]. The Q-Sepharose eluate was

concentrated using a Centriprep-30 device (Amicon, 2.9 mg of functional receptor fusion protein available after concentration) and stored in liquid nitrogen. In preparation for the NMR experiments, the concentrated NTS1 fusion protein was diluted with detergent-containing buffer to give final concentrations of 25 mM TrisHCl pH 7.4, 5% glycerol, 1mM EDTA and 50mM NaCl. The receptor was concentrated at 3°C using Ultrafree-15 Millipore MWCO 50K and Microcon YM-30 (Amicon) devices. Protein determination [236] and [³H]NT binding analysis [237] of the concentrated sample gave a value of 7563 pmol/mg (565 µl at 3.68 mg/ml). A theoretical value of 10361 pmol/mg is calculated for MBP-rT43NTS1-TrxA-H10 (molecular mass of 96.5 kDa) assuming one ligand binding site per receptor molecule. 73% of the concentrated receptor preparation hence binds agonist. 2.3 µg uniformly [¹³C, ¹⁵N]-labeled NT(8-13) (molecular mass of 973 Da) was then added to the receptor preparation (0.37 mg) (agonist/receptor ratio of 0.6 M/M, based on total protein content) and incubated for 2 hours on ice. The NT(8-13)/receptor sample (100 µl) was placed into a 4mm MAS rotor, frozen on dry ice and subjected to NMR analysis. To titrate the amount of bound agonist, an additional 10µg of uniformly [¹³C, ¹⁵N]-labeled NT(8-13) were added gradually to the receptor preparation and analyzed. Sample NT/NTS-1A contains in total 0.37 mg of receptor protein and 12.3 µg of uniformly [¹³C, ¹⁵N]-labeled NT(8-13) (agonist/receptor ratio of 3.3 M/M, based on total protein content). Consideration of the ligand binding data gives an agonist/functional receptor ratio of 4.5 M/M in the sample NT/NTS-1A.

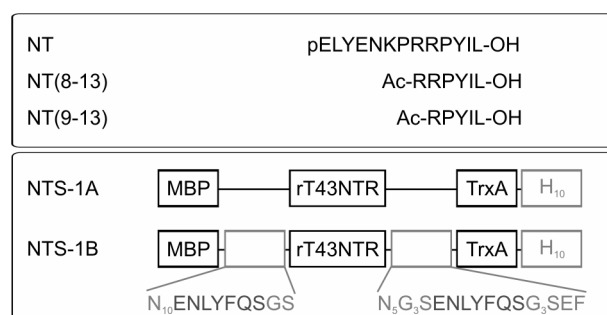


Figure 4.16. Schematic representation of the neurotensin and its receptor NTS1 fusion proteins. Amino acids are given in single letter notation (gray).

Subsequently, a sample containing lipid-reconstituted NTS1 in complex with uniformly [¹³C, ¹⁵N]-labeled NT(8-13) was prepared: *sample NT/NTS-1B*. The NTS-1B fusion protein MBP-N10-Tev-T43NTR-N5G3S-Tev-G3S-TrxA-H10 is shown schematically in Figure 4.16. The receptor fusion protein was expressed in functional form in *E. coli* (90 liters) and purified

(50ml Ni-NTA column, followed by a 10ml NT column; 5.2 mg purified protein from 3 purifications). For reconstitution into lipid vesicles, receptors (final concentration of 0.13 mg/ml) were incubated with LM-saturated brain polar lipids (Avanti Polar Lipids, final concentration of 0.4 mg/ml) for 4-5 hours at 4°C in a volume of 13 ml, followed by the addition of Bio-beads SM-2 (BioRad, 1.5 gram). The Bio-beads were exchanged 4 times over a time period of 3 days. Proteoliposomes were recovered by ultracentrifugation, and resuspended in 50 mM TrisHCl pH 7.4, 1mM EDTA at a protein concentration of 2 to 2.5 mg/ml. We estimated from [³H]NT binding assays [238] that 66% of the reconstituted receptors are accessible to ligand, with the remaining receptors either not binding agonist or having their ligand binding sites facing inside the lipid vesicles (data not shown). For the NMR experiments, 22 µg of uniformly [¹³C, ¹⁵N]-labeled NT(8-13) were added to 3.8 mg of reconstituted receptor fusion protein (molecular mass of 101 kDa) (agonist/receptor ratio of 0.6 M/M, based on total protein content). After incubation for 4 hours at 4°C, the sample was centrifuged at 40000 rpm (70 Ti rotor) for ½ hour and loaded as a pellet into a 4 mm MAS rotor. Consideration of the ligand binding data gives an agonist/functional receptor ratio of 0.9 M/M in the sample NT/NTS-1B.

All HR-SSNMR experiments were performed on a wide bore 600 MHz (¹H resonance frequency, Bruker/Germany) spectrometer using double (¹H, ¹³C) or triple (¹H, ¹³C, ¹⁵N) resonance MAS (magic angle spinning [8]) probe heads. Experiments on solid-phase uniformly [¹³C, ¹⁵N]-labeled NT(9-13) samples were conducted at 5°C, while experiments involving buffer/protein solutions and reconstituted sample NT/NTS-1B were performed at -80°C or -85°C. An MAS spinning rate of 7 kHz was utilized employing TPPM [10] at 110 kHz radio-frequency amplitude during free evolution and detection periods. Cross polarization [17, 232] (CP) experiments involved amplitude modulated radio-frequency fields [179]. Double-quantum filtering experiments were performed using the POST-C7 [43] dipolar recoupling scheme with 32-step phase cycling to suppress unwanted single-quantum signals. These phase cycles were tested by performing 2Q filtering experiments in the side chain region of the natural abundance tri-peptide Ala-Gly-Gly (as shown above). Additional test experiments on mixtures of labeled and unlabeled amino acids confirmed the suppression of single quantum signals by at least a factor 100 in the 2Q-spectra in line with the theoretical expectation. In Figure 4.17, details about the employed r.f. pulse scheme for the double-

quantum correlation experiments are presented. As a result, microgram peptide quantities can be reliably detected in the presence of a large background signal.

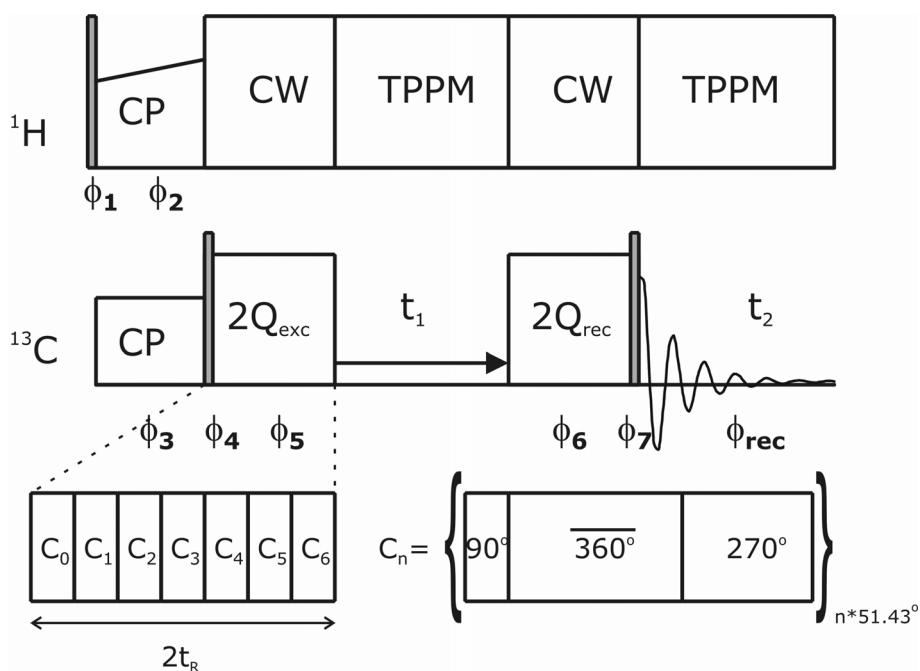


Figure 4.17. Schematic representation of the r.f. pulse sequence for the double-quantum correlation experiment. The POST-C7 [43] sequence was employed to recouple the homonuclear dipolar interactions. Here, 7 C_n elements were used for both excitation ($2Q_{\text{exc}}$) and reconversion ($2Q_{\text{rec}}$). High-power proton decoupling using CW (during recoupling periods) or TPPM (during evolution and acquisition times) was implemented. The phase cycle is given by: $\phi_1 = \{90^\circ\} \cdot 4 \{270^\circ\} \cdot 4$, $\phi_2 = \{0^\circ\} \cdot 8$, $\phi_3 = \{0^\circ\} \cdot 8$, $\phi_4 = \{270^\circ\} \cdot 8$, $\phi_5 = \{0^\circ\} \cdot 8$, $\phi_6 = \{0^\circ \ 90^\circ \ 180^\circ \ 270^\circ\} \cdot 2$, $\phi_7 = \{90^\circ \ 180^\circ \ 270^\circ \ 0^\circ\} \cdot 2$, $\phi_{\text{rec}} = \{0^\circ \ 270^\circ \ 180^\circ \ 90^\circ \ 180^\circ \ 90^\circ \ 0^\circ \ 270^\circ\}$. Additionally, all phases were incremented by 90° every 8 scans. For TPPI, $\phi_{3,4,5}$ were increased by 45° for each subsequent t_1 increment and ϕ_6 was adjusted as in [239] to ensure rotor synchronization of the recoupling sequence during excitation and reconversion.

For the construction of the backbone model of NTS1-bound NT(8-13), the TALOS [113] package was employed. As recently demonstrated in the context of fibrous peptides [105, 183, 231], TALOS analyses NMR chemical shifts assignments of three consecutive peptide residues employing a statistical homology search to arrive at an estimation of the dihedral angles of the peptide of interest. Within this framework, backbone dihedral angles of NT(8-13) can be obtained for residues Arg⁹-Ile¹² (see Table 4.1). For each residue, more than 80% of the predicted dihedral angles sets are consistent with an elongated peptide conformation. Additional information regarding ψ of Arg⁸ and ϕ of Leu¹³ is accessible from considering an extended sequence Pro⁷-NT(8-13)-X¹⁴ where Pro⁷ corresponds to the residue of the full length

agonist NT and X is varied. This approach predicts ψ (Arg⁸) = $-34 \pm 15^\circ$ and ϕ (Leu¹³) = $-104 \pm 16^\circ$ for X = Ala, Pro, Thr.

4.2.5. Results on NTS1-bound neurotensin(8-13)

Four preparations containing uniformly [¹³C, ¹⁵N]-labeled neurotensin peptides were analyzed by solid-state NMR: (a) solid-phase NT(9-13) as a spectroscopic reference, (b) NT(8-13) in detergent-containing buffer to investigate the structure of the free ligand, (c) NT(8-13) in complex with the purified, detergent solubilized receptor (sample NT/NTS-1A) and (d) NT(8-13) in complex with lipid-reconstituted NTS1 (sample NT/NTS-1B). The latter samples allow determining the conformation of NT(8-13) when bound to its GPCR with high affinity. For this purpose, NMR signals arising from microgram quantities of peptide ligand must be detected in the presence of large background signals resulting from buffer components glycerol and detergents (in sample NT/NTS-1A), or lipids (in sample NT/NTS-1B). Since $L/NAB < 10^{-2}$, conventional single-quantum experiments are not suitable to probe ligand binding in the current context (as shown in Figure 4.18).

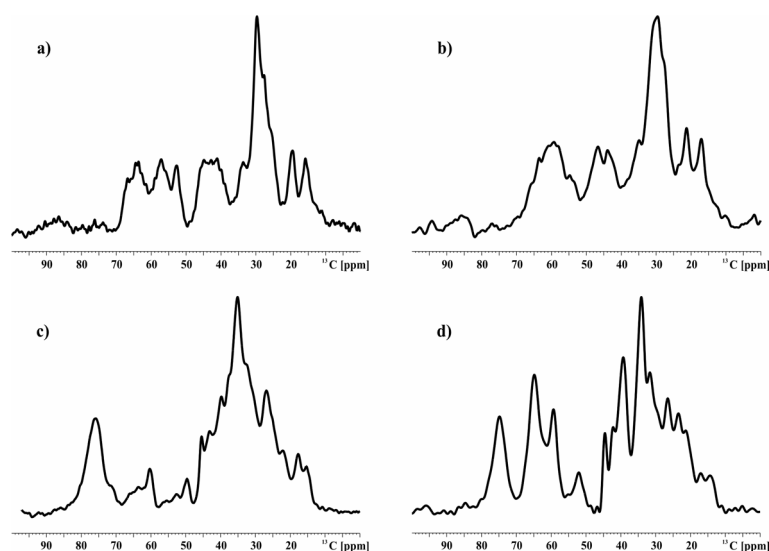


Figure 4.18. One-dimensional ¹³C ramped CP MAS spectra (side chain resonances) of (a) 2 mg of solid-phase NT(9-13) and (b) 0.1 mg of NT(8-13) in detergent-containing buffer. In (c) and (d), ¹³C data were recorded on NT(8-13) in complex with detergent solubilized receptor (sample NT/NTS-1A) and lipid-reconstituted NTS1 (sample NT/NTS-1B), respectively. TPPM decoupling (of 110 kHz) was employed during acquisition at a MAS rate of 7 kHz. Experiment (a) was performed using 64 scans while in (b, c and d) 1024 scans were taken.

Instead, double-quantum filtering methods that select for pairs of nearby ¹³C-¹³C nuclei (e.g. directly bonded) are mandatory. Measurements on the purified NTS1 fusion protein (0.27 mg

of functional receptor, sample NT/NTS-1A) in the presence of increasing amounts of NT(8-13) in microgram quantities gave 2Q signals that changed upon agonist addition (data not shown), reflecting adequate sensitivity of our 2QF experiments. One-dimensional spectra obtained on the four samples (as in Figure 4.18) by employing double-quantum filtering are shown in Figure 4.19. For the spectral identification of the individual peptide residues and the subsequent side chain ^{13}C resonance assignment, two-dimensional 2Q correlation experiments are compulsory and are discussed below.

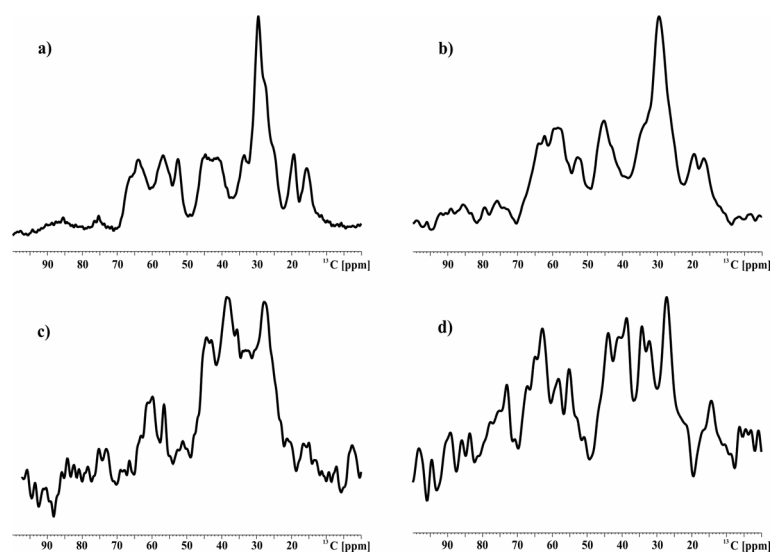


Figure 4.19. One-dimensional double-quantum filtered ^{13}C CP MAS spectra for (a) solid-phase NT(9-13) and (b) frozen NT(8-13) in detergent-containing buffer. (c) and (d) correspond to the NT(8-13)/receptor preparations NT/NTS-1A and NT/NTS-1B, respectively. In (a) and (b) 1024 scans were accumulated. In (c) and (d) results of 10k and 11k scans, respectively, measured at an MAS rate of 7 kHz, are shown.

Figure 4.20 contains results of a two-dimensional ^{13}C - ^{13}C 2Q correlation experiment for (a) free NT(9-13) and (b) NT(8-13) in detergent solution. The observed 2D patterns agree well with standard correlation maps [6, 59] expected from the NT primary sequence. The observed 1Q line width varies between 1 and 2.5 ppm and amounts to about 1.5 ppm for the majority of the observed correlations. For sensitivity reasons, except the spectrum in Figure 4.20.a, the results were obtained using a smaller number of t_1 increments. As a result, the 2Q line width is enlarged, but does not affect the spectral analysis presented here. If rare-spin polarization transfer is utilized, inter- and intra-residue correlation experiments are in general necessary to unambiguously assign the NMR resonances of larger polypeptides under MAS conditions [6].

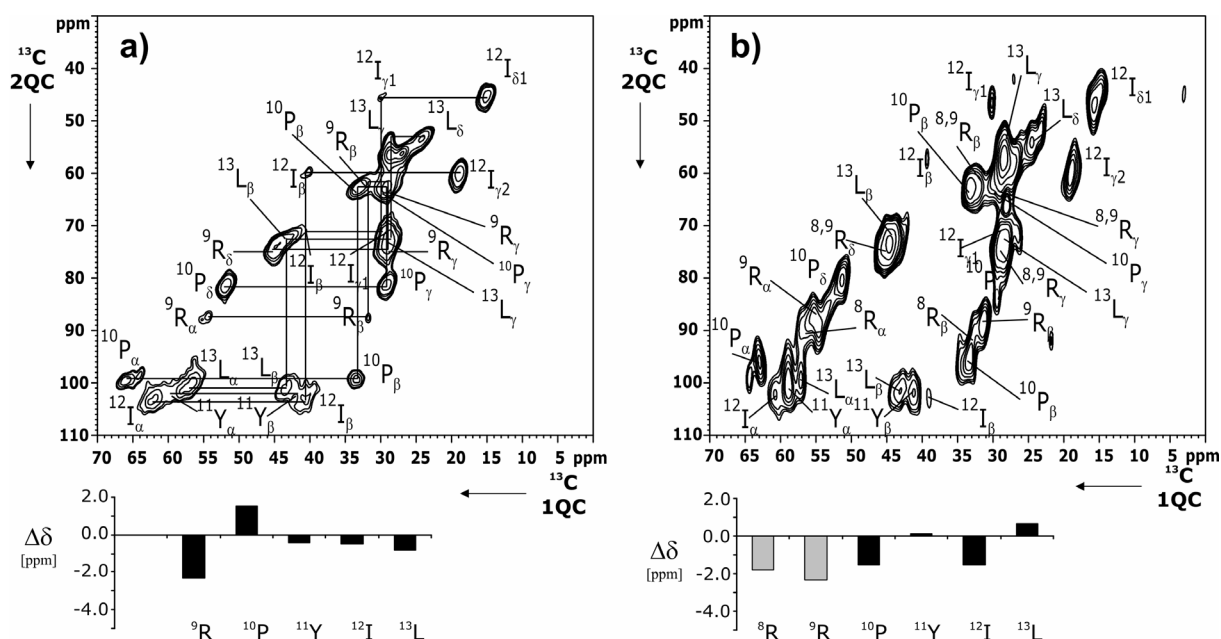


Figure 4.20. Two-dimensional ^{13}C - ^{13}C (2Q,1Q)-correlation experiments for (a) 2 mg of solid-phase NT(9-13) and (b) 0.1 mg of frozen NT(8-13) in detergent solution. In (a) and (b), 128 and 44 t_1 experiments, respectively, were recorded. Residue assignments are given in single letter notation; in (a), intra-residue side-chain correlations are indicated. Data shown in (a) and (b) result from 256 and 1536 scans, respectively. Below each 2D correlation spectrum, secondary chemical shifts $\Delta\delta$ as obtained from the chemical shift assignment are given. In (b) Arg⁸ and Arg⁹ $\Delta\delta$ values are shaded to indicate that secondary chemical shifts are here only tentatively assigned.

In the (2Q,1Q) correlation experiment considered here, resonance frequencies of two dipolar coupled spins detected in the 1Q dimension must resonate at the sum frequency along the ω_1 (2QC) axis. Hence, knowledge of the characteristic ^{13}C chemical shifts of the five (NT(9-13)) or six (NT(8-13)) involved residues and construction of the corresponding standard two-dimensional 2Q correlation map [6] is sufficient to assign resonances for all residues in the spectrum (shown in Figure 4.21). In particular, all backbone correlations involving C_α and C_β spins are easily identified (shown in Table 4.1). Knowledge of the isotropic chemical shift values can be utilized to interpret the observed spectra in terms of a three-dimensional backbone conformation of NT(9-13) and NT(8-13). For this purpose, we can calculate the parameter $\Delta\delta$ that reflects the conformation-dependent chemical shift of C_α and C_β resonances [59] and relates the experimentally observed carbon chemical shifts under MAS conditions to standard, isotropic random coil [131] values. These parameters are plotted in Figure 4.20 for the C-terminal residues of neurotensin. In particular, negative values of $\Delta\delta$ are consistent with large positive values of the backbone dihedral angle ψ , while $\Delta\delta > 0$ is indicative of helical (i.e. $\psi < 0$) peptide backbone conformations [59].

From Figure 4.20, we find that secondary chemical shifts for free NT(9-13) and NT(8-13) exposed to detergent-containing buffer are in general small and vary in sign. Significant changes in $\Delta\delta$ between both preparations are detected for Pro¹⁰, Ile¹² and Leu¹³. From the homonuclear correlation experiment described here, alone, we cannot assign the Arg side chain correlations to either Arg⁸ or Arg⁹. For this reason, Arg⁸ and Arg⁹ $\Delta\delta$ values are shaded in Figure 4.20.b. Notably, the Arg assignment obtained for NT(9-13) matches one set of (C_{α}, C_{β}) Arg chemical shifts detected in all other considered preparations (see below). Therefore, the corresponding correlations were tentatively assigned to Arg⁹. Irrespective of this ambiguity, we conclude from the data presented in Figure 4.20 that NT(9-13) and NT(8-13) remain largely unstructured in the absence of the receptor.

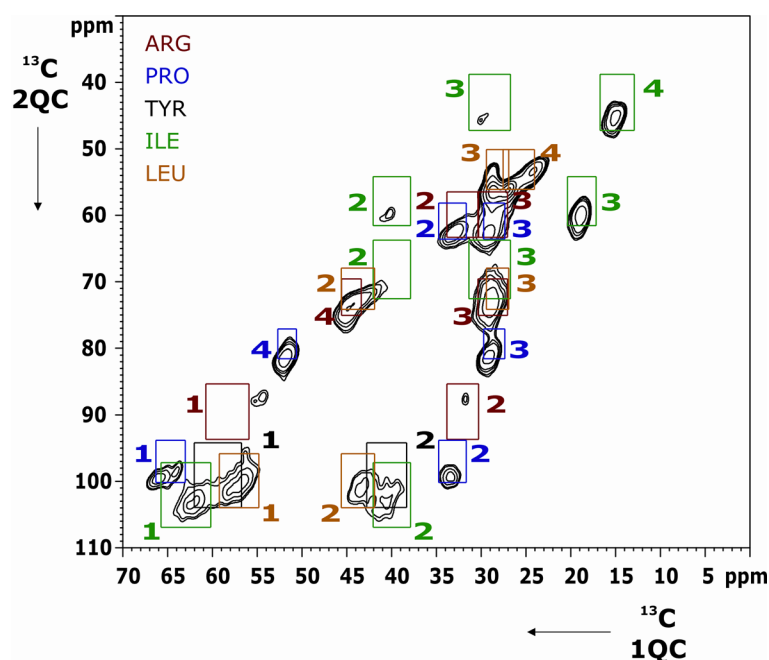


Figure 4.21. Statistical chemical shift analysis of the two-dimensional double-quantum correlation spectra of NT(9-13). The spectrum from Figure 4.20 is superimposed with rectangles that represent the expected chemical shift range for the individual resonances. The boxes are centered at the average chemical shifts and their size is determined by two times the standard deviation. These values were taken from the most recent entries in “Restricted set of amino acid chemical shifts” found in BioMagResBank [131]. The coloring of the rectangles denotes the individual residues (as in the upper-left corner of the spectrum) and the digits relate to: 1 – C_{α} , 2 – C_{β} , 3 – C_{γ} , 4 – C_{δ} .

Next, we investigated the interaction of NT(8-13) with purified NTS-1 receptor in detergent solution (sample NT/NTS-1A, Figure 4.22.a). The ratio of agonist/functional receptor in sample NT/NTS-1A is 4.5 M/M. Since the ligand-receptor interaction is characterized by a high binding affinity, a significant fraction of the detected peptide signal must have resulted

from receptor-bound NT(8-13) under these experimental conditions. In line with 1D results (in Figure 4.18 and Figure 4.19), we observe in the 2Q correlation experiment broad signals around 60 ppm and 30 ppm in ω_1 and ω_2 , respectively. These signals most likely stem from natural abundance 2Q contributions of the detergents and other buffer components. On the other hand, well separated side chain resonances and the (C_α , C_β) correlations of interest lie outside this range and can be identified (shown in Table 4.1). Again, these resonance assignments do not permit discriminating between Arg⁸ and Arg⁹ but they can be utilized to define conformation dependent chemical shifts $\Delta\delta$ summarized in Figure 4.22.a. Except for Leu¹³, all residues are now described by negative values of $\Delta\delta$.

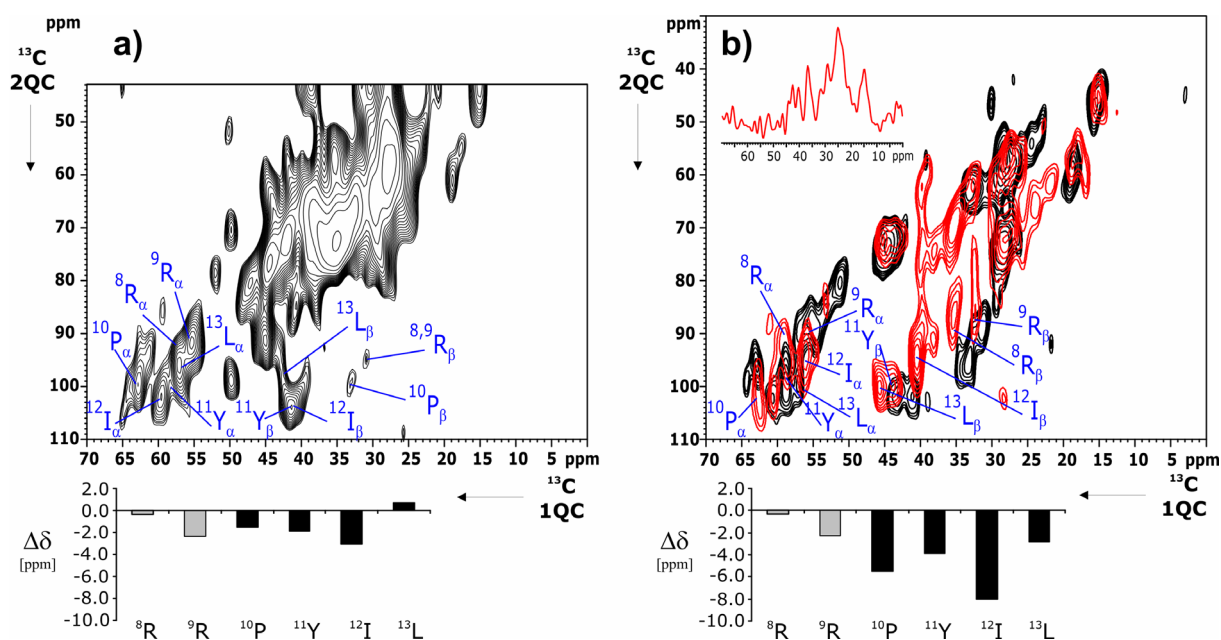


Figure 4.22. Two-dimensional ^{13}C - ^{13}C (2Q,1Q) correlation experiments for the two [^{13}C , ^{15}N]-NT(8-13)/receptor preparations NT/NTS-1A (a) and NT/NTS-1B (b, in red). In both cases, 32 t_1 experiments were recorded. Residue assignments are given in single letter notation. In (a) and (b) 13568 and 11136 scans, respectively, were accumulated for each t_1 experiment. Below each 2D correlation spectrum, secondary chemical shifts $\Delta\delta$ as obtained from the chemical shift assignment are given. In (a) and (b) Arg⁸ and Arg⁹ $\Delta\delta$ values are shaded to indicate that secondary chemical shifts are here only tentatively assigned. In (b), a 1D slice (in red) along the t_1 axis (54 ppm) and 2D results from frozen detergent-solubilized NT(8-13) (in black) are included for reference.

The interpretation of Figure 4.22.a in terms of secondary chemical shifts is not only influenced by the occurrence of strong detergent and buffer signals, but also by a relatively low NT(8-13) signal intensity as a consequence of the limited amount of purified receptor in the NMR rotor. To increase the amount of functional receptor and hence the amount of bound NT(8-13) for HR-SSNMR measurements, and to reduce the noise contributions from

detergent and buffer components, the NTS1 fusion protein was reconstituted into lipid, which allows for packing of the receptor at higher density (2.5 mg of functional receptors) into the NMR rotor. As a result, the amount of NT(8-13) (22 μ g) could be significantly increased in sample NT/NTS-1B. At a peptide/receptor molar ratio of 0.9M/M, we can assume that the NMR signals must predominantly result from bound NT(8-13) molecules. Figure 4.22.b shows a 2Q correlation pattern (in red) of the sample NT/NTS-1B. Consistent with 1D 2Q experiments (Figure 4.19), the major part of the spectrum is free of lipid correlations and the general (2Q, 1Q) correlation pattern for NT(8-13) can be readily identified. In particular, the detection of virtually all side chain resonances allows for an unambiguous identification of Ile¹² and Leu¹³ residues. The resulting C _{α} and C _{β} chemical shift assignments are given in Figure 4.22.b and Table 4.1.

		Arg ⁸	Arg ⁹	Pro ¹⁰	Tyr ¹¹	Ile ¹²	Leu ¹³
C _{α}	NT(9-13)	--	55.1 \pm 0.5	66.1 \pm 1.0	60.1 \pm 1.0	62.6 \pm 1.0	56.1 \pm 1.0
	NT(8-13)	58.1 \pm 0.5	56.1 \pm 1.0	64.1 \pm 1.0	60.1 \pm 0.5	61.6 \pm 1.0	58.1 \pm 1.0
	NT/NTS-1A	58.6 \pm 1.0	56.6 \pm 1.0	64.1 \pm 1.0	58.1 \pm 1.0	61.1 \pm 1.0	57.1 \pm 1.0
	NT/NTS-1B	60.1 \pm 1.0	56.1 \pm 1.0	62.6 \pm 1.0	58.6 \pm 1.0	55.6 \pm 1.0	56.6 \pm 1.0
C _{β}	NT(9-13)	--	31.1 \pm 0.5	33.1 \pm 0.5	41.6 \pm 1.0	40.1 \pm 0.5	43.6 \pm 1.0
	NT(8-13)	33.6 \pm 0.5	32.1 \pm 0.5	34.1 \pm 1.5	41.1 \pm 0.5	40.1 \pm 0.5	44.1 \pm 0.5
	NT/NTS-1A	32.6 \pm 1.5	32.6 \pm 1.0	34.1 \pm 1.5	41.1 \pm 1.0	41.1 \pm 1.5	43.1 \pm 1.0
	NT/NTS-1B	34.1 \pm 1.5	32.1 \pm 1.0	36.6 \pm 1.5	43.6 \pm 1.0	40.6 \pm 1.5	46.1 \pm 1.0
$\Delta\delta$	NT(9-13)	--	-2.3 \pm 1.0	1.5 \pm 1.5	-0.4 \pm 2.0	-0.5 \pm 1.5	-0.8 \pm 2.0
	NT(8-13)	-1.8 \pm 1.0	-2.3 \pm 1.5	-1.5 \pm 2.5	0.1 \pm 1.0	-1.5 \pm 1.5	0.7 \pm 1.5
	NT/NTS-1A	-0.3 \pm 2.5	-2.3 \pm 2.0	-1.5 \pm 2.5	-1.9 \pm 2.0	-3.0 \pm 2.5	0.7 \pm 2.0
	NT/NTS-1B	-0.3 \pm 2.5	-2.3 \pm 2.0	-5.5 \pm 2.5	-3.9 \pm 2.0	-8.0 \pm 2.5	-2.8 \pm 2.0
ψ		-34 \pm 15	136 \pm 25	146 \pm 15	131 \pm 19	134 \pm 24	--
ϕ		--	-134 \pm 31	-147 \pm 16	-121 \pm 22	-114 \pm 8	-104 \pm 16

Table 4.1. Chemical shift C _{α} and C _{β} assignments for free NT(9-13), NT(8-13) in detergent buffer, NT(8-13) in complex with detergent solubilized receptor (sample NT/NTS-1A) and NT(8-13) in complex with lipid-reconstituted NTS1 (sample NT/NTS-1B). All values are given in ppm. Dihedral angles (ψ , ϕ) as obtained from an analysis using TALOS are indicated at bottom for NTS1-bound NT(8-13).

For reference, results of NT(8-13) in detergent buffer are included in black and reveal that the side chain resonances do not significantly change upon receptor binding. In contrast, one observes that the spectral separation between C _{α} and C _{β} resonances diminishes considerably upon receptor binding. Correspondingly, the conformation-dependent chemical shifts are strongly negative (see Figure 4.22 and Table 4.1). Remarkably, results of Figure 4.22 lead to

similar secondary chemical shifts suggesting that both preparations reflect similar ligand-receptor interactions.

In the following, we discuss for the first time direct structural information of a high-affinity ligand bound to its GPCR. In the presence of its receptor NTS-1, the agonist NT(8-13) changes from a disordered state into a defined β -strand conformation. Our structural model of the receptor-bound ligand could represent a viable template for 3D pharmacophore studies [240].

Comparison of Figure 4.20 and Figure 4.22 allows for a qualitative structural interpretation of the observed chemical shift variations of NT(8-13). The size and the sign changes of $\Delta\delta$ imply that solid-phase NT(9-13) and NT(8-13) immobilized in detergent buffer remain largely unstructured. Our SSNMR data are hence in qualitative agreement with previous solution-state NMR studies of neurotensin in aqueous, methanol and SDS solutions [241, 242], which indicated an inherent conformational flexibility with no discernible elements of secondary structure in water and methanol. Notably, the observed chemical changes with respect to the random coil are largest for the Arg⁸-Arg⁹-Pro¹⁰ segment in buffer-detergent solution, consistent with previously postulated charge-charge interactions of the peptide with surrounding detergent molecules [241]. In the same manner, the observed NMR correlations can be analyzed for NT(8-13) in the presence of functional NTS-1 receptor (Figure 4.22). For both samples NT/NTS-1A and NT/NTS-1B, comparable chemical shift changes are observed. Except for Leu¹³, both signal sets indicate negative values of $\Delta\delta$. Due to the higher concentration of NT(8-13) and therefore higher signal to noise ratio in our NMR studies on NT/NTS-1B (Figure 4.22.b), we conclude that the peptide conformation (i.e. also Leu¹³) is described by negative values for secondary chemical shifts $\Delta\delta$. Knowledge of $\Delta\delta$ and the peptide primary sequence allow for an estimation of the backbone dihedral angles of NT(8-13) in the receptor-bound form. For this purpose, the chemical shift assignments of Fig. 3 were utilized as entry parameters within the TALOS [113] prediction routine. Similar to recent SSNMR studies on fibrous proteins [183, 231], the resulting dihedral angles can be utilized to construct a three-dimensional model of the backbone conformation of receptor-bound NT(8-13) which is shown in Figure 4.23. Our data suggest a β -strand conformation of the agonist bound to NTS-1. The current analysis does not yet permit the refinement of the

side chain conformations of NT(8-13). For this reason, all side chains in Figure 4.23 are shaded and only indicated for reference.

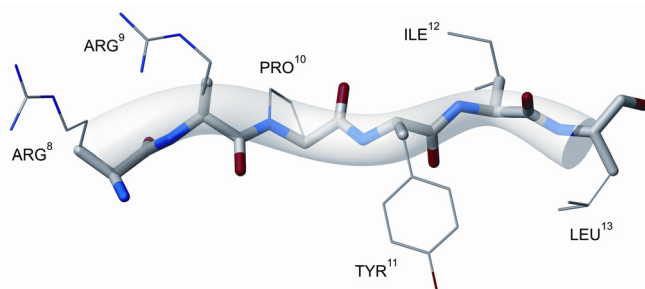


Figure 4.23 The backbone conformation of neurotensin(8-13) when bound to its GPCR NTS-1 as determined with solid-state NMR. Backbone dihedral angles as obtained from TALOS (see Table 4.1) and standard potentials were used to sample the allowed conformational space within CNS [243]. Here, a representative structure together with a transparent hose-shaped object reflecting the ensemble distribution of a set of 100 determined structures are shown. The data is consistent with an extended conformation, while the orientation of the sidechains (depicted with thin lines for reference only) can not be defined with the present data.

Previously published molecular modeling studies [244, 245] of NT bound to the NTS-1 receptor resulted in conflicting information about the presumed structure of the bound agonist. Pang et al. [244] predicted a compact conformation of NT(8-13), with a proline type I turn for the segment Arg⁹-Pro¹⁰-Tyr¹¹-Ile¹². The corresponding backbone angles (ϕ, ψ) for Pro¹⁰ and Tyr¹¹ would be given by (-60°, -30°) and (-90°, 0°), respectively, contradicting the SSNMR data presented here. More recently, mutagenesis and structure-activity studies combined with modeling techniques were utilized to predict the receptor binding site and the conformation of bound NT(8-13) [245, 246]. In this model, NT(8-13) adopts a linear backbone conformation in qualitative agreement with our SSNMR results. The receptor-NT(8-13) side chain contacts proposed by Barroso et al. [245] will be investigated by additional HR-SSNMR experiments that measure interatomic distances in the NT(8-13)-receptor complex.

To date, no structural information at the molecular level has been reported on neurotensin bound to its high-affinity receptor. We have utilized two-dimensional HR-SSNMR correlation experiments to elucidate the interaction of NT(8-13) with the rat NTS-1 receptor. The observed chemical shifts not only allow for a comparative study of the NT conformation in different chemical environments, but also enable a direct interpretation of the NMR signals in terms of the local backbone conformation of the neuropeptide.

Our results on solid-phase NT(9-13) and on NT(8-13) immobilized in a detergent environment indicate that the peptide remains largely unstructured in the absence of the receptor. When bound to NTS-1, the secondary chemical shifts observed in the solid-state considerably change for most of the amino acid residues of NT(8-13). The corresponding backbone torsion angles ψ are consistent with a β -strand arrangement of the agonist in complex with its receptor, both purified and reconstituted into lipid. Our selected NMR approach, utilizing chemical shift information only, was largely dictated by signal to noise considerations. The accuracy of the reported backbone dihedral angles could be further refined by dipolar double-quantum dephasing experiments [247] or by chemical shift-selective distance measurements. These experiments along with additional ^{15}N - ^{13}C and CHHC [84] correlation experiments are ongoing in our laboratory.

To our knowledge, the presented HR-SSNMR data provide for the first time direct experimental evidence for a distinct conformation of a neuropeptide bound with high affinity to its G-protein-coupled receptor, and demonstrate the general applicability of HR-SSNMR to probe ligand-receptor interactions in GPCRs. We have analyzed microgram ligand quantities in the presence of milligram receptor quantities, and demonstrate that HR-SSNMR experiments are suitable for structural studies on membrane protein systems for which structural information at the atomic level is currently lacking.

4.3. Confining the two ubiquinones in the Q_o pocket of bc_1

Solid-state NMR can yield insight into how membrane embedded enzymes and receptors are involved in energy and signal transduction through studies of selectively labeled proteins. MAS based methods allow to measure chemical shifts, internuclear distances and torsion angles of interest. Selective labeling can be achieved, for example, by adding labeled substrates, inhibitors, cofactors or ligands. Homonuclear techniques like RR (rotational resonance, [92]) and heteronuclear methods like REDOR (rotational echo double resonance, [156]) that recouple dipole-dipole interactions under MAS have been used to probe various internuclear distances in ^{13}C - ^{13}C , ^{13}C - ^{15}N , ^{13}C - ^{19}F and ^{15}N - ^{19}F spin pairs (see recent reviews [1, 2, 14]).

Although the structure of a membrane protein in a particular state may be solved, open questions will remain with respect to its biological functions. A good example is the cytochrome bc_1 complex which is part of the energy conversion apparatus of the respiratory and photosynthetic electron transfer chains. Found in the inner mitochondrial membrane of eukaryotic cells and in some aerobic photosynthetic bacteria, this enzyme catalyzes electron transfer from ubiquinol to cytochrome c , which is coupled to translocation of protons across the membrane [248]. X-ray structures of the complex isolated from bovine heart [249, 250], from chicken heart (see Figure 4.24, [251]) and from yeast [252] have been obtained.

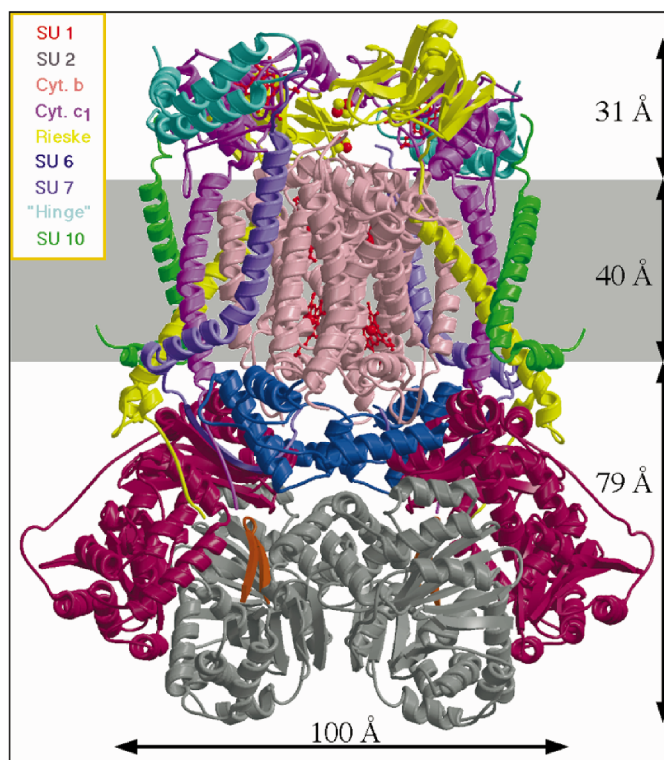


Figure 4.24. Ribbon view of the (dimer) chicken bc_1 complex spanning the (gray) membrane, as determined in [251]. Subunits are colored differently as shown in the inset and the important subunits are: core 1 (SU1), core 2 (SU2), cytochrome b (cyt. b), cytochrome c_1 (cyt. c_1) and the Rieske protein (Rieske).

The so called Q cycle (Figure 4.25) is the proposed mechanism for the coupling of the electron transfer to the proton transport across the membrane. The cycle starts with two molecules of ubiquinol that bind to the oxidation reaction centre Q_o and are subsequently oxidized to ubiquinone. As a result, four protons and four electrons are released in cascade. The four protons diffuse towards the cytosolic side of the membrane. Two of the electrons flow via the Rieske 2Fe-2S cluster to the cytochrome c_1 and will reduce two molecules of cytochrome c which are freed and diffuse away from the enzyme. The other two electrons flow via cytochrome b_L and b_H to the reduction site Q_i where will reduce a molecule of ubiquinone to ubiquinol. The two protons needed are taken up from matrix side of the bc_1 complex. At the end of the cycle, one molecule of ubiquinol is oxidized to ubiquinone, two molecules of cytochrome c are reduced and two protons are transported outside the matrix.

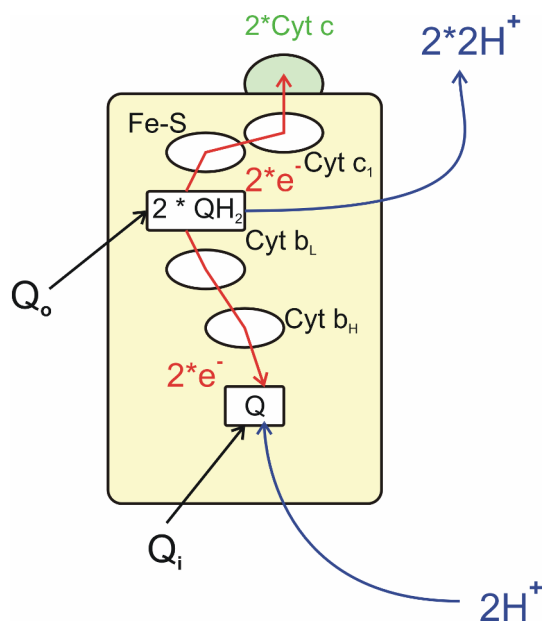


Figure 4.25. The mechanism for the coupling of electron transfer to transmembrane proton transport: the Q cycle. Abbreviations used: ubiquinone (Q), ubiquinol (QH₂), Rieske 2Fe-2S cluster (Fe-S), cytochrome (cyt).

The existence of the two quinol reduction and quinone oxidation centers (Q_o, Q_i, respectively) was also confirmed by the determination of site-specific inhibitors like stigmatellin for Q_o and antimycin for Q_i. Some of their natural substrates or inhibitors bind in high affinity and are observed in X-ray structures if they are added in stoichiometric excess during crystallization ([251], Figure 4.26). This is not the case for the binding of ubiquinol in the Q_o pocket where ubiquinone binds with low affinity. Only recently, EPR [253] and solution-state NMR [254] studies showed that two ubiquinone molecules bind simultaneously to the Q_o pocket. Up to date, there is no direct evidence for a double occupancy and the relative orientation of the two molecules in the rather spacious pocket Q_o remains unknown.

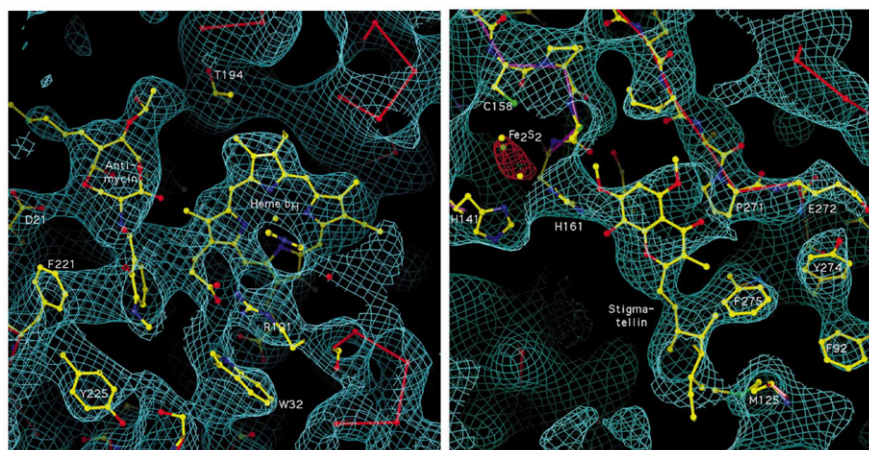


Figure 4.26. The electron-density maps for the inhibitors antimycin (left) and stigmatellin (right) binding sites as found in the chicken cytochrome bc_1 complex [251].

Whenever the distance between two nuclear spins is to be determined by solid-state NMR under MAS, several factors have to be properly addressed. (1) Generally, the range of determinable distances is dictated by the nature of the spins: ^{13}C - ^{13}C and ^{13}C - ^{15}N distances may be probed up to a few angstroms. The range of the detectable distances can only be extended by making use of nuclei with higher gyromagnetic ratios like ^{19}F . (2) In biological applications, especially related to membrane protein applications where large amounts of either detergents or phospholipids are present, the signal resulting from ^{13}C nuclei in natural abundance may obscure the signal of interest. Since dipolar recoupling sequences are being used to determine the distance, they can be conveniently combined with double-quantum filtering techniques that suppress natural abundance signal. (3) In many cases, the size of other spin interactions, like chemical shielding anisotropy, couplings to other spins (^1H) or other relaxation mechanisms, may further interfere with the transfer methods used to probe distances. We shall address some of these points in the following and apply the proposed experiments to the bc_1 complex.

4.3.1. Test experiments

Under MAS, r.f. irradiation can be used to restore homonuclear and heteronuclear dipole-dipole couplings via manipulation of the spin variables in the Hamiltonian. R.f.-driven recoupling techniques that rely on the excitation of double-quantum or zero-quantum coherences and result in the determination of internuclear distances, torsion angles or relative orientation of CSA and/or dipolar tensors have been proposed. Current applications to

biological problems therefore heavily rely on the efficiency with which 2Q coherences can be generated. The first r.f.-driven recoupling techniques like DRAMA [255], RFDR [155] and USEME [256] were sensitive to isotropic chemical shift differences, the size of the CSAs of the recoupled spins, r.f. inhomogeneities, etc. Later, r.f. sequences like RIL [257], MELODRAMA [52] and DRAWS [258] were designed to correct some of these problems (e.g. improved bandwidth) but their theoretical 2QF efficiency was still about 50%. The newest proposed sequences, which are built on symmetry properties (C7 [259], POST-C7 [43] and SPC5 [44]) are compensated for high-order error terms and perform broadband homonuclear dipole-dipole recoupling sequences. Importantly, they belong to the γ -encoded family of recoupling sequences (first implemented in HORROR [27]) and exhibit therefore improved theoretical 2QF efficiencies (73%).

When applied to pairs of spins (like ^{13}C - ^{13}C) with small CSA, sequences like SPC5 [44] (which is also moderate with respect to r.f. amplitude requirements) are the best choice for reintroducing dipolar couplings in high efficiency. When probing large distances, the influence of residual ^{13}C - ^1H couplings or r.f.-induced probe-head heating have to be considered. Recently a constant-time version of a RFDR-based double-quantum filtered experiment was proposed [129]. Here, the usual double-quantum excitation and reconversion block is supplemented, up to a constant time with a refocused dipolar evolution period. In this way, dipolar evolution curves can be recorded with reduced influence from residual carbon-proton couplings, transverse relaxation processes or probe heating.

Next, we apply the constant-time double-quantum filtered experiment using the SPC5 sequence (SPC5 CT-2QF, Figure 4.27.b) and compare the results with normal 2QF experiments (SPC5 2QF, Figure 4.27.a) in the high-power decoupling regime. In Figure 4.29, results are shown on uniformly ^{13}C , ^{15}N labeled valine for both SPC5 2QF and CT-2QF for increasing ^1H decoupling r.f. fields. As expected, the CT-2QF version of the experiment shows reduced dependence on the applied proton decoupling. The usual SPC5 2QF experiment resembles very well full quantum mechanical simulations for ^1H decoupling fields exceeding 80 kHz. The 2Q buildup was simulated for a pair of ^{13}C spins with selected internuclear distances using a GAMMA-based [16] program. The results are shown in Figure 4.28.

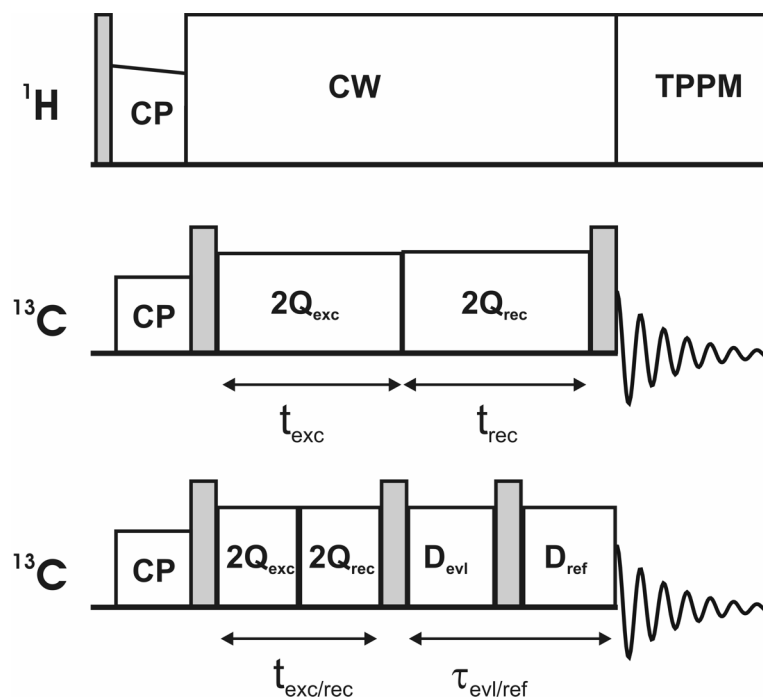


Figure 4.27. (a) The pulse sequence for a double-quantum filtered experiment using the SPC5 [44] sequence for 2Q excitation and reconversion (t_{exc} and t_{rec}). A 2Q buildup curve is normally obtained by mapping out the signal intensity as a function of the total time $t_{\text{exc}}+t_{\text{rec}}$. (b) A constant-time version of the previous experiment. Two blocks (D_{evl} and D_{ref}) using the same dipolar recoupling sequence (e.g. SPC5) are added to the sequence before acquisition for the times t_{evl} respectively t_{ref} . A $\pi/2$ pulse is used in between them such that the dipolar evolution that takes place during D_{evl} is refocused during D_{ref} . During the measurement of the 2Q buildup, the total time $t_{\text{exc}}+t_{\text{rec}}+t_{\text{evl}}+t_{\text{ref}}$ is kept constant. CP [17, 18] is used to create initial ^{13}C transversal magnetization. Proton CW [11] and TPPM [10] decoupling are employed during ^{13}C homonuclear dipolar recovery sequences and respectively acquisition.

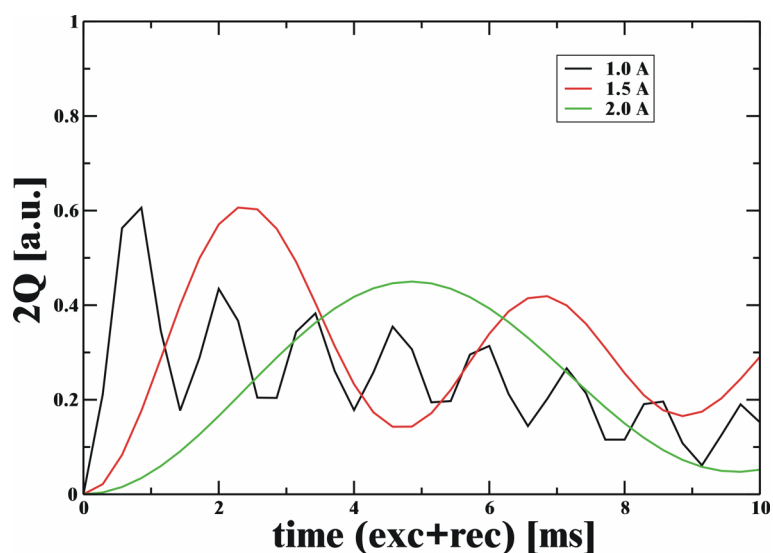


Figure 4.28. 2Q buildup simulated for a pair of ^{13}C spins separated by distances of 1.0 Å, 1.5 Å and 2.0 Å (as shown in the inset). The SPC5 sequence was used for 2Q excitation and reconversion; the simulation included the phase cycling as implemented in the experiment to acquire selection of double-quantum coherences. CSA and scalar couplings were not included into the simulations.

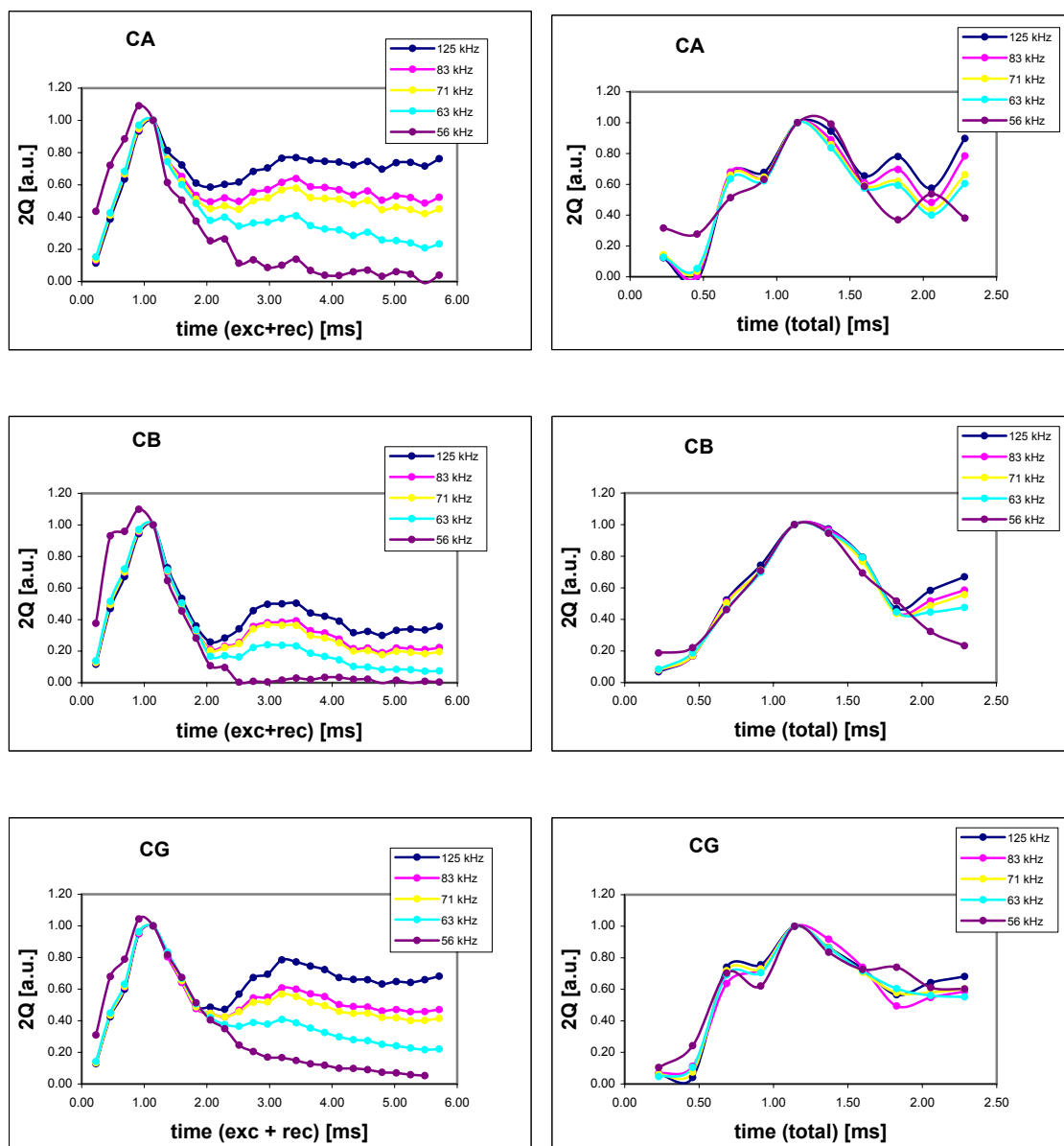


Figure 4.29. 2QF (left) and CT-2QF (right) experiments performed on uniformly ^{13}C , ^{15}N labeled valine. For dipolar recoupling the r.f. sequence SPC5 [44] was employed. Total mixing time in the CT-2QF filtered experiment was set to 8 rotor periods. Experiments were performed on a 600 MHz magnet at 7 kHz MAS and 5°C . CW ^1H decoupling r.f. fields during SPC5 recoupling trains on the ^{13}C used are shown in the insets; during acquisition decoupling using ^1H 80 kHz TPPM was employed. The intensities of C_α (CA), C_β (CB) and C_γ (CG) are monitored (both $\text{C}_{\gamma 1}$ and $\text{C}_{\gamma 2}$ exhibit identical behavior). Intensities are normalized to unity for maximum 2Q efficiency (found for excitation time of 2 rotor periods).

Alternatively, we can analyze the ^1H decoupling dependence of the transfer profile for a ^{13}C - ^{13}C spin pair using a SPC5 DQF experiment both experimentally and theoretically. In Figure 4.30.a, under 7 kHz MAS, the intensity of the 1Q signal of uniformly ^{13}C , ^{15}N labeled valine after a 2Q filtering block (set to result in maximum excitation for directly bonded carbons) was monitored for the C_α , C_β and C_γ spins as a function of ^1H r.f. decoupling. Experimentally

it is observed that ratios ^1H decoupling r.f. field to ^{13}C recoupling r.f. field exceeding about 2.5, full efficiency is expected for the SPC5 2QF scheme.

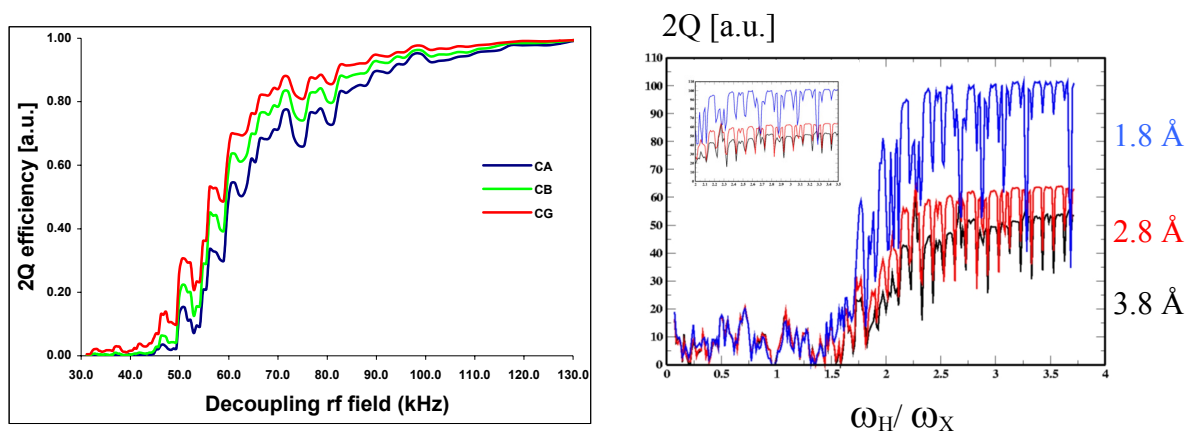


Figure 4.30. (a) 2Q efficiency monitored during a 2QF experiment as a function of the ^1H CW decoupling field during 2Q excitation and reconversion blocks. The SPC5 recoupling sequence was used and 2Q excitation and reconversion total time was set to 8 rotor periods (which yields maximum 2Q efficiency for strong ^1H CW decoupling fields). See Figure 4.29 for further experimental details. Similar behavior is observed for all spins C_α (CA), C_β (CB) and C_γ (CG) which are shown in the inset; full 2Q intensity acquired at high ^1H CW fields was normalized. (b) Simulations of the 2Q ^{13}C - ^{13}C efficiency in a CCHH spin system as a function of the ^1H CW decoupling field. In the GAMMA-based simulation program each of the two carbons was considered to have a directly attached proton while three CC distances were used (1.8, 2.8 and 3.8 Å).

The influence of ^1H - ^{13}C couplings during the ^{13}C - ^{13}C 2Q filtering can be also examined theoretically. For this purpose, the SPC5 2Q filtering efficiency was investigated in a four spin system ^1H - ^{13}C - ^{13}C - ^1H containing all (homo and heteronuclear) dipolar couplings as a function of the ^1H decoupling field for several ^{13}C - ^{13}C distances (Figure 4.30.b). Interestingly, when the 2QF efficiency is monitored as a function of the ratio ^1H decoupling r.f. field to ^{13}C recoupling r.f. field ω_H/ω_X , maximum efficiency is also reached for $\omega_H/\omega_X > 2.5$ in line with experimental results.

We conclude that, with respect to residual proton-carbon couplings during carbon-carbon recoupling sequences, the CT-2QF experiment is equivalent to a normal 2QF experiment under high-power decoupling (ratios ^1H to ^{13}C r.f. fields typically exceeding 2.5). We exemplify this result on the tripeptide Ala-Gly-Gly doubly ^{13}C labeled at C_α position of the two glycines. The internuclear distance in this case is calculated to 3.8Å and is fixed (e.g. does not depend on the torsion angles). The 2Q build-up curve obtained using SPC5 compared with quantum mechanical simulations involving a two ^{13}C spin system is shown in Figure

4.31. The experimental results obtained under high-power decoupling (90 kHz) agree well with the corresponding simulation without any further consideration of proton-carbon couplings.

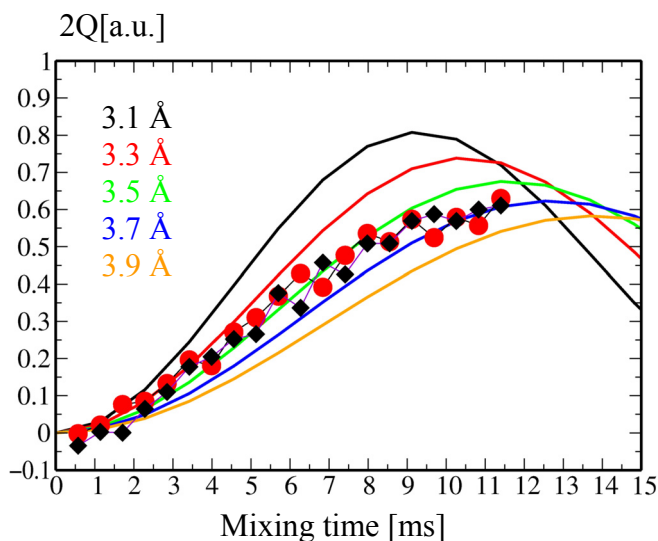


Figure 4.31. 2Q buildup measured on a doubly labeled Ala- $^{13}\text{C}_\alpha$ Gly- $^{13}\text{C}_\alpha$ Gly sample. The 2Q filtered experiments were performed using SPC5 as the ^{13}C recoupling sequence for total (e.g. 2Q excitation and reconversion) times shown. 2Q efficiency was monitored as a function of this time and normalized to direct ^{13}C CPMAS signal. Intensities for both spins are shown as red circles and black diamonds. See Figure 4.29 for further experimental details. Simulations of the expected 2Q buildups are shown for ^{13}C - ^{13}C pairs of spins separated by selected distances shown in the inset with different colors. The 2Q filtering (the equivalent of the selection of 2Q coherences by phase cycling in the real experiment) was fully included in the simulation program.

The r.f. sequence of choice has to be insensitive not only to large isotropic chemical shift differences and r.f. inhomogeneities, but also to large CSA if present. R.f.-driven sequences like C7 and SPC5 fail to recouple the dipolar interaction in such cases, and use of other, less efficient, sequences has to be made. Here we resort to the previously used RFDR sequence in the context of CT-2QF. The experimental setup was tested on a sample of alanine, ^{13}C labeled at the carbonyl position. We have prepared a polycrystalline sample where, according to the L-alanine crystal structure [260], a shortest intermolecular distance of 4.16 Å is expected between carbonyls. The experimental 2Q buildup curve is shown in Figure 4.32.a. For comparison, the corresponding buildup curve was also recorded for uniformly ^{13}C labeled glycine – here the internuclear ^{13}C - ^{13}C distance is 1.5 Å (directly bonded carbons) and the buildup curve reaches its maximum at a DQ excitation time of about 1ms.

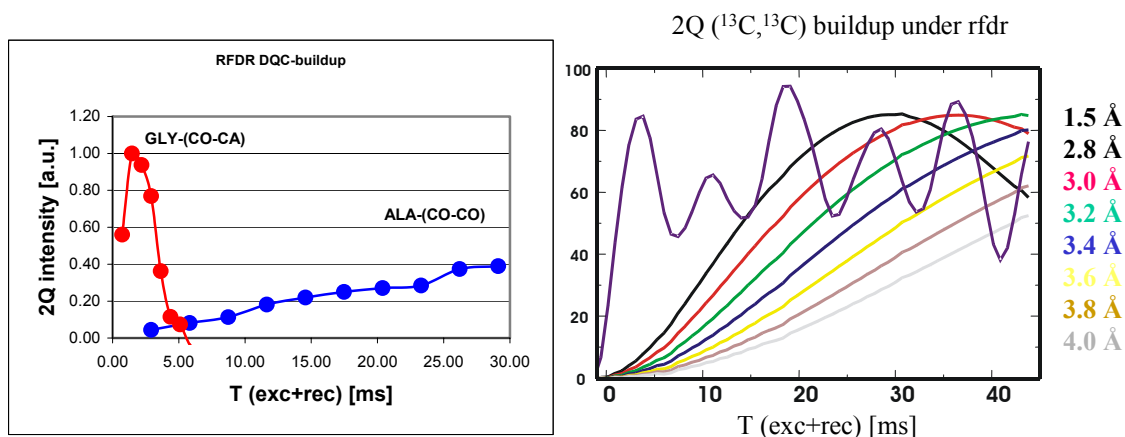


Figure 4.32. (a) 2Q filtered buildup for a spin pair CO-CA (red) in uniformly labeled glycine and CO-CO (blue) in a sample of [¹³CO] labeled Ala using RFDR as the recoupling sequence. Intensities are normalized to the direct CPMAS signal and the distances between the pairs of spins are 1.5Å respectively 4.16Å. CW ¹H decoupling fields of 80 kHz were used during ¹³C RFDR trains and ¹³C RFDR- π pulses were set to 50 kHz. Experiments were performed on a 600 MHz magnet at 7 kHz MAS and 5° C. (b) The 2Q efficiency for a ¹³C-¹³C spin pair using RFDR as calculated using a simulation program in GAMMA. A CSA anisotropy of $\delta=66$ ppm was used for both spins and different CC distances were considered (depicted with different colors in the plot).

In Figure 4.32.b, quantum mechanical simulations (performed in GAMMA) of the RFDR 2Q buildup are presented for a ¹³C two spin system with CSA anisotropy of 66 ppm (10 kHz under a 600 MHz magnet). This spin system analogous to the Ala sample has been considered under a wide range of distances (from 1.5 Å to 4.0 Å). Qualitative agreement between experimental data and quantum mechanical simulations for the expected distance of 4.16 Å is observed.

4.3.2. Applications to bc₁

Samples of lipid reconstituted bc₁ containing ubiquinone molecules singly ¹³C labeled at various positions were investigated. Only the two ubiquinone molecules bound at the Q₀ oxidation pocket will give rise to 2Q filtered signal, as all the other molecules are too far away from each other as they diffuse free in the liposome preparation. Moreover, signal from natural abundance ¹³C found in the lipids and the bc₁ complex is filtered out by the 2Q filtering resulting in spectra exhibiting only the resonances of the labeled ¹³C sites of the bound ubiquinones. The 2Q buildup curves of these resonances translate directly in distance constraints for the relative orientation of the two molecules in the Q₀ site.

For example, the sample obtained using [5-¹³C] labeled ubiquinone (shown in Figure 4.33) was investigated. A CPMAS spectrum recorded at -85°C, 7 kHz MAS on a 600 MHz magnet is shown in Figure 4.34.a. Large contributions from natural abundance ¹³C are seen in the spectrum while the resonance of interest is obscured.

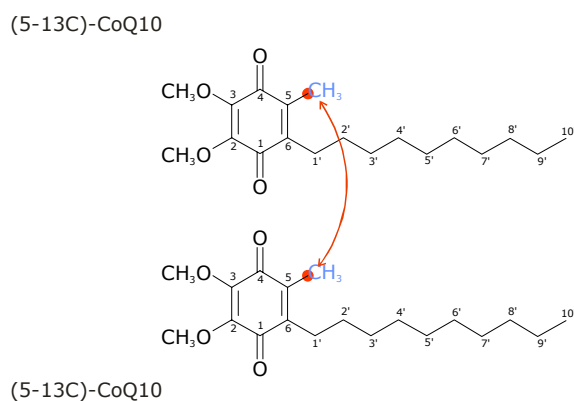


Figure 4.33. Example of a ¹³C labeling pattern used for ubiquinone, in this case [5-¹³C] labeled ubiquinone. The intermolecular ¹³C-¹³C distance between the two molecules to be probed in the Q₀ pocket of the cytochrome bc₁ complex is shown in red.

A 2Q filtered spectrum is also shown in Figure 4.34 for a chosen 2Q mixing time of 4.5ms. Here only one resonance is found in the spectrum at 32 ppm and downfield from the expected frequency of a methyl carbon. To test the validity of our experiments we have prepared a sample where the Q₀ inhibitor stigmatellin was added to the sample. Because it is a strong competitor for ubiquinone at the Q₀ site of bc₁, we expect that no ubiquinone molecules will be found in the oxidation pocket. Experimentally, this concept is validated by the disappearance of the 2Q filtered signal in the previously described sample (Figure 4.35).

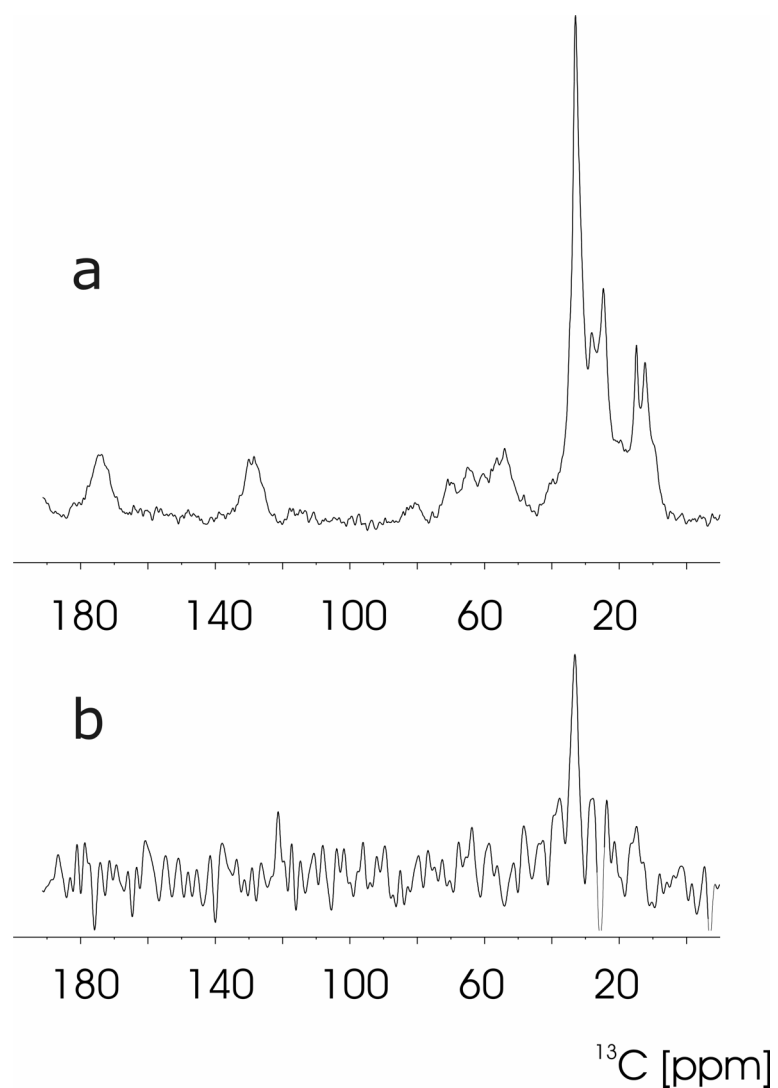


Figure 4.34. (Top) CPMAS spectrum recorded on a sample containing the complex bc_1 reconstituted in lipids and $[5\text{-}^{13}\text{C}]$ labeled ubiquinone. Spectrum was recorded on a 600 MHz magnet at 7 kHz MAS and -80°C . (Bottom) the 2Q filtered recorded on the same sample and same conditions using SPC5 for ^{13}C - ^{13}C recoupling (4.5 ms excitation and reconversion time in total). Only the resonance of the $5\text{-}^{13}\text{C}$ of ubiquinone is found in the spectrum due to the 2Q filtering of the natural abundance (1Q) signal.

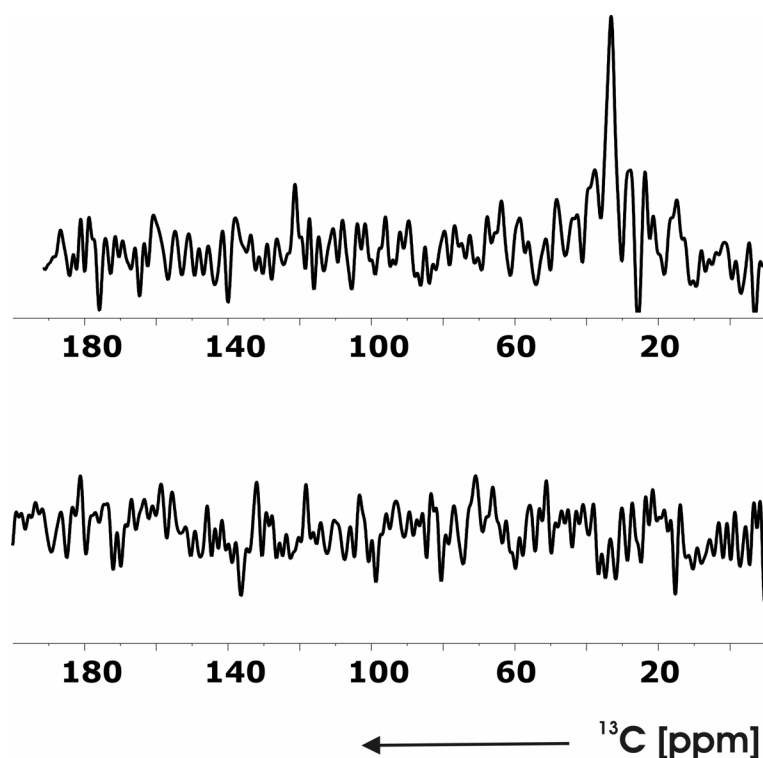


Figure 4.35. 2QF spectra as in Figure 4.34.b on a sample of reconstituted bc_1 with ubiquinone. Two samples without (top) and with (bottom) the Q_o ubiquinone inhibitor stigmatellin were analyzed. In the latter case, the signal from the labeled ubiquinone is lost due to the fact that ubiquinone cannot bind to the Q_o pocket.

The measurement of the 2Q buildup curve and subsequent comparison to the simulated curves is shown in Figure 4.36. The experimental data is consistent with an intermolecular {5-CoQ10}-{5-CoQ10} distance of 3.0 ± 0.2 Å. Additionally, samples with [2'- ^{13}C] labeled ubiquinone and stoichiometric mixture of [5- ^{13}C] and [2'- ^{13}C] labeled ubiquinone were used to determine additional distance constraints. These parameters are summarized in Table 4.2. In these cases, 2Q buildup curves could not be recorded due to low signal-to-noise, but internuclear contacts were nevertheless probed.

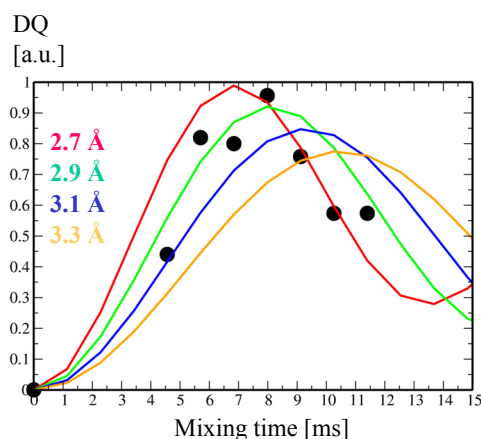


Figure 4.36. The 2Q buildup (experimental points shown as black dots) obtained by performing the 2Q filtered experiment in Figure 4.34 and monitoring the 2Q efficiency as a function of the total (2Q excitation and reconversion) time. As in Figure 4.31, simulations of the 2Q buildup curves are shown for the CC distances close to the best fit.

Samples with [1-¹³C] or [4-¹³C] labeled ubiquinone and with stoichiometric mixture of [1-¹³C] and [4-¹³C] were also studied. Here, knowledge of CSA tensor is necessary to perform accurate quantum mechanical simulations. We determined the CSA tensor anisotropy $\delta=113$ ppm and asymmetry $\eta=0.53$ by measuring the amplitude of sidebands at different MAS spinning rates (Figure 4.37) and direct comparison with plots of sideband intensities expected for $\frac{1}{2}$ -spins [261]. For the spin pairs involving carbonyls, we did not detect any signal after 2Q filtering. These experimental observations could be explained by the following reasons: (1) too large internuclear distances which result in very low efficiencies for the current 2Q excitation times, (2) a shift of resonances or excessive relaxation due to the nearby [2Fe-2S] paramagnetic center. We conclude that the corresponding distances have to be larger than the detectable 4.0 Å upper limit of our experiments.

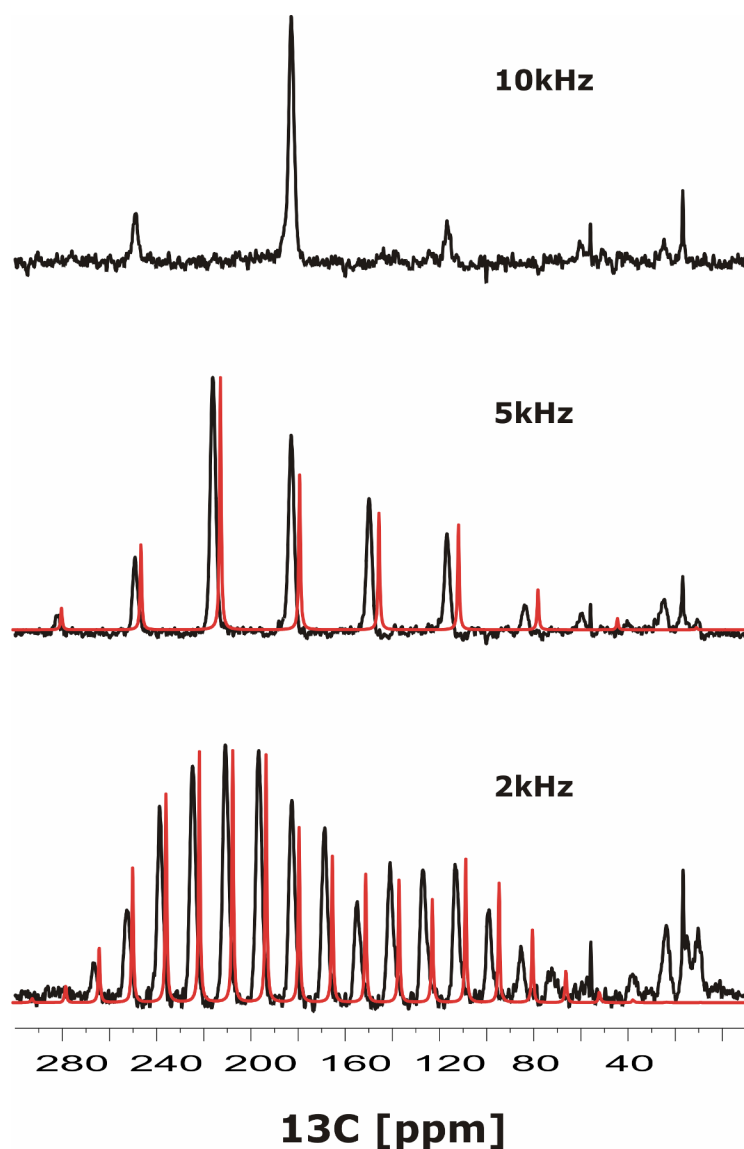


Figure 4.37. CPMAS experiments recorded on a sample containing [4- ^{13}C] labeled ubiquinone at different MAS rates (10, 5 and 2 kHz). The intensities of the spinning sidebands were used to calculate the CSA tensor of the [4- ^{13}C] spin as in [261]. Simulation of the sidebands for a powder distribution of ^{13}C spins with a CSA tensor of anisotropy $\delta=113$ ppm and asymmetry $\eta=0.5$ (values determined from the experiment) using MAS rates of 5 and 2 kHz are shown in red (and slightly shifted to allow for comparison with the experiment).

In our solid-state NMR study we showed that ^{13}C - ^{13}C internuclear distances can be probed for spins with small and large CSA tensors by employing 2Q filtering methods. We have further investigated the effect of residual ^1H - ^{13}C dipolar couplings on the 2Q efficiency and its dependence on the ^1H CW decoupling field during the ^{13}C homonuclear recoupling sequences like SPC5. In this respect we have shown that high-proton decoupling is largely sufficient. CT-2Q filtered experiments proposed previously by Bennett et al. [129] are of limited use in the context of rotating frame 2Q recoupling.

R.f.-driven sequence	Spin-pair	Chemical shifts	Distance constrains
SPC5	{5-CoQ10}-{5-CoQ10}	32 & 32 ppm	$3.0 \pm 0.2 \text{ \AA}$
	{2'-CoQ10}-{2'-CoQ10}	13 & 13 ppm	$> 4.5 \text{ \AA}$
	{5-CoQ10}-{2'-CoQ10}	32 & 13 ppm	$> 4.0 \text{ \AA}$
RFDR	{1-CoQ10}-{1-CoQ10}	not observed	
	{4-CoQ10}-{4-CoQ10}		
	{1-CoQ10}-{4-CoQ10}		

Table 4.2. The summary of the intermolecular distance constraints obtained in our solid-state NMR study. The r.f. sequence used to recouple ^{13}C - ^{13}C dipolar interaction is shown for each spin pair as well as the isotropic chemical shifts of the resonances observed.

These methods were applied to a variety of selectively ^{13}C -labeled ubiquinol pair molecules in complex with the bc_1 enzyme. Our HH-SSNMR data provide, for the first time, direct experimental evidence for a double occupancy of the Q_o reaction center. In addition, a number of 6 intermolecular contacts (summarized in Table 4.2) could be derived. These constraints can be used to model the relative orientation of the two ubiquinone molecules in the Q_o pocket.

5. Conclusions

In the recent years, high-resolution conditions have been established in solid-state NMR by the combination of magic angle spinning, state-of-the-art r.f. pulse schemes and the introduction of ultra-high magnetic fields. Similar to what is now routine in solution-state NMR, this has opened the way for structure determination by HR-SSNMR methods.

Complete structural or dynamical characterization of the biomolecule of interest is most easily achieved if multiple or even uniformly [^{13}C , ^{15}N]-labeled versions are studied. In a first step, experiments that allow the complete assignment of the ^{13}C and ^{15}N resonances have been recently designed. To date, nearly complete chemical shift assignments were reported for two well-ordered proteins, the α -spectrin SH3 domain and the Crh protein. The SSNMR analysis of the later protein has been presented in Section 4.1.

For SSNMR applications, not the molecular size or solubility, but the spectral resolution can be of crucial importance. Experimental parameters and sample inherent conditions such molecular disorder may reduce the overall spectral dispersion. In these circumstances, techniques that allow for spectral simplification without the need of elaborated biochemical procedures (of isotope labeling) are of special importance. In Section 2, several spectral editing methods have been proposed. These methods not only select resonances due to changes in the physical and chemical environment of the nucleus but they can also directly probe molecular properties such as dynamics and conformational heterogeneity.

Once the chemical shifts are available for the biomolecule of interest, methods that permit to obtain structural restraints can be applied. In the case of multiply isotope labeled proteins, such techniques can in principle result in multiple structural parameters. In Section 3.1, we

have shown that, similar to solution-state NMR, secondary chemical shifts can be readily employed to study the local backbone conformation. In addition, distance constraints between protons may be encoded in high-resolution on rare spins like ^{13}C and ^{15}N and measured. Finally, carbon-carbon constraints may be probed by employing frequency selective r.f. pulse schemes. These dihedral and distance constraints may subsequently lead to the determination of protein secondary to tertiary structure from a single protein sample.

In Section 4.2, we have shown that high-affinity ligand binding to membrane proteins can be investigated with solid-state NMR. Here, the neuropeptide neurotensin which binds to the G-protein coupled receptor NTS1 in sub-nanomolar affinity was investigated. Except for the case of rhodopsin, there is currently no information on the high-resolution structure of any other GPCR or a corresponding high-affinity ligand. Our SSNMR results identify, for the first time, a distinct binding mode of neurotensin that could be of considerable relevance for further pharmacological studies.

As exemplified in section 4.3, HR-SSNMR based structural studies can also assist in refining existing (X-ray or solution-state NMR) membrane-protein structures. The presented results provide, for the first time, direct experimental evidence for a double occupancy of the Q_0 binding site in the ubiquinone-*bcl* complex and may provide the basis for the complete 3D structural determination of the ubiquinone binding pocket.

Advancements regarding sample preparation (for example, including modular labeling, in vitro expression and intein technology) and improvements in NMR hardware instrumentation could open up new areas of solid-state NMR research such as the investigation of large protein-protein complexes or the complete 3D characterization of larger membrane proteins. Solid-state NMR studies of multiply-labeled biomolecules will furthermore profit from improved procedures for calculating 3D structures, in particular in the presence of ambiguous or a limited number of structural constraints.

Unlike X-ray crystallography, protein motion does not hinder solid-state NMR methods. In fact, complementary to solution-state NMR, it may provide a very efficient means to study protein folding, flexibility and function under biologically relevant conditions. Hand in hand with solution-state techniques and crystallographic methods, solid-state NMR could provide

insight into protein function and the chemistry of life with unprecedented accuracy and flexibility.

6. Abbreviations

0Q, 0QC, 0QF.....	zero-quantum, 0Q coherence, 0Q filter
1Q, 1QC, 1QF.....	single-quantum, 1Q coherence, 1Q filter
2Q, 2QC, 2QF.....	double-quantum, 2Q coherence, 2Q filter
3Q, 3QC, 3QF.....	triple-quantum, 3Q coherence, 3Q filter
CS, CSA.....	chemical shift, chemical shift anisotropy
GPCR.....	G-protein coupled receptor
HR-SSNMR.....	high-resolution SSNMR
LAB.....	laboratory frame
MAS.....	magic angle spinning
NMR.....	nuclear magnetic resonance
PAS.....	principal axis frame
ROT.....	rotor fixed frame
RR, CT-RR.....	rotational resonance, constant-time RR
RRTR.....	RR in the tilted frame
S/D.....	sum and difference experiment
SSNMR.....	solid-state NMR

7. Index

- CC experiment, 29
- chemical shielding, 11
- chemical shift selective recoupling, 88
- coherence order, 36
- coherence transfer, 24
- commutation rules, 22
- Crh, protein, 101
- density operator, 20
- dipolar coupling, 11
- dipolar dephasing, 62
- double-quantum filtering, 41
- Dyson operator, 21
- Euler angles, 15
- g-protein-coupled receptors, 117
- high-field approximation, 13
- irreducible spherical tensors, 15
- Larmor frequencies, 10
- Liouville space, 22
- Liouville-von Neumann equation, 20
- magic angle spinning, 17
- Magnus expansion, 21
- mixing operator, 26
- multiple-quantum coherences, 35
- NCACB experiment, 30
- NCOCACB experiment, 30
- neurotensin, 116
- preparation operator, 26
- principal axis system, 12
- r.f. irradiation, 11
- random coil, 73
- reduced spin system, 94
- rotating frame, 14
- rotor fixed frame, 17
- S/D experiment, 54
- scalar coupling, 11
- secondary chemical shifts, 73
- second-rank tensor, 12
- secular approximation, 13
- spectral assignment, 29
- spectral overlap, 31
- spin angular momentum, 10
- time reversal, 41
- two-dimensional experiments, 25
- Wigner rotation matrices, 15
- Zeeman interaction, 10

8. Appendices

8.1. Bruker pulse programs

8.1.1. Proton-driven spin diffusion

```
;homo-sd.lsm

"l31=1"
#define cyclops if "l31<=8" goto 100 \n\
  lm ip0 \n lm ip1 \n lm ip2 \n\
  lm ip3 \n lm ip4 \n lm ip31 \n\
  lm ru31 \n lm du31 \n 100 lm iu31

define delay dwone
"dwone=0.2u"

1 ze
2 d1
;cp f2 -> f1
  lu pl2:f2
  p2:f2 ph1
  lu pl5:f1 pl6:f2
  (pl5 ph2):f1 (pl5:spf0 pl6 ph0):f2
;tl evolution
  lu pl12:f1
  lu cpds2:f2
  dwone
  2u do:f2
;mix - spin-diff

  lu pl1:f1
  pl:f1 ph3
  d10
  pl:f1 ph4
;acquisition
  5u pl12:f2
  5u cpds2:f2
  gosc ph31
  lm do:f2
  cyclops
  lo to 2 times ns
  100m wr #0 if #0 zd
  "dwone = dwone + dw"
  lm ip2
  lo to 1 times tdl
exit

ph0 = 0
ph1 = 1 1 1 1 3 3 3 3
ph2 = 0
ph3 = 1
ph4 = 3 0 1 2
ph31= 0 1 2 3 2 3 0 1
```

8.1.2. Double-quantum filter with SPC5

```
;spc5-2qf.lsm

"l31=1"
#define cyclops if "l31<=8" goto 100 \n\
  lm ip0 \n lm ip1 \n lm ip2 \n\
  lm ip4 \n lm ip5 \n lm ip31 \n\
  lm ip6*2048 \n\
  lm ip7*2048 \n\
  lm ip8*2048 \n\
  lm ip9*2048 \n\
  lm ru31 \n lm du31 \n 100 lm iu31

;cnst31 spinning rate (Hz)
;15 10 = 4 rotor periods

"p11=(1s/cnst31)/20"

1 ze
2 d1
  lm rpp6
  lm rpp7
  lm rpp8
  lm rpp9
  lu pl2:f2
  p2:f2 ph1
  lu pl5:f1 pl6:f2
  (pl5 ph2):f1 (pl5:spf0 pl6 ph0):f2
  lu pl13:f2
  lu cw:f2
;2QC excitation with spc-5
  lu pl1:f1
  pl:f1 ph4
  lu pl11:f1
3 p11*1:f1 ph6 ipp8
  p11*4:f1 ph7^ ipp9
  p11*3:f1 ph6^

  lo to 3 times l5
;2QC reconversion with spc-5
4 p11*1:f1 ph8
  p11*4:f1 ph9^
  p11*3:f1 ph8^
  lo to 4 times l5
  lu pl1:f1
  pl:f1 ph5
;acquisition
  5u pl12:f2
  5u cpds2:f2
  gosc ph31
  lm do:f2
  lm ip5
  lm ip8*2048
  lm ip9*2048
  cyclops
  lo to 2 times ns
  100m wr #0
exit

ph0 = 0
ph1 = 1 1 1 1 3 3 3 3
ph2 = 0
ph4 = 3
ph5 = 1
ph6 = (8192) 0 1638 3277 4915 6554 4096 5734 7373
819 2458
ph7 = (8192) 4096 5734 7373 819 2458 0 1638 3277
4915 6554
ph8 = (8192) 0 1638 3277 4915 6554 4096 5734 7373
819 2458
ph9 = (8192) 4096 5734 7373 819 2458 0 1638 3277
4915 6554
ph31= 0 3 2 1 2 1 0 3
```

8.1.3. Double-quantum filter with SPC5 (constant-time)

```
;spc5-2qfct.lsm

;cnst31 spinning rate (Hz)
;15 DQ excitation time [10=4T]
```

```

;17          total constant time

"p11=(1s/cnst31)/20"

1 ze
2 dl
"l6=17-15"
  lm rpp6
  lm rpp7
  lm rpp8
  lm rpp9
  lm rpp10
  lm rpp11
  lm rpp12
  lm rpp13
  lu pl2:f2
  p2:f2 ph1
  lu pl5:f1 pl6:f2
  (p15 ph2):f1 (p15:spf0 pl6 ph0):f2
  lu pl13:f2
  lu cw:f2
;2QC excitation with spc-5
  lu pl1:f1
  pl:f1 ph4
  lu pl11:f1
3 pl1*1:f1 ph6 ipp8
  pl1*4:f1 ph7^ ipp9
  pl1*3:f1 ph6^
  lo to 3 times 15
;2QC reconversion with spc-5
4 pl1*1:f1 ph8
  pl1*4:f1 ph9^
  pl1*3:f1 ph8^
  lo to 4 times 15
  lu pl1:f1
  pl:f1 ph5
;refocus
  lu pl11:f1
5 pl1*1:f1 ph10 ipp12
  pl1*4:f1 ph11^ ipp13
  pl1*3:f1 ph10^
  lo to 5 times 16

```

```

  lu pl1:f1
  pl:f1 ph14
  lu pl11:f1
6 pl1*1:f1 ph12
  pl1*4:f1 ph13^
  pl1*3:f1 ph12^
  lo to 6 times 16
;aquisition
  5u pl12:f2
  5u cpds2:f2
  gosc ph31
  lm do:f2
  lm ip5
  lm ip8*2048
  lm ip9*2048
  lo to 2 times ns
  100m wr #0
exit

ph0 = 0
ph1 = 1 1 1 1   3 3 3 3
ph2 = 0
ph4 = 3
ph5 = 1
ph6 = (8192)   0 1638 3277 4915 6554 4096 5734 7373
819 2458
ph7 = (8192) 4096 5734 7373 819 2458   0 1638 3277
4915 6554
ph8 = (8192)   0 1638 3277 4915 6554 4096 5734 7373
819 2458
ph9 = (8192) 4096 5734 7373 819 2458   0 1638 3277
4915 6554
ph10= (8192)   0 1638 3277 4915 6554 4096 5734 7373
819 2458
ph11= (8192) 4096 5734 7373 819 2458   0 1638 3277
4915 6554
ph12= (8192)   0 1638 3277 4915 6554 4096 5734 7373
819 2458
ph13= (8192) 4096 5734 7373 819 2458   0 1638 3277
4915 6554
ph14= 0 1 2 3
ph31= 0 3 2 1   2 1 0 3

```

8.1.4. Double-quantum correlation with SPC5

```

;spc5-2qs.lsm

"l31=1"
#define cyclops if "l31<=8" goto 100 \n\
  lm ru31 \n lm du31 \n lm ip0 \n\
  lm ip1 \n lm ip2*2 \n lm ip4*2 \n\
  lm ip5 \n lm ip6*2048 \n lm ip7*2048 \n\
  lm ip31 \n 100 lm iu31

;cnst31          spinning rate (Hz)
;15              80 = 4 rotor periods

"p11=1s/(cnst31*20)"
define delay adjust
"adjust=p11/2"
"d0=p11"
;"d0=2*p11"
define delay dwone
"dwone = 0.2u"

1 ze
2 dl
  lm rpp6
  lm rpp7
  lu pl2:f2
  p2:f2 ph1
  lu pl5:f1 pl6:f2
  (p15 ph2):f1 (p15:spf0 pl6 ph0):f2
  lu pl13:f2
  lu cw:f2
;2QC excitation with spc-5

```

```

  lu pl1:f1
  pl:f1 ph4
  lu pl11:f1
3 pl1:f1 ph6^ ipp7
  lo to 3 times 15
;t1 2qc evolution
  adjust cpds2:f2
  dwone
  adjust cw:f2
;2QC reconversion with spc-5
5 pl1:f1 ph7^
  lo to 5 times 15
  lu pl1:f1
  pl:f1 ph5
;aquisition
  5u pl12:f2
  5u cpds2:f2
  gosc ph31
  lm do:f2
  lm ip5
  lm ip7*2048
  cyclops
  lo to 2 times ns
  100m wr #0 if #0 zd
  "dwone=dwone+d0"
  lm ip2
  lm ip4
  lm ip6*1024
  lo to 1 times tdl
exit

```

```

ph0 = 0
ph1 = 1 1 1 1   3 3 3 3
ph2 = (8) 0
ph4 = (8) 6
ph5 = 1
ph6 = (8192)    0 4096 4096 4096 4096    0 0 0
              1638 5734 5734 5734 5734 1638 1638 1638
              3277 7373 7373 7373 7373 3277 3277 3277
              4915 819 819 819 819 4915 4915 4915
              6554 2458 2458 2458 2458 6554 6554 6554
              4096 0 0 0 0 0 4096 4096 4096
              5734 1638 1638 1638 1638 5734 5734 5734
              7373 3277 3277 3277 3277 7373 7373 7373
              819 4915 4915 4915 4915 819 819 819

```

```

                2458 6554 6554 6554 6554 2458 2458 2458
ph7 = (8192)   4096 4096 4096 4096    0 0 0
              1638 5734 5734 5734 5734 1638 1638 1638
              3277 7373 7373 7373 7373 3277 3277 3277
              4915 819 819 819 819 4915 4915 4915
              6554 2458 2458 2458 2458 6554 6554 6554
              4096 0 0 0 0 0 4096 4096 4096
              5734 1638 1638 1638 1638 5734 5734 5734
              7373 3277 3277 3277 3277 7373 7373 7373
              819 4915 4915 4915 4915 819 819 819
              2458 6554 6554 6554 6554 2458 2458 2458
              0
ph31= 0 3 2 1   2 1 0 3

```

8.1.5. NCACB with HORROR transfer

```

;ncacb-horror.lsm

define delay dwone
"dwone = 0.2u"

1 ze
2 dl
;cp f2 -> f3
  lu pl2:f2
  p2:f2 ph1
  lu pl5:f3 pl6:f2
  (p15 ph2):f3 (p15:spf0 pl6 ph0):f2
;t1 evolution 15N
  lu pl12:f2
  lu cpds2:f2
  dwone
  lu pl13:f2
  lu cw:f2
;cp f3 -> f2
  lu pl15:f3 pl16:f1
  (p25 ph3):f3 (p25:spf1 pl16 ph4):f1

```

```

;mix - horror
  lu pl11:f1
  pl1:f1 ph4
;aquisition
  5u pl12:f2
  5u cpds2:f2
  gosc ph31
  lm do:f2
  lo to 2 times ns
  100m wr #0 if #0 zd
  "dwone = dwone + d0"
  lm ip2
  lo to 1 times td1
exit

ph0 = 0
ph1 = 1 1 1 1   3 3 3 3
ph2 = 0
ph3 = 0 0 0 0   0 0 0 0   2 2 2 2   2 2 2 2
ph4 = 0 1 2 3
ph31= 0 1 2 3   2 3 0 1   2 3 0 1   0 1 2 3

```

8.1.6. NCACB with RFDR and SD transfer steps

```

;ncoca-rfdr-sd.lsm

define delay dwone
"dwone = 0.2u"

;cnst31          spinning rate (Hz)
;dl0             spin-diffusion time

"d11=(0.5s/cnst31)-p1"

1 ze
2 dl
;cp f2 -> f3
  lu pl2:f2
  p2:f2 ph1
  lu pl5:f3 pl6:f2
  (p15 ph2):f3 (p15:spf0 pl6 ph0):f2
;t1 evolution f3
  lu pl12:f2
  lu cpds2:f2
  dwone
;cp f3 -> f1
  lu pl15:f3 pl16:f1
  (p25 ph3):f3 (p25:spf1 pl16 ph4):f1
;mix - RFDR
  lu pl1:f1
  p1:f1 ph5
3 dl1
  p1*2:f1 ph6
  dl1 ipp6
  lo to 3 times l5

```

```

  p1:f1 ph7
;mix - spin-diffusion
  lu do:f2
  lu pl1:f1
  p1:f1 ph8
  dl0
  p1:f1 ph9
;aquisition
  5u pl12:f2
  5u cpds2:f2
  gosc ph31
  lm do:f2
  lo to 2 times ns
  100m wr #0 if #0 zd
  "dwone = dwone + d0"
  lm ip2
  lo to 1 times td1
exit

ph0 = 0
ph1 = 1 1 1 1   3 3 3 3
ph2 = 0
ph3 = 0 0 0 0   0 0 0 0   2 2 2 2   2 2 2 2
ph4 = 0 1 2 3
ph5 = 1 2 3 0
ph6 = 3 0 1 2
ph7 = 3 0 1 2
ph8 = 3 0 1 2
ph9 = 3 0 1 2
ph31= 0 1 2 3   2 3 0 1   2 3 0 1   0 1 2 3

```


8.2. GAMMA-based simulation programs

8.2.1. Homonuclear double-quantum transfer using SPC5

```
#include "gamma.h"
#define MA 54.73561

// this file is: spc5-dqt.cc
// compiled against gamma 4.0.5B

int main (int argc, char *argv[])

{
    int p=1;

    coord B(0,0,1);
    int field;
    query_parameter (argc,argv,p++, "mag. field = ",field);

    spin_system SPIN(2);

    double iso0,del0,eta0;
    query_parameter (argc,argv,p++, "CS isotropic (0) = ",iso0);iso0*=field;
    query_parameter (argc,argv,p++, "CSA asymetry (0) = ",del0);del0*=field;
    query_parameter (argc,argv,p++, "CSA anysotropy (0) = ",eta0);
    space_T cs0_pas=A2 (iso0,del0,eta0,0.,0.,0.);

    double iso1,del1,etal;
    query_parameter (argc,argv,p++, "CS isotropic (1) = ",iso1);iso1*=field;
    query_parameter (argc,argv,p++, "CSA asymetry (1) = ",del1);del1*=field;
    query_parameter (argc,argv,p++, "CSA anysotropy (1) = ",etal);
    space_T cs1_pas=A2 (iso1,del1,etal,130.,60.,45.);

    double d01,dip01;
    query_parameter (argc,argv,p++, "Internuclear distance (01) = ",d01);
    dip01=120e3/(4*4)/(d01*d01*d01);
    space_T d01_pas=A2(0.,dip01,0.,0.,0.,0.);

    double omegar;
    query_parameter (argc,argv,p++, "Spinning frequency = ",omegar);

    double omegarF;
    query_parameter (argc,argv,p++, "RF amplitude = ",omegarF);

    space_T cs0_rot,cs0_lab;
    spin_T Tcs0=T_CS2 (SPIN,0,B);

    space_T cs1_rot,cs1_lab;
    spin_T Tcs1=T_CS2 (SPIN,1,B);

    space_T d01_rot,d01_lab;
    spin_T Td01=T_D (SPIN,0,1);

    gen_op H,sigma,U,dU;

    gen_op sigma0 =Iz (SPIN,0);
    gen_op detect0=Iz (SPIN,0);
    gen_op detect1=Iz (SPIN,1);

    double dwtime,period;
    period=1./omegar;

    dwtime=period;

    int NP=128;
    row_vector spect0 (NP),specsum0 (NP),data0 (NP);
    row_vector spect1 (NP),specsum1 (NP),data1 (NP);

    double phi,theta,gamma;
    double phase,RFphase;

    int NCP=360;
    int step=10;
    double norm=0;

    for (int a=1;a<4616;a+=step)
    {
        cout<<"orientations: "<<a*100/4616<<"\r"<<flush;

        sigma=sigma0;

        theta=180./(4616.)*a;
        phi =360./(4616.)*((107*a)%(4616));
        gamma=360./(4616.)*((271*a)%(4616));

        norm+=sin(theta*PI/180);

        cs0_rot=cs0_pas.rotate(phi,theta,gamma);
        cs1_rot=cs1_pas.rotate(phi,theta,gamma);

        d01_rot=d01_pas.rotate(phi,theta,gamma);

        U=Ie (SPIN,0);

        for (int b=0;b<2*NCP;b++)
        {

            if (b<NCP) phase=(360.)*b/NCP;
            else phase=(360.)*(b-NCP)/NCP;

            int bb;
            if (b< 2*NCP/5) {RFphase=0*2*PI/5; bb=b;}
            else if (b< 4*NCP/5) {RFphase=1*2*PI/5; bb=b-2*NCP/5;}
            else if (b< 6*NCP/5) {RFphase=2*2*PI/5; bb=b-4*NCP/5;}
            else if (b< 8*NCP/5) {RFphase=3*2*PI/5; bb=b-6*NCP/5;}
            else if (b<10*NCP/5) {RFphase=4*2*PI/5; bb=b-8*NCP/5;}

            if (bb>NCP/20 && bb<5*NCP/20) RFphase+=PI;

            cs0_lab=cs0_rot.rotate(phase,MA,0.);
            cs1_lab=cs1_rot.rotate(phase,MA,0.);

            d01_lab=d01_rot.rotate(phase,MA,0.);

            H =cs0_pas.component (0,0)*Tcs0.component (0,0);
            H+=cs1_pas.component (0,0)*Tcs1.component (0,0);

            H+=cs0_lab.component (2,0)*Tcs0.component (2,0);
            H+=cs1_lab.component (2,0)*Tcs1.component (2,0);

            H+=d01_lab.component (2,0)*Td01.component (2,0);
```

```

H+=sin(RFphase)*omegaRF*Ix (SPIN,0)+cos(RFphase)*omegaRF
*Iy (SPIN,0);

H+=sin(RFphase)*omegaRF*Ix (SPIN,1)+cos(RFphase)*omegaRF
*Iy (SPIN,1);

    dU=prop (H,-dwttime/NCP);
    U=dU*U;
}

for (int c=0;c<NP;c++)
{
    spect0 (c)=sin (theta*PI/180)*trace (sigma,detect0);
    spect1 (c)=sin (theta*PI/180)*trace (sigma,detect1);
    evolve_ip (sigma,U);
}

specsum0+=spect0;
specsum1+=spect1;
}

```

```

for (int j=0;j<NP;j++)
{
    data0 (j)=complex (2*j*dwttime*1e3,Re (specsum0 (j)))/norm;
    data1 (j)=complex (2*j*dwttime*1e3,Re (specsum1 (j)))/norm;
}

string outFileNme;
query_parameter (argc,argv,p++,"Generic name for files:
=",outFileNme);
string outGP0=outFileNme+"-1st.dat";
string outGP1=outFileNme+"-2nd.dat";

GP_xy (outGP0,data0);
GP_xy (outGP1,data1);

cout<<endl<<" Done ..."<<endl;
return 0;
}

```

8.2.2. Double-quantum filter employing SPC5

```

#include "gamma.h"
#define MA 54.73561

// this file is: spc5-dqf.cc
// compiled against gamma 4.0.5B

int main (int argc, char *argv[])
{
    int p=1;

    coord B(0,0,1);
    int field;
    query_parameter (argc,argv,p++,"mag. field = ",field);

    spin_system SPIN(2);

    double iso0,del0,eta0;
    query_parameter (argc,argv,p++,"CS isotropic (0) =
",iso0);iso0*=field;
    query_parameter (argc,argv,p++,"CSA asymetry (0) =
",del0);del0*=field;
    query_parameter (argc,argv,p++,"CSA anysotropy (0) =
",eta0);
    space_T cs0_pas=A2 (iso0,del0,eta0,0.,0.,0.);

    double isol,dell,etal;
    query_parameter (argc,argv,p++,"CS isotropic (1) =
",isol);isol*=field;
    query_parameter (argc,argv,p++,"CSA asymetry (1) =
",dell);dell*=field;
    query_parameter (argc,argv,p++,"CSA anysotropy (1) =
",etal);
    space_T cs1_pas=A2 (isol,dell,etal,0.,0.,0.);

    double d01,dip01;
    query_parameter (argc,argv,p++,"Internuclear distance
(01) = ",d01);
    dip01=2*120e3/(4*4)/(d01*d01*d01);
    space_T d01_pas=A2 (0.,dip01,0.,0.,0.,0.);

    double omegar;
    query_parameter (argc,argv,p++,"Spinning frequency =
",omegar);

    double omegaRF;
    query_parameter (argc,argv,p++,"RF amplitude =
",omegaRF);

    space_T cs0_rot,cs0_lab;
    spin_T Tcs0=T_CS2 (SPIN,0,B);

```

```

    space_T cs1_rot,cs1_lab;
    spin_T Tcs1=T_CS2 (SPIN,1,B);

    space_T d01_rot,d01_lab;
    spin_T Td01=T_D (SPIN,0,1);

    gen_op H,dU;
    gen_op Ha1,Ha2,Hb1,Hb2,Hc1,Hc2,Hd1,Hd2;
    gen_op Ua1,Ua2,Ub1,Ub2,Uc1,Uc2,Ud1,Ud2;
    gen_op Ua,Ub,Uc,Ud;

    gen_op sigma;
    gen_op sigma0 =-Iz (SPIN,0)-Iz (SPIN,1);
    gen_op detect0=Iz (SPIN,0);
    gen_op detect1=Iz (SPIN,1);

    double dwttime,period;
    period=1./omegar;
    dwttime=period;

    int NP=64;
    row_vector spect0 (NP),specsum0 (NP),data0 (NP);
    row_vector spect1 (NP),specsum1 (NP),data1 (NP);

    double phi,theta,gamma;
    double phase,RFphase;

    int NCP=360;
    int step=10;
    double norm=0;

    for (int a=1;a<4616;a+=step)
    {
        cout<<"orientations: "<<a*100/4616<<"\r"<<flush;

        theta=180./(4616.)*a;
        phi =360./(4616.)*((107*a)%4616);
        gamma=360./(4616.)*((271*a)%4616);

        norm+=sin (theta*PI/180);

        cs0_rot=cs0_pas.rotate (phi,theta,gamma);
        cs1_rot=cs1_pas.rotate (phi,theta,gamma);

        d01_rot=d01_pas.rotate (phi,theta,gamma);

        Ua=Ie (SPIN,0);Ua1=Ie (SPIN,0);Ua2=Ie (SPIN,0);
        Ub=Ie (SPIN,0);Ub1=Ie (SPIN,0);Ub2=Ie (SPIN,0);
        Uc=Ie (SPIN,0);Uc1=Ie (SPIN,0);Uc2=Ie (SPIN,0);
        Ud=Ie (SPIN,0);Ud1=Ie (SPIN,0);Ud2=Ie (SPIN,0);

```

```

for (int b=0;b<2*NCP;b++)
{
    if (b<NCP) phase=(360.)*b/NCP;
    else phase=(360.)*(b-NCP)/NCP;

    int bb;
    if (b<2*NCP/5) {RFphase=0*2*PI/5; bb=b;}
    else if (b<4*NCP/5) {RFphase=1*2*PI/5; bb=b-
2*NCP/5;}
    else if (b<6*NCP/5) {RFphase=2*2*PI/5; bb=b-
4*NCP/5;}
    else if (b<8*NCP/5) {RFphase=3*2*PI/5; bb=b-
6*NCP/5;}
    else if (b<10*NCP/5) {RFphase=4*2*PI/5; bb=b-
8*NCP/5;}

    if (bb>NCP/20 && bb<5*NCP/20) RFphase+=PI;

    cs0_lab=cs0_rot.rotate(phase,MA,0.);
    cs1_lab=cs1_rot.rotate(phase,MA,0.);

    d01_lab=d01_rot.rotate(phase,MA,0.);

    H =cs0_pas.component(0,0)*Tcs0.component(0,0);
    H+=cs1_pas.component(0,0)*Tcs1.component(0,0);

    H+=cs0_lab.component(2,0)*Tcs0.component(2,0);
    H+=cs1_lab.component(2,0)*Tcs1.component(2,0);

    H+=d01_lab.component(2,0)*Td01.component(2,0);

    Hal=H;

    Hal+=sin(RFphase)*omegaRF*Ix(SPIN,0)+cos(RFphase)*omeg
aRF*Iy(SPIN,0);

    Hal+=sin(RFphase)*omegaRF*Ix(SPIN,1)+cos(RFphase)*omeg
aRF*Iy(SPIN,1);
    Ha2=H;

    Ha2+=sin(RFphase+PI)*omegaRF*Ix(SPIN,0)+cos(RFphase+PI
)*omegaRF*Iy(SPIN,0);

    Ha2+=sin(RFphase+PI)*omegaRF*Ix(SPIN,1)+cos(RFphase+PI
)*omegaRF*Iy(SPIN,1);

    Hb1=H;

    Hb1+=sin(RFphase+PI/2)*omegaRF*Ix(SPIN,0)+cos(RFphase+
PI/2)*omegaRF*Iy(SPIN,0);

    Hb1+=sin(RFphase+PI/2)*omegaRF*Ix(SPIN,1)+cos(RFphase+
PI/2)*omegaRF*Iy(SPIN,1);
    Hb2=H;

    Hb2+=sin(RFphase+PI/2+PI)*omegaRF*Ix(SPIN,0)+cos(RFpha
se+PI/2+PI)*omegaRF*Iy(SPIN,0);

    Hb2+=sin(RFphase+PI/2+PI)*omegaRF*Ix(SPIN,1)+cos(RFpha
se+PI/2+PI)*omegaRF*Iy(SPIN,1);

    Hc1=H;

    Hc1+=sin(RFphase+PI)*omegaRF*Ix(SPIN,0)+cos(RFphase+PI
)*omegaRF*Iy(SPIN,0);

    Hc1+=sin(RFphase+PI)*omegaRF*Ix(SPIN,1)+cos(RFphase+PI
)*omegaRF*Iy(SPIN,1);
    Hc2=H;

    Hc2+=sin(RFphase+PI+PI)*omegaRF*Ix(SPIN,0)+cos(RFphase
+PI+PI)*omegaRF*Iy(SPIN,0);

    Hc2+=sin(RFphase+PI+PI)*omegaRF*Ix(SPIN,1)+cos(RFphase
+PI+PI)*omegaRF*Iy(SPIN,1);

```

```

Hd1=H;

Hd1+=sin(RFphase+3*PI/2)*omegaRF*Ix(SPIN,0)+cos(RFphas
e+3*PI/2)*omegaRF*Iy(SPIN,0);

Hd1+=sin(RFphase+3*PI/2)*omegaRF*Ix(SPIN,1)+cos(RFphas
e+3*PI/2)*omegaRF*Iy(SPIN,1);
    Hd2=H;

Hd2+=sin(RFphase+3*PI/2+PI)*omegaRF*Ix(SPIN,0)+cos(RFp
hase+3*PI/2+PI)*omegaRF*Iy(SPIN,0);

Hd2+=sin(RFphase+3*PI/2+PI)*omegaRF*Ix(SPIN,1)+cos(RFp
hase+3*PI/2+PI)*omegaRF*Iy(SPIN,1);

    dU=prop(Ha1,-dwttime/NCP);Ua1=dU*Ua1;
    dU=prop(Ha2,-dwttime/NCP);Ua2=dU*Ua2;
    dU=prop(Hb1,-dwttime/NCP);Ub1=dU*Ub1;
    dU=prop(Hb2,-dwttime/NCP);Ub2=dU*Ub2;
    dU=prop(Hc1,-dwttime/NCP);Uc1=dU*Uc1;
    dU=prop(Hc2,-dwttime/NCP);Uc2=dU*Uc2;
    dU=prop(Hd1,-dwttime/NCP);Ud1=dU*Ud1;
    dU=prop(Hd2,-dwttime/NCP);Ud2=dU*Ud2;
}

Ua=Ua2*Ua1;
Ub=Ub2*Ub1;
Uc=Uc2*Uc1;
Ud=Ud2*Ud1;

sigma=sigma0;
for (int c=0;c<NP;c++)
{
    spect0(c)=sin(theta*PI/180)*trace(sigma,detect0);
    spect1(c)=sin(theta*PI/180)*trace(sigma,detect1);
    sigma=sigma0;
    for (int c1=0;c1<=c;c1++) evolve_ip(sigma,Ua);
    for (int c1=0;c1<=c;c1++) evolve_ip(sigma,Ua);
}
specsum0+=spect0*complex(1,0);
specsum1+=spect1*complex(1,0);

sigma=sigma0;
for (int c=0;c<NP;c++)
{
    spect0(c)=sin(theta*PI/180)*trace(sigma,detect0);
    spect1(c)=sin(theta*PI/180)*trace(sigma,detect1);
    sigma=sigma0;
    for (int c1=0;c1<=c;c1++) evolve_ip(sigma,Ua);
    for (int c1=0;c1<=c;c1++) evolve_ip(sigma,Ub);
}
specsum0+=spect0*complex(-1,0);
specsum1+=spect1*complex(-1,0);

sigma=sigma0;
for (int c=0;c<NP;c++)
{
    spect0(c)=sin(theta*PI/180)*trace(sigma,detect0);
    spect1(c)=sin(theta*PI/180)*trace(sigma,detect1);
    sigma=sigma0;
    for (int c1=0;c1<=c;c1++) evolve_ip(sigma,Ua);
    for (int c1=0;c1<=c;c1++) evolve_ip(sigma,Uc);
}
specsum0+=spect0*complex(1,0);
specsum1+=spect1*complex(1,0);

sigma=sigma0;
for (int c=0;c<NP;c++)
{
    spect0(c)=sin(theta*PI/180)*trace(sigma,detect0);
    spect1(c)=sin(theta*PI/180)*trace(sigma,detect1);
    sigma=sigma0;
    for (int c1=0;c1<=c;c1++) evolve_ip(sigma,Ua);
    for (int c1=0;c1<=c;c1++) evolve_ip(sigma,Ud);
}
specsum0+=spect0*complex(-1,0);

```

```

    specsум1+=spect1*complex(-1,0);
}

for (int j=0;j<NP;j++)
{

data0(j)=complex(8*j*dwttime*1e3,Re(specsum0(j))/norm/4
);

data1(j)=complex(8*j*dwttime*1e3,Re(specsum1(j))/norm/4
);
}

```

```

string outFile_name;
query_parameter(argc,argv,p++,"Generic name for
files: = ",outFile_name);
string outGP0=outFile_name+"-1st.dat";
string outGP1=outFile_name+"-2nd.dat";

GP_xy(outGP0,data0);
GP_xy(outGP1,data1);

cout<<endl<<" Done ..."<<endl;
return 0;
}

```

9. List of publications

The work presented in this thesis is based on the following publications.

Chapter 1

1. High-resolution solid-state NMR applied to polypeptides and membrane proteins, S. Luca, H. Heise and M. Baldus, manuscript submitted 2003.

Chapter 2

2. Multiple-quantum spectroscopy of fully labeled polypeptides under MAS: a statistical and experimental analysis, S. Luca, D.V. Filippov, B. Angerstein, G.A. van der Marel, J.H. van Boom and M. Baldus, *Focus on Structural Biology* 1 (2001) 33-43.
3. Enhanced spectral resolution in immobilized peptides and proteins by combining chemical shift sum and difference spectroscopy, S. Luca and M. Baldus, *Journal of Magnetic Resonance* 159 (2002) 243-249.
4. Combining multiple-quantum spectroscopy and anisotropic dephasing in rotating solids: A tool for spectral simplification and structure elucidation, S. Luca, H. Heise and M. Baldus, manuscript in preparation.

Chapter 3

5. Secondary chemical shifts in immobilized peptides and proteins: A qualitative basis for structure refinement under magic angle spinning, S. Luca, D.V. Filippov, J.H. van Boom,

H. Oschkinat, H.J.M de Groot and M. Baldus, *Journal of Biomolecular NMR* 20 (2001) 325-331.

6. Structural constraints from proton-mediated rare-spin correlation spectroscopy in rotating solids, A. Lange, S. Luca and M. Baldus, *Journal of the American Chemical Society* 124 (2002) 9704-9705.
7. Three-dimensional structure determination using proton-proton contacts in rotating solids, A. Lange, K. Seidel, L. Verdier, S. Luca, M. Baldus, manuscript submitted 2003.
8. Distance determination in uniformly labeled biomolecules, L. Sonnenberg, S. Luca and M. Baldus, manuscript in preparation.

Chapter 4

9. Solid-state NMR sequential resonance assignments and conformational analysis of the 2x10.4 kDa dimeric form of the *Bacillus subtilis* protein Crh, A. Bockmann, A. Lange, N. Giraud, S. Luca, H. Heise, A. Galinier, M. Juy, R. Montserret, F. Penin and M. Baldus, manuscript submitted 2003.
10. The conformation of neurotensin bound to its G-protein coupled receptor, S. Luca, J.F. White, A.K. Sohal, D. Phillipov, J.V. Boom, R. Grisshammer and M. Baldus, manuscript submitted 2003.

10. References

1. Tycko, R., *Biomolecular solid state NMR: Advances in structural methodology and applications to peptide and protein fibrils*. Annual Review of Physical Chemistry, 2001. **52**: p. 575-606.
2. Thompson, L.K., *Solid-state NMR studies of the structure and mechanisms of proteins*. Current Opinion in Structural Biology, 2002. **12**(5): p. 661-669.
3. Luca, S., H. Heise, and M. Baldus, *High-resolution solid-state NMR applied to polypeptides and membrane proteins*. submitted, 2003.
4. Ernst, R.R., G. Bodenhausen, and A. Wokaun, *Principles of nuclear magnetic resonance in one and two dimensions*. 1987, Oxford: Clarendon Press.
5. Mehring, M., *Principles of high resolution NMR in solids*. 2 ed. 1983, Berlin: Springer.
6. Baldus, M., *Correlation experiments for assignment and structure elucidation of immobilized polypeptides under magic angle spinning*. Progress in Nuclear Magnetic Resonance Spectroscopy, 2002. **41**(1-2): p. 1-47.
7. Baldus, M. and B.H. Meier, *Total correlation spectroscopy in the solid state. The use of scalar couplings to determine the through-bond connectivity*. Journal of Magnetic Resonance Series A, 1996. **121**(1): p. 65-69.
8. Andrew, E.R., A. Bradbury, and R.G. Eades, *Nuclear magnetic resonance spectra from a crystal rotated at high speed*. Nature, 1958. **182**(4650): p. 1659-1659.
9. Herzfeld, J. and A.E. Berger, *Sideband intensities in NMR spectra of samples spinning at the magic angle*. Journal of Chemical Physics, 1980. **73**(12): p. 6021-6030.
10. Bennett, A.E., C.M. Rienstra, M. Auger, K.V. Lakshmi, and R.G. Griffin, *Heteronuclear decoupling in rotating solids*. Journal of Chemical Physics, 1995. **103**(16): p. 6951-6958.
11. Schaefer, J. and E.O. Stejskal, *¹³C nuclear magnetic resonance of polymers spinning at magic angle*. Journal of the American Chemical Society, 1976. **98**(4): p. 1031-1032.
12. Lee, M. and W.I. Goldberg, *Nuclear magnetic resonance line narrowing by a rotating r.f. field*. Physical Review, 1965. **140**(4A): p. 1261-&.
13. Waugh, J.S., L.M. Huber, and Haeberle, U., *Approach to high-resolution NMR in solids*. Physical Review Letters, 1968. **20**(5): p. 180-&.

14. Griffin, R.G., *Dipolar recoupling in MAS spectra of biological solids*. Nature Structural Biology, 1998. **5**: p. 508-512.
15. Dusold, S. and A. Sebald, *Dipolar recoupling under magic-angle spinning conditions*, in *Annual Reports on Nmr Spectroscopy, Vol 41*. 2000. p. 185-264.
16. Smith, S.A., T.O. Levante, B.H. Meier, and R.R. Ernst, *Computer simulations in magnetic resonance: An object-oriented programming approach*. Journal of Magnetic Resonance Series A, 1994. **106**(1): p. 75-105.
17. Hartmann, S.R. and E.L. Hahn, *Nuclear double resonance in rotating frame*. Physical Review, 1962. **128**(5): p. 2042-&.
18. Pines, A., M.G. Gibby, and J.S. Waugh, *Proton enhanced NMR of dilute spins in solids*. Journal of Chemical Physics, 1973. **59**(2): p. 569-590.
19. Bodenhausen, G., R.L. Vold, and R.R. Vold, *Multiple quantum spin-echo spectroscopy*. Journal of Magnetic Resonance, 1980. **37**(1): p. 93-106.
20. Munowitz, M. and A. Pines, *Principles and applications of multiple quantum NMR*. Advances in Chemical Physics, 1987. **66**: p. 1-152.
21. Munowitz, M. and A. Pines, *Multiple quantum nuclear magnetic resonance spectroscopy*. Science, 1986. **233**(4763): p. 525-531.
22. Baum, J., M. Munowitz, A.N. Garroway, and A. Pines, *Multiple quantum dynamics in solid state NMR*. Journal of Chemical Physics, 1985. **83**(5): p. 2015-2025.
23. Baldus, M., A.T. Petkova, J. Herzfeld, and R.G. Griffin, *Cross polarization in the tilted frame: assignment and spectral simplification in heteronuclear spin systems*. Molecular Physics, 1998. **95**(6): p. 1197-1207.
24. Pauli, J., M. Baldus, B. van Rossum, H. de Groot, and H. Oschkinat, *Backbone and side-chain C-13 and N-15 signal assignments of the alpha-spectrin SH3 domain by magic angle spinning solid-state NMR at 17.6 tesla*. Chembiochem, 2001. **2**(4): p. 272-281.
25. Bloembergen, N., *On the interaction of nuclear spins in a crystalline lattice*. Physica, 1949. **15**: p. 386-426.
26. Bockmann, A., A. Lange, N. Giraud, S. Luca, H. Heise, A. Galinier, M. Juy, R. Montserret, F. Penin, and M. Baldus, *Solid-state NMR sequential resonance assignments and conformational analysis of the 2x10.4 kDa dimeric form of the Bacillus subtilis protein Crh*. submitted, 2003.
27. Nielsen, N.C., H. Bildsoe, H.J. Jakobsen, and M.H. Levitt, *Double-quantum homonuclear rotary resonance. Efficient dipolar recovery in magic angle spinning nuclear magnetic resonance*. Journal of Chemical Physics, 1994. **101**(3): p. 1805-1812.
28. Seidel, K., L. Verdier, S. Luca, A. Lange, H. Heise, and M. Baldus, *Structure determination of proteins using MAS solid-state NMR*. to be published, 2003.
29. Yatsiv, S., *Multiple-quantum transitions in nuclear magnetic resonance*. Physical Review, 1959. **113**(6): p. 1522-1537.
30. Anderson, W.A., R. Freeman, and C.A. Reilly, *Assignment of NMR spectra with aid of double-quantum transitions*. Journal of Chemical Physics, 1963. **39**(6): p. 1518-&.

31. Hatanaka, H., T. Terao, and T. Hashi, *Excitation and detection of coherence between forbidden levels in 3-level spin system by multistep processes*. Journal of the Physical Society of Japan, 1975. **39**(3): p. 835-836.
32. Vega, S., T.W. Shattuck, and A. Pines, *Fourier-Transform Double-Quantum Nmr in Solids*. Physical Review Letters, 1976. **37**(1): p. 43-46.
33. Munowitz, M., A. Pines, and M. Mehring, *Multiple-Quantum Dynamics in Nmr - a Directed Walk through Liouville Space*. Journal of Chemical Physics, 1987. **86**(6): p. 3172-3182.
34. Bax, A., R. Freeman, and S.P. Kempell, *Natural abundance ^{13}C - ^{13}C coupling observed via double-quantum coherence*. Journal of the American Chemical Society, 1980. **102**(14): p. 4849-4851.
35. Menger, E.M., S. Vega, and R.G. Griffin, *Observation of carbon carbon connectivities in rotating solids*. Journal of the American Chemical Society, 1986. **108**(9): p. 2215-2218.
36. Feike, M., R. Graf, I. Schnell, C. Jager, and H.W. Spiess, *Structure of crystalline phosphates from P-31 double-quantum NMR spectroscopy*. Journal of the American Chemical Society, 1996. **118**(40): p. 9631-9634.
37. Dollase, W.A., M. Feike, H. Forster, T. Schaller, I. Schnell, A. Sebald, and S. Steuernagel, *A 2D P-31 MAS NMR study of polycrystalline Cd-3(PO₄)(2)*. Journal of the American Chemical Society, 1997. **119**(16): p. 3807-3810.
38. Lesage, A., C. Auger, S. Caldarelli, and L. Emsley, *Determination of through-bond carbon-carbon connectivities in solid-state NMR using the INADEQUATE experiment*. Journal of the American Chemical Society, 1997. **119**(33): p. 7867-7868.
39. Hong, M., *Solid-state dipolar INADEQUATE NMR spectroscopy with a large double-quantum spectral width*. Journal of Magnetic Resonance, 1999. **136**(1): p. 86-91.
40. BioMagResBank, *A repository for data from NMR spectroscopy on proteins, peptides and nucleic acids*, <http://www.bmrwisc.edu/index.html>.
41. Eden, M. and M.H. Levitt, *Excitation of carbon-13 triple-quantum coherence in magic angle spinning NMR*. Chemical Physics Letters, 1998. **293**(3-4): p. 173-179.
42. Eden, M., *Order-selective multiple-quantum excitation in magic-angle spinning NMR: creating triple-quantum coherences with a trilinear Hamiltonian*. Chemical Physics Letters, 2002. **366**(5-6): p. 469-476.
43. Hohwy, M., H.J. Jakobsen, M. Eden, M.H. Levitt, and N.C. Nielsen, *Broadband dipolar recoupling in the nuclear magnetic resonance of rotating solids: A compensated C7 pulse sequence*. Journal of Chemical Physics, 1998. **108**(7): p. 2686-2694.
44. Hohwy, M., C.M. Rienstra, C.P. Jaroniec, and R.G. Griffin, *Fivefold symmetric homonuclear dipolar recoupling in rotating solids: Application to double quantum spectroscopy*. Journal of Chemical Physics, 1999. **110**(16): p. 7983-7992.
45. Romi, R., M. Crest, M. Gola, F. Sampieri, G. Jacquet, H. Zerrouk, P. Mansuelle, O. Sorokine, A. Vandorsselaer, H. Rochat, M.F. Martineauclaire, and J. Vanrietschoten, *Synthesis and Characterization of Kaliotoxin - Is the 26-32 Sequence Essential for Potassium Channel Recognition*. Journal of Biological Chemistry, 1993. **268**(35): p. 26302-26309.

46. Crest, M., G. Jacquet, M. Gola, H. Zerrouk, A. Benslimane, H. Rochat, P. Mansuelle, and M.F. Martineauclaire, *Kaliotoxin, a Novel Peptidyl Inhibitor of Neuronal Bk-Type Ca²⁺-Activated K⁺ Channels Characterized from Androctonus-Mauretanicus-Mauretanicus Venom*. Journal of Biological Chemistry, 1992. **267**(3): p. 1640-1647.
47. Legros, C., V. Pollmann, H.G. Knaus, A.M. Farrell, H. Darbon, P.E. Bougis, M.F. Martin-Eauclaire, and O. Pongs, *Generating a high affinity scorpion toxin receptor in KcsA-Kv1.3 chimeric potassium channels*. Journal of Biological Chemistry, 2000. **275**(22): p. 16918-16924.
48. Aiyar, J., J.M. Withka, J.P. Rizzi, D.H. Singleton, G.C. Andrews, W. Lin, J. Boyd, D.C. Hanson, M. Simon, B. Dethlefs, C.L. Lee, J.E. Hall, G.A. Gutman, and K.G. Chandy, *Topology of the Pore-Region of a K⁺ Channel Revealed by the Nmr-Derived Structures of Scorpion Toxins*. Neuron, 1995. **15**(5): p. 1169-1181.
49. Grissmer, S., A.N. Nguyen, J. Aiyar, D.C. Hanson, R.J. Mather, G.A. Gutman, M.J. Karmilowicz, D.D. Auperin, and K.G. Chandy, *Pharmacological Characterization of 5 Cloned Voltage-Gated K⁺ Channels, Types Kv1.1, Kv1.2, Kv1.3, Kv1.5, and Kv3.1, Stably Expressed in Mammalian-Cell Lines*. Molecular Pharmacology, 1994. **45**(6): p. 1227-1234.
50. Gairi, M., R. Romi, I. Fernandez, H. Rochat, M.F. Martin-Eauclaire, J. Van Rietschoten, M. Pons, and E. Giralt, *3D structure of kaliotoxin: Is residue 34 a key for channel selectivity?* Journal of Peptide Science, 1997. **3**(4): p. 314-319.
51. Xu, X.P. and D.A. Case, *Automated prediction of ¹⁵N, ¹³C_α, ¹³C_β and ¹³C' chemical shifts in proteins using a density functional database*. Journal of Biomolecular NMR, 2001. **21**(4): p. 321-333.
52. Sun, B.Q., P.R. Costa, D. Kocisko, P.T. Lansbury, and R.G. Griffin, *Internuclear distance measurements in solid-state nuclear magnetic resonance. Dipolar recoupling via rotor synchronized spin locking*. Journal of Chemical Physics, 1995. **102**(2): p. 702-707.
53. Sternlicht, H. and D. Wilson, *Magnetic Resonance Studies of Macromolecules. I Aromatic-Methyl Interactions and Helical Structure Effects in Lysozyme*. Biochemistry, 1967. **6**(9): p. 2881-2892.
54. Markley, J.L., D.H. Meadows, and O. Jardetzky, *Nuclear Magnetic Resonance Studies of Helix-Coil Transitions in Polyamino Acids*. Journal of Molecular Biology, 1967. **27**: p. 25-40.
55. Gross, K.H. and H.R. Kalbitzer, *Distribution of chemical shifts in ¹H nuclear magnetic resonance spectra of proteins*. Journal of Magnetic Resonance, 1988. **76**(1): p. 87-99.
56. Spera, S. and A. Bax, *Empirical correlation between protein backbone conformation and C_α and C_β ¹³C nuclear magnetic resonance chemical shifts*. Journal of the American Chemical Society, 1991. **113**(14): p. 5490-5492.
57. Saito, H., *Conformation-dependent ¹³C chemical shifts: A new means of conformational characterization as obtained by high-resolution solid-state ¹³C NMR*. Magnetic Resonance in Chemistry, 1986. **24**(10): p. 835-852.
58. Saito, H., S. Tuzi, and A. Naito, *Empirical versus nonempirical evaluation of secondary structure of fibrous and membrane proteins by solid-state NMR: a practical approach*. Annual Reports on NMR spectroscopy, 1998. **36**: p. 79-121.

59. Luca, S., D.V. Filippov, J.H. van Boom, H. Oschkinat, H.J.M. de Groot, and M. Baldus, *Secondary chemical shifts in immobilized peptides and proteins: A qualitative basis for structure refinement under Magic Angle Spinning*. Journal of Biomolecular NMR, 2001. **20**(4): p. 325-331.
60. Wishart, D.S. and B.D. Sykes, *Chemical shifts as a tool for structure determination*. Nuclear Magnetic Resonance, Pt C, 1994. **239**: p. 363-392.
61. Dedios, A.C., J.G. Pearson, and E. Oldfield, *Secondary and tertiary structural effects on protein NMR chemical shifts - an abinitio approach*. Science, 1993. **260**(5113): p. 1491-1496.
62. Kozlov, G., I. Ekiel, N. Beglova, A. Yee, A. Dharamsi, A. Engel, N. Siddiqui, A. Nong, and K. Gehring, *Rapid fold and structure determination of the archaeal translation elongation factor 1 beta from Methanobacterium thermoautotrophicum*. Journal of Biomolecular NMR, 2000. **17**(3): p. 187-194.
63. Iwadate, M., T. Asakura, and M.P. Williamson, *C α and C β carbon-13 chemical shifts in proteins from an empirical database*. Journal of Biomolecular NMR, 1999. **13**(3): p. 199-211.
64. Müller, L., *Mapping of spin-spin coupling via zero-quantum coherence*. Journal of Magnetic Resonance, 1984. **59**: p. 326-331.
65. Koons, J.M., G.E. Pavlovskaya, A.A. Jones, and P.T. Inglefield, *Determination of interatomic distances by zero-quantum correlation spectroscopy under rotational-resonance conditions*. Journal of Magnetic Resonance, 1997. **124**(2): p. 499-502.
66. Spaniol, T.P., A. Kubo, and T. Terao, *Resolution enhancement of magic-angle spinning NMR spectra for paramagnetic solids by zero-quantum NMR*. Molecular Physics, 1999. **96**(5): p. 827-834.
67. Metz, G., X.L. Wu, and S.O. Smith, *Ramped-amplitude cross-polarization in magic angle spinning NMR*. Journal of Magnetic Resonance Series A, 1994. **110**(2): p. 219-227.
68. Hediger, S., B.H. Meier, N.D. Kurur, G. Bodenhausen, and R.R. Ernst, *NMR cross-polarization by adiabatic passage through the Hartmann-Hahn condition (APHH)*. Chemical Physics Letters, 1994. **223**(4): p. 283-288.
69. Verel, R., M. Baldus, M. Ernst, and B.H. Meier, *A homonuclear spin-pair filter for solid-state NMR based on adiabatic-passage techniques*. Chemical Physics Letters, 1998. **287**(3-4): p. 421-428.
70. Verel, R., M. Baldus, M. Nijman, J.W.M. van Os, and B.H. Meier, *Adiabatic homonuclear polarization transfer in magic angle spinning solid-state NMR*. Chemical Physics Letters, 1997. **280**(1-2): p. 31-39.
71. Szyperki, T., B. Banecki, D. Braun, and R.W. Glaser, *Sequential resonance assignment of medium-sized ¹⁵N/¹³C labeled proteins with projected 4D triple resonance NMR experiments*. Journal of Biomolecular Nmr, 1998. **11**(4): p. 387-405.
72. Szyperki, T., G. Wider, J.H. Bushweller, and K. Wüthrich, *Reduced dimensionality in triple-resonance NMR Experiments*. Journal of the American Chemical Society, 1993. **115**(20): p. 9307-9308.

73. Astrof, N.S., C.E. Lyon, and R.G. Griffin, *Triple resonance solid state NMR experiments with reduced dimensionality evolution periods*. Journal of Magnetic Resonance, 2001. **152**(2): p. 303-307.
74. Vijaykumar, S., C.E. Bugg, and W.J. Cook, *Structure of ubiquitin refined at 1.8 Å resolution*. Journal of Molecular Biology, 1987. **194**(3): p. 531-544.
75. Cornilescu, G., J.L. Marquardt, M. Ottiger, and A. Bax, *Validation of protein structure from anisotropic carbonyl chemical shifts in a dilute liquid crystalline phase*. Journal of the American Chemical Society, 1998. **120**(27): p. 6836-6837.
76. Andrew, E.R., Bradbury, A. and Eades, R.G, *Nuclear Magnetic Resonance Spectra from a crystal rotated at high speed*. Nature, 1958. **182**: p. 1659.
77. Wilbur, D.J. and J. Jonas, *Fourier transform NMR in liquids at high pressure. 3. Spin-lattice relaxation in toluene-d₈*. Journal of Chemical Physics, 1975. **62**(7): p. 2800-2807.
78. Maus, D.C., V. Copie, B.Q. Sun, J.M. Griffiths, R.G. Griffin, S.F. Luo, R.R. Schrock, A.H. Liu, S.W. Seidel, W.M. Davis, and A. Grohmann, *A solid-state NMR study of tungsten methyl group dynamics in [W(η^5 -C₅Me₅)Me₄][PF₆]*. Journal of the American Chemical Society, 1996. **118**(24): p. 5665-5671.
79. Copie, V., A.E. McDermott, K. Beshah, J.C. Williams, M. Spijkerassink, R. Gebhard, J. Lugtenburg, J. Herzfeld, and R.G. Griffin, *Deuterium solid-state nuclear magnetic resonance studies of methyl group dynamics in bacteriorhodopsin and retinal model compounds: Evidence for a 6-s-trans chromophore in the protein*. Biochemistry, 1994. **33**(11): p. 3280-3286.
80. Beshah, K., E.T. Olejniczak, and R.G. Griffin, *Deuterium NMR study of methyl group dynamics in L-alanine*. Journal of Chemical Physics, 1987. **86**(9): p. 4730-4736.
81. Batchelder, L.S., C.H. Niu, and D.A. Torchia, *Methyl reorientation in polycrystalline amino acids and peptides: A ²H NMR spin-lattice relaxation study*. Journal of the American Chemical Society, 1983. **105**(8): p. 2228-2231.
82. Munowitz, M.G. and R.G. Griffin, *Two-dimensional nuclear magnetic resonance in rotating solids: An analysis of line-shapes in chemical shift-dipolar spectra*. Journal of Chemical Physics, 1982. **76**(6): p. 2848-2858.
83. Opella, S.J. and M.H. Frey, *Selection of Non-Protonated Carbon Resonances in Solid-State Nuclear Magnetic-Resonance*. Journal of the American Chemical Society, 1979. **101**(19): p. 5854-5856.
84. Lange, A., S. Luca, and M. Baldus, *Structural constraints from proton-mediated rare-spin correlation spectroscopy in rotating solids*. Journal of the American Chemical Society, 2002. **124**(33): p. 9704-9705.
85. McDermott, A., T. Polenova, A. Bockmann, K.W. Zilm, E.K. Paulsen, R.W. Martin, and G.T. Montelione, *Partial NMR assignments for uniformly (¹³C, ¹⁵N)-enriched BPTI in the solid state*. Journal of Biomolecular NMR, 2000. **16**(3): p. 209-219.
86. Straus, S.K., T. Bremi, and R.R. Ernst, *Experiments and strategies for the assignment of fully ¹³C/¹⁵N-labelled polypeptides by solid state NMR*. Journal of Biomolecular NMR, 1998. **12**(1): p. 39-50.
87. Egorova-Zachernyuk, T.A., J. Hollander, N. Fraser, P. Gast, A.J. Hoff, R. Cogdell, H.J.M. de Groot, and M. Baldus, *Heteronuclear 2D-correlations in a uniformly C-13*,

- N-15 labeled membrane-protein complex at ultra-high magnetic fields.* Journal of Biomolecular Nmr, 2001. **19**(3): p. 243-253.
88. LeMaster, D.M. and D.M. Kushlan, *Dynamical mapping of E-coli thioredoxin via C-13 NMR relaxation analysis.* Journal of the American Chemical Society, 1996. **118**(39): p. 9255-9264.
 89. Hong, M. and K. Jakes, *Selective and extensive C-13 labeling of a membrane protein for solid-state NMR investigations.* Journal of Biomolecular Nmr, 1999. **14**(1): p. 71-74.
 90. Castellani, F., B. van Rossum, A. Diehl, M. Schubert, K. Rehbein, and H. Oschkinat, *Structure of a protein determined by solid-state magic-angle- spinning NMR spectroscopy.* Nature, 2002. **420**(6911): p. 98-102.
 91. Reif, B., B.J. van Rossum, F. Castellani, K. Rehbein, A. Diehl, and H. Oschkinat, *Characterization of H-1-H-1 distances in a uniformly H-2,N-15- labeled SH3 domain by MAS solid-state NMR spectroscopy.* Journal of the American Chemical Society, 2003. **125**(6): p. 1488-1489.
 92. Raleigh, D.P., M.H. Levitt, and R.G. Griffin, *Rotational Resonance in Solid-State NMR.* Chemical Physics Letters, 1988. **146**(1-2): p. 71-76.
 93. Takegoshi, K., K. Nomura, and T. Terao, *Selective homonuclear polarization transfer in the tilted rotating frame under magic angle spinning in solids.* Journal of Magnetic Resonance, 1997. **127**(2): p. 206-216.
 94. Takegoshi, K., K. Nomura, and T. Terao, *Rotational resonance in the tilted rotating frame.* Chemical Physics Letters, 1995. **232**(5-6): p. 424-428.
 95. Jaroniec, C.P., B.A. Tounge, J. Herzfeld, and R.G. Griffin, *Frequency selective heteronuclear dipolar recoupling in rotating solids: Accurate ¹³C-¹⁵N distance measurements in uniformly ¹³C, ¹⁵N-labeled peptides.* Journal of the American Chemical Society, 2001. **123**(15): p. 3507-3519.
 96. Williamson, P.T.F., A. Verhoeven, M. Ernst, and B.H. Meier, *Determination of internuclear distances in uniformly labeled molecules by rotational-resonance solid-state NMR.* Journal of the American Chemical Society, 2003. **125**(9): p. 2718-2722.
 97. Sonnenberg, L., S. Luca, and M. Baldus, *Distance determination in uniformly labeled biomolecules.* manuscript in preparation, 2003.
 98. Lange, A., K. Seidel, L. Verdier, S. Luca, and M. Baldus, *Three-dimensional structure determination using proton-proton contacts in rotating solids.* submitted, 2003.
 99. Wuthrich, K., *The way to NMR structures of proteins.* Nature Structural Biology, 2001. **8**(11): p. 923-925.
 100. Jeener, J. *Pulsed pair techniques in high resolution NMR.* in *Ampere International Summer school.* 1971. Basko Polje, Yugoslavia.
 101. Wüthrich, K., *NMR of proteins and nucleic acids.* 1986, New York: Wiley Interscience.
 102. Pease, L.G., M.H. Frey, and S.J. Opella, *Observation of Conformationally Distinct Proline Residues in 2 Cyclic-Peptides by Solid-State Nuclear Magnetic-Resonance.* Journal of the American Chemical Society, 1981. **103**(2): p. 467-468.

103. Ishida, M., T. Asakura, M. Yokoi, and H. Saito, *Solvent-Induced and Mechanical-Treatment-Induced Conformational Transition of Silk Fibroins Studied by High-Resolution Solid-State C-13 Nmr-Spectroscopy*. *Macromolecules*, 1990. **23**(1): p. 88-94.
104. Kamihira, M., A. Naito, S. Tuzi, A.Y. Nosaka, and H. Saito, *Conformational transitions and fibrillation mechanism of human calcitonin as studied by high-resolution solid-state C-13 NMR*. *Protein Science*, 2000. **9**(5): p. 867-877.
105. Balbach, J.J., Y. Ishii, O.N. Antzutkin, R.D. Leapman, N.W. Rizzo, F. Dyda, J. Reed, and R. Tycko, *Amyloid fibril formation by A beta(16-22), a seven-residue fragment of the Alzheimer's beta-amyloid peptide, and structural characterization by solid state NMR*. *Biochemistry*, 2000. **39**(45): p. 13748-13759.
106. Tuzi, S., K. Shinzawaitoh, T. Erata, A. Naito, S. Yoshikawa, and H. Saito, *A High-Resolution Solid-State C-13-Nmr Study on Crystalline Bovine Heart Cytochrome-C-Oxidase and Lysozyme - Dynamic Behavior of Protein and Detergent in the Complex*. *European Journal of Biochemistry*, 1992. **208**(3): p. 713-720.
107. Saito, H., S. Tuzi, S. Yamaguchi, M. Tanio, and A. Naito, *Conformation and backbone dynamics of bacteriorhodopsin revealed by C-13-NMR*. *Biochimica Et Biophysica Acta-Bioenergetics*, 2000. **1460**(1): p. 39-48.
108. Cross, T.A. and S.J. Opella, *Solid-State Nmr Structural Studies of Peptides and Proteins in Membranes*. *Current Opinion in Structural Biology*, 1994. **4**(4): p. 574-581.
109. Watts, A., *NMR of drugs and ligands bound to membrane receptors*. *Current Opinion in Biotechnology*, 1999. **10**(1): p. 48-53.
110. Siegal, G., J. van Duynhoven, and M. Baldus, *Biomolecular NMR: recent advances in liquids, solids and screening*. *Current Opinion in Chemical Biology*, 1999. **3**(5): p. 530-536.
111. Tycko, R., *Solid-state NMR as a probe of amyloid fibril structure*. *Current Opinion in Chemical Biology*, 2000. **4**(5): p. 500-506.
112. Cavanagh, J., Fairbrother, W.J., Palmer, A.G., Skelton, N.J., *Protein NMR spectroscopy, Principles and Practice*. 1996, San Diego: Academic Press.
113. Cornilescu, G., F. Delaglio, and A. Bax, *Protein backbone angle restraints from searching a database for chemical shift and sequence homology*. *Journal of Biomolecular NMR*, 1999. **13**(3): p. 289-302.
114. Dyson, H.J. and P.E. Wright, *Equilibrium NMR studies of unfolded and partially folded proteins*. *Nature Structural Biology*, 1998. **5**: p. 499-503.
115. Pauli, J., M. Baldus, B. van Rossum, H. de Groot, and H. Oschkinat, *Backbone and side-chain ¹³C and ¹⁵N signal assignments of the alpha-spectrin SH3 domain by magic angle spinning solid-state NMR at 17.6 tesla*. *ChemBiochem*, 2001. **2**(4): p. 272-281.
116. Hong, M. and R.G. Griffin, *Resonance assignments for solid peptides by dipolar-mediated C-13/N-15 correlation solid-state NMR*. *Journal of the American Chemical Society*, 1998. **120**(28): p. 7113-7114.
117. Nomura, K., K. Takegoshi, T. Terao, K. Uchida, and M. Kainosho, *Determination of the complete structure of a uniformly labeled molecule by rotational resonance solid-*

- state NMR in the tilted rotating frame*. Journal of the American Chemical Society, 1999. **121**(16): p. 4064-4065.
118. Rienstra, C.M., M. Hohwy, M. Hong, and R.G. Griffin, *2D and 3D N-15-C-13-C-13 NMR chemical shift correlation spectroscopy of solids: Assignment of MAS spectra of peptides*. Journal of the American Chemical Society, 2000. **122**(44): p. 10979-10990.
 119. Hong, M., *Resonance assignment of $^{13}\text{C}/^{15}\text{N}$ labeled solid proteins by two- and three-dimensional magic-angle-spinning NMR*. Journal of Biomolecular NMR, 1999. **15**(1): p. 1-14.
 120. Egorova-Zachernyuk, T.A., J. Hollander, N. Fraser, P. Gast, A.J. Hoff, R. Cogdell, H.J.M. de Groot, and M. Baldus, *Heteronuclear 2D-correlations in a uniformly [^{13}C , ^{15}N] labeled membrane-protein complex at ultra-high magnetic fields*. Journal of Biomolecular NMR, 2001. **19**(3): p. 243-253.
 121. Gan, Z.H. and D.M. Grant, *Rotational Resonance in a Spin-Lock Field for Solid-State Nmr*. Chemical Physics Letters, 1990. **168**(3-4): p. 304-308.
 122. Sodickson, D.K., M.H. Levitt, S. Vega, and R.G. Griffin, *Broad-Band Dipolar Recoupling in the Nuclear-Magnetic-Resonance of Rotating Solids*. Journal of Chemical Physics, 1993. **98**(9): p. 6742-6748.
 123. Bennett, A.E., R.G. Griffin, and S. Vega, *Recoupling of Homo- and Heteronuclear Dipolar interactions in Rotating solids*. NMR Basic Principles and Progress, 1994. **33**: p. 1-77.
 124. Vanderhart, D.L., *Influence of Molecular Packing on Solid-State C-13 Chemical-Shifts - the N-Alkanes*. Journal of Magnetic Resonance, 1981. **44**(1): p. 117-125.
 125. Musacchio, A., M. Noble, R. Pauptit, R. Wierenga, and M. Saraste, *Crystal-Structure of a Src-Homology-3 (Sh3) Domain*. Nature, 1992. **359**(6398): p. 851-855.
 126. Pauli, J., B. van Rossum, H. Forster, H.J.M. de Groot, and H. Oschkinat, *Sample optimization and identification of signal patterns of amino acid side chains in 2D RFDR spectra of the alpha-spectrin SH3 domain*. Journal of Magnetic Resonance, 2000. **143**(2): p. 411-416.
 127. McDermott, G., S.M. Prince, A.A. Freer, A.M. Hawthornthwaitelawless, M.Z. Papiz, R.J. Cogdell, and N.W. Isaacs, *Crystal-Structure of an Integral Membrane Light-Harvesting Complex from Photosynthetic Bacteria*. Nature, 1995. **374**(6522): p. 517-521.
 128. Subramanian, E., Lalitha, V., *Crystal Structure of a Tripeptide, L-Alanyl-Glycyl-Glycine and Its Relevance to the Poly(glycine)-II Type of Conformation*. Biopolymers, 1983. **22**: p. 833-838.
 129. Bennett, A.E., D.P. Weliky, and R. Tycko, *Quantitative conformational measurements in solid state NMR by constant-time homonuclear dipolar recoupling*. Journal of the American Chemical Society, 1998. **120**(19): p. 4897-4898.
 130. Baldus, M., M. Tomaselli, B.H. Meier, and R.R. Ernst, *Broad-Band Polarization-Transfer Experiments for Rotating Solids*. Chemical Physics Letters, 1994. **230**(4-5): p. 329-336.
 131. BioMagResBank: A repository for data from NMR spectroscopy on proteins, p.a.n.a., <http://www.bmrb.wisc.edu/index.html>.

132. Havlin, R.H., H.B. Le, D.D. Laws, A.C. deDios, and E. Oldfield, *An ab initio quantum chemical investigation of carbon-13 NMR shielding tensors in glycine, alanine, valine, isoleucine, serine, and threonine: Comparisons between helical and sheet tensors, and the effects of (x)(1) on shielding*. Journal of the American Chemical Society, 1997. **119**(49): p. 11951-11958.
133. Tycko, R., D.P. Weliky, and A.E. Berger, *Investigation of molecular structure in solids by two- dimensional NMR exchange spectroscopy with magic angle spinning*. Journal of Chemical Physics, 1996. **105**(18): p. 7915-7930.
134. Feng, X., P.J.E. Verdegem, M. Eden, D. Sandstrom, Y.K. Lee, P.H.M. Bovee-Geurts, W.J. de Grip, J. Lugtenburg, H.J.M. de Groot, and M.H. Levitt, *Determination of a molecular torsional angle in the metarhodopsin-I photointermediate of rhodopsin by double-quantum solid-state NMR*. Journal of Biomolecular NMR, 2000. **16**(1): p. 1-8.
135. Meiler, J., W. Peti, and C. Griesinger, *DipoCoup: A versatile program for 3D-structure homology comparison based on residual dipolar couplings and pseudocontact shifts*. Journal of Biomolecular Nmr, 2000. **17**(4): p. 283-294.
136. Chou, J.J., S.P. Li, and A. Bax, *Study of conformational rearrangement and refinement of structural homology models by the use of heteronuclear dipolar couplings*. Journal of Biomolecular Nmr, 2000. **18**(3): p. 217-227.
137. Bowers, P.M., C.E.M. Strauss, and D. Baker, *De novo protein structure determination using sparse NMR data*. Journal of Biomolecular Nmr, 2000. **18**(4): p. 311-318.
138. Zhang, S., B.H. Meier, and R.R. Ernst, *Polarization Echoes in NMR*. Physical Review Letters, 1992. **69**(14): p. 2149-2151.
139. Tomaselli, M., S. Hediger, D. Suter, and R.R. Ernst, *Nuclear magnetic resonance polarization and coherence echoes in static and rotating solids*. Journal of Chemical Physics, 1996. **105**(24): p. 10672-10681.
140. Wilhelm, M., H. Feng, U. Tracht, and H.W. Spiess, *2D CP/MAS C-13 isotropic chemical shift correlation established by H-1 spin diffusion*. Journal of Magnetic Resonance, 1998. **134**(2): p. 255-260.
141. Mulder, F.M., W. Heinen, M. van Duin, J. Lugtenburg, and H.J.M. de Groot, *Spin diffusion with C-13 selection and detection for the characterization of morphology in labeled polymer blends with MAS NMR*. Journal of the American Chemical Society, 1998. **120**(49): p. 12891-12894.
142. Ishii, Y. and R. Tycko, *Sensitivity enhancement in solid state N-15 NMR by indirect detection with high-speed magic angle spinning*. Journal of Magnetic Resonance, 2000. **142**(1): p. 199-204.
143. Oas, T.G., R.G. Griffin, and M.H. Levitt, *Rotary Resonance Recoupling of Dipolar Interactions in Solid- State Nuclear Magnetic-Resonance Spectroscopy*. Journal of Chemical Physics, 1988. **89**(2): p. 692-695.
144. Nielsen, N.C., F. Creuzet, R.G. Griffin, and M.H. Levitt, *Enhanced Double-Quantum Nuclear-Magnetic-Resonance in Spinning Solids at Rotational Resonance*. Journal of Chemical Physics, 1992. **96**(8): p. 5668-5677.
145. Baldus, M., T.O. Levante, and B.H. Meier, *Numerical-Simulation of Magnetic-Resonance Experiments - Concepts and Applications to Static, Rotating and Double Rotating Experiments*. Zeitschrift Fur Naturforschung Section a-a Journal of Physical Sciences, 1994. **49**(1-2): p. 80-88.

146. Bennett, A.E., J.H. Ok, R.G. Griffin, and S. Vega, *Chemical-Shift Correlation Spectroscopy in Rotating Solids - Radio Frequency-Driven Dipolar Recoupling and Longitudinal Exchange*. Journal of Chemical Physics, 1992. **96**(11): p. 8624-8627.
147. Suter, D. and R.R. Ernst, *Spectral Spin Diffusion in the Presence of an Extraneous Dipolar Reservoir*. Physical Review B, 1982. **25**(9): p. 6038-6041.
148. Suter, D. and R.R. Ernst, *Spin Diffusion in Resolved Solid-State Nmr-Spectra*. Physical Review B, 1985. **32**(9): p. 5608-5627.
149. Kubo, A. and C.A. McDowell, *Spectral Spin Diffusion in Polycrystalline Solids under Magic-Angle Spinning*. Journal of the Chemical Society-Faraday Transactions I, 1988. **84**: p. 3713-3730.
150. Hohlwein, D., *Photographic neutron diffraction study of L-histidine-HCl-H₂O by modified Laue method*. Acta Crystallographica Section A, 1977. **33**(JUL1): p. 649-654.
151. Jeener, J., B.H. Meier, P. Bachmann, and R.R. Ernst, *Investigation of Exchange Processes by 2-Dimensional Nmr- Spectroscopy*. Journal of Chemical Physics, 1979. **71**(11): p. 4546-4553.
152. Smith, S.O., K. Aschheim, and M. Groesbeek, *Magic angle spinning NMR spectroscopy of membrane proteins*. Quarterly Reviews of Biophysics, 1996. **29**(4): p. 395-449.
153. Andrew, E.R., A. Bradbury, R.G. Eades, and V.T. Wynn, *Nuclear cross-relaxation induced by specimen rotation*. Physics Letters, 1963. **4**(2): p. 99-100.
154. Andrew, E.R., S. Clough, L.F. Farnell, T.D. Gledhill, and I. Roberts, *Resonant rotational broadening of nuclear magnetic resonance spectra*. Physics Letters, 1966. **21**(5): p. 505-&.
155. Bennett, A.E., J.H. Ok, R.G. Griffin, and S. Vega, *Chemical shift correlation spectroscopy in rotating solids: radio frequency driven dipolar recoupling and longitudinal exchange*. Journal of Chemical Physics, 1992. **96**(11): p. 8624-8627.
156. Gullion, T. and J. Schaefer, *Rotational-echo double-resonance NMR*. Journal of Magnetic Resonance, 1989. **81**(1): p. 196-200.
157. Balazs, Y.S. and L.K. Thompson, *Practical methods for solid-state NMR distance measurements on large biomolecules: Constant-time rotational resonance*. Journal of Magnetic Resonance, 1999. **139**(2): p. 371-376.
158. Colombo, M.G., B.H. Meier, and R.R. Ernst, *Rotor-driven spin diffusion in natural abundance ¹³C spin systems*. Chemical Physics Letters, 1988. **146**(3-4): p. 189-196.
159. Costa, P.R., B.Q. Sun, and R.G. Griffin, *Rotational resonance tickling: Accurate internuclear distance measurement in solids*. Journal of the American Chemical Society, 1997. **119**(44): p. 10821-10830.
160. Bechmann, M., X. Helluy, and A. Sebald, *Double-quantum-filtered rotational-resonance MAS NMR in the presence of large chemical shielding anisotropies*. Journal of Magnetic Resonance, 2001. **152**(1): p. 14-25.
161. Hediger, S., B.H. Meier, and R.R. Ernst, *Adiabatic Passage Hartmann-Hahn Cross-Polarization in Nmr under Magic-Angle Sample-Spinning*. Chemical Physics Letters, 1995. **240**(5-6): p. 449-456.

162. Levitt, M.H., D.P. Raleigh, F. Creuzet, and R.G. Griffin, *Theory and Simulations of Homonuclear Spin Pair Systems in Rotating Solids*. Journal of Chemical Physics, 1990. **92**(11): p. 6347-6364.
163. Helmle, M., Y.K. Lee, P.J.E. Verdegem, X. Feng, T. Karlsson, J. Lugtenburg, H.J.M. de Groot, and M.H. Levitt, *Anomalous rotational resonance spectra in magic-angle spinning NMR*. Journal of Magnetic Resonance, 1999. **140**(2): p. 379-403.
164. Karlsson, T. and M.H. Levitt, *Longitudinal rotational resonance echoes in solid state nuclear magnetic resonance: Investigation of zero quantum spin dynamics*. Journal of Chemical Physics, 1998. **109**(13): p. 5493-5507.
165. Peersen, O.B., M. Groesbeek, S. Aimoto, and S.O. Smith, *Analysis of Rotational Resonance Magnetization Exchange Curves from Crystalline Peptides*. Journal of the American Chemical Society, 1995. **117**(27): p. 7228-7237.
166. Ye, C.H., R.Q. Fu, J.Z. Hu, L. Hou, and S.W. Ding, *Carbon-13 chemical shift anisotropies of solid amino acids*. Magnetic Resonance in Chemistry, 1993. **31**(8): p. 699-704.
167. Hong, M., *Solid-state NMR determination of C-13 alpha chemical shift anisotropies for the identification of protein secondary structure*. Journal of the American Chemical Society, 2000. **122**(15): p. 3762-3770.
168. Nilges, M., *Ambiguous distance data in the calculation of NMR structures*. Folding & Design, 1997. **2**(4): p. S53-S57.
169. Bruckner, R. and F. Titgemeyer, *Carbon catabolite repression in bacteria: choice of the carbon source and autoregulatory limitation of sugar utilization*. FEMS Microbiology Letters, 2002. **209**(2): p. 141-148.
170. Galinier, A., J. Haiech, M.C. Kilhoffer, M. Jaquinod, J. Stulke, J. Deutscher, and I. Martin-Verstraete, *The Bacillus subtilis crh gene encodes a HPr-like protein involved in carbon catabolite repression*. Proceedings of the National Academy of Sciences of the United States of America, 1997. **94**(16): p. 8439-8444.
171. Galinier, A., M. Kravanja, R. Engelmann, W. Hengstenberg, M.C. Kilhoffer, J. Deutscher, and J. Haiech, *New protein kinase and protein phosphatase families mediate signal transduction in bacterial catabolite repression*. Proceedings of the National Academy of Sciences of the United States of America, 1998. **95**(4): p. 1823-1828.
172. Deutscher, J., A. Galinier, and I. Martin-Verstraete, in *Bacillus subtilis and its closest relatives: From genes to cells*, A.L. Sonenschein, J.A. Hoch, and R. Losick, Editors. 2001, ASM Press: Washington. p. 129-150.
173. Deutscher, J., E. Kuster, U. Bergstedt, V. Charrier, and W. Hillen, *Protein Kinase-Dependent Hpr/CcpA Interaction Links Glycolytic Activity to Carbon Catabolite Repression in Gram-Positive Bacteria*. Molecular Microbiology, 1995. **15**(6): p. 1049-1053.
174. Jones, B.E., V. Dossonnet, E. Kuster, W. Hillen, J. Deutscher, and R.E. Klevit, *Binding of the catabolite repressor protein CcpA to its DNA target is regulated by phosphorylation of its corepressor HPr*. Journal of Biological Chemistry, 1997. **272**(42): p. 26530-26535.
175. Stulke, J. and W. Hillen, *Regulation of carbon catabolism in Bacillus species*. Annual Review of Microbiology, 2000. **54**: p. 849-880.

176. Juy, M., F. Penin, A. Favier, A. Galinier, R. Montserret, R. Haser, J. Deutscher, and A. Bockmann, submitted, 2003.
177. Favier, A., B. Brutscher, M. Blackledge, A. Galinier, J. Deutscher, F. Penin, and D. Marion, *Solution structure and dynamics of Crh, the Bacillus subtilis catabolite repression HPr*. Journal of Molecular Biology, 2002. **317**(1): p. 131-144.
178. Penin, F., A. Favier, R. Montserret, B. Brutscher, J. Deutscher, D. Marion, and A. Galinier, *Evidence for a dimerisation state of the Bacillus subtilis catabolite repression HPr-like protein, Crh*. Journal of Molecular Microbiology and Biotechnology, 2001. **3**(3): p. 429-432.
179. Metz, G., X.L. Wu, and S.O. Smith, *Ramped-amplitude cross-polarization in Magic-Angle-Spinning NMR*. Journal of Magnetic Resonance Series A, 1994. **110**(2): p. 219-227.
180. Straus, S.K., T. Bremi, and R.R. Ernst, *Resolution enhancement by homonuclear J decoupling in solid-state MAS NMR*. Chemical Physics Letters, 1996. **262**(6): p. 709-715.
181. Nielsen, N.C., H. Bildsoe, H.J. Jakobsen, and M.H. Levitt, *Double-quantum homonuclear rotary resonance: Efficient dipolar recovery in magic-angle spinning nuclear magnetic resonance*. Journal of Chemical Physics, 1994. **101**(3): p. 1805-1812.
182. Detken, A., E.H. Hardy, M. Ernst, M. Kainosho, T. Kawakami, S. Aimoto, and B.H. Meier, *Methods for sequential resonance assignment in solid, uniformly C-13, N-15 labelled peptides: Quantification and application to antamanide*. Journal of Biomolecular Nmr, 2001. **20**(3): p. 203-221.
183. Jaroniec, C.P., C.E. MacPhee, N.S. Astrof, C.M. Dobson, and R.G. Griffin, *Molecular conformation of a peptide fragment of transthyretin in an amyloid fibril*. Proc. Natl. Acad. Sci., 2002. **99**: p. 16748-16753.
184. Petkova, A.T., M. Baldus, M. Belenky, M. Hong, R.G. Griffin, and J. Herzfeld, Journal of Magnetic Resonance, 2003. **160**: p. 1-12.
185. Guex, N. and M.C. Peitsch, *SWISS-MODEL and the Swiss-PdbViewer: An environment for comparative protein modeling*. Electrophoresis, 1997. **18**(15): p. 2714-2723.
186. Fieulaine, S., S. Morera, S. Poncet, I. Mijakovic, A. Galinier, J. Janin, J. Deutscher, and S. Nessler, *X-ray structure of a bifunctional protein kinase in complex with its protein substrate HPr*. Proceedings of the National Academy of Sciences of the United States of America, 2002. **99**(21): p. 13437-13441.
187. Carraway, R. and S.E. Leeman, *Isolation of a new hypotensive peptide, neurotensin, from bovine hypothalami*. Journal of Biological Chemistry, 1973. **248**(19): p. 6854-6861.
188. Martin, S., J.M. Botto, J.P. Vincent, and J. Mazella, *Pivotal role of an aspartate residue in sodium sensitivity and coupling to G proteins of neurotensin receptors*. Molecular Pharmacology, 1999. **55**(2): p. 210-215.
189. Vita, N., P. Laurent, S. Lefort, P. Chalon, X. Dumont, M. Kaghad, D. Gully, G. Lefur, P. Ferrara, and D. Caput, *Cloning and expression of a complementary-DNA encoding a aigh-affinity human neurotensin receptor*. Febs Letters, 1993. **317**(1-2): p. 139-142.

190. Tanaka, K., M. Masu, and S. Nakanishi, *Structure and functional expression of the cloned rat neurotensin receptor*. *Neuron*, 1990. **4**(6): p. 847-854.
191. Watson, M., P.J. Isackson, M. Makker, M.S. Yamada, M. Yamada, B. Cusack, and E. Richelson, *Identification of a polymorphism in the human neurotensin receptor gene*. *Mayo Clinic Proceedings*, 1993. **68**(11): p. 1043-1048.
192. Chalon, P., N. Vita, M. Kaghad, M. Guillemot, J. Bonnin, B. Delpech, G. LeFur, P. Ferrara, and D. Caput, *Molecular cloning of a levocabastine-sensitive neurotensin binding site*. *Febs Letters*, 1996. **386**(2-3): p. 91-94.
193. Mazella, J., J.M. Botto, E. Guillemare, T. Coppola, P. Sarret, and J.P. Vincent, *Structure, functional expression, and cerebral localization of the levocabastine-sensitive neurotensin/neuromedin N receptor from mouse brain*. *Journal of Neuroscience*, 1996. **16**(18): p. 5613-5620.
194. Gully, D., M. Canton, R. Boigegrain, F. Jeanjean, J.C. Molimard, M. Poncelet, C. Gueudet, M. Heaulme, R. Leyris, A. Brouard, D. Pelaprat, C. Labbejullie, J. Mazella, P. Soubrie, J.P. Maffrand, W. Rostene, P. Kitabgi, and G. Lefur, *Biochemical and Pharmacological Profile of a Potent and Selective Nonpeptide Antagonist of the Neurotensin Receptor*. *Proceedings of the National Academy of Sciences of the United States of America*, 1993. **90**(1): p. 65-69.
195. Vincent, J.P., J. Mazella, and P. Kitabgi, *Neurotensin and neurotensin receptors*. *Trends in Pharmacological Sciences*, 1999. **20**(7): p. 302-309.
196. Pierce, K.L., R.T. Premont, and R.J. Lefkowitz, *Seven-transmembrane receptors*. *Nature Reviews Molecular Cell Biology*, 2002. **3**(9): p. 639-650.
197. Chalmers, D.T. and D.P. Behan, *The use of constitutively active GPCRs in drug discovery and functional genomics*. *Nature Reviews Drug Discovery*, 2002. **1**(8): p. 599-608.
198. Palczewski, K., T. Kumasaka, T. Hori, C.A. Behnke, H. Motoshima, B.A. Fox, I. Le Trong, D.C. Teller, T. Okada, R.E. Stenkamp, M. Yamamoto, and M. Miyano, *Crystal structure of rhodopsin: A G protein-coupled receptor*. *Science*, 2000. **289**(5480): p. 739-745.
199. Klabunde, T. and G. Hessler, *Drug design strategies for targeting G-protein-coupled receptors*. *Chembiochem*, 2002. **3**(10): p. 929-944.
200. Labbe-Jullie, C., S. Barroso, D. Nicolas-Eteve, J.L. Reversat, J.M. Botto, J. Mazella, J.M. Bernassau, and P. Kitabgi, *Mutagenesis and modeling of the neurotensin receptor NTR1 - Identification of residues that are critical for binding SR 48692, a nonpeptide neurotensin antagonist*. *Journal of Biological Chemistry*, 1998. **273**(26): p. 16351-16357.
201. Barroso, S., F. Richard, D. Nicolas-Etheve, J.L. Reversat, J.M. Bernassau, P. Kitabgi, and C. Labbe-Jullie, *Identification of residues involved in neurotensin binding and modeling of the agonist binding site in neurotensin receptor 1*. *Journal of Biological Chemistry*, 2000. **275**(1): p. 328-336.
202. Richard, F., S. Barroso, D. Nicolas-Etheve, P. Kitabgi, and C. Labbe-Jullie, *Impaired G protein coupling of the neurotensin receptor 1 by mutations in extracellular loop 3*. *European Journal of Pharmacology*, 2001. **433**(1): p. 63-71.

203. Balaram, P., Bothnerb.Aa, and E. Breslow, *Nuclear Magnetic-Resonance Studies of Interaction of Peptides and Hormones with Bovine Neurophysin*. *Biochemistry*, 1973. **12**(23): p. 4695-4704.
204. Clore, G.M. and A.M. Gronenborn, *Theory and Applications of the Transferred Nuclear Overhauser Effect to the Study of the Conformations of Small Ligands Bound to Proteins*. *Journal of Magnetic Resonance*, 1982. **48**(3): p. 402-417.
205. Blommers, M.J.J., W. Stark, C.E. Jones, D. Head, C.E. Owen, and W. Jahnke, *Transferred cross-correlated relaxation complements transferred NOE: Structure of an IL-4R-derived peptide bound to STAT-6*. *Journal of the American Chemical Society*, 1999. **121**(9): p. 1949-1953.
206. Carlomagno, T., I.C. Felli, M. Czech, R. Fischer, M. Sprinzl, and C. Griesinger, *Transferred cross-correlated relaxation: Application to the determination of sugar pucker in an aminoacylated tRNA-mimetic weakly bound to EF-Tu*. *Journal of the American Chemical Society*, 1999. **121**(9): p. 1945-1948.
207. Inooka, H., T. Ohtaki, O. Kitahara, T. Ikegami, S. Endo, C. Kitada, K. Ogi, H. Onda, M. Fujino, and M. Shirakawa, *Conformation of a peptide ligand bound to its G-protein coupled receptor*. *Nature Structural Biology*, 2001. **8**(2): p. 161-165.
208. Sargent, D.F. and R. Schwyzer, *Membrane lipid phase as catalyst for peptide receptor interactions*. *Proceedings of the National Academy of Sciences of the United States of America*, 1986. **83**(16): p. 5774-5778.
209. White, S.H. and W.C. Wimley, *Hydrophobic interactions of peptides with membrane interfaces*. *Biochimica Et Biophysica Acta-Reviews on Biomembranes*, 1998. **1376**(3): p. 339-352.
210. Lerch, M., V. Gafner, R. Bader, B. Christen, G. Folkers, and O. Zerbe, *Bovine pancreatic polypeptide (bPP) undergoes significant changes in conformation and dynamics upon binding to DPC micelles*. *Journal of Molecular Biology*, 2002. **322**(5): p. 1117-1133.
211. Bader, R., G. Rytz, M. Lerch, A.G. Beck-Sickinger, and O. Zerbe, *Key motif to gain selectivity at the neuropeptide Y-5-receptor: Structure and dynamics of micelle-bound Ala(31), Pro(32) -NPY*. *Biochemistry*, 2002. **41**(25): p. 8031-8042.
212. Okada, T., Y. Fujiyoshi, M. Silow, J. Navarro, E.M. Landau, and Y. Shichida, *Functional role of internal water molecules in rhodopsin revealed by x-ray crystallography*. *Proceedings of the National Academy of Sciences of the United States of America*, 2002. **99**(9): p. 5982-5987.
213. Klein-Seetharaman, J., P.J. Reeves, M.C. Loewen, E.V. Getmanova, L. Chung, H. Schwalbe, P.E. Wright, and H.G. Khorana, *Solution NMR spectroscopy of alpha-N-15 lysine-labeled rhodopsin: The single peak observed in both conventional and TROSY-type HSQC spectra is ascribed to Lys-339 in the carboxyl-terminal peptide sequence*. *Proceedings of the National Academy of Sciences of the United States of America*, 2002. **99**(6): p. 3452-3457.
214. Gardner, K.H. and L.E. Kay, *The use of H-2, C-13, N-15 multidimensional NMR to study the structure and dynamics of proteins*. *Annual Review of Biophysics and Biomolecular Structure*, 1998. **27**: p. 357-406.
215. Hwang, P.M., W.Y. Choy, E.I. Lo, L. Chen, J.D. Forman-Kay, C.R.H. Raetz, G.G. Prive, R.E. Bishop, and L.E. Kay, *Solution structure and dynamics of the outer*

- membrane enzyme PagP by NMR*. Proceedings of the National Academy of Sciences of the United States of America, 2002. **99**(21): p. 13560-13565.
216. Patzelt, H., B. Simon, A. terLaak, B. Kessler, R. Kuhne, P. Schmieder, D. Oesterhelt, and H. Oschkinat, *The structures of the active center in dark-adapted bacteriorhodopsin by solution-state NMR spectroscopy*. Proceedings of the National Academy of Sciences of the United States of America, 2002. **99**(15): p. 9765-9770.
 217. Hilty, C., C. Fernandez, G. Wider, and K. Wüthrich, *Side chain NMR assignments in the membrane protein OmpX reconstituted in DHPC micelles*. Journal of Biomolecular Nmr, 2002. **23**(4): p. 289-301.
 218. Arora, A., F. Abildgaard, J.H. Bushweller, and L.K. Tamm, *Structure of outer membrane protein A transmembrane domain by NMR spectroscopy*. Nature Structural Biology, 2001. **8**(4): p. 334-338.
 219. Fernandez, C., K. Adeishvili, and K. Wüthrich, *Transverse relaxation-optimized NMR spectroscopy with the outer membrane protein OmpX in dihexanoyl phosphatidylcholine micelles*. Proceedings of the National Academy of Sciences of the United States of America, 2001. **98**(5): p. 2358-2363.
 220. de Groot, H.J.M., *Solid-state NMR spectroscopy applied to membrane proteins*. Current Opinion in Structural Biology, 2000. **10**(5): p. 593-600.
 221. Williamson, P.T.F., S. Bains, C. Chung, R. Cooke, and A. Watts, *Probing the environment of neurotensin whilst bound to the neurotensin receptor by solid state NMR*. Febs Letters, 2002. **518**(1-3): p. 111-115.
 222. Creuzet, F., A. McDermott, R. Gebhard, K. Vanderhoef, M.B. Spijkerassink, J. Herzfeld, J. Lugtenburg, M.H. Levitt, and R.G. Griffin, *Determination of Membrane-Protein Structure by Rotational Resonance Nmr - Bacteriorhodopsin*. Science, 1991. **251**(4995): p. 783-786.
 223. Creemers, A.F.L., S. Kiihne, P.H.M. Bovee-Geurts, W.J. DeGrip, J. Lugtenburg, and H.J.M. de Groot, *H-1 and C-13 MAS NMR evidence for pronounced ligand-protein interactions involving the ionone ring of the retinylidene chromophore in rhodopsin*. Proceedings of the National Academy of Sciences of the United States of America, 2002. **99**(14): p. 9101-9106.
 224. Weliky, D.P., A.E. Bennett, A. Zvi, J. Anglister, P.J. Steinbach, and R. Tycko, *Solid-state NMR evidence for an antibody-dependent conformation of the V3 loop of HIV-1 gp120*. Nature Structural Biology, 1999. **6**(2): p. 141-145.
 225. Bax, A., R. Freeman, and S.P. Kempell, *Natural Abundance C-13-C-13 Coupling Observed Via Double-Quantum Coherence*. Journal of the American Chemical Society, 1980. **102**(14): p. 4849-4851.
 226. Munowitz, M. and A. Pines, *Principles and Applications of Multiple-quantum NMR*. Adv. Chem. Phys., 1987. **66**: p. 1-152.
 227. Dedios, A.C., J.G. Pearson, and E. Oldfield, *Secondary and Tertiary Structural Effects on Protein Nmr Chemical-Shifts - an Abinitio Approach*. Science, 1993. **260**(5113): p. 1491-1496.
 228. Saito, H., *Conformation-Dependent C-13 Chemical-Shifts - a New Means of Conformational Characterization as Obtained by High-Resolution Solid-State C-13 Nmr*. Magnetic Resonance in Chemistry, 1986. **24**(10): p. 835-852.

229. Heller, J., D.D. Laws, M. Tomaselli, D.S. King, D.E. Wemmer, A. Pines, R.H. Havlin, and E. Oldfield, *Determination of dihedral angles in peptides through experimental and theoretical studies of alpha-carbon chemical shielding tensors*. Journal of the American Chemical Society, 1997. **119**(33): p. 7827-7831.
230. Laws, D.D., H.M.L. Bitter, K. Liu, H.L. Ball, K. Kaneko, H. Wille, F.E. Cohen, S.B. Prusiner, A. Pines, and D.E. Wemmer, *Solid-state NMR studies of the secondary structure of a mutant prion protein fragment of 55 residues that induces neurodegeneration*. Proceedings of the National Academy of Sciences of the United States of America, 2001. **98**(20): p. 11686-11690.
231. Petkova, A.T., Y. Ishii, J.J. Balbach, O.N. Antzutkin, R.D. Leapman, F. Delaglio, and R. Tycko, *A structural model for Alzheimer's beta-amyloid fibrils based on experimental constraints from solid state NMR*. Proc. Natl. Acad. Sci., 2002. **99**(26): p. 16742-16747.
232. Pines, A., M.G. Gibby, and J.S. Waugh, *Proton-enhanced NMR of dilute spins in solids*. Journal of Chemical Physics, 1973. **59**(2): p. 569-590.
233. Atherthon, E. and R.C. Sheppard, *Solid phase peptide synthesis: A practical approach*. 1989, Oxford: IRL Press.
234. Grisshammer, R. and J. Tucker, *Quantitative evaluation of neurotensin receptor purification by immobilized metal affinity chromatography*. Protein Expression and Purification, 1997. **11**(1): p. 53-60.
235. Grisshammer, R., T. Grunwald, and A.K. Sohal, *Characterization of an antibody Fv fragment that binds to the human, but not to the rat neurotensin receptor NTS-1*. Protein Expression and Purification, 2002. **24**(3): p. 505-512.
236. Schaffner, W. and C. Weissmann, *A rapid, sensitive, and specific method for the determination of protein in dilute solution*. Analytical Biochemistry, 1973. **56**(2): p. 502-514.
237. Grisshammer, R., P. Averbek, and A.K. Sohal, *Improved purification of a rat neurotensin receptor expressed in Escherichia coli*. Biochemical Society Transactions, 1999. **27**: p. 899-903.
238. Grisshammer, R. and E. Hermans, *Functional coupling with Goa and Goi1 protein subunits promotes high-affinity agonist binding to the neurotensin receptor NTS-1 expressed in Escherichia coli*. FEBS Letters, 2001. **493**: p. 101-105.
239. Brinkmann, A., M. Eden, and M.H. Levitt, *Synchronous helical pulse sequences in magic-angle spinning nuclear magnetic resonance: Double quantum recoupling of multiple-spin systems*. Journal of Chemical Physics, 2000. **112**(19): p. 8539-8554.
240. Klabunde, T. and G. Hessler, *Drug design strategies for targeting G-protein-coupled receptors*. Chembiochem, 2002. **3**: p. 928-944.
241. Xu, G.-Y. and C.M. Deber, *Conformations of neurotensin in solution and in membrane environments studied by 2-D NMR spectroscopy*. International Journal of Peptide and Protein Research, 1991. **37**(6): p. 528-535.
242. Nieto, J.L., M. Rico, J. Santoro, J. Herranz, and F.J. Bermejo, *Assignment and conformation of neurotensin in aqueous solution by 1H NMR*. Int. J. Peptide Protein Res., 1986. **28**: p. 315-323.

243. Brunger, A.T., P.D. Adams, G.M. Clore, W.L. DeLano, P. Gros, R.W. Grosse-Kunstleve, J.S. Jiang, J. Kuszewski, M. Nilges, N.S. Pannu, R.J. Read, L.M. Rice, T. Simonson, and G.L. Warren, *Crystallography & NMR system: A new software suite for macromolecular structure determination*. Acta Crystallographica Section D-Biological Crystallography, 1998. **54**: p. 905-921.
244. Pang, Y.-P., B. Cusack, K. Groshan, and E. Richelson, *Proposed ligand binding site of the transmembrane receptor for neurotensin(8-13)*. Journal of Biological Chemistry, 1996. **271**(25): p. 15060-15068.
245. Barroso, S., F. Richard, D. Nicolas-Ethève, J.-L. Reversat, J.-M. Bernassau, P. Kitabgi, and C. Labbé-Jullié, *Identification of residues involved in neurotensin binding and modeling of the agonist binding site in neurotensin receptor 1*. Journal of Biological Chemistry, 2000. **275**(1): p. 328-336.
246. Richard, F., S. Barroso, D. Nicolas-Ethève, P. Kitabgi, and C. Labbé-Jullié, *Impaired G protein coupling of the neurotensin receptor 1 by mutations in extracellular loop 3*. European Journal of Pharmacology, 2001. **433**(1): p. 63-71.
247. Feng, X., P.J.E. Verdegem, Y.K. Lee, D. Sandstrom, M. Eden, P. BoveeGeurts, W.J. deGrip, J. Lugtenburg, H.J.M. deGroot, and M.H. Levitt, *Direct determination of a molecular torsional angle in the membrane protein rhodopsin by solid-state NMR*. Journal of the American Chemical Society, 1997. **119**(29): p. 6853-6857.
248. Hatefi, Y., *The mitochondrial electron transport and oxidative phosphorylation system*. Annual Review of Biochemistry, 1985. **54**: p. 1015-1069.
249. Xia, D., C.A. Yu, H. Kim, J.Z. Xian, A.M. Kachurin, L. Zhang, L. Yu, and J. Deisenhofer, *Crystal structure of the cytochrome bc₁ complex from bovine heart mitochondria*. Science, 1997. **277**(5322): p. 60-66.
250. Iwata, S., J.W. Lee, K. Okada, J.K. Lee, M. Iwata, B. Rasmussen, T.A. Link, S. Ramaswamy, and B.K. Jap, *Complete structure of the 11-subunit bovine mitochondrial cytochrome bc₁ complex*. Science, 1998. **281**(5373): p. 64-71.
251. Zhang, Z.L., L.S. Huang, V.M. Shulmeister, Y.I. Chi, K.K. Kim, L.W. Hung, A.R. Crofts, E.A. Berry, and S.H. Kim, *Electron transfer by domain movement in cytochrome bc₁*. Nature, 1998. **392**(6677): p. 677-684.
252. Hunte, C., J. Koepke, C. Lange, T. Rossmann, and H. Michel, *Structure at 2.3 angstrom resolution of the cytochrome bc₁ complex from the yeast Saccharomyces cerevisiae co-crystallized with an antibody Fv fragment*. Structure with Folding & Design, 2000. **8**(6): p. 669-684.
253. Ding, H., C.C. Moser, D.E. Robertson, M.K. Tokito, F. Daldal, and P.L. Dutton, *Ubiquinone pair in the Q_o site central to the primary energy conversion reactions of cytochrome bc₁ complex*. Biochemistry, 1995. **34**(49): p. 15979-15996.
254. Bartoschek, S., M. Johansson, B.H. Geierstanger, J.G. Okun, C.R.D. Lancaster, E. Humpfer, L. Yu, C.A. Yu, C. Griesinger, and U. Brandt, *Three molecules of ubiquinone bind specifically to mitochondrial cytochrome bc₁ complex*. Journal of Biological Chemistry, 2001. **276**(38): p. 35231-35234.
255. Tycko, R. and G. Dabbagh, *Measurement of nuclear magnetic dipole-dipole couplings in magic angle spinning NMR*. Chemical Physics Letters, 1990. **173**(5-6): p. 461-465.

256. Fujiwara, T., A. Ramamoorthy, K. Nagayama, K. Hioka, and T. Fujito, *Dipolar Hohaha under MAS conditions for solid-state NMR*. Chemical Physics Letters, 1993. **212**(1-2): p. 81-84.
257. Baldus, M., M. Tomaselli, B.H. Meier, and R.R. Ernst, *Broadband polarization transfer experiments for rotating solids*. Chemical Physics Letters, 1994. **230**(4-5): p. 329-336.
258. Gregory, D.M., D.J. Mitchell, J.A. Stringer, S. Kiihne, J.C. Shiels, J. Callahan, M.A. Mehta, and G.P. Drobny, *Windowless dipolar recoupling. The detection of weak dipolar couplings between spin-1/2 nuclei with large chemical shift anisotropies*. Chemical Physics Letters, 1995. **246**(6): p. 654-663.
259. Lee, Y.K., N.D. Kurur, M. Helmle, O.G. Johannessen, N.C. Nielsen, and M.H. Levitt, *Efficient dipolar recoupling in the NMR of rotating solids: A sevenfold symmetrical radiofrequency pulse sequence*. Chemical Physics Letters, 1995. **242**(3): p. 304-309.
260. Lehmann, M.S., T.F. Koetzle, and W.C. Hamilton, *Precision Neutron-Diffraction Structure Determination of Protein and Nucleic-Acid Components .1. Crystal and Molecular Structure of Amino-Acid L-Alanine*. Journal of the American Chemical Society, 1972. **94**(8): p. 2657-&.
261. Herzfeld, J. and A.E. Berger, *Sideband Intensities in Nmr-Spectra of Samples Spinning at the Magic Angle*. Journal of Chemical Physics, 1980. **73**(12): p. 6021-6030.

Zusammenfassung

Spektroskopie erlaubt die Eigenschaften und Struktur der Materie durch Einsatz elektromagnetischer Strahlung auf molekularer Ebene zu untersuchen. Die Kernspinresonanz (NMR) ist ein spezielles Gebiet der Spektroskopie, die die magnetischen Eigenschaften der Atomkerne auswertet. Ein kurzer Überblick über die historischen Weiterentwicklungen im Bereich der NMR ergibt sich aus einer Betrachtung der Nobelpreise, die bisher im Zusammenhang der NMR vergeben wurden: 1952 empfangen Felix Bloch und Edward Purcell den Nobelpreis in Physik "für ihre Entwicklung neuer Methoden zur magnetische Kernmessung und damit verbundener Entdeckungen". Später wurden die Grundlage der modernen NMR, die Fourier-Transformation, von Richard R. Ernst vorgestellt. R.R. Ernst erhielt den Nobelpreis für Chemie im Jahre 1991 "für seine Beiträge zur methodischen Entwicklung der Hoch-auflösungs-NMR-Spektroskopie". Diese NMR Methoden konnten bei vielen biologischen Fragestellungen wichtige strukturelle Antworten liefern. Daher wurde Kurt Wüthrich im letzten Jahr der Nobelpreis für Chemie "für seine Entwicklung der NMR-Spektroskopie zur Bestimmung der dreidimensionalen Struktur biologischer Makromoleküle in Flüssigkeit" zuerkannt.

Bisher wurden drei-dimensionale Strukturuntersuchungen im wesentlichen durch die Röntgenstrahlkristallographie und Flüssigkeits-NMR durchgeführt. Beide Methoden erfordern in der Regel Proben mit gutem Löslichkeitsverhalten. In löslicher Umgebung kann die schnelle Molekülbewegung zu hoher spektraler Auflösung der NMR Frequenzen führen. Demgegenüber tritt die räumliche Abhängigkeit der magnetischen Interaktionen in einem starken äußeren Magnetfeld in der Festphase explizit auf und beeinflusst das NMR-Spektrum in direkter Weise. Diese Schwierigkeiten behinderten zunächst die Entwicklung von NMR Methoden, die ähnlich zur Situation in Lösungen, vollständige strukturelle Analysen erlauben. Heute können in vielen Fällen hochauflösende spektrale Bedingungen in der Festkörper-NMR durch den Einsatz der magic angle spinning (MAS) oder der makroskopischen Probenorientierung erreicht werden. Diese Bedingungen haben zum Beispiel zur Aufklärung der 3D Struktur von Gramicidin A in seiner natürlichen Membrenumgebung oder eines mikrokristallinen Proteins geführt.

Diese Beispiele zeigen, dass die Festkörper-NMR prinzipiell die Möglichkeit bietet, Moleküle in unterschiedlichen räumlichen oder chemischen Umgebungen zu studieren. Die Festkörper-NMR eignet sich daher besonders um wichtige biologische Fragen in Membran-ständigen, polymerisierten oder falsch gefalteten Proteinen zu beantworten. Neben der strukturellen Analyse dieser System bietet die Festkörper-NMR darüber hinaus die einzigartige Möglichkeit, dynamische und damit funktionelle Aspekte in den o.g. Biomolekülen zu untersuchen.

In dieser Arbeit sollten biomolekulare Anwendungen der MAS Festkörper-NMR-Spektroskopie untersucht werden. Die in der jüngsten Zeit zugänglich gewordenen ultrahohen Magnetfelder und modernste NMR-Hardware führte zu einer erheblichen Steigerung von Empfindlichkeit und Auflösung in der Festkörper-NMR-Spektroskopie. In Folge dessen wurde es möglich, mehrfach oder gleichförmig isotoopenmarkierte Proben zu untersuchen. Diese Vorgehensweise erhöht die Effizienz von NMR-Spektroskopie enorm, da im Prinzip eine Vielzahl von Informationen über die untersuchte Probe in einem einzigen Experiment zugänglich wird. Andererseits erfordert diese Herangehensweise ein spezielles Design der verwendeten Experimente.

In Kapitel 2 der vorliegenden Arbeit werden Methoden vorgestellt, mit denen die Auflösung in Spektren gleichförmig isotoopenmarkierter Proteine erhöht werden kann. Sie basieren darauf, dass in Polypeptiden die chemische Verschiebung abhängig von der lokalen Peptidrückgrat- und Seitenkettenkonformation ist. Die chemische Verschiebung, welche die Position der Resonanzen im Spektrum bestimmt, wird durch die elektronische Umgebung der Kerne bestimmt. Aus experimentellen Daten sind einige dieser Einflüsse bekannt und lassen sich dazu ausnutzen, die Resonanzfrequenzen zu manipulieren und so die Auflösung zu steigern.

In Abschnitt 2.1 werden Mehrfach-Quanten Korrelationsexperimente vorgestellt. Diese Experimente sind in der Lage, sowohl Diagonalpeaks als auch Hintergrundsignale von ^{13}C in natürlicher Häufigkeit zu unterdrücken und somit die Analyse des Spektrums zu vereinfachen. In enger Verbindung hierzu wird in Abschnitt 2.2 ein Experiment vorgestellt, mit dem die Summe und die Differenz der chemischen Verschiebungen gekoppelter Kerne bestimmt werden kann. Diese besitzen im Falle von $^{13}\text{C}_\alpha$ und $^{13}\text{C}_\beta$ eine starke Abhängigkeit von der

Konformation des Peptidrückgrats, so dass eine Bestimmung der Sekundärstruktur des Proteins erfolgen kann.

Weiterhin lässt sich die spektrale Auflösung erhöhen, indem Unterschiede in magnetischen Wechselwirkungen, Relaxationsmechanismen oder dynamische Eigenschaften der Kerne ausgenutzt werden. Insbesondere können verschieden starke dipolare Kopplungen, Anisotropien der chemischen Verschiebung und die außergewöhnlich schnelle Rotation der CH₃ Gruppe verwendet werden. In Abschnitt 2.2 wird dargestellt, wie sich die oben genannten Unterschiede im Rahmen von Dephasierungsexperimenten verwenden lassen.

Als nächstes ist es wichtig, eine Vorgehensweise zur Strukturbestimmung vollständig isotoopenmarkierter Proteine zu entwickeln (Kapitel 3). Bei Proteinen muss zunächst die Sekundärstruktur untersucht werden. In NMR-Spektren gelöster Proteine sind die isotropen chemischen Verschiebungen verschiedener Kerne, darunter auch ¹³C_α und ¹³C_β von der Konformation des Peptidrückgrates abhängig. In Abschnitt 3.1 untersuchen wir anhand dreier repräsentativer Peptide und Proteine, in wie weit dieses Konzept auch auf Festkörper-NMR-Spektroskopie angewendet werden kann. Diese Vorgehensweise ist anderen Methoden, die nur zur Bestimmung von Torsionswinkeln in selektiv markierten Verbindungen geeignet sind, vorzuziehen.

Die Tertiärstruktur kann im Festkörper durch Messen der dipolaren Kopplungen zwischen vielen Spinpaaren bestimmt werden. Die Kern-Kern-Abstände, die aus den Dipolkopplungen erhalten werden, können zur Berechnung der natürlichen Faltung des Proteins herangezogen werden. Wegen der höheren spektralen Auflösung werden im Festkörper grundsätzlich die Heterokerne ¹³C und ¹⁵N detektiert. Unter diesen Umständen können nur starke Wechselwirkungen quantitativ ermittelt werden, und im Falle von Kohlenstoff und Stickstoff sind dies nur die trivialen Abstände zwischen direkt gebundenen Atomen. Eine Möglichkeit, dieses Problem zu umgehen, ist die Bestimmung von Abständen zwischen Protonen, wie es in Lösung üblich ist, indem die Information über Proton-Proton-Abstände zur Evolution und Detektion auf benachbarte ¹³C und/oder ¹⁵N Spins übertragen wird. In Abschnitt 3.2 wird das dafür entwickelte C/NHHC Experiment erläutert. Eine weitere Methode ist es, bestimmte ¹³C-¹³C Dipolkopplungen selektiv in vollständig markierten Proben zu bestimmen. So können mit Hilfe frequenzselektiver Pulssequenzen mehrere Grenzwerte für Atomabstände ermittelt

werden, wie in Abschnitt 3.3 beschrieben. Obwohl diese Einschränkungen nicht zur vollständigen Strukturbestimmung ausreichen, können sie zur Verfeinerung der Struktur herangezogen werden.

In Kapitel 4 werden Anwendungen auf biologisch relevante Systeme gezeigt. Anhand der üblichen Experimente wurden die ^{13}C und ^{15}N NMR-Signale des „Catabolite repression histidine-containing phosphocarrier“ (Crh) Proteins in mikrokristalliner Phase vollständig zugeordnet (Abschnitt 4.1). Anschließend konnte die Sekundärstruktur untersucht und mit der Struktur aus Flüssigkeits-NMR und Röntgenstrukturanalyse verglichen werden. Der Übergang zwischen monomerer (in Lösung) und dimerer Form (im Kristall) kann so genauer untersucht werden.

Festkörper-NMR-Spektroskopie ist eine geeignete Methode zur Strukturbestimmung von Peptiden, die mit hoher Affinität an membrangebundene Proteine binden. Das größte Hindernis bei der Anwendung dieser Methode auf einen GPCR-Peptidliganden ist die geringe Empfindlichkeit. In Abschnitt 4.2 untersuchen wir die Konformation des rezeptorgebundenen N-Terminus von Neurotensin sowohl in Detergenzlösung als auch in der Membran. Die Festkörper-NMR Ergebnisse weisen auf eine gestreckte Rückgratkonformation des gebundenen Neurotensin –Peptides hin.

Selbst wenn die Struktur eines Proteins oder Proteinkomplexes bekannt ist, sind weitere Verfeinerungen oft erforderlich um fehlende oder schlecht definierte Strukturelemente zu untersuchen. Zum Beispiel konnte die Struktur des Enzymkomplexes *bc₁* und sogar dessen Interaktion mit einigen Substraten durch Röntgen-Kristallographie aufgeklärt werden. Diese Experimente konnten jedoch nicht das Bindungsmotif zweier Ubiquinol Moleküle in dem Oxidation Reaktionszentrum Q_o beleuchten. Wie in Abschnitt 4.3 beschrieben, konnten wir durch selektive ^{13}C Isotopenmarkierung intermolekulare Abstände, die die räumliche Lage dieser Moleküle charakterisieren, mit Festkörper-NMR Methoden bestimmen.

Weitere Fortschritte im Bereich der Probenvorbereitung (zum Beispiel durch modulare Isotopenmarkierung, *in vitro* Proteinexpression und der intein Technologie) und Verbesserungen in der NMR Methodik könnten zukünftig neue Anwendungen der Festkörper-NMR wie die Untersuchung großer Protein-Protein Komplexe oder die komplette

3D Beschreibung größerer Membrane Proteine ermöglichen. Festkörper-NMR Studien an mehrfach Isotopen-markierten Biomolekülen werden außerdem von verbesserten Verfahren zur 3D Strukturberechnung, z.B. bei einer begrenzten Anzahl von strukturellen Parametern, profitieren.

Anders als im Fall der Röntgenstrahlkristallographie, stellt die Proteinbewegung keine prinzipielle Schwierigkeit für Festkörper-NMR Anwendungen dar. Ergänzend zur Flüssigkeits-NMR, könnte sie sich vielmehr zu einer sehr leistungsfähigen Methode entwickeln um Protein Struktur, Dynamik oder Funktion unter biologisch relevanten Bedingungen zu studieren. Die Kombination dieser Techniken könnte zum Verständnis biologischer Funktion und damit der Chemie des Lebens mit bisher beispielloser Genauigkeit führen.

Lebenslauf

Sorin Luca, geboren am 14. März 1976 in Bacau, Rumänien.

- Seit Mai 2000: Doktorarbeit bei Dr. Marc Baldus am Max-Planck-Institut für biophysikalische Chemie Göttingen, Strukturuntersuchung an Proteinen mit Festkörper-NMR-Spektroskopie. Thema: „Solid-state NMR studies of globular and membrane proteins“.
- Januar – Juli 1999: Diplomarbeit bei Prof. Dr. Arnold Hoff am Leiden Universität, Biophysikabteilung. Thema: „EPR studies on Photosystem I activity“.
- 1994-1999: Physik Grundstudium am Bukarest Universität, Rumänien.
- 1994: Abitur, G. Lazar Gymnasium am Bukarest, Rumänien.
- 1990-1994: G. Bacovia Gymnasium am Bacau, Rumänien.